

Investigation of high- p_T phenomena within a partonic transport model

Dissertation
zur Erlangung des Doktorgrades
der Naturwissenschaften

vorgelegt beim Fachbereich Physik
der Johann Wolfgang Goethe-Universität
in Frankfurt am Main

von

Oliver Fochler

aus Frankfurt am Main

Frankfurt am Main 2011
(D 30)

Vom Fachbereich Physik (13) der Johann Wolfgang Goethe-Universität
als Dissertation angenommen.

Dekan: Prof. Dr. Michael Huth

Gutachter: Prof. Dr. Carsten Greiner, Prof. Dr. Marcus Bleicher

Datum der Disputation:

Contents

List of Figures	v
Deutschsprachige Zusammenfassung	vii
1. Overview	1
1.1. Abstract	1
1.2. Structure of this document	2
2. Introduction	3
2.1. Quantum chromodynamics	3
2.1.1. Confinement	4
2.1.2. Asymptotic freedom	4
2.2. Exploring the phase diagram of nuclear matter	6
2.3. Little big bangs in the laboratory	11
2.4. The purpose of this work	14
3. The transport model BAMPS	17
3.1. The simulation framework	17
3.1.1. Basic concept	17
3.1.2. Collision probabilities, matrix elements and cross sections	19
3.1.3. Small angle approximation in the $2 \rightarrow 3$ cross section	21
3.1.4. Modeling of the LPM effect	23
3.1.5. Evaluation of phase space integrals and sampling of momenta	31
3.2. The Gunion-Bertsch matrix element	32
3.2.1. Kinematics and approximations	32
3.2.2. Computation of the bremsstrahlung Feynman diagrams	34
3.2.3. Comparison of Gunion-Bertsch to the exact result	39
3.3. Selected results from BAMPS	42
3.3.1. Early thermalization	42
3.3.2. Small viscosity	43
3.3.3. Hydrodynamic behavior and shock phenomena	43
3.3.4. Heavy quarks	44
3.4. The inclusion of light quarks	45
3.4.1. $2 \rightarrow 2$ processes containing light quarks	45
3.4.2. $2 \leftrightarrow 3$ processes containing light quarks	46
3.4.3. Numerical test of detailed balance in a static medium	48
4. High energy partons in a static medium	51
4.1. Interaction rates and mean free paths	51

4.2.	Energy loss in a static medium	53
4.2.1.	Energy loss from $2 \rightarrow 2$ interactions	56
4.2.2.	Energy loss including $2 \leftrightarrow 3$ interactions	59
4.3.	Detailed investigation of energy loss in $2 \rightarrow 3$ processes	61
4.3.1.	Radiation spectra from the Gunion-Bertsch matrix element	62
4.3.2.	Energy loss per $2 \rightarrow 3$ process versus radiated energy	64
4.3.3.	Typical phase space configurations in $2 \rightarrow 3$ processes	67
4.4.	Conversion of jet partons	69
4.5.	Momentum broadening of jet partons	73
5.	Simulations of heavy ion collisions	77
5.1.	High- p_T physics and elliptic flow in ultra-relativistic heavy ion collisions	77
5.1.1.	Jet quenching	77
5.1.2.	Elliptic flow	80
5.2.	Setup for simulations of heavy ion collisions with BAMPS	81
5.2.1.	Initial parton distribution and technical setup	81
5.2.2.	Simulation strategy for high- p_T observables	83
5.2.3.	Impact parameters and centrality classes	84
5.3.	Spectra and fragmentation of high- p_T partons	85
5.3.1.	Hadronization via fragmentation functions	85
5.3.2.	Fits to parton spectra from BAMPS	87
5.3.3.	Fragmented hadron spectra from BAMPS	89
5.4.	Elliptic flow and thermalization at RHIC from simulations with BAMPS	92
5.4.1.	Elliptic flow in a purely gluonic medium	92
5.4.2.	Thermalization of the medium including light quarks	94
5.4.3.	Elliptic flow including light quarks	97
5.5.	Jet quenching at RHIC from simulations with BAMPS	99
5.5.1.	Nuclear modification factor of high- p_T particles	99
5.5.2.	Origin and interaction history of high- p_T particles	106
5.6.	Sensitivity of the results on the LPM cutoff	109
5.6.1.	Scaling the LPM cutoff	109
5.6.2.	LPM effect via a radiation formation factor	113
5.7.	Jet quenching and elliptic flow at LHC from simulations with BAMPS	114
5.7.1.	Thermalization of the medium in Pb + Pb at 2.76 A TeV	114
5.7.2.	Particle spectra and nuclear modification factor	114
5.7.3.	Elliptic flow	115
6.	Summary and conclusions	121
6.1.	Summary of the findings presented in this work	121
6.1.1.	High energy particles in a static medium	122
6.1.2.	Simulations of heavy ion collisions	123
6.2.	Future projects and possible extensions of the model	126
6.2.1.	Implementation of running coupling	126
6.2.2.	Reassessment of Gunion-Bertsch and the modeling of the LPM effect	127
6.2.3.	Investigation of possible hadronization scenarios	128
6.2.4.	Systematic studies of the sensitivity on initial conditions and fluctuations	129

Appendices	133
A. Notation and conventions	133
A.1. Units	133
A.2. Notation	134
A.3. On the term “jet”	135
B. Matrix elements and cross sections	137
B.1. The invariant matrix element	137
B.2. The definition of the cross section	138
B.3. Parton-parton cross sections in small angle approximation	139
B.3.1. Kinematics	139
B.3.2. The small angle approximation	140
B.3.3. Binary parton-parton cross sections	141
B.4. Computation of the differential $2 \rightarrow 3$ cross section	144
C. Interaction rates and probabilities	147
C.1. Computation of thermal rates	147
C.2. Scaling factors for $2 \leftrightarrow 3$ processes including light quarks	149
D. Numerical sampling methods	153
D.1. Inverse transform sampling	153
D.2. Rejection sampling	154
D.3. Metropolis sampling	154
E. Power law fits to parton spectra	157
Bibliography	162
Danksagung	177
Erklärung	179
Lebenslauf	181

List of Figures

2.1. Summary of $\alpha_s(Q)$ measurements	5
2.2. Phase diagram of nuclear matter	7
2.3. Energy density from lattice calculations	10
3.1. Mean free path with fixed double counting in $2 \rightarrow 3$	22
3.2. Illustration of medium induced gluon radiation	23
3.3. Illustration of reference frames for the LPM cutoff	25
3.4. Sampling in the y - k_\perp phase space	26
3.5. Cross sections with the improved LPM cutoff	28
3.6. Boosts and rapidities entering the LPM cutoff	30
3.7. Feynman diagrams for gluon radiation – Overview	33
3.8. Feynman diagram for gluon radiation from diagram \mathcal{M}_1	35
3.9. Feynman diagram for gluon radiation from diagram \mathcal{M}_2	36
3.10. Feynman diagram for gluon radiation from diagram \mathcal{M}_3	37
3.11. Comparison of Gunion-Bertsch to the exact result – Part 1	40
3.12. Comparison of Gunion-Bertsch to the exact result – Part 2	41
3.13. p_T -spectrum and η/s in central Au + Au at 200 A GeV.	43
3.14. Studies of hydrodynamic shocks within the BAMPS framework	44
3.15. Heavy quark studies within the BAMPS framework	45
3.16. Detailed balance including light quarks.	48
4.1. Thermal mean free path of gluons and quarks	52
4.2. Mean free paths of gluon and quark jets	54
4.3. Interaction rates of gluon and quark jets	55
4.4. Differential energy loss from $2 \rightarrow 2$ processes	57
4.5. Evolution of a gluon jet induced by $2 \rightarrow 2$ processes	58
4.6. Differential energy loss including $2 \leftrightarrow 3$ processes	60
4.7. Evolution of a gluon jet including $2 \leftrightarrow 3$ processes	61
4.8. Gunion-Bertsch radiation spectrum	63
4.9. ΔE_{23} as a function of k_\perp and q_\perp	65
4.10. Energy loss from single $2 \rightarrow 3$ interactions	66
4.11. Distribution of outgoing energies in $2 \rightarrow 3$ processes	67
4.12. Illustration of randomly selected $2 \rightarrow 3$ interactions	70
4.13. Conversion of jet partons	74
4.14. Transverse momentum broadening of jets	75
5.1. Compilation of R_{AA} measurements for identified hadrons	78
5.2. Compilation of elliptic flow data for identified hadrons	80
5.3. Parton spectra from BAMPS for $b = 3.4$ fm and $b = 9.6$ fm	88

5.4. Examples of parton spectra folded with fragmentation functions	91
5.5. Fragmentation contribution from gluons, quark and antiquarks	92
5.6. Hadron spectra from fragmentation of BAMPS results for $b = 3.4$ fm and $b = 9.6$ fm	93
5.7. Differential elliptic flow for $N_f = 0$ from previous studies	95
5.8. Differential elliptic flow for $N_f = 3$	96
5.9. Time evolution of elliptic flow and parton spectra	97
5.10. Overview of π^0 suppression from BAMPS for different centralities	101
5.11. R_{AA} of π^0 from BAMPS compared to PHENIX results	102
5.12. Comparison of integrated R_{AA} to experimental results	107
5.13. Illustration of the geometric origin of high- p_T particles	108
5.14. In-medium path length of emerging high- p_T particles	110
5.15. Interaction numbers of emerging high- p_T particles	110
5.16. Comparison of different schemes for the LPM cutoff	112
5.17. Parton spectra for Pb + Pb at LHC	116
5.18. R_{AA} and v_2 for Pb + Pb at 2.76 A TeV	117
6.1. Thermal mean free path and energy loss as a function of α_s	127

Deutschsprachige Zusammenfassung

Übersicht

In der vorliegenden Arbeit wird das mikroskopische Transportmodell BAMPS (*Boltzmann Approach to Multi-Parton Scatterings*) [XG05] eingesetzt um die Eigenschaften des heißen partonischen Mediums – des sogenannten *Quark-Gluon Plasmas* – zu untersuchen, wie es in hochenergetischen Schwerionenkollisionen erzeugt wird. Die Verwendung eines mikroskopischen Transportmodells ermöglicht dabei die detaillierte Untersuchung der zeitlichen Entwicklung verschiedenster Observablen bei gleichzeitiger Berücksichtigung der vollen Dynamik des Systems. Der Schwerpunkt der in dieser Arbeit vorgestellten Studien liegt dabei auf der gleichzeitigen Untersuchung des nuklearen Modifizierungsfaktors, R_{AA} , und des elliptischen Flusses, v_2 , im Rahmen eines gemeinsamen und konsistenten Modells. Die in dieser Arbeit vorgestellten Resultate beziehen sich im wesentlichen auf Au + Au-Kollisionen bei einer Schwerpunktsenergie pro Nukleon-Nukleon-Paar von $\sqrt{s_{NN}} = 200$ GeV, wie sie am Relativistic Heavy Ion Collider (RHIC) experimentell untersucht werden. Erste Ergebnisse für Pb + Pb-Kollisionen bei der ungleich höheren Schwerpunktsenergie $\sqrt{s_{NN}} = 2,76$ TeV, wie sie am kürzlich in Betrieb gegangenen Large Hadron Collider (LHC) untersucht werden, werden ebenfalls präsentiert.

Der nukleare Modifizierungsfaktor quantifiziert den Einfluss des Mediums auf die Anzahl der produzierten Teilchen bei gegebenen Transversalimpulsen indem mit den erwarteten Werten aus entsprechend skalierten Proton-Proton-Kollisionen verglichen wird

$$R_{AA} = \frac{d^2 N_{AA}/dy dp_T}{N_{\text{coll}} d^2 N_{pp}/dy dp_T},$$

wobei der Skalierungsfaktor N_{coll} die Anzahl der binären Nukleon-Nukleon-Interaktionen in der Schwerionenkollision ist. Experimentell wird bei höheren Transversalimpulsen, $p_T \gtrsim 5$ GeV, eine starke Abweichung vom Referenzwert $R_{AA} = 1$ festgestellt. In Au + Au-Kollisionen am RHIC wird beispielsweise für neutrale Pionen ein Wert $R_{AA} \approx 0.2$ gemessen, annähernd unabhängig vom Transversalimpuls p_T . Diese Unterdrückung von Teilchen mit hohem p_T im Vergleich zur skalierten p + p-Referenz, das sogenannte *Jet Quenching*, wird üblicherweise einem partonischen Energieverlust der Jets beim Durchqueren des Mediums, des Quark-Gluon Plasmas, zugeschrieben. Während die Betrachtung von R_{AA} im Rahmen dieser Arbeit somit auf die Untersuchung der Auswirkungen des Mediums auf seltene hochenergetische Jet-Teilchen abzielt, beschreibt der elliptische Fluss kollektive Eigenschaften dieses Mediums, primär bei niedrigen und mittleren Transversalimpulsen. Quantifiziert wird der elliptische Fluss, eine Anisotropie in der Impulsverteilung der gemessenen Hadronen, mittels des Koeffizienten v_2 einer Fourier-Zerlegung der Winkelverteilung relativ zur Reaktionsebene Ψ_R

$$E \frac{d^3 N}{d^3 p} = \frac{1}{2\pi} \frac{d^2 N}{dy dp_T} \left(1 + \sum_{n=1}^{\infty} 2v_n \cos [n(\phi - \Psi_R)] \right).$$

Experimentell beobachtet wird in nicht-zentralen Schwerionenkollisionen ein positiver und deutlich von Null verschiedener Wert für v_2 , was eine starke Kollektivität des Mediums und eine äußerst effektive Umsetzung der anfänglichen räumlichen Anisotropie in eine Anisotropie im Impulsraum indiziert. Dies weist auf starke beziehungsweise effiziente Wechselwirkungen im Medium hin und in der Tat kann der beobachtete elliptische Fluss gut durch hydrodynamische Rechnungen mit sehr kleiner oder gar verschwindender Viskosität beschrieben werden [HKH⁺01, KH03, RR07].

In früheren Studien [XGS08, XG09] wurde das Transportmodell BAMPS bereits erfolgreich zur Beschreibung der Zentralitätsabhängigkeit des integrierten elliptischen Flusses eingesetzt, basierend auf Simulationen eines rein gluonischen Mediums. In der vorliegenden Arbeit soll nun untersucht werden, inwieweit das Modell auch zur gleichzeitigen Beschreibung des Energieverlustes und der daraus resultierenden Unterdrückung von Teilchen mit hohem Transversalimpuls eingesetzt werden kann.

Das Transportmodell und vorgestellte Erweiterungen

Das Transportmodell BAMPS beschreibt die Interaktionen im partonischen Medium basierend auf Matrixelementen und Wirkungsquerschnitten in erster Ordnung störungstheoretischer Entwicklungen der Quantenchromodynamik (QCD). Neben binären Prozessen deren Behandlung mittels üblicher Wirkungsquerschnitte in Kleinwinkel-Näherung umgesetzt wird, ermöglicht das Modell eine konsistente Behandlung von Produktions- und Anihilationsprozessen in $2 \leftrightarrow 3$ Interaktionen basierend auf dem Gunion-Bertsch Matrixelement [GB82]. Die diesem Matrixelement zugrunde liegenden Näherungen und Annahmen werden in der vorliegenden Arbeit eingehender untersucht und numerische Vergleiche mit exakten Lösungen angestellt. Der Landau-Pomeranchuk-Migdal-Effekt (LPM-Effekt) [LP53, Mig56], ein Kohärenzphänomen bei induzierter mehrfacher Gluonabstrahlung, wird in BAMPS durch eine Restriktion des Phasenraums modelliert. Basierend auf einem Vergleich der mittleren freien Weglänge des propagierenden Teilchens mit der Formierungszeit des abgestrahlten Gluons werden alle potentiell kohärenten Beiträge verworfen. Die konsistente Berücksichtigung der für diesen Vergleich relevanten Lorentz-Bezugssysteme und die Auswirkungen auf den Phasenraum und den Energieverlust in $2 \rightarrow 3$ Interaktionen werden detailliert diskutiert. Des weiteren wird die Sensitivität der Ergebnisse auf parametrische Änderungen der Phasenraumrestriktion untersucht.

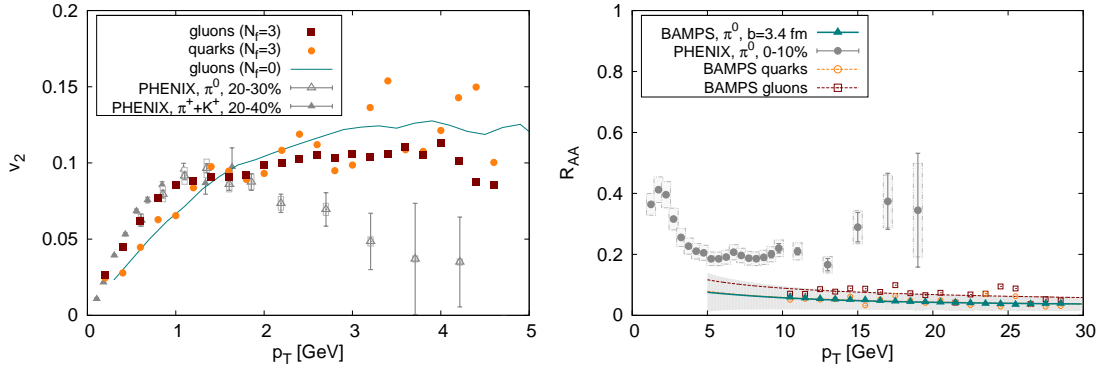
In seiner bisherigen Version war das Transportmodell BAMPS auf die Beschreibung rein gluonischer Systeme beschränkt, die Erweiterung auf leichte, masselose, Quarks und Anti-quarks wird in dieser Arbeit präsentiert. Die Einbindung leichter Quarks in das Modell ist an vielen Stellen entscheidend für den quantitativen Vergleich mit experimentellen Daten, beispielsweise für den Vergleich des differentiellen elliptischen Flusses bei mittleren Transversalimpulsen mit hadronischen Daten. Im Rahmen dieser Arbeit ist aber vor allem die Extraktion eines hadronischen Wertes für R_{AA} bei hohen Transversalimpulsen aus den partonischen Resultaten der BAMPS-Rechnungen von Interesse. Dafür werden die Partonen mit hohem Transversalimpuls einer Fragmentation in Hadronen unterzogen. Diese Fragmentation wird unabhängig von möglichen Beeinflussungen der Jets durch das Medium betrachtet, daher im Vakuum durchgeführt. Sie basiert auf einem Satz von Fragmentationsfunktionen, die von ALBINO, KNEIHL und KRAMER [AKK08] aus globale Fits an Daten gewonnen wur-

den und wird im Rahmen dieser Arbeit mittels einer Faltung der partonischen Spektren mit diesen Fragmentationsfunktionen durchgeführt.

Ergebnisse

Um eine systematische Analyse des Energieverlusts hochenergetischer Partonen in vollständig dynamischen Simulationen von Schwerionenkollisionen zu ermöglichen, wird deren Verhalten zunächst in einer deutlich vereinfachten Umgebung studiert. Dazu wird die Propagation dieser Jet-Teilchen in einem thermischen und statischen Medium verfolgt und analysiert. Hauptaugenmerk liegt dabei auf der Untersuchung des Energieverlusts verursacht durch die in BAMPS implementierten Interaktionen mit den Konstituenten des Mediums. Dabei stellt sich heraus, dass $2 \rightarrow 3$ Prozesse, basierend auf dem Gunion-Bertsch Matrixelement, den Energieverlust deutlich dominieren und einen letztlich nahezu linearen Anstieg des differentiellen Energieverlustes mit der Jet-Energie verursachen. Der resultierende Energieverlust ist recht stark, so erfährt beispielsweise ein Gluon mit $E = 50$ GeV in einem Medium der Temperatur $T = 0,4$ GeV ($N_f = 3$) einen Energieverlust von $dE/dx \approx 39,1$ GeV fm⁻¹. Verantwortlich dafür ist ein komplexes Zusammenspiel des Gunion-Bertsch Matrixelements mit den Einschränkungen des Phasenraums durch die Modellierung des LPM-Effekts. Dieses bevorzugt bei hohen Jet-Energien eine Emission der abgestrahlten Gluonen in Rückwärtsrichtung (bezogen auf den Impuls des Jet-Teilchens), wobei die Energie der abgestrahlten Teilchen im Schwerpunktsystem vergleichbar mit denen der beiden weiteren auslaufenden Teilchen sein kann. Im Laborsystem ist diese Energie des abgestrahlten Gluons dann zwar gering, die bevorzugte Abstrahlung in Rückwärtsrichtung ermöglicht aber Konfigurationen in denen die beiden anderen Teilchen nach vorne emittiert werden, sich dabei die verbleibende Energie nahezu gleichmäßig aufteilen und so einen großen Energieverlust verursachen. Des Weiteren ist der Unterschied des Energieverlustes zwischen Quarks und Gluonen recht gering, Quarks verlieren in BAMPS lediglich circa 20 % weniger Energie als Gluonen, obwohl das zugrunde liegende Gunion-Bertsch Matrixelement mit den üblichen Farbfaktoren skaliert ist und somit zunächst ein Unterschied um circa einen Faktor 9/4 zu erwarten wäre. Dieser Unterschied wird jedoch durch die Abhängigkeit der Phasenraumrestriktion des LPM-Effekts von der aktuellen Interaktionsrate abgeschwächt, die eine iterative Berechnung der wahren Interaktionsraten nötig macht.

Der nukleare Modifizierungsfaktor in Simulationen von Au + Au-Kollisionen bei der RHIC-Energie von 200 A GeV zeigt eine äußerst leichte Abnahme hin zu höheren Transversalimpulsen, kann im Rahmen der statistischen Fehler allerdings auch als flach, daher unabhängig von p_T , betrachtet werden. In Übereinstimmung mit experimentellen Ergebnissen ist dieses Verhalten unabhängig von der Zentralität der betrachteten Kollisionen. Allerdings liegt der in BAMPS berechnete Wert von R_{AA} deutlich unter den experimentell bestimmten Werten, um circa einen Faktor zwei bis vier. Bild 0.1b zeigt als Beispiel den Unterdrückungsfaktor für neutrale Pionen in zentralen Au + Au-Kollisionen verglichen mit experimentellen Ergebnissen. Die starke Unterdrückung von Jet-Teilchen in BAMPS-Simulationen korrespondiert mit dem bereits in den Rechnungen für statische Medien beobachteten starken Energieverlust. Zusätzlich spielen Konversionsprozesse von Quark- in Gluon-Jets eine entscheidende Rolle, die letztlich dazu führen, dass leichte Quarks entgegen der Erwartungen etwas stärker als Gluonen unterdrückt sind. Auch die Zentralitätsabhängigkeit der Unterdrückung ist nicht



- (a) Differenzieller elliptischer Fluss von Gluonen und Quarks aus BAMPS Simulationen bei einem Stoßparameter $b = 7,0$ fm für $|\eta| < 0.5$. Die experimentellen Daten des PHENIX-Experiments [PHENIX03, PHENIX09a] sind zu Vergleichszwecken mit der Anzahl der Valenzquarks skaliert, $v_2(p_T/n_q)/n_q$.
- (b) R_{AA} für neutrale Pionen, sowie für Quarks und Gluonen, aus BAMPS-Rechnungen mit $b = 3,4$ fm verglichen mit experimentellen Daten [PHENIX08a] für 0%–10% zentrale Kollisionen.

Abbildung 0.1.: BAMPS Resultate für den elliptischen Fluss v_2 und den nuklearen Modifizierungsfaktor R_{AA} in Au + Au-Kollisionen bei $\sqrt{s_{NN}} = 200$ GeV.

in Übereinstimmung mit experimentellen Ergebnissen. Ein Fit des integrierten R_{AA} mittels $R_{AA} = (1 - S_0 N_{\text{part}}^a)^{n-2}$ ergibt einen charakteristischen Exponenten $a = 0,39 \pm 0,02$, während die experimentellen Daten $a = 0,57 \pm 0,13$ aufweisen.

Der differentielle elliptische Fluss $v_2(p_T)$ von Quarks und Gluonen ist in Simulationen von Au + Au-Kollisionen bei 200 A GeV nahezu identisch, lediglich bei $p_T \lesssim 1$ GeV ist eine leichte Erhöhung des gluonischen v_2 gegenüber der Quarks feststellbar, vgl. hierzu Bild 0.1a. Verglichen mit älteren Resultaten für rein gluonische Medien ändert sich $v_2(p_T)$ nur leicht, eine nennenswerte Änderung des integrierten elliptischen Flusses ist daher nicht zu erwarten. Die maximale Magnitude des elliptischen Flusses stimmt gut mit experimentellen Daten überein, sofern eine Skalierung der hadronischen Messwerte mit der Anzahl der Valenzquarks vorgenommen wird. Die Position des beobachteten Maximums von $v_2(p_T)$ ist in diesem Bild der Skalierung mit der Quarkanzahl jedoch nicht mit der Position des experimentell bestimmten Maximums in Übereinstimmung zu bringen.

Erste Ergebnisse für Pb + Pb-Kollisionen bei $\sqrt{s_{NN}} = 2,76$ TeV zeigen keinerlei Veränderung in der Unterdrückung hochenergetischer Teilchen verglichen mit den RHIC-Simulationen. Auch hier ist die Unterdrückung deutlich stärker als der experimentell bestimmte Wert. Zusätzlich zeigen die ersten Daten des ALICE-Experiments einen klaren Anstieg von R_{AA} für höhere Werte des Transversalimpulses [ALICE11], der von den BAMPS-Ergebnissen nicht reproduziert wird. Der berechnete differentielle elliptische Fluss ändert sich verglichen mit den Resultaten für Au + Au-Kollisionen bei $\sqrt{s_{NN}} = 200$ GeV ebenfalls nur marginal. Eine solche bemerkenswerte Ähnlichkeit des differentiellen elliptischen Flusses am LHC verglichen mit den RHIC-Resultaten wird auch in den ersten Ergebnissen des ALICE-Experiments beobachtet [ALICE10b].

Ausgehend von diesen Ergebnissen und Beobachtungen werden abschließend mögliche Er-

weiterungen und Verbesserungen des Transportmodells BAMPS vorgeschlagen. Insbesondere die Berücksichtigung der laufenden Kopplung – alle Ergebnisse in dieser Arbeit sind mit fixem $\alpha_s = 0.3$ berechnet – und mögliche alternative Behandlungen des LPM-Effekts sind viel versprechend. Mit ihnen könnten die Ergebnisse der mikroskopischen Transportrechnungen in deutlich bessere quantitative Übereinstimmung mit den experimentellen Resultaten gebracht werden. Ihre Umsetzung jedoch dürfte als mindestens mittelfristiges Projekt angesehen werden.

1. Overview

1.1. Abstract

In this work the microscopic transport model BAMPS (*Boltzmann Approach to Multi-Parton Scatterings*) is applied to simulate the time evolution of the hot partonic medium that is created in Au + Au collisions at the *Relativistic Heavy Ion Collider* (RHIC) and in Pb + Pb collisions at the recently started *Large Hadron Collider* (LHC). The study is especially focused on the investigation of the nuclear modification factor R_{AA} , that quantifies the suppression of particle yields at large transverse momentum with respect to a scaled p + p reference, and the simultaneous description of the collective properties of the medium in terms of the elliptic flow v_2 within a common framework.

BAMPS is a microscopic transport model aimed at simulating the early stage of heavy ion collisions on the partonic level via leading order perturbative QCD interactions and consistently includes parton creation and annihilation processes based on the Gunion-Bertsch matrix element. The approximations and assumptions underlying this matrix element are studied. The Landau-Pomeranchuk-Migdal (LPM) effect is modeled via the introduction of a cutoff that effectively discards coherent contributions from multiple induced gluon radiation. In this work the correct treatment of Lorentz frames involved in this cutoff is presented and the consequences on the phase space in radiative $2 \rightarrow 3$ processes are discussed. As the implementation of the LPM effect via a phase space cutoff is crucial to the results presented within this work, the sensitivity of these results on parametric changes of the cutoff is studied.

The extension of the transport model BAMPS to include light quark degrees of freedom is presented in this work. This facilitates a more detailed comparison to experimental results and is especially crucial at large transverse momenta where the spectra at RHIC energies become quark dominated. For high- p_T observables, such as the nuclear modification factor, in-vacuum fragmentation on the level of single parton spectra is applied to obtain hadronic observables. The fragmentation is based on a recent set of fragmentation functions that provides global fits to experimental data.

The evolution of high energy gluons and quarks inside a static and thermal medium is systematically studied, with a focus on the energy loss of parton jets due to interactions with the medium constituents. Radiative $2 \rightarrow 3$ processes are found to be the dominant source of energy loss in computations within the BAMPS framework. Detailed investigations reveal that the rather strong energy loss in $2 \rightarrow 3$ interactions is caused by a complex interplay of kinematics according to the Gunion-Bertsch matrix element and restrictions on the phase space imposed by the cutoff modeling the LPM effect.

The suppression of high- p_T particles is systematically studied in simulations of Au + Au collisions at an energy per nucleon pair of $\sqrt{s_{NN}} = 200$ GeV and compared to experimental data from the PHENIX collaboration for different centralities. While the shape of the suppression pattern is in reasonable agreement with experimental observations, the quenching

of high- p_T hadrons extracted from simulations with BAMPS is distinctly stronger than indicated by the experimental data. The centrality dependence of the integrated R_{AA} is found to differ from the experimental data on a quantitative level. In an extension of previous studies that have been limited to gluonic degrees of freedom, the differential elliptic flow of light quarks at low and intermediate transverse momenta is investigated. It is found to scarcely differ from the elliptic flow of gluons. From a common fit to v_2 in the low and intermediate p_T region and to v_2 of jet particles in the high- p_T region up to 25 GeV, a maximum in $v_2(p_T)$ is found. This is in good qualitative agreement with recent high- p_T flow data from PHENIX. In the picture of quark number scaling of the observed hadronic v_2 , the maximum magnitude of quark elliptic flow from BAMPS is found to be in good agreement with experimental data. The position of the peak, however, appears to be located at slightly higher transverse momenta, $p_T \approx 3$ GeV than is suggested by the data.

First results on the nuclear modification factor and on the differential elliptic flow from simulations of Pb + Pb collisions at $\sqrt{s_{NN}} = 2.76$ TeV, as probed at the LHC, are presented and compared to recent experimental data from the ALICE collaboration. The suppression of charged hadrons in Pb + Pb collisions at LHC is found to be identical to that computed for Au + Au collisions at RHIC due to a strong surface bias in the BAMPS model. As for RHIC simulations the BAMPS result overestimates the suppression of high- p_T particles. While for RHIC the shape of the suppression pattern from BAMPS is in reasonable agreement with the experimental R_{AA} , the high statistic data from ALICE clearly indicate a trend towards less suppression at high transverse momenta that is not reproduced in BAMPS. The differential elliptic flow extracted from BAMPS simulations of Pb + Pb collisions at LHC energy is found to be also very similar to that extracted from Au + Au collisions at RHIC energy. This observation is in qualitative agreement with experimental findings that indicate no changes in the differential elliptic flow from when going from RHIC to LHC.

1.2. Structure of this document

Chapter 2 provides a general introduction to the field of heavy ion collisions and sets the stage for the themes, jet quenching and elliptic flow, that are discussed in this work. The transport model BAMPS is thoroughly introduced in chapter 3. Special emphasis is put on extensions to the model, such as the incorporation of light quarks, the consistent treatment of the small angle approximation in radiative processes or the treatment of Lorentz frames in the implementation of the LPM cutoff. Also the Gunion-Bertsch matrix element, on which the treatment of radiative processes is based, is studied in some detail and underlying assumptions and approximations are discussed. Chapter 4 then provides the baseline for studies of jet particles in the expanding and dynamic medium in simulations of heavy ion collisions by investigating the propagation of high energy partons inside a static and thermal medium. Primarily the energy loss of jet-like particles induced by interactions with constituents of the medium is discussed. The results on jet suppression and elliptic flow from fully dynamic simulations of heavy ion collisions at RHIC and LHC are then presented in chapter 5, before the work is summarized in chapter 6.

2. Introduction

This chapter provides an overview of the theoretical and experimental background that is needed to put the work presented in this thesis into context. As a matter of course, both theoretical and experimental findings can merely be listed here. In-depth derivations or explanations of the presented facts cannot be provided by such an introduction. For these the reader is kindly referred to the given literature.

2.1. Quantum chromodynamics

The fundamental interaction governing nuclear physics is the strong force. It is one of the four fundamental forces in nature, along with electromagnetism, weak interaction and gravitation. Theoretically strong interactions are described by a non-abelian gauge theory called quantum chromodynamics (QCD). The charge associated with this gauge theory is referred to as *color* and can take three different values as the underlying symmetry group is $SU(3)$, a special unitary group of degree three. It is the invariance under local $SU(3)$ symmetry transformations in the color space whose gauging leads to QCD.

The color charge is carried by spin- $1/2$ fermions called quarks, subatomic particles that – to the best of our current knowledge – have no substructure and are the fundamental particles of QCD. The term *quark* was coined by Murray GELL-MANN and allegedly originates from a passage of James JOYCE’s “Finnegans Wake”¹ [Gel95]. The strong force between the quarks is mediated by *gluons*, the exchange particles of QCD. Due to the non-abelian nature of the theory, the gluons carry color charge and are thus subject to interactions via the strong force themselves. This is a feature quite distinct from quantum electrodynamics (QED), where the exchange bosons—photons—do not couple to each other directly, and leads to wide consequences. Gluons are spin-1 vector bosons and come in eight types, corresponding to the color octet generated by $SU(3)$. There is no gluon color singlet. In general, for a $SU(N)$ symmetry there are $N^2 - 1$ force carriers.

The whole complexity of the theory can be condensed into the innocent looking Lagrangian of QCD [PDG10, PS95]

$$\mathcal{L}_{QCD} = i \sum_q \bar{\psi}_q^k \gamma^\mu (D_\mu)_{kl} \psi_q^l - \frac{1}{4} F_{\mu\nu}^a F^{a,\mu\nu} - \sum_q m_q \bar{\psi}_q^k \psi_{q,k} \quad (2.1)$$

where ψ_q^k is the color component k ($k = 1, \dots, N_c = 3$) of the quark field of flavor q and mass m_q .

$$F_{\mu\nu}^a = \partial_\mu A_\nu^a - \partial_\nu A_\mu^a - g_s f_{abc} A_\mu^b A_\nu^c \quad (2.2)$$

¹Three quarks for Muster Mark!

Sure he has not got much of a bark

And sure any he has it’s all beside the mark. [Joy99]

is the field tensor, given by the gluon fields A_μ^a ($a = 1, \dots, N_c^2 - 1 = 8$) and the structure constants f_{abc} of QCD. The last term in the field tensor is due to the non-abelian nature of QCD. It couples gluons with gluons and sets QCD apart from an abelian gauge theory such as QED. $(D_\mu)_{kl} = \delta_{kl}\partial_\mu - ig_s \sum_a T_{kl}^a A_\mu^a$ is the covariant derivative and the T^a are the eight generators of QCD.

In the following this introduction will focus on prominent features of QCD and phenomena arising from QCD, but will not go any further into the rich theoretical details of gauge theories or the history of experimental confirmations of QCD.

Two of the most striking features of QCD go by the names of *confinement* and *asymptotic freedom*.

2.1.1. Confinement

Confinement reflects the experimental experience that no free bare quarks or gluons are ever observed. They are always confined inside of *hadrons*², for example inside of protons and neutrons, the building blocks of atomic nuclei. Hadrons are typically categorized into *baryons*³ and *mesons*⁴. Baryons consist of three valence quarks and are thus fermions. Prominent examples of baryons are protons and neutrons. Mesons on the contrary are bosons and consist of two valence quarks. Prominent examples are pions and kaons.

Qualitatively confinement can be described by the notion of a potential between two quarks that can be parametrized as

$$V(r) = -a\frac{1}{r} + br, \quad (2.3)$$

with $a, b \in \mathbb{R}^+$. This potential, sometimes called Cornell potential, consists of a Coulomb-like proportional to $\frac{1}{r}$ part and a confining part proportional to r . The latter then leads to a growth in potential energy as the two quarks are separated and confines them inside a hadron. Of course this is only a very simplified and qualitative picture. But still the potential (2.3) serves as a popular starting point for models describing quarkonium states, systems of two heavy quarks.

Though it is evident that confinement should originate from the non-abelian structure of QCD and the unique self-interaction of gluons, an analytic ab initio derivation of confinement is still not known today. However, confinement is observed in lattice gauge calculations. Solving QCD by discretizing the Lagrangian on the lattice is numerically challenging but currently provides the most fundamental and quantitative approach to the non-perturbative regime of the theory and over the past years increasingly accurate results are becoming available. See [Phi10] for an overview.

2.1.2. Asymptotic freedom

The asymptotic freedom of quantum chromodynamics is another unique feature of non-abelian gauge theories that is thus not present in quantum electrodynamics. In 2004 GROSS, WILCZEK and POLITZER have been awarded the Nobel prize in physics for their 1973 “discovery of asymptotic freedom in the theory of strong interaction” [Nob10].

²From the Greek word “hadrós”, meaning “stout”, “thick”.

³From the Greek “barys”, “heavy”.

⁴From the Greek “mesos”, “intermediate”.

In contrast to confinement the phenomenon of asymptotic freedom can be investigated analytically. The renormalization of quantum field theories leads to a running of the physical coupling⁵ with the energy scale of the considered process. In QED the coupling becomes strong at large momentum scales (corresponding to small distances) and is weaker at small momentum scale (corresponding to large distances). Qualitatively this can be understood in terms of vacuum polarization. Virtual e^+e^- pairs screen the charge that is to be probed and cause an effective weakening of the charge. At high momentum transfers, corresponding to small distances, the screening cloud is penetrated and the observed effective charge is thus stronger.

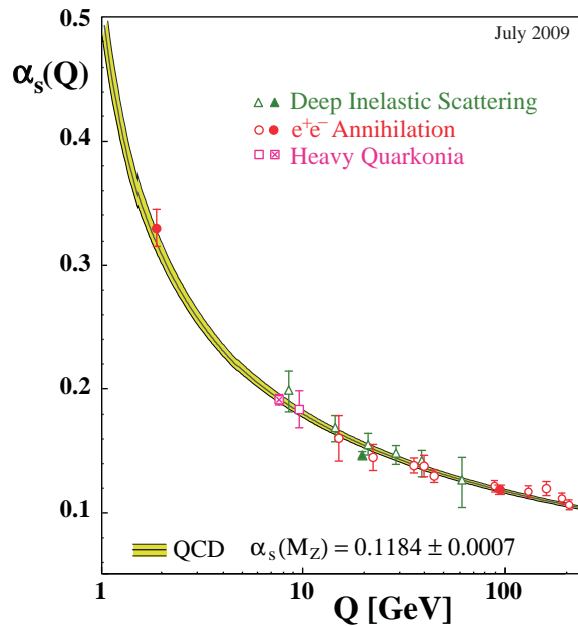


Figure 2.1.: Summary of measurements of the strong coupling $\alpha_s(Q)$ at various energy scales. Figure taken from [Bet09]. The curve represents the 2009 world average of α_s at the Z^0 -boson pole mass, $\alpha_s(M_{Z^0}) = 0.1184 \pm 0.0007$.

This screening effect is present for any abelian gauge theory and also in the non-abelian case. In QCD virtual quark-antiquark pairs screen the color charge in very much the same way virtual e^+e^- pairs screen the electric charge in QED. In non-abelian gauge theories however, there is an additional antiscreening effect due to the peculiar way in which the exchange bosons carry charge themselves (loosely speaking, they carry a combination of charge and anticharge). The question which of the effects—screening or antiscreening—prevails, is a quantitative one. In QCD one finds that for a sufficiently small number of flavors, N_f , the antiscreening prevails and leads to asymptotic freedom.

⁵Though the term “coupling constant” is often used quite loosely, the physically relevant coupling in general varies with the energy scale and is thus not a constant. Only the bare couplings entering the underlying Lagrangians are constant. In QED the bare coupling is denoted by e and in QCD by g . In analogy to the electromagnetic fine structure constant $\alpha = \frac{e^2}{4\pi}$, one usually defines $\alpha_s = \frac{g^2}{4\pi}$ for strong interactions.

The running of the strong coupling can be expressed in leading order as

$$\alpha_s(Q^2) = \frac{4\pi}{(11 - \frac{2}{3}N_f) \ln(Q^2/\Lambda_{QCD}^2)}, \quad (2.4)$$

where Q^2 is the momentum transfer of the process under consideration. For the number of active flavors $N_f \leq 16$ the coupling α_s decreases with increasing momentum scale Q^2 , corresponding to small distances. Since in nature the number of flavors is at most six⁶, eq. (2.4) embodies asymptotic freedom. Λ_{QCD} is the QCD scale and in principle the only free parameter of QCD. It needs to be fixed by experiment and has a value of $\Lambda_{QCD} \approx 200\text{MeV}$. Only for $Q \gg \Lambda_{QCD}$ the coupling is weak, $\alpha_s \ll 1$, and a perturbative expansion of quantum chromodynamics is possible.

The running of the strong coupling, together with various other aspects of QCD, has been experimentally verified with tremendous success. See fig. 2.1 for a summary of various measurements on $\alpha_s(Q)$, nicely illustrating the decrease in $\alpha_s(Q)$ for large Q . When the results of all measurements are evolved to a certain scale, they can be conveniently combined into a world average. Typically the pole mass of the Z^0 -boson is chosen and the current (2009) world average of the strong coupling at this scale is [Bet09]

$$\alpha_s(M_{Z^0}) = 0.1184 \pm 0.0007. \quad (2.5)$$

2.2. Exploring the phase diagram of nuclear matter

One would think that with the knowledge of QCD as the fundamental theory everything was set and all properties of nuclear matter could simply be computed from the Lagrangian (2.1). While this is in principle true, it is quite far from reality.

From the simple underlying Lagrangian arises a vast complexity that renders most parts of low and high energy nuclear physics impossible to derive from first principles. The fact that virtually any observable in nuclear physics is based on multiparticle dynamics of very large systems and the self-interaction of the force carriers, are only two of the main reasons for this. Also the established method of expanding the theory into a perturbation series is not applicable for phenomena on soft⁷ energy scales. For example the composition of nucleons (protons, neutrons etc.) from the fundamental particles of QCD falls into this category. It involves the interactions of the constituent quarks and a whole sea of virtual quarks, antiquarks and gluons down to basically arbitrary soft scales, that only together form the nucleon and dynamically generate its mass.

But none the less, a profound knowledge of the properties of nuclear matter is crucial to modern physics. Not only as an end in itself but also as a basis to, for example, astrophysics and cosmology. Thus, where calculations from first principles are not possible—or are simply not necessary—effective theories and models step in and precise experiments are needed to extend and confirm our knowledge.

Investigating the phase diagram is a very general concept used in physics to characterize the global properties of matter. Water is most certainly the best known example from

⁶Depending on the energy scale a number between 3 and 6 flavors can be active. This is due to the fact that charm ($m_c = 1.27_{-0.09}^{+0.07}\text{GeV}$), bottom ($m_b = 4.19_{-0.06}^{+0.18}\text{GeV}$) and top ($m_t = 172.0 \pm 0.9 \pm 1.3\text{GeV}$) quarks are heavy and require a certain threshold energy to be produced. Quark masses from [PDG10].

⁷ $Q \lesssim \Lambda_{QCD}$, see discussion in section 2.1.2.

everyday life of matter that can exist in various phases. At standard atmospheric pressure (101.325 kPa) water is a solid for temperatures below $T = 0^\circ\text{C}$, a liquid above and vaporizes at $T = 100^\circ\text{C}$ ⁸. But it is also well known that a change in pressure changes the exact position of these transitions. For example going to higher altitudes, i.e. to regions of lower atmospheric pressure, lowers the boiling point of water. The properties of matter are therefore often represented by a phase diagram in a plane given by temperature T and pressure P .

In relativistic systems the number density is in general not conserved. Therefore the state variables of a grand canonical ensemble, T and μ , are typically used instead of T and P . μ is the chemical potential, controlling the mean value of a conserved quantity in grand canonical systems. For the characterization of nuclear matter usually the baryon chemical potential μ_B is chosen. It ensures the conservation of baryon number B , which is defined to be +1 for all baryons (+1/3 for quarks) and -1 for all antibaryons (-1/3 for antiquarks). Accordingly, B can also be expressed in terms of the quark and antiquark densities

$$B = \frac{1}{3}(n_q - n_{\bar{q}}). \quad (2.6)$$

A system with baryon chemical potential $\mu_B > 0$ has a positive baryon number, thus an excess of baryons over antibaryons—as is the case for normal nuclear matter. Alternative to the baryon chemical potential, the quark chemical potential $\mu_q = \frac{1}{3}\mu_B$ can be used to express the same relations. A quark chemical potential $\mu_q > 0$ implies a non-vanishing net quark density $\bar{n}_q = n_q - n_{\bar{q}}$ and thus $B > 0$.

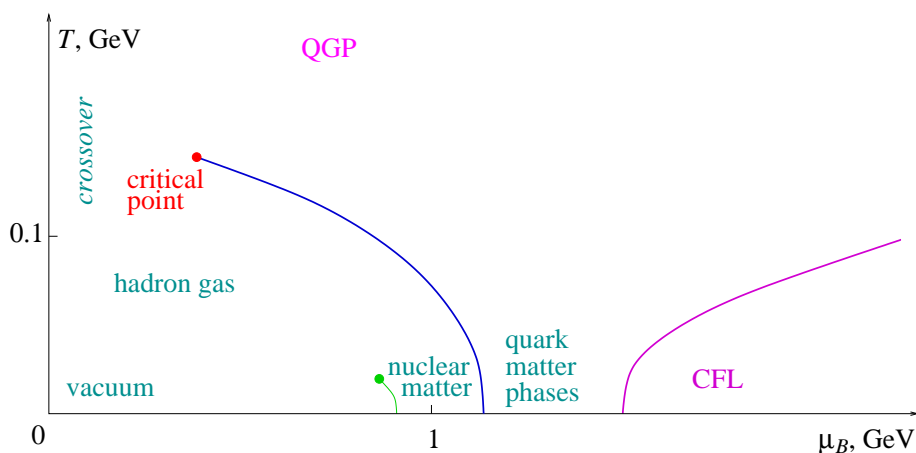


Figure 2.2.: Schematic view of the phase diagram of nuclear matter in the μ_B - T plane. Figure taken from [Ste06].

Figure 2.2 shows a sketch of the QCD phase diagram in the μ_B - T plane. The single tiny region in this diagram about which profound knowledge exists, is located around $T =$

⁸Actually, this is not completely true. The Celsius scale used indeed to be defined by the melting (0°C) and boiling (100°C) points of water at normal pressure of 101.325 kPa. But from 1954 on it has been fixed to the Kelvin scale that is defined by the triple point of water at 273.16 K (0 K being *absolute zero*) [dPeM06]. Adhering to this definition, the boiling point of water is actually slightly below 100°C at $T_b = 373.124\text{ K} = 99.964^\circ\text{C}$ [Wag99].

0 MeV and $\mu_B \simeq 924$ MeV, the ground state of nuclear matter with a baryon density of $\rho_B \simeq 0.17 \text{ fm}^{-3}$. The knowledge about the vast remaining area of the phase diagram is, to say the least, incomplete and has only been the subject of theoretical and experimental investigations for a few decades. It is one of the main objectives of modern nuclear physics to investigate the properties of nuclear matter at very high temperatures and/or high baryon chemical potential and thus to explore the phase diagram.

Knowledge of the properties of nuclear matter under extreme conditions is not only of academic interest. The properties of matter at low baryon chemical potential ($\mu_B \sim 0$ MeV) and very high temperatures are of relevance for the evolution of the early universe. According to standard cosmology, the temperature of the early universe exceeded 200 MeV ($2.32 \cdot 10^{12}$ K, see appendix A.1) for roughly the first couple of microseconds after the Big Bang⁹. Going along the temperature axis towards high temperatures at vanishing chemical potential is therefore, in a sense, equivalent to going backwards in the cosmic evolution. Also the other extreme, going to high chemical potentials at zero temperature, is relevant to astrophysics. Cold nuclear matter at extremely high baryon densities is expected to exist in stellar remnants, most prominently in neutron stars [LP04].

When heating up matter to extreme temperatures it seems somewhat natural to assume that its properties might change drastically, that it undergoes a transition to a different phase. Indeed, first ideas that new states of matter might be explored by experimentally creating volumes with high energy or nucleon densities date back to the late 1960s and early 1970s [Bay02]. But only after the advent of QCD as the theory of strong interactions and the discovery of asymptotic freedom (see section 2.1) it was realized that such a novel state of nuclear matter might in fact be composed of deconfined quarks and gluons [CP75, BC76, FM77, CN77]. The now commonly used term *quark-gluon plasma* (QGP) was later coined by SHURYAK [Shu78b, Shu78a, Shu80]. The method of choice to experimentally create the high densities that are needed to create the QGP, is to collide the nuclei of heavy atoms at high energies. This will be discussed in more detail in section 2.3.

One can get a first idea of the qualitative behavior of the transition from the hadron regime to the quark-gluon plasma from the combination of different models¹⁰.

Bag model

From the MIT bag model [CJJ⁺74], originally conceived to describe quarks confined inside hadrons, the thermodynamics of the partonic phase can be estimated by computing the properties of an asymptotically infinite bag containing a large number of quarks and gluons. Comparing to the equation of state for the hadronic phase—in the most simplified version an ideal gas of pions—one can construct the phase boundary and estimate the critical temperature at $\mu_B \approx 0$. The so obtained value for T_c is dependent on the bag constant as $T_c \propto B^{1/4}$ [Bub05] and roughly ranges from $T_c \sim 100$ MeV for $B^{1/4} \sim 150$ MeV to $T_c \sim 160$ MeV for $B^{1/4} \sim 220$ MeV. These values are either distinctly ($T_c \sim 100$ MeV) or slightly ($T_c \sim 160$ MeV) below current and more quantitative calculations, as will be discussed below. The phase transition within the bag model is of first order for all chemical potentials.

⁹See for example the extensive reviews of the Particle Data Group [PDG10] or [BdVS06] and references therein.

¹⁰See [BMW08, Ste06] and references therein for an overview.

NJL model

More information can be obtained from models that investigate the chiral aspects of strongly interacting matter. In the ground state chiral symmetry¹¹ is spontaneously broken, i.e. the expectation value of the quark-antiquark condensate¹² $\langle \bar{q}q \rangle$ is non-zero. One of the most popular models that implement the spontaneous breaking of chiral symmetry in the vacuum is the NJL model, originally conceived by NAMBU and JONA-LASINIO in 1961 [NJL61a, NJL61b] in pre-QCD times. In its modern application the NJL model can describe the dynamic generation of nucleon masses via constituent masses of the quarks arising from the breaking of chiral symmetry.

The phase transition in the NJL model is investigated in terms of the quark-antiquark condensate $\langle \bar{q}q \rangle$ as an order parameter. Having a finite expectation value in the spontaneously broken ground state, it vanishes when the chiral symmetry is restored. This is to be expected for high temperatures and/or quark (baryon) chemical potential and the transition should roughly coincide with the confinement-deconfinement transition. Indeed, calculations in the NJL model show that chiral symmetry gets restored at high temperatures and at high chemical potentials. Furthermore, a quite robust result is the finding that the phase transition at small T and large μ_B is of first order, i.e. that there is a discontinuity in the order parameter [Bub05].

Lattice QCD

The most fundamental approach to the problem is provided by lattice QCD. In fact, calculations on the lattice are currently the only known way of solving non-perturbative QCD problems from first principles. Lattice gauge theory relies on solving the path integral formalism of quantum field theory on a discretized euclidean space-time¹³. Though the problem is in principle solvable, the theoretical and numerical challenges are enormous.

But still, finite temperature lattice QCD provides the best way of exploring the phase transition at small μ_B in an exact and quantitative way. And over the past few years the level of sophistication of the calculations is continuously increasing, together with the numerical precision.

Figure 2.3 is probably one of the most famous plots from lattice QCD. It shows the evolution of the energy density with temperature at vanishing baryon chemical potential. Between roughly $T \sim 150$ MeV and $T \sim 200$ MeV a distinct increase in energy density is clearly visible—this is the phase transition to the quark-gluon plasma. Though the Stefan-Boltzmann limit of an ideal gas of free and massless quarks and gluons is not completely reached, the energy density in the high-temperature phase is getting quite close to it. The lattice results show that at zero chemical potential the transition to the quark-gluon plasma

¹¹Chiral symmetry is the symmetry of a Lagrangian under chiral transformations $\psi \rightarrow e^{i\alpha\gamma^5} \psi$ with $\gamma^5 = i\gamma^0\gamma^1\gamma^2\gamma^3$ being a combination of the usual γ -matrices [PS95]. The corresponding conserved current is the axial vector current $j^{\mu 5} = \bar{\psi}\gamma^\mu\gamma^5\psi$. The derivative term $\bar{\psi}\gamma^\mu D_\mu\psi$ of a Lagrangian such as eq. (2.1) is invariant under such transformations. But the mass term $m\bar{\psi}\psi$ mixes left- and right-handed components and explicitly breaks chiral symmetry. Since the bare quark masses are small, chiral symmetry is sometimes said to be an approximate symmetry of QCD. See [Koc97] for a nice introduction to chiral symmetry.

¹²Often also called *chiral condensate* and denoted as $\langle \bar{\psi}\psi \rangle$.

¹³See [MW00] and [Phi10] for excellent reviews on the topic.

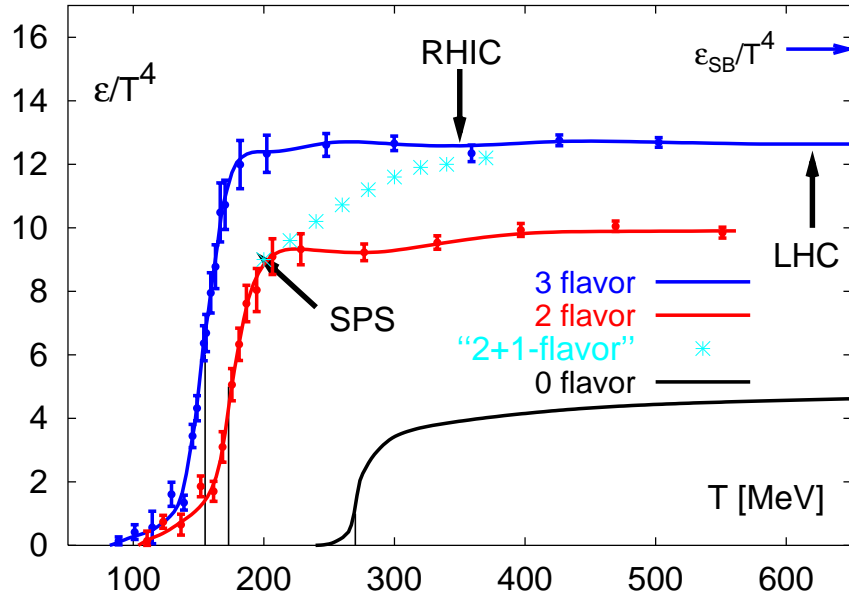


Figure 2.3.: Energy density scaled by $1/T^4$ as a function of temperature from lattice QCD calculations for different number of flavors. Estimates of the temperatures reached by different experiments (see section 2.3) are indicated by arrows. Figure taken from [GM05].

phase is rapid, but smooth. Thus it is not a first order phase transition but rather a so called cross over, a rapid but continuous increase in energy density around a critical temperature T_c [AEF⁺06].

As to the exact value of T_c there has been some disagreement between two major groups in the field since 2006. Based on the chiral susceptibility the Bielefeld-Brookhaven-Columbia-Riken group (in an extended version now called *HotQCD collaboration*) has reported a value for the critical temperature of $T_c = 192(7)(4)\text{MeV}$ [CCD⁺06], while the Wuppertal-Budapest group gives $T_c = 151(3)(3)\text{MeV}$ for the same observable and $T_c = 175(2)(4)\text{MeV}$ for the strange quark number [AFKS06]. This discrepancy has triggered great efforts in understanding and resolving the problem and it seems that recently the lattice results on the critical temperature at $\mu_B = 0$ are converging towards a value of $T_c \approx 150\text{ MeV}$ to 160 MeV [BP10, B⁺10, Kan10, Sol10].

The qualitative picture of the QCD phase diagram

Collecting all the information, a picture of the phase diagram of strongly interacting matter emerges. At small temperatures and baryon chemical potentials the matter is in the familiar confined, hadronic phase. At small chemical potential $\mu_B \sim 0$ there is a cross over to a deconfined quark-gluon plasma phase at a critical temperature of $T_c \approx 150\text{ MeV}$ to 160 MeV . At small temperatures but high chemical potentials, results from the NJL model, however,

suggest a first order phase transition. This implies the existence of a second order critical endpoint to the line of first order phase transitions as illustrated in fig. 2.3. The critical point of QCD is tremendously difficult to locate and predictions from models or lattice QCD basically vary all over the place. See [Ste06, Sch06] for reviews on methods and results. Furthermore, some lattice results suggest that the mere existence of a critical point is not assured for the physical quark masses [dFP07, dFP08].

Of course the qualitative picture discussed above is incomplete. Even for water a variety of particular phases—different sorts of ice—exist at the extreme edges of the phase diagram. For nuclear matter color superconducting and color-flavor locked phases are conjectured to exist at small temperatures but very high baryon chemical potentials, with possibly a vast number of distinct subregions in the phase space [SRMF09].

2.3. Little big bangs in the laboratory

As already mentioned in the previous section, colliding the nuclei of heavy elements is the experimental way to create matter at high temperatures ($T \gtrsim T_c$) and/or at high baryon densities. Such experiments are commonly called *heavy ion collisions*. Since the total energy that can be used to heat up or compress the system is naturally limited by the center of momentum (c.m.) energy per colliding nucleon pair, $\sqrt{s_{NN}}$, and thus the beam energy needs to be very high, the prefix *relativistic* or even *ultra-relativistic* is often added. When heavy ion collisions create such high temperatures that a deconfined phase is reached as it is expected to have existed in the very early cosmic history (see section 2.2), they are sometimes referred to as *little Big Bangs*.

Simple as this concept may sound, the challenges are tremendous and manifold. Some of the technological challenges will be covered in this section and some of the conceptual problems in section 2.4 and throughout this work.

The era of systematic relativistic heavy ion physics started over three decades ago with the BEVALAC accelerator at the LBNL¹⁴. It facilitated the exploration of excited and compressed hadronic matter at center of mass energies on the order of roughly 2 GeV to 6 GeV per nucleon pair. It was succeeded in terms of accessible beam energy by the *Alternating Gradient Synchrotron* (AGS) at the BNL¹⁵ that provided up to 11.5 A GeV for heavy ions. The *Super Proton Synchrotron* (SPS) at CERN¹⁶ later provided up to $\sqrt{s} = 17.3$ A GeV.

Fixed target experiments at SPS claim to have seen the onset of deconfinement [GSS03, NA4904]. While this is quite probably the case, the exploration of a deconfined phase of matter gathered momentum with the commissioning of the *Relativistic Heavy Ion Collider* at BNL in 2000. It has been the first heavy ion accelerator that is able to operate in collider mode and provides energies up to $\sqrt{s} = 200$ A GeV, mostly colliding gold nuclei (Au + Au). RHIC originally featured four experiments, STAR, PHENIX, BRAHMS and PHOBOS, of which only the two major ones, STAR¹⁷ and PHENIX¹⁸, are still in operation.

¹⁴LBNL = *Lawrence Berkley National Laboratory*

¹⁵BNL = *Brookhaven National Laboratory*

¹⁶The *European Organization for Nuclear Research*. Literally the acronym CERN stands for *Conseil Européen pour la Recherche Nucléaire* (European Council for Nuclear Research), the provisional council that was formed in 1952 to set up the research center.

¹⁷STAR = *Solenoidal Tracker at RHIC*

¹⁸PHENIX = *Pioneering High Energy Nuclear Interactions eXperiment*

At the very moment these pages are written, the first heavy ion run at the *Large Hadron Collider* (LHC) at CERN is underway. The LHC is the largest and strongest accelerator ever built, running at its design values it will collide protons at $\sqrt{s} = 14$ TeV and lead ions at $\sqrt{s_{NN}} = 5.5$ TeV. Though the energies in the first physics runs, $\sqrt{s} = 7$ TeV for p + p and $\sqrt{s_{NN}} = 2.76$ TeV for Au + Au, are not yet reaching these design values, they are already now setting new world records. The ALICE¹⁹ experiment is specifically designed for heavy ion physics but the two general purpose experiments CMS²⁰ and ATLAS²¹ also feature dedicated heavy ion programs.

While the heavy ion experiments at the LHC will probe unprecedented energy densities and temperatures—and thus basically move along the T -axis at $\mu_B \approx 0$ in the phase diagram as is also the case for RHIC experiments—the planned *Facility for Antiproton and Ion Research* (FAIR) at GSI²² (scheduled to start operation somewhere between 2014 and 2016) will probe the phase diagram at large net baryon densities (and large temperatures).

As the physics covered in this work is almost exclusively based on the observations made at the large RHIC experiments, the following discussion will focus on the results obtained at RHIC. Table 2.1 provides an overview of systems and energies probed at RHIC in various runs over the past decade. Already the first couple of years of running provided conclusive evidence that in collisions of gold nuclei at 200 A GeV a new state of matter is indeed created. These results have been published in a joint effort by all RHIC experiments in so called *white papers* in 2005 [STAR05a, PHENIX05, BRAHMS05, PHOBOS05b].

The findings presented in these papers feature two crucial observations on the properties of the medium created in high energy heavy ion collisions at RHIC:

- The medium exhibits a strong collective flow pattern.
- Particles with high transverse momentum are strongly modified by the medium.

The collective properties of the medium are commonly investigated by looking at the *elliptic flow* that is quantified in terms of the second Fourier coefficient v_2 of the distribution of particles in the azimuthal angle perpendicular to the beam line. The modification of high- p_T particles, called *jet quenching*, is quantified in terms of the *nuclear modification factor* R_{AA} , that compares the yield at high transverse momenta in heavy ion collisions to the scaled yield in proton-proton collisions. These two key observables will be covered in more detail in section 5.1.

Furthermore, the fact that the observed hadrons emerging from the fireball are to a large extent in chemical and thermal equilibrium hints to a production from a thermally equilibrated medium. Measurements of the early temperature via direct photons [PHENIX10a] confirm that the initial temperature of the medium is on the order of $T_{init} \sim 300$ MeV to 600 MeV and thus distinctly above the critical temperature expected from lattice QCD or other models.

Comparison of flow data to hydrodynamical simulations has shown that the medium can be surprisingly well described by ideal hydrodynamics [HKH⁺01, KH03]. This requires an early thermalization of the medium on a time scale on the order of $1 \text{ fm } c^{-1}$ and it has

¹⁹ALICE = *A Large Ion Collider Experiment*

²⁰CMS = *Compact Muon Solenoid*

²¹ATLAS = *A Toroidal LHC Apparatus*

²²GSI = *Gesellschaft für Schwerionenforschung*

	Year	System	Energy
Run 1	2000	Au + Au	130.4 GeV
Run 2	2001/2002	Au + Au	200 GeV
		p + p	200 GeV
Run 3	2002/2003	d + Au	200 GeV
Run 4	2003/2004	Au + Au	62.4 GeV
		Au + Au	200 GeV
Run 5	2004/2005	Cu + Cu	62.4 GeV
		Cu + Cu	200 GeV
		p + p	200 GeV
Run 6	2006	p + p	200 GeV
Run 7	2006/2007	Au + Au	200 GeV
Run 8	2007/2008	d + Au	200 GeV
		p + p	200 GeV
Run 9	2008/2009	p + p	200 GeV
		p + p	500 GeV
Run 10	2009/2010	Au + Au	7.7 GeV
		Au + Au	11.5 GeV
		Au + Au	39.0 GeV
		Au + Au	64.2 GeV
		Au + Au	200 GeV

Table 2.1.: An (incomplete) overview of the collision systems and energies probed at the Relativistic Heavy Ion Collider over the past decade. See [Fis10] for more details.

led to the popular notion of the quark-gluon plasma being a perfect liquid [BNL05]. This discovery has shifted the early paradigm that the QGP was a weakly interacting gas of free quarks and gluons towards the conception that the QGP is rather a fluid of strongly coupled quarks and gluons [GM05, Shu05, Lee05], sometimes labeled the sQGP for *strongly coupled QGP*.

This has also triggered considerable efforts in describing RHIC observables in terms of a correspondence between conformal field theory and string theory in an Anti-de-Sitter space [Mal98, Wit98, GKP98, GKT98], the so called AdS/CFT correspondence. Instead of expanding in a weak coupling parameter α as in perturbative QCD, this approach employs a holographic principle and uses string theory techniques to make connections between a $(d+1)$ -dimensional gravitational theory and a d -dimensional field theory. The $5d$ Anti-de-Sitter space is mapped to a 4-dimensional conformal field theory at large N_c and strong coupling. Based on this mapping, observables such as the elliptic flow, the viscosity and the energy loss of heavy quarks are investigated in the limit of strong (infinite) coupling [NGT09].

However, one has to keep in mind that as interesting as these holographic approaches are, QCD is not a conformal field theory and the number of colors is not infinity. Conformal field theories for example do not exhibit asymptotic freedom. So it will be exciting to see how much and what can be actually learned from these correspondences regarding QCD phenomena. And although the notion that the medium created in ultra-relativistic heavy ion collisions can be actually described in terms of hydrodynamics is commonly accepted, the question how strongly the quark-gluon plasma is actually coupled and what mechanisms cause the hydrodynamic behavior is subject to many debates.

2.4. The purpose of this work

Heavy ion collisions are highly complicated. This is probably one of the few things that all physicists in the field, experimental and theoretical, would readily agree on.

The hot and dense medium created in ultra-relativistic heavy ion collisions exists only for a couple of fm c^{-1} , i.e. for an unimaginably tiny instant on the order of 10^{-23} seconds. Confinement prevents a direct observation of partonic degrees of freedom and only hadrons reach the detectors, thus rendering any observation of the QGP inherently indirect. Additionally, the large abundance of produced particles, a couple of thousand per event, mostly pions, makes the extraction of interesting signals from the vast background very challenging in many cases. Not to mention the highly complicated detector technology, the triggers, the calibration issues, the acceptance corrections, the elaborate data analysis etc.

Leaving the experimental issues aside, the challenges on the theoretical side are equally numerous and severe. With the confirmation from the RHIC white papers [[STAR05a](#), [PHENIX05](#), [BRAHMS05](#), [PHOBOS05b](#)] that a new state of matter is indeed created in ultra-relativistic Au + Au collisions, heavy ion physics has turned from the mere quest for the quark-gluon plasma towards precision measurements of the properties of the quark-gluon plasma. In order to deduce the properties of the QGP from the hadronic signals measured in the detectors after the medium has long ceased to exist, one needs theories or models that relate final state observable to the properties of the short-lived hot and dense medium as unambiguously as possible.

Indeed, such models are needed for various stages and aspects of the evolution of a heavy ion collision. The following list is certainly non-exhaustive but mentions the most important aspects that need to be modeled on a quantitative level in order to gain some insight into the properties of the QGP:

- Initial state
- Evolution of the medium²³
- High- p_T phenomena
- Phase transition
- Hadronization

²³The medium in this context is often referred to as the *bulk*. This term comprises all ordinary particles, i.e. particles that do not stick out by for example having a high transverse momentum or a large mass.

Any of these aspects alone has provided years, if not decades, of occupation to dozens of scientists and will do so for many years to come. So it is no surprise that as of now there is no model that can simultaneously describe all, or even most, of the aspects mentioned above. But there are quite a number of tools and frameworks that are applied to different aspects of heavy ion collisions, with varying accuracy and success. The following list is of course non-exhaustive again:

- Parametrizations (e.g. Bjorken model [Bjo83])
- Hydrodynamics
- Transport models
- Lattice QCD
- Perturbative QCD
- AdS/CFT

Especially the description of jet quenching and elliptic flow within one common framework is a major challenge. Most energy loss formalisms attribute the quenching of jets to medium induced radiative processes, where gluons are emitted in bremsstrahlungs-like interactions, and are based on perturbative QCD [Zak96, BDM⁺97, BDMS98, GLV01, AMY02, JM05, SW03, WHDG07]. The bulk evolution, most prominently the elliptic flow, on the other hand is commonly studied within hydrodynamical models that only deal with collective properties of the medium. Recently the efforts to combine pQCD-based jet physics with hydrodynamic modeling of the medium have been intensified, for instance results from hydrodynamical simulations are used as an input for the medium evolution in jet quenching calculations (see [BGM⁺09] for an overview) and as ingredients in Monte Carlo event generators, e.g. [SGJ09]. However, these approaches still treat medium physics and jet physics in the QGP on very different grounds. Moreover, so far no schemes are available that cover the full dynamics of the interplay between jets and the medium. These issues will be discussed in some more detail in section 5.1.

Partonic transport models might provide means to investigate bulk properties of the QGP and high energy parton jets within a common physical framework automatically including the full dynamics of the evolution of the system. To large extends based on the publications [FXG09, FXG10] it is the purpose of this work to explore the prospects of the transport model BAMPS (*Boltzmann Approach to Multi-Parton Scatterings*) [XG05] in this respect. Unlike other partonic transport models that are limited to binary interactions [Zha98, MG00, BMS03, LKL⁺05], BAMPS consistently features inelastic $2 \leftrightarrow 3$ processes based on pQCD matrix elements. This has enabled BAMPS to describe many bulk properties—such as the strong elliptic flow, a small viscosity and an early thermalization—with remarkable success²⁴. In order to explore the predictive power and the limitations of such a model, it is instructive to take it beyond the region it has originally been conceived for. In the case at hand, this means taking BAMPS beyond the investigation of bulk properties and exploring high- p_T phenomena within its framework.

²⁴See chapter 3 for more details and references.

3. The transport model BAMPS

This chapter provides information on the partonic transport model BAMPS that is used throughout this work. It has been developed by XU and GREINER [XG05] to investigate the thermalization of gluonic matter created in heavy ion collisions at RHIC energies and since then been applied to various observables.

The following sections cover the basic functionality of the model, review some previous results and discuss extensions of the original model that have been made in the course of this work—namely the treatment of boosted reference frames for the evaluation of the LPM cutoff, section 3.1.4, and the inclusion of light quarks, section 3.4. Specific details are covered where they are relevant to the simulation of high- p_T phenomena or otherwise related to the investigations presented here. For further technical details and verifications of the model, please see [XG05].

3.1. The simulation framework

3.1.1. Basic concept

BAMPS (*Boltzmann Approach to Multi-Parton Scatterings*) [XG05, XG07] is a microscopic Monte Carlo transport model aimed at simulating the early stage of heavy ion collisions on the partonic level via perturbative QCD interactions consistently including parton creation and annihilation processes. It operates with massless on-shell Boltzmann particles, i.e. no Bose enhancement or Pauli blocking is taken into account.

The basic idea is to solve the relativistic Boltzmann equation [Gro80]

$$p^\mu \partial_\mu f(x, p) = \mathcal{C}(x, p) \tag{3.1}$$

via a stochastic collision algorithm. The Boltzmann equation describes the evolution of the distribution function $f(x, p)$ induced by the collision term $\mathcal{C}(x, p)$. The collisionless, free streaming, case would be trivially given by $\mathcal{C}(x, p) = 0$. In general the collision term embodies the information on all possible interactions between the particles described by $f(x, p)$. The collision term can be expanded in contributions from different types of processes, with BAMPS incorporating $2 \rightarrow 3$, $2 \rightarrow 2$ and $3 \rightarrow 2$ processes¹, i.e.

$$\mathcal{C}_{\text{BAMPS}}(x, p) = \mathcal{C}_{22}(x, p) + \mathcal{C}_{23}(x, p). \tag{3.2}$$

In order to be able to include the three-body interactions that are contained in $\mathcal{C}_{23}(x, p)$, BAMPS relies on a stochastic algorithm to solve the Boltzmann equation. Space and time are discretized into small cells with volume ΔV and time steps Δt . Within a given Δt particles may only interact with particles that are located in the same spatial cell ΔV . The

¹Where $M \rightarrow N$ is a shorthand for: Interaction with a M -body initial state and a N -body final state, see appendix A.2 for notation and conventions.

very core of the collision algorithm can then be summarized as sketched in [algorithm 1](#). Particles propagate on straight lines in between collisions. The cell size² Δz , with $\Delta V = (\Delta z)^3$ should be chosen such that it is smaller than the mean free path λ of the particles to avoid numerical artifacts [[BMN⁺10](#)]. The time steps Δt are always chosen to be smaller than the cell size, $\Delta t \ll \Delta z$, to avoid strong local fluctuations.

Algorithm 1: Schematic view of the stochastic collision algorithm used in BAMPS

```

t = 0
while t < tfinal do
  foreach cell ΔV do
    foreach particle pair (triplet) in the current cell do
      Compute collision probability P
      Generate random number x ∈ [0, 1)
      if x < P then // collision takes place
        Sample new momenta of outgoing particles
        Assign new momenta to outgoing particles
      t = t + Δt
  Propagate particles to time t

```

The procedure relies on the Monte Carlo sampling of collision probabilities P . In contrast to a geometrical collision algorithm that is used in many transport models, e.g. [[Zha98](#), [LKL⁺05](#), [BBB⁺98](#), [BZS⁺99](#)], and that relies on the geometrical interpretation of cross sections, the stochastic algorithm allows for the incorporation of $N \rightarrow 2$ processes with $N > 2$. Thus the collision term \mathcal{C}_{23} can be consistently included, respecting detailed balance in the simulations.

The test particle method is employed to reduce statistical fluctuations and is implemented such that the mean free path is left invariant. To accomplish this, the collision probability needs to be scaled by the number of test particles per real particle [[XG05](#)], N_{test} , according to

$$P_{2 \rightarrow Y} \rightarrow \frac{P_{2 \rightarrow Y}}{N_{\text{test}}} \quad P_{3 \rightarrow Y} \rightarrow \frac{P_{3 \rightarrow Y}}{N_{\text{test}}^2}. \quad (3.3)$$

The Boltzmann equation ([3.1](#)) is solved exactly in the limit $\Delta t, \Delta V \rightarrow 0$ and $N_{\text{test}} \rightarrow \infty$. Numerically this is of course not feasible, but tuning the number of test particles such that there are roughly 10 to 20 test particles in a given cell $\Delta V = (\Delta z)^3$ (with $\Delta z < \lambda$) already gives reasonably good results [[XG05](#), [BMN⁺10](#)].

In its original version BAMPS operates at the number of flavors set to zero, $N_f = 0$, i.e. it only considers gluonic degrees of freedom. Since the medium created in heavy ion collisions is initially strongly gluon dominated, this simplification is justified. For precise comparison to experimental data, especially in the high- p_T sector, however, light quarks can be important. A first attempt to include light quarks into BAMPS is presented in section [3.4](#). The inclusion of heavy quarks is also underway, see [[UFXG10a](#)] and section [3.3.4](#).

²The generalization to irregular cell shapes, $\Delta V = \Delta x \cdot \Delta y \cdot \Delta z$, is trivial.

3.1.2. Collision probabilities, matrix elements and cross sections

In principle the collisions probabilities discussed above can be chosen quite arbitrarily, as long as detailed balance is observed. But usually they will be based on physical cross sections or invariant matrix elements. And though fixed isotropic cross sections for binary processes are used for systematic studies of the model characteristics, in the standard version of BAMPS the collision probabilities are based on cross sections and matrix elements from leading order perturbative QCD.

A comparison of the rate obtained from the collision term to the definition of the cross section yields the probability for a given $2 \rightarrow N$ process to occur within Δt and ΔV [XG05, Gro80]

$$P_{2N} = v_{\text{rel}} \sigma_{2N} \frac{\Delta t}{\Delta V}. \quad (3.4)$$

The relative velocity of the two incident particles A and B is given by

$$v_{\text{rel}} = |\mathbf{v}_A - \mathbf{v}_B| = \frac{\sqrt{(p_A p_B)^2 - m_A^2 m_B^2}}{E_A E_B}. \quad (3.5)$$

In the case of massless particles this simplifies to

$$v_{\text{rel}} = \frac{s}{2E_A E_B}. \quad (3.6)$$

The cross section σ_{2N} for a $2 \rightarrow N$ process in terms of the invariant matrix element $|\mathcal{M}_{AB \rightarrow 12 \dots N}|^2$ is given by

$$\sigma_{2N} = \frac{1}{2s} \frac{1}{\nu} \left(\prod_{i=1}^N \int \frac{d^3 p_i}{(2\pi)^3 2E_i} \right) (2\pi)^4 \delta^{(4)}(p_A + p_B - \sum_{i=1}^N p_i) |\mathcal{M}_{AB \rightarrow 12 \dots N}|^2, \quad (3.7)$$

with a factor $1/\nu$ to account for identical particles in the final state. See appendix B for more information on the definition and computation of cross sections and invariant matrix elements.

For $3 \rightarrow 2$ processes the computation of the collision probability is similar to eq. (3.4), however the concept of a cross section does not make sense in the case of three incoming particles, therefore the probability is given by

$$P_{32} = \tilde{I}_{32} \frac{\Delta t}{(\Delta V)^2} = \frac{1}{8E_A E_B E_C} I_{32} \frac{\Delta t}{(\Delta V)^2}, \quad (3.8)$$

where I_{32} is the phase space integral over the matrix element that corresponds to the cross section in eq. (3.4). It is given by

$$I_{32} = \frac{1}{\nu} \iint \frac{d^3 p_1}{8\pi^3 2E_1} \frac{d^3 p_2}{8\pi^3 2E_2} (2\pi)^4 \delta^{(4)}(p_A + p_B + p_C - p_1 - p_2) |\mathcal{M}_{ABC \rightarrow 12}|^2. \quad (3.9)$$

The cross sections used for elastic $2 \rightarrow 2$ processes are computed from leading order pQCD in small angle approximation. For a binary collision of gluons, $gg \rightarrow gg$, the differential cross section in the transverse momentum transfer \mathbf{q}_\perp^2 reads

$$\frac{d\sigma_{gg \rightarrow gg}}{d\mathbf{q}_\perp^2} = 9\pi\alpha_s^2 \frac{1}{(\mathbf{q}_\perp^2 + m_D^2)^2}. \quad (3.10)$$

In order to avoid infrared divergences the gluon propagators of the underlying Feynman diagrams are screened by the Debye mass m_D . It is dynamically computed from the distribution of gluons, f_g , (and quarks, f_q , if $N_f > 0$) according to

$$m_D^2 = d_G \pi \alpha_s \int \frac{d^3 p}{(2\pi)^3} \frac{1}{p} (N_c f_g + N_f f_q). \quad (3.11)$$

Technically this is done by replacing the integral over the distribution function by a discrete sum over (test) particles. In thermal equilibrium the Debye mass evaluates to

$$m_D^2|_{\text{thermal}} = (3 + N_f) \frac{8}{\pi} \alpha_s T^2, \quad (3.12)$$

exhibiting the well-known $m_D^2 \sim g^2 T^2$ behavior. Please see appendix B.3 for more information on cross sections in small angle scattering and the screening of infrared divergences.

The collision probability for the bremsstrahlung process $gg \rightarrow ggg$ processes is computed from the matrix element derived by GUNION and BERTSCH [GB82] with added Debye screening [XG05]

$$|\mathcal{M}_{gg \rightarrow ggg}|^2 = \left(72 \pi^2 \alpha_s^2 \frac{s^2}{(\mathbf{q}_\perp^2 + m_D^2)^2} \right) \left(48 \pi \alpha_s \frac{\mathbf{q}_\perp^2}{\mathbf{k}_\perp^2 [(\mathbf{k}_\perp - \mathbf{q}_\perp)^2 + m_D^2]} \right) \quad (3.13)$$

via eqs. (3.4) and (3.7). As before, \mathbf{q}_\perp is the transverse component of the momentum transfer and \mathbf{k}_\perp denotes the transverse momentum of the radiated gluon, both given in the center of momentum frame of the colliding particles. The corresponding matrix element for gluon annihilation $ggg \rightarrow gg$ is obtained from eq. (3.13) via the principle of detailed balance, yielding

$$|\mathcal{M}_{ggg \rightarrow gg}|^2 = \frac{1}{d_g} |\mathcal{M}_{gg \rightarrow ggg}|^2, \quad (3.14)$$

where the factor $d_g = 16 = 2 \cdot 8$ is just the gluon degeneracy.

When computing the total cross section for $gg \rightarrow ggg$ processes via the integration over the final phase space (3.7), it is convenient to convert eq. (3.13) into a multivariate differential cross section [XG05]

$$\frac{d\sigma_{gg \rightarrow ggg}}{dq_\perp^2 dk_\perp^2 dy d\phi} = \frac{d_g}{256 \pi^4 s} \frac{1}{\nu} |\mathcal{M}_{gg \rightarrow ggg}|^2 \sum \left(\left| \frac{\partial F}{\partial y_1} \right|_{F=0} \right)^{-1}, \quad (3.15)$$

which is then used as a starting point. This expression is also better suited for the sampling of final momenta, see section 3.1.5. The factor containing the sum over the roots of F stems from the properties of the δ function in eq. (3.7). After integration over $d^3 p_2$ the δ function reads $\delta(F)$ with $F = (p_A + p_B - p_1 - p_3)^2$. Further integration over the rapidity y_1 of particle 1 as seen from the center of momentum frame then yields the above expression. The result can be cast into a rather lengthy expression of the variables s , q_\perp , k_\perp , ϕ and y [XG05], where ϕ denotes the relative angle between \mathbf{q}_\perp and \mathbf{k}_\perp and y is the rapidity of the emitted particle in the c.m. frame. ν accounts for identical particles in the final state. See appendix B.4 for a detailed computation.

3.1.3. Small angle approximation in the $2 \rightarrow 3$ cross section

In principle the requirement $F = 0$ from the transformed delta function in eq. (3.15) yields two possible solutions, eqs. (B.40) and (B.41), for the longitudinal momentum component $p_{1,z}$ of the outgoing particle 1 in inelastic $2 \rightarrow 3$ processes, as discussed in more detail in appendix B.4. These solutions correspond to two additive contributions to the differential (3.15) or the total (B.39) cross section since the matrix element $|\mathcal{M}_{2 \rightarrow 3}|^2$ in Gunion-Bertsch approximation does not explicitly depend on the rapidity y_1 .

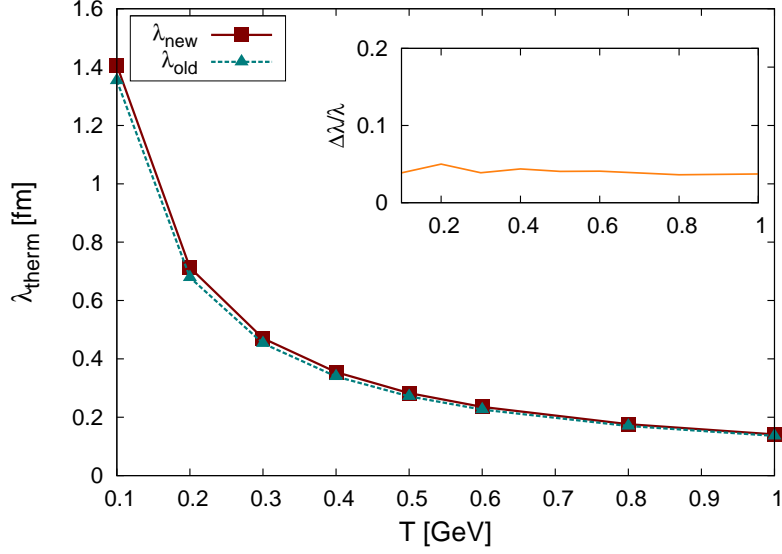
To illustrate this further, consider the limit where $k_\perp = 0$. The argument (B.32) of the delta function in eq. (B.31) then simplifies to $F = s - 2q_\perp \sqrt{s} \cosh y_1$ with the possible roots $y_1 = \pm \cosh^{-1} \frac{\sqrt{s}}{2q_\perp}$. The derivative of F with respect to y_1 in this limit is simply $\frac{\partial F}{\partial y_1} = 2\sqrt{s}q_\perp \sinh y_1$. Thus the term in eq. (3.15) from the transformation of the momentum conserving delta function becomes

$$\sum \left(\left| \frac{\partial F}{\partial y_1} \right|_{F=0} \right)^{-1} = \sum \frac{1}{|2\sqrt{s}q_\perp \sinh y_1|_{F=0}} = \frac{2}{s\sqrt{1 - \frac{4q_\perp^2}{s}}}, \quad (3.16)$$

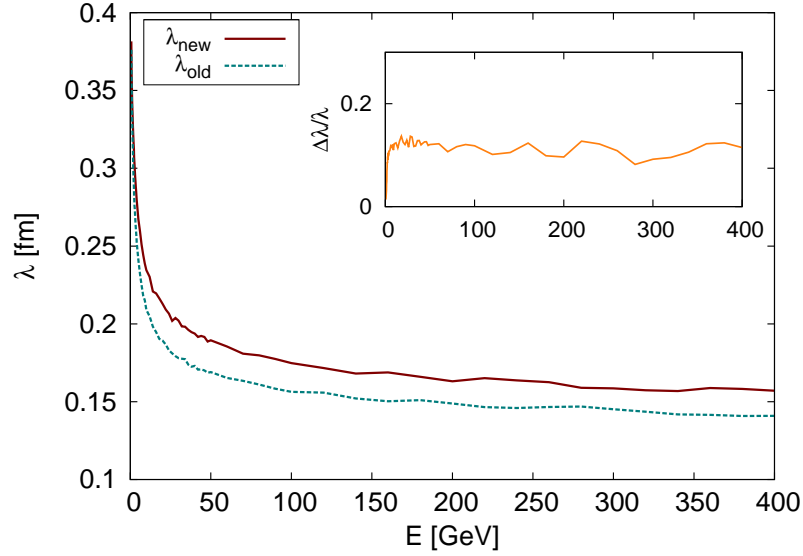
where the sum runs over all possible solutions to $F = 0$ and together with the absolute value leads to the factor 2 in the nominator of the last expression. In the limit $q_\perp = 0$ this would further simplify to $\sum (|\partial F / \partial y_1|_{F=0})^{-1} = 2/s$. The contributions from the positive and negative solutions to $p_{1,z}$ in this limit therefore lead to an overall factor of 2 in the differential (3.15) and total (B.39) cross section for the $2 \rightarrow 3$ process. For the generic case, with solutions eqs. (B.40) and (B.41) for $p_{1,z}$, the situation is more involved and the sum in eq. (3.16) will not lead to a simple overall factor of 2, but the general line of argument still holds.

Solutions with $p_{1,z} < 0$, however, are not within the approximations leading to the Gunion-Bertsch matrix element that is employed in BAMPS. Similar to the small angle approximation in binary collisions, see appendix B.3, the approximations underlying the Gunion-Bertsch matrix element rely on soft momentum transfer, i.e. $q_\perp \ll \sqrt{s}$ and the incoming momenta p_A and p_B do not revert their directions as would be the case for $p_{1,z} < 0$. See section 3.2 for a detailed discussion of the approximations in Gunion-Bertsch.

Therefore, in order to avoid double counting in the total cross section for $2 \rightarrow 3$ processes, contributions with $p_{1,z} < 0$ should be discarded. In previous versions of BAMPS this subtle constraint had been overlooked, but the effect on the thermal mean free path is very small. Figure 3.1a shows the mean free path of a gluon inside a thermal medium with $N_f = 3$ as a function of the temperature with (*new*) and without (*old*) taking the constraint $p_{1,z} > 0$ into account. The thermal mean free path only increases by about 5%, independent of the medium temperature. For energetic particles the effect should be more pronounced since for large \sqrt{s} and $\sqrt{s} \gg q_\perp$, k_\perp the limit $k_\perp = q_\perp = 0$ as sketched above should become more realistic. Indeed, the increase in the mean free path for an energetic gluon traversing a thermal medium when constraining $p_{1,z}$ to positive values is stronger than in the thermal case but still rather weak, only on a level of about 15%, see fig. 3.1b. This is partially due to the inclusion of the LPM effect for radiative processes via a momentum cutoff that depends on the mean free path, see the discussion in section 3.1.4. This cutoff requires an iterative procedure, eq. (3.18), for the computation of the actual mean free path of energetic particles that effectively self-quenches changes in the cross section for $2 \rightarrow 3$ processes. Without this



(a) Thermal mean free path of gluons in a $N_f = 3$ medium as a function of the medium temperature T before (*old*) and after (*new*) fixing the double counting of the longitudinal momentum components $p_{1,z}$ from eqs. (B.40) and (B.41). See text for details. The inset shows the relative difference of the two curves, $(\lambda_{\text{new}} - \lambda_{\text{old}})/\lambda_{\text{old}}$.



(b) Mean free path of a high energy gluon inside a medium with $T = 0.4$ GeV and $N_f = 3$ as a function of the energy E before (*old*) and after (*new*) fixing the double counting of the longitudinal momentum components $p_{1,z}$ from eqs. (B.40) and (B.41). See text for details. The inset shows the relative difference of the two curves, $(\lambda_{\text{new}} - \lambda_{\text{old}})/\lambda_{\text{old}}$.

Figure 3.1.: Comparison of the mean free path including all possible $2 \rightarrow 2$ and $2 \leftrightarrow 3$ processes before and after fixing the double counting of the contributions from the transformed delta function in eq. (3.15) as described in the text.

iterative procedure the difference in the mean free path for a high energy parton with and without taking the constraint $p_{1,z} > 0$ into account would be on the order of 35 % to 40 %.

While the quantitative effect of the constraint $p_{1,z} > 0$ on the mean free path—or equivalently the total cross section—is rather weak, it also influences the sampling of momenta from eq. (3.15) and therefore has some effect on the energy loss of jet partons. Furthermore it affects the flavor conversion probability of energetic partons in $2 \rightarrow 3$ processes. These effects will be discussed in chapters 4 and 5 as appropriate. However, the general finding that the quantitative effect is rather mild holds for all observables. This is mainly due to the Lorentz boost incorporated into the LPM cutoff that especially for large jet energies prefers radiation into the backward direction, thus typically $p_{3,z} < 0$, as discussed in section 3.1.4. Together with eqs. (B.40), (B.41) and (B.43) this leads to solutions for $p_{1,z}$ that are predominantly positive. Consequently, especially for interactions involving high energy jets, only a comparatively small fraction of events would feature solutions with $p_{1,z} < 0$ that are removed by the newly introduced constraint. If the radiated gluon was to be emitted equally into the forward and the backward direction—as would be the case if the boost in the LPM effect was neglected, again cf. section 3.1.4—the small angle constraint would however introduce a correction by a factor of 2 for interactions at very large \sqrt{s} .

3.1.4. Modeling of the LPM effect

The LPM cutoff

When considering bremsstrahlung-like processes such as $gg \rightarrow ggg$ the LPM-effect [LP53, Mig56], a coherence effect named after LANDAU, POMERANCHUK and MIGDAL, needs to be taken into account that leads to a suppression of the emission rate for high energy particles.

In a quantum electrodynamical treatment of medium-induced photon radiation from a high energy electrically charged particle, LANDAU, POMERANCHUK and MIGDAL discovered already in the 1950s that the amplitudes of subsequent scatterings with medium constituents interfere destructively. This is due to a finite formation time of the emitted photons. In QCD the case is even more complicated since the radiated gluons themselves can rescatter and pick up additional transverse momentum from the medium, see fig. 3.2 for an illustration, effectively altering their formation time.

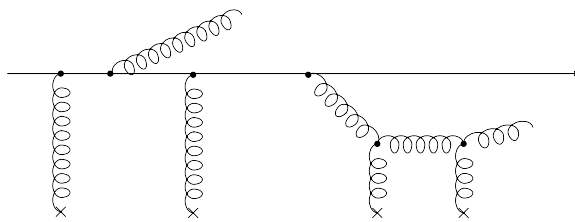


Figure 3.2.: Illustration of multiple medium induced gluon radiation from a high energy parton and rescatterings of the emitted gluons.

Since such an interference effect cannot be incorporated directly into a semi-classical microscopic transport model such as BAMPS, an effective approach is chosen by introducing a cutoff in phase space. It is represented by a step function that modifies the Gunion-Bertsch

matrix element from eq. (3.13) as

$$|\mathcal{M}_{gg \rightarrow ggg}|^2 \rightarrow |\mathcal{M}_{gg \rightarrow ggg}|^2 \Theta(\lambda - \tau). \quad (3.17)$$

The step function $\Theta(\lambda - \tau)$ implies that the formation time τ of the emitted gluon must not exceed the mean free path λ of the parent jet particle, ensuring that successive radiative processes are independent of each other.

Through this cutoff the total cross section depends on the current mean free path, which in turn depends on the total cross section. The evaluation of the total cross section including inelastic processes based on the matrix element (3.17) thus becomes highly involved. For processes where the mean free path is expected to be far from the thermal average, e.g. for high energy jets, this calls for an iterative procedure. The true mean free path is then evaluated as

$$\lambda = \lim_{i \rightarrow \infty} \lambda_i = \lim_{i \rightarrow \infty} \frac{1}{R_{22} + R_{23}(\lambda_{i-1}) + R_{32}(\lambda_{i-1})} \quad (3.18)$$

where R_{22} , R_{23} and R_{32} denote the sums of the rates for all $2 \rightarrow 2$, $2 \rightarrow 3$ and $3 \rightarrow 2$ processes, respectively. R_{23} and R_{32} depend on the mean free path via the LPM cutoff (3.17), thus $R_{23} = R_{23}(\lambda)$ and $R_{32} = R_{32}(\lambda)$. The iterated value λ is then used as an input for the computation of the actual collision probabilities. The numerical convergence of this procedure has been investigated and confirmed in [Foc06].

When comparing the formation time to the mean free path, i.e. the time between successive interactions of the parent jet, special attention needs to be paid to the frames of reference. In this case three different reference frames are involved. Let Σ denote the local frame that is co-moving with the average velocity of the medium in each computational cell. In this frame the mean free path λ is computed from the interaction rates. Σ' is the center of momentum frame of the colliding particles in which the matrix element eq. (3.13) is computed. Finally, Σ'' denotes the reference frame in which the gluon is emitted purely transversal with respect to the axis defined by the colliding particles in the c.m. frame and thus $\tau'' = 1/k_{\perp}$.

In order to compare λ to τ'' in the step function modeling the LPM cutoff via $\Theta(\lambda - \tau) = \Theta\left(\frac{\lambda}{\gamma} - \tau''\right)$, the overall boost

$$\gamma = \gamma' \gamma'' (1 + \beta' \beta'') = \frac{\cosh y}{\sqrt{1 - \beta'^2}} (1 + \beta' \tanh y \cos \theta) \quad (3.19)$$

from Σ to Σ'' needs to be taken into account. γ' and β' denote the boost and the boost velocity respectively from Σ to Σ' . $\gamma'' = \cosh y$ and $\beta'' = \tanh y$ are the boost and boost velocity from Σ' to Σ'' . The latter can be expressed in terms of the rapidity y of the emitted gluon measured from the c.m. frame Σ' . θ is the angle ($0 \leq \theta < \pi/2$) between β' and the axis of the colliding particles in the c.m. frame as seen from Σ . See fig. 3.3 for an exemplary illustration.

With this the Theta function entering the bremsstrahlung matrix element can be written as

$$\Theta(\lambda - \tau) = \Theta\left(k_{\perp} - \frac{\gamma}{\lambda}\right) = \Theta\left(k_{\perp} \lambda - \frac{\cosh y}{\sqrt{1 - \beta'^2}} (1 + \beta' \tanh y \cos \theta)\right). \quad (3.20)$$

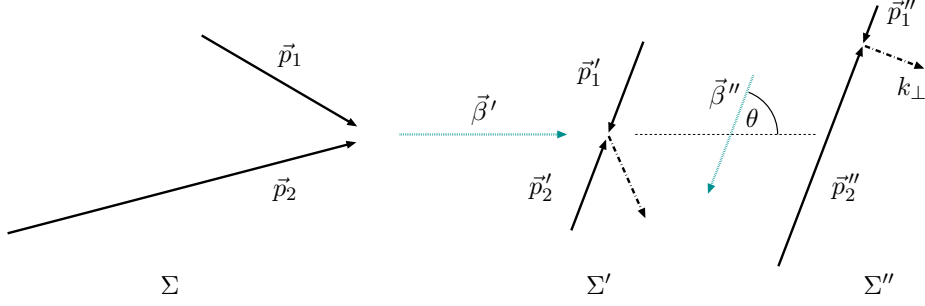


Figure 3.3.: Illustration of the reference frames involved when comparing the mean free path λ measured in frame Σ to the formation time of the emitted gluon $\tau'' = 1/k_{\perp}$ measured in frame Σ'' . \mathbf{p}_i , \mathbf{p}'_i and \mathbf{p}''_i are the momenta of the incoming particles 1 and 2 in the respective frame, the thick dashed arrow (labeled k_{\perp}) depicts the radiated gluon. See text for more details.

In this example $|\mathbf{p}_2| = 2|\mathbf{p}_1|$ and $\sphericalangle(\mathbf{p}_1, \mathbf{p}_2) = 45^\circ$ are chosen, leading to $\beta' \approx 0.933$ and $\theta \approx 69^\circ$. The gluon in this example is emitted with $\cosh y = \gamma'' = \sqrt{2}$.

For thermal energies the boost velocity β' becomes small, $\gamma \approx \cosh y$, and the Θ function effectively reduces to

$$\Theta(k_{\perp}\lambda - \cosh y) \quad (3.21)$$

as employed in the original version of BAMPS [XG05].

Constraints on the phase space for $2 \rightarrow 3$ processes

The cutoff eq. (3.20) restricts the phase space for the differential $gg \rightarrow ggg$ cross section (3.15) in the transverse momentum of the emitted gluon, k_{\perp} , and the rapidity of the emitted gluon in the c.m. frame, y . The requirement is $k_{\perp} > \frac{\gamma}{\lambda}$ with $\gamma = \frac{\cosh y}{\sqrt{1-\beta'^2}}(1 + \beta' \tanh y \cos \theta)$ from eq. (3.19).

Since $\gamma \geq 1$ the restriction on the transverse momentum is simply

$$k_{\perp} \geq \frac{1}{\lambda} \quad (3.22)$$

as was already the case in the original version of the LPM cutoff (3.21). The restriction for the rapidity y is either given from kinematical requirements

$$\cosh y < \frac{\sqrt{s}}{2k_{\perp}} \quad (3.23)$$

or from the LPM cutoff $k_{\perp}\lambda > \frac{\cosh y}{\sqrt{1-\beta'^2}}(1 + \beta' \tanh y \cos \theta)$. The latter condition can be rewritten as

$$\frac{\cosh y + A \sinh y}{B} < 1 \quad (3.24)$$

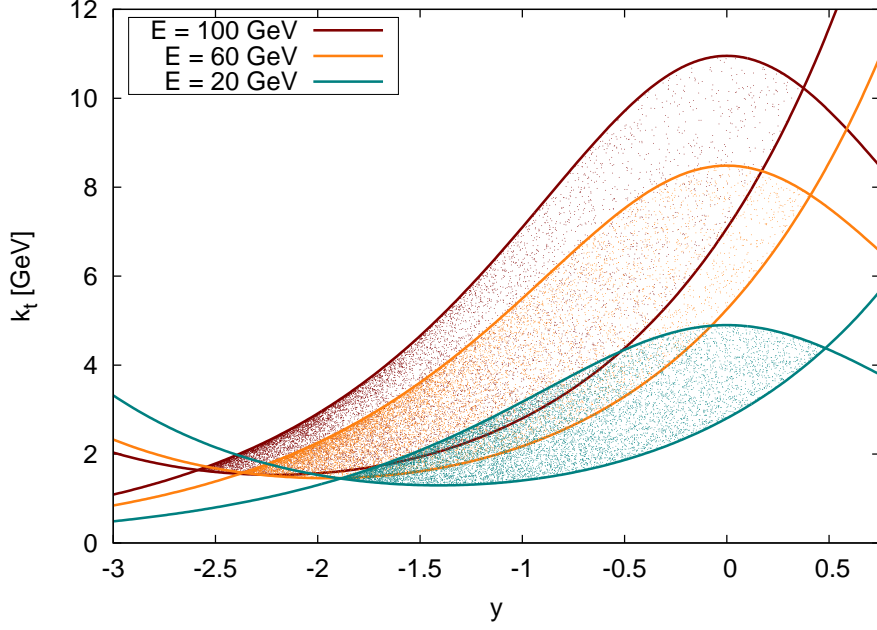


Figure 3.4.: Points in the y - k_{\perp} phase space sampled from the Gunion-Bertsch matrix element (3.13) including the constraints from the LPM cutoff (3.20) for cases in which the boosts β' and β'' are parallel. y is the rapidity of the emitted gluon in the c.m. frame, k_{\perp} its transverse momentum. The limits from the kinematic constraint (3.28) and the LPM cutoff (3.30) are shown as solid lines. See text for more details.

The four-vectors used as initial states are $p_A = (E, 0, 0, E)$ and $p_B = (3T, 0, 0, -3T)$ with $T = 0.4$ GeV and $E = 20$ GeV, 60 GeV or 100 GeV.

For $E = 20$ GeV the parameters are: $s = 96$ GeV², $\lambda = 0.772$ GeV⁻¹ and $\Delta y = 1.407$.

For $E = 60$ GeV: $s = 288$ GeV², $\lambda = 0.686$ GeV⁻¹ and $\Delta y = 1.956$.

For $E = 100$ GeV: $s = 480$ GeV², $\lambda = 0.653$ GeV⁻¹ and $\Delta y = 2.211$.

with $A = \beta' \cos \theta$ and $B = k_{\perp} \lambda \sqrt{1 - \beta'^2}$. In general this yields limits for the rapidity at a given transverse momentum k_{\perp} :

$$y_{\min} = \max \left\{ \ln \left(\frac{B - \sqrt{A^2 + B^2 - 1}}{A + 1} \right), -\cosh^{-1} \left(\frac{\sqrt{s}}{2k_{\perp}} \right) \right\} \quad (3.25a)$$

$$y_{\max} = \min \left\{ \ln \left(\frac{B + \sqrt{A^2 + B^2 - 1}}{A + 1} \right), \cosh^{-1} \left(\frac{\sqrt{s}}{2k_{\perp}} \right) \right\}. \quad (3.25b)$$

In the special case $\beta' = 0$, i.e. $A = 0$ and $B > 1$, this reduces to

$$y_{\min} = \max \left\{ -\cosh^{-1}(k_{\perp}\lambda), \quad -\cosh^{-1} \left(\frac{\sqrt{s}}{2k_{\perp}} \right) \right\} \quad (3.26a)$$

$$y_{\max} = \min \left\{ \cosh^{-1}(k_{\perp}\lambda), \quad \cosh^{-1} \left(\frac{\sqrt{s}}{2k_{\perp}} \right) \right\}, \quad (3.26b)$$

reproducing the kinematic cutoffs of the original BAMPS version. For the special cases $A = 0 \wedge B < 1$, $B = 0$ or $B < \sqrt{1+A}\sqrt{1-A}$ there is no solution, i.e. no available phase space.

The available area in the y - k_{\perp} phase space is thus given by the area enclosed by the curves

$$f(y) = \frac{\cosh y + A \sinh y}{\tilde{B}} \quad (3.27)$$

and

$$g(y) = \frac{\sqrt{s}}{2 \cosh y} \quad (3.28)$$

with $\tilde{B} = \lambda\sqrt{1-\beta'^2}$ and $A = \beta' \cos \theta$ as above. The minimum value of $f(y)$ is at $y_{f,0} = \frac{1}{2} \ln \frac{1-A}{1+A}$ and $f(y_{f,0}) = \frac{\sqrt{1-A^2}}{\tilde{B}}$, while the constraint $g(y)$ from the kinematics is symmetric around zero with its maximum value at $y_{g,0} = 0$ and $g(y_{g,0}) = \frac{\sqrt{s}}{2}$. The intersection points³ of eqs. (3.27) and (3.28) are given by

$$y_{\text{left/right}} = \frac{1}{2} \ln \left(\frac{C \mp \sqrt{A^2 + C^2 - 1}}{A + 1} \right) \quad (3.29)$$

with $C = \sqrt{s}\tilde{B} - 1$ and \tilde{B} , A from above.

It is illustrative to investigate the available phase space for the special case where the boosts β' and β'' are parallel, i.e. $\theta = 0$. In this case the LPM constraint eq. (3.27) reduces to

$$f(y) = \frac{\cosh(y + \Delta y)}{\lambda} \quad (3.30)$$

with $\tanh \Delta y = \beta'$. This is simply a hyperbolic cosine shifted by Δy . For $\Delta y = 0$, as was the case in the original BAMPS version, it is thus a hyperbolic cosine symmetric around $y = 0$. Since the kinematic constraint (3.28) is symmetric around zero in any case, this would imply an equal phase space for the emission of the radiated gluon into the forward direction, $y > 0$, and into the backward direction, $y < 0$. For a high energy particle traveling in positive z -direction, however, $\Delta y > 0$, shifting the available phase space towards negative y and preferring emission into the backward direction. Figure 3.4 illustrates this situation for gluon jets with different energies interacting with a gluon that has thermal energy and whose momentum is oriented opposite to that of the high energy gluon, i.e. giving $\theta = 0$. The increasing shift of the allowed phase space towards negative y with increasing boost $\Delta y = \tanh \beta' = \tanh \left(\left| \frac{\mathbf{p}_A + \mathbf{p}_B}{E_A + E_B} \right| \right)$ is clearly visible. In addition fig. 3.4 demonstrates that

³If the parameters A and \tilde{B} are such that there exists an enclosed area.

the points sampled by the Monte Carlo routines of BAMPS (see section 3.1.5) indeed fall into the allowed region given by eqs. (3.28) and (3.30). Additionally, a closer investigation of the distribution of the sampled points reveals that not only is the allowed region shifted towards negative y , but also that the probability as given by eq. (3.15) is higher towards the low- y edge of the allowed phase space.

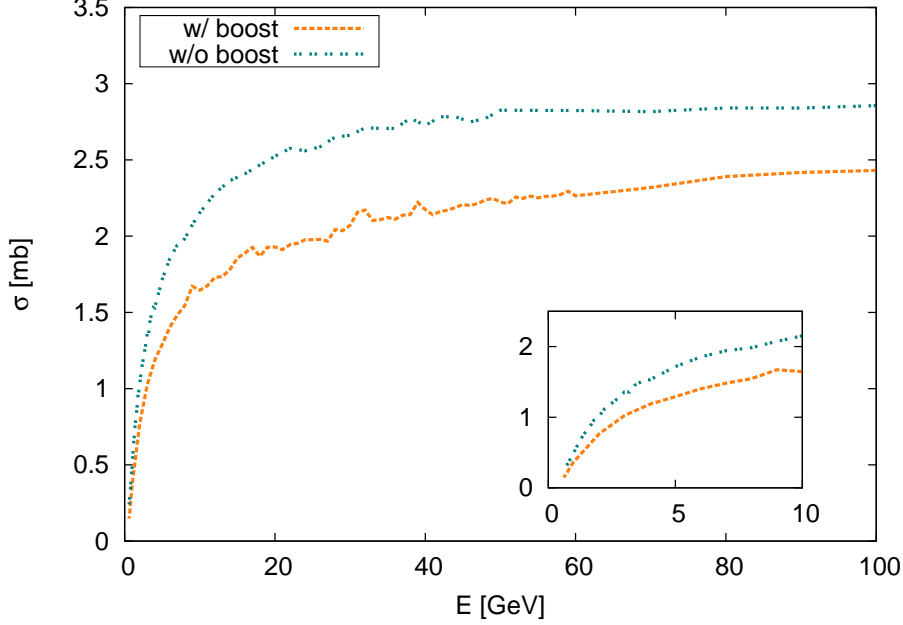


Figure 3.5.: Cross section $\sigma_{gg \rightarrow ggg}$ for $gg \rightarrow ggg$ processes ($N_f = 0$) as a function of jet energy E . The original version of the LPM cutoff (w/o boost, eq. (3.21)) is compared to the new version of the LPM cutoff (w/ boost, eq. (3.20)).

Constraints on the phase space for $3 \rightarrow 2$ processes

In order to ensure detailed balance, the constraints from the LPM cutoff (3.20) need to be consistently incorporated also into the integration and sampling of the matrix element for particle annihilation processes (3.14). The phase space integral I_{32} from eq. (3.9) can be expressed as [XG05]

$$I_{32} = \int_0^1 d\cos\vartheta \int_0^\phi d\varphi \alpha_s^3 U \frac{s^2}{(\mathbf{q}_\perp^2 + m_D^2)^2} \frac{\mathbf{q}_\perp^2}{\mathbf{k}_\perp^2 [(\mathbf{k}_\perp - \mathbf{q}_\perp)^2 + m_D^2]} \Theta\left(k_\perp - \frac{\gamma}{\lambda}\right), \quad (3.31)$$

where U contains all prefactors. To evaluate this integral—or to sample from the integrand—the integrand needs to be rewritten by introducing the angles

$$\vartheta = \angle(\mathbf{p}_1, \mathbf{p}_A) \quad (3.32a)$$

$$\delta = \angle(\mathbf{p}_1, \mathbf{p}_C) \quad (3.32b)$$

$$\varphi = \angle(\mathbf{e}_x, \mathbf{p}_1) \quad (3.32c)$$

$$\zeta = \angle(\mathbf{p}_A, \mathbf{p}_C). \quad (3.32d)$$

The angle ζ between the incoming particles A and C is known, together with E_A , E_B , E_C , \sqrt{s} and m_D^2 . The transverse momenta are then given by

$$q_{\perp} = E_A \sin \vartheta \quad (3.33a)$$

$$k_{\perp} = E_C \sin \delta \quad (3.33b)$$

and the scalar product by

$$\mathbf{k}_{\perp} \cdot \mathbf{q}_{\perp} = -E_A E_C (\cos \zeta \sin^2 \vartheta - \sin \zeta \sin \varphi \cos \vartheta \cos \varphi) . \quad (3.34)$$

The constraint from the LPM cutoff $k_{\perp} > \frac{\gamma}{\lambda}$ eq. (3.20) can then be expressed in terms of these variables by using $\cosh y = \frac{E_C}{k_{\perp}}$ and $\tanh y = \frac{2\mathbf{p}_1 \cdot \mathbf{p}_C}{\sqrt{s} E_C} = \cos \delta$ together with

$$\cos \Theta = \frac{\boldsymbol{\beta}' \cdot \mathbf{p}_1}{\beta' |\mathbf{p}_1|} = \frac{\beta'_1 \sin \vartheta \cos \varphi + \beta'_2 \sin \vartheta \sin \varphi + \beta'_3 \cos \vartheta}{\beta'} . \quad (3.35)$$

It gives a constraint in terms of the kinematic angles from eq. (3.32a) and the quantities E_C , β' and λ

$$k_{\perp}^2 > \frac{E_C}{\lambda \sqrt{1 - \beta'^2}} (1 + \beta' \cos \delta \cos \theta) . \quad (3.36)$$

Summary

In summary, the cross section for a $gg \rightarrow ggg$ process⁴ can be computed from the integral

$$\sigma_{gg \rightarrow ggg} = \int_0^{s/4} dq_{\perp}^2 \int_{1/\lambda^2}^{s/4} dk_{\perp}^2 \int_{y_{\min}}^{y_{\max}} dy \int_0^{\pi} d\phi \frac{d\sigma_{gg \rightarrow ggg}}{dq_{\perp}^2 dk_{\perp}^2 dy d\phi} , \quad (3.37)$$

with y_{\min} and y_{\max} determined from eq. (3.25) and the differential cross section from eq. (3.15). The boost factor (3.19) reduces the total cross section with respect to the simpler expression $\Theta(k_{\perp} \lambda - \cosh y)$ since the phase space for the k_{\perp} integration gets reduced. However, the reduction is not very drastic as can be seen in fig. 3.5. It changes the total cross section for $gg \rightarrow ggg$ processes by roughly 20%. More essential for the kinematics of the outgoing particles is the peculiar way in which eq. (3.20) distorts the shape of the available phase space as discussed above.

Most notably the rapidity of the emitted gluon in the center of momentum frame with respect to the incoming jet momentum gets strongly shifted to negative values with increasing γ , see lower panel of fig. 3.6. For comparison the upper panel of fig. 3.6 shows the rapidity $\Delta y = \tanh^{-1}(\beta')$ associated with the boost from laboratory to c.m. frame. Note that in general y and Δy are not additive due to the angle θ in eq. (3.19). While for thermal energies, $\gamma \approx \cosh y$, the available phase space for the rapidity y is on the average essentially symmetric around $y = 0$, for larger jet energies the boost velocity β' becomes large and the emission in the c.m. frame is strongly shifted to the backward direction. With this, even for small k_{\perp} , the energy of the emitted gluon can become large in the c.m. frame but will still be small in the laboratory frame due to the boost. The consequences of such configurations for the energy loss of partons are investigated in more detail in chapter 4.

⁴ $2 \rightarrow 3$ processes are much more important for the energy loss of high energy partons in BAMPS as will be discussed in chapter 4.

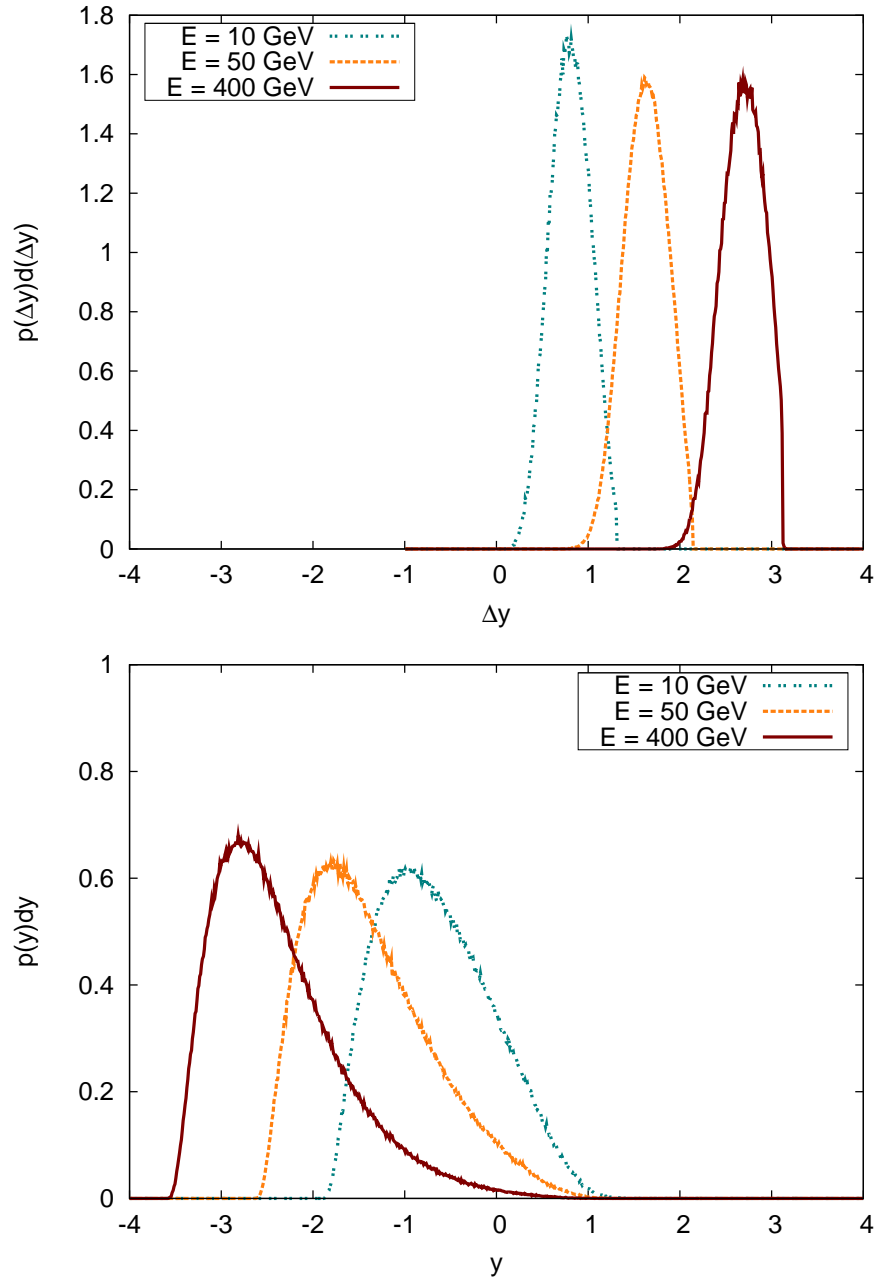


Figure 3.6.: Upper panel: Distribution of the magnitude of the boost from the laboratory frame to the center of momentum frame (c.m.) for different jet energies E (laboratory system) and $T = 0.4$ GeV expressed in terms of the rapidity $\Delta y = \tanh^{-1}(\beta')$.

Lower panel: Rapidity distribution of the emitted gluon in the c.m. frame with respect to the incoming gluon jet momentum for different jet energies E (laboratory system). The medium temperature is $T = 0.4$ GeV.

3.1.5. Evaluation of phase space integrals and sampling of momenta

Evaluation of phase space integrals for $2 \leftrightarrow 3$ processes

The cross section for $2 \rightarrow 3$ processes is computed from the four-dimensional integral (3.37). The integration is performed numerically via the VEGAS algorithm [Lep78, PTVF07], a Monte Carlo integration method. After the explicit dependence on the center of mass energy s is eliminated by rescaling the variables, the result depends on four parameters, namely m_D^2 , β' , $\cos\theta$ and λ . And since the evaluation of the integral is rather time consuming, the results are tabulated on a grid of these parameters. The value for a given parameter set is then obtained from linear interpolation in the parameter space.

For $3 \rightarrow 2$ processes the situation is slightly different. The integral (3.31) is only two-dimensional but the result depends on nine real parameters E_A , E_B , β' , m_D^2 , s , λ and $\cos\zeta$. Though an interpolation method from tabulated values as for the $\sigma_{2 \rightarrow 3}$ integral is in principle possible, the large number of parameters renders this method numerically demanding and no interpolation method has been found so far that would offer considerable advantage over a direct or estimated evaluation of the two-dimensional integral. Thus, even though in practice an estimation scheme of the integral value is often used instead of a straightforward integration via the VEGAS algorithm, the computation of the integral I_{32} for any possible particle triplet is the most time-consuming part of the BAMPS algorithm. It thus offers probably the most room for future numerical improvements.

Sampling of momenta

When, based on the collisions probabilities, it is decided in the simulation framework⁵ that a given pair or triplet of particles should collide, the momenta of the outgoing particles need to be sampled according to the underlying cross section or matrix element. Appendix D summarizes some numerical sampling methods that are employed in BAMPS to this end.

For binary, $2 \rightarrow 2$, interactions the momentum transfer \mathbf{q}_\perp^2 is simply sampled from the small angle differential cross section, for example from eq. (3.10) for $gg \rightarrow gg$ processes or from the other cross sections listed in appendix B.3.3. This is done via the method of inverse transform sampling, see appendix D.1. The cumulative distribution function eq. (D.1) based on the differential cross section is given by

$$F(x) = \frac{1}{\sigma} \int_0^x \frac{d\sigma}{d\mathbf{q}_\perp^2} d\mathbf{q}_\perp^2, \quad (3.38)$$

where σ is the total cross section $\sigma = \int_0^{s/4} \frac{d\sigma}{d\mathbf{q}_\perp^2} d\mathbf{q}_\perp^2$ (see appendix B.3.3) that is inserted for normalization. For the cross sections in small angle scattering that are employed in BAMPS, $F(x)$ can be inverted and thus x can be sampled by generating a random number y from $[0, 1)$. For example, for $gg \rightarrow gg$ processes the transverse momentum transfer $\mathbf{q}_\perp^2 = x$ can be sampled as

$$x = \frac{y\sigma m_D^4}{9\pi\alpha_s^2 - y\sigma m_D^2}. \quad (3.39)$$

For particle production or annihilation processes based on the Gunion-Bertsch matrix element (3.13) the sampling of the outgoing momenta is considerably more complex since

⁵See algorithm 1.

one deals with multivariate distributions for which the method of inverse transform sampling is not applicable.

For $2 \rightarrow 3$ processes the momenta are sampled from the differential cross section (3.15) via the rejection method, see appendix D.2. \mathbf{q}_\perp^2 , \mathbf{k}_\perp^2 , y and ϕ are sampled uniformly within the limits given in eq. (3.37). Since the limits (y_{\min} , y_{\max}) are dependent on the previously sampled value of k_\perp the sampling function is multiplied by $(y_{\max} - y_{\min})$. For the envelope function

$$g(\mathbf{q}_\perp^2, \mathbf{k}_\perp^2, y) = D \frac{y_{\text{right}} - y_{\text{left}}}{\mathbf{k}_\perp^2 (\mathbf{q}_\perp^2 + m_D^2)} \quad (3.40)$$

is chosen, with y_{left} and y_{right} from eq. (3.29). The factor D estimates the factor $\sum \left(\left| \frac{\partial F}{\partial y_1} \right|_{F=0} \right)^{-1}$ stemming from the delta function. Its value needs to be obtained empirically and is usually fixed at $D = 1 \cdot 10^3$.

Though the sampling for $3 \rightarrow 2$ processes is only two-dimensional in the variables $\cos \vartheta$ and φ , see eq. (3.31), a reasonable envelope function for usage in the rejection method is considerably difficult to find. Due to this the Metropolis algorithm—see appendix D.3—is used for the sampling of the momenta in $3 \rightarrow 2$ processes.

3.2. The Gunion-Bertsch matrix element

The matrix element eq. (3.13) that is employed in BAMPS to describe inelastic $2 \leftrightarrow 3$ processes is an approximation to the full QCD matrix element and has been derived by GUNION and BERTSCH in 1981 [GB82]. Their original work aimed at describing particle production in the central rapidity region of (soft) hadronic collisions by bremsstrahlung of gluons. To this end they considered the lowest order perturbative gluon production diagrams in quark-quark scattering as illustrated in fig. 3.7.

This section sketches the derivation of the Gunion-Bertsch matrix element with a special focus on the kinematics and the approximations that lead to their result⁶. Subsequently, in section 3.2.3, the Gunion-Bertsch approximation is compared numerically to the exact result obtained by BERENDS et al. [BKDC⁺81] for some typical choices of the momenta.

3.2.1. Kinematics and approximations

Following the notation of the original publication by GUNION and BERTSCH the four-vectors in this section are given in light-cone notation, i.e. $p = (p^+, p^-, \mathbf{p}_\perp)$ with $p^+ = p^0 + p^3$ and $p^- = p^0 - p^3$. The inverse transformation from light-cone to standard Minkowski representation is then obviously given by $p^0 = (p^+ + p^-)/2$ and $p^3 = (p^+ - p^-)/2$. An energetic particle with large p^+ but small p^- is traveling along the forward (light-cone) direction, while it is traveling into the backward direction for small p^+ but large p^- . The product of four-vectors in light-cone notation is given by $p \cdot q = (p^+ q^- + p^- q^+)/2 - \mathbf{p}_\perp \mathbf{q}_\perp$ and accordingly $p^2 = p^+ p^- - \mathbf{p}_\perp^2$.

All momenta in the following computations are given in the center of momentum frame. The external momenta of the particles involved in the bremsstrahlung process are fixed

⁶The discussion is based on notes kindly provided by Mauricio Martinez Guerrero from a collaborative effort to investigate the regions of validity for the Gunion-Bertsch matrix element.

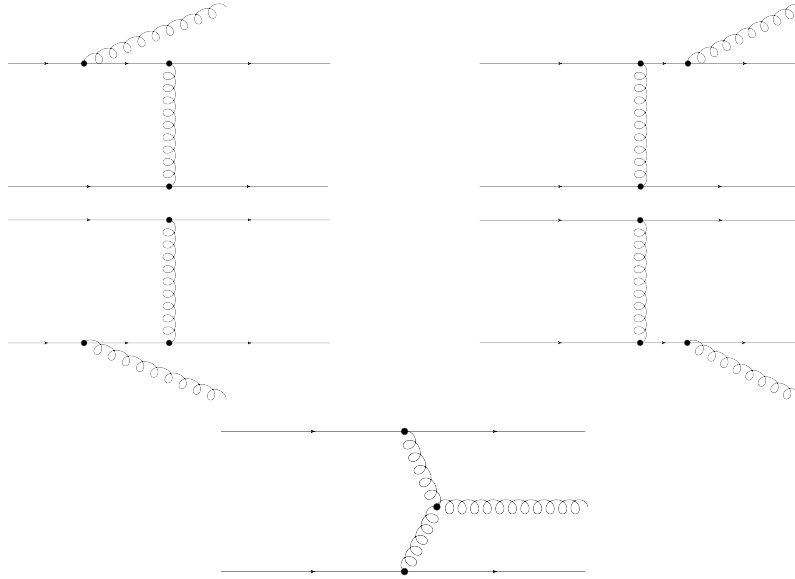


Figure 3.7.: Lowest order Feynman diagrams for gluon radiation in quark-quark scattering as considered by GUNION and BERTSCH in [GB82].

as follows: p_A and p_B are the incoming momenta of the upper and lower quark lines respectively, while p_1 and p_2 are the outgoing momenta of the upper and lower quark lines. The momentum of the radiated gluon is denoted by k and the four-momentum of the soft exchanged gluon is given by q . All external particles are considered to be massless and on-shell, i.e. $p_A^2 = p_B^2 = p_1^2 = p_2^2 = k^2 = 0$. The incoming quark momentum p_A is chosen to be along the positive z -axis and thus p_B along the negative z -axis accordingly. The radiated gluon carries away a fraction x of the positive light-cone momentum⁷ of particle A . The kinematics are then given by

$$p_A = (\sqrt{s}, 0, 0, 0) \quad (3.41)$$

$$p_B = (0, \sqrt{s}, 0, 0) \quad (3.42)$$

$$k = (x\sqrt{s}, \frac{k_{\perp}^2}{x\sqrt{s}}, \mathbf{k}_{\perp}) \quad (3.43)$$

$$q = (q^+, q^-, \mathbf{q}_{\perp}), \quad (3.44)$$

where a specific direction for the transverse momentum of the emitted gluon is arbitrarily chosen, and momentum conservation gives

$$p_1 = p_A + q - k \quad (3.45)$$

$$p_2 = p_B - q. \quad (3.46)$$

⁷Note that this fraction is a Lorentz-invariant quantity.

Together with the on-shell conditions this yields

$$q^+ = -\frac{q_\perp^2}{\sqrt{s}} \quad (3.47)$$

$$q^- = \frac{k_\perp^2/x + q_\perp^2 - 2\mathbf{q}_\perp \mathbf{k}_\perp}{(1-x)\sqrt{s}} \quad (3.48)$$

where the expression for q^- is obtained under the assumption that the exchanged momentum is almost on the light-cone, i.e. $q^+q^- \approx 0$.

For the radiated gluon field $A_\mu \sim \sum_i \epsilon_\mu^{(i)} e^{ik \cdot x}$ the light-cone gauge is chosen $A^+ = 0$, or equivalently $\epsilon^+ = 0$. In this gauge the gluon radiation from the lower quark line, i.e. from the quark with small + light-cone momentum, is either exactly zero (radiation from the initial lower quark line, p_B) or negligible (radiation from the final lower quark line, p_2) in the case $q_\perp \ll \sqrt{s}$. Therefore the diagrams from the second line of fig. 3.3 need not be considered in the computation of the total matrix element. Note that the choice $A^- = 0$ would select radiation from the lower quark lines accordingly. A possible choice for the polarization vectors is

$$\epsilon^{(i)} = \left(0, \frac{2\mathbf{k}_\perp \boldsymbol{\epsilon}_\perp^{(i)}}{x\sqrt{s}}, \boldsymbol{\epsilon}_\perp^{(i)}\right) \quad (3.49)$$

with $\boldsymbol{\epsilon}_\perp^{(1)} = (1, 0)$ and $\boldsymbol{\epsilon}_\perp^{(2)} = (0, 1)$, thus fulfilling $\epsilon^{(1)} \cdot \epsilon^{(2)} = 0$.

The rapidity of the emitted gluon can be expressed in terms of the above defined quantities as

$$y = \frac{1}{2} \ln \frac{k^+}{k^-} = \ln \frac{x\sqrt{s}}{k_\perp} \quad (3.50)$$

and thus the central rapidity region that GUNION and BERTSCH were interested in is given by $x \sim k_\perp/\sqrt{s}$. The matrix element is derived in the limit of soft momentum transfers, i.e. small q_\perp , and soft radiation, i.e. small k_\perp and x . More explicitly the approximations read

$$q_\perp \ll \sqrt{s} \quad (3.51)$$

$$k_\perp \ll \sqrt{s} \quad (3.52)$$

and

$$xq_\perp \ll k_\perp. \quad (3.53)$$

The latter conditions specifies the above mentioned requirement that x be small. Even though the light-cone momentum fraction of the radiated gluon is small, $x \ll 1$, it must not be taken entirely into the limit $x \rightarrow 0$ in order to still include the central rapidity region $x \sim k_\perp/\sqrt{s}$.

3.2.2. Computation of the bremsstrahlung Feynman diagrams

Analyzing the result, for example by comparing to the simpler case of gluon radiation in $e^+e^- \rightarrow q\bar{q}$ processes, one finds that the spin structure of the external fermions is irrelevant for the problem at hand. Therefore one can use scalar QCD where the Feynman rule for the quark-gluon vertex gets replaced by the vertex of a scalar field coupling to the gluon:



This trick simplifies the computation of the diagrams and is used in the following together with the kinematic approximations, eqs. (3.51) to (3.53), that allow for the neglect of subleading terms in \sqrt{s} .

Diagram 1

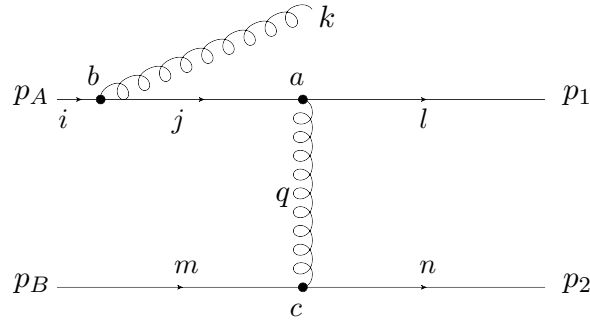


Figure 3.8.: Matrix element \mathcal{M}_1 contributing to the gluon radiation in quark-quark scattering.

The matrix element corresponding to gluon radiation from the initial quark leg—see fig. 3.8 for the Feynman diagram and the definition of color indices, momenta etc.—is given by

$$i\mathcal{M}_1 = (-ig_s)^3 T_{jl}^a T_{ij}^b T_{mn}^c \delta_{ac} \frac{(2p_A - 2k + q)^\mu (2p_B - q)_\mu}{(p_A - k)^2 q^2} (2p_A - k)^\lambda \epsilon_\lambda^{(i)*}, \quad (3.54)$$

where the T^a are the generators of color $SU(3)$, see section 2.1, and g_s denotes the bare strong coupling.

Employing the kinematic approximations eqs. (3.51) and (3.52), i.e. neglecting terms proportional to k_\perp/\sqrt{s} or q_\perp/\sqrt{s} , together with the definitions of the momenta, the individual terms can be simplified:

$$(2p_A - k)^\lambda \epsilon_\lambda^{(i)*} \approx \frac{2\mathbf{k}_\perp \epsilon_\perp^{(i)}}{x} \quad (3.55)$$

$$(2p_A - 2k + q)^\mu (2p_B - q)_\mu \approx 2s(1 - x) \quad (3.56)$$

$$(p_A - k)^2 = -\frac{k_\perp^2}{x} \quad (3.57)$$

$$q^2 \approx q_\perp^2 \quad (3.58)$$

Putting everything together, the matrix element for the diagram in fig. 3.8 reads

$$i\mathcal{M}_1 \approx (-ig_s)^3 T_{jl}^a T_{ij}^b T_{mn}^c \delta_{ac} (1-x) \frac{2s}{q_\perp^2} \frac{2\mathbf{k}_\perp \boldsymbol{\epsilon}_\perp^{(i)}}{k_\perp^2}. \quad (3.59)$$

Diagram 2

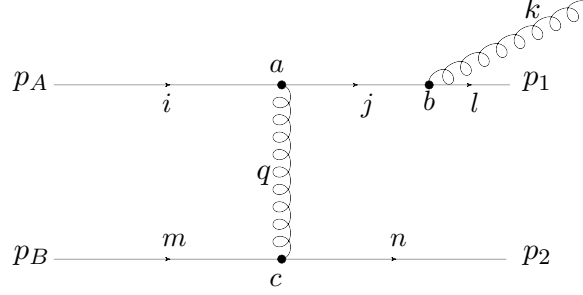


Figure 3.9.: Matrix element \mathcal{M}_2 contributing to the gluon radiation in quark-quark scattering.

The computation of the amplitude \mathcal{M}_2 for gluon radiation from the final quark leg—see fig. 3.9—is very similar to the computation of \mathcal{M}_1 . In its generic form the matrix element reads

$$i\mathcal{M}_2 = (-ig_s)^3 T_{ij}^a T_{jl}^b T_{mn}^c \delta_{ac} \frac{(2p_A + q)^\mu (2p_B - q)_\mu}{(p_A + q)^2 q^2} (2p_A + 2q - k)^\lambda \epsilon_\lambda^{(i)*}. \quad (3.60)$$

As before the individual terms can be approximated and rewritten

$$(2p_A + q)^\mu (2p_B - q)_\mu \approx 2s \quad (3.61)$$

$$(2p_A + 2q - k)^\lambda \epsilon_\lambda^{(i)*} \approx \frac{2}{x} (\mathbf{k}_\perp - x\mathbf{q}_\perp) \boldsymbol{\epsilon}_\perp^{(i)} \quad (3.62)$$

$$(p_A + q)^2 = \frac{(\mathbf{k}_\perp - x\mathbf{q}_\perp)^2}{x(1-x)} \quad (3.63)$$

$$q^2 \approx q_\perp^2, \quad (3.64)$$

yielding the final result

$$i\mathcal{M}_2 \approx (ig_s)^3 T_{ij}^a T_{jl}^b T_{mn}^c \delta_{ac} (1-x) \frac{2s}{q_\perp^2} \frac{2(\mathbf{k}_\perp - x\mathbf{q}_\perp) \boldsymbol{\epsilon}_\perp^{(i)}}{(\mathbf{k}_\perp - x\mathbf{q}_\perp)^2}. \quad (3.65)$$

Diagram 3

The final diagram embodies the unique QCD-contribution to the total bremsstrahlung amplitude, in which the bremsstrahlung gluon is emitted from the exchanged soft gluon, see

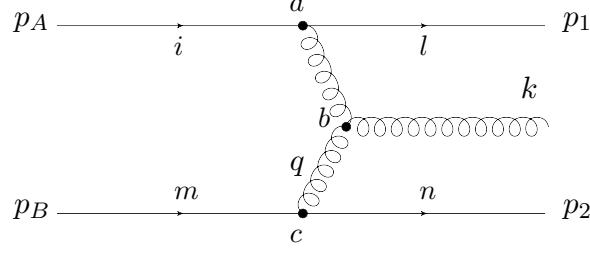


Figure 3.10.: Matrix element \mathcal{M}_3 contributing to the gluon radiation in quark-quark scattering.

fig. 3.10. It thus involves a three-gluon vertex, rendering the evaluation of \mathcal{M}_3 somewhat more tedious. The amplitude in scalar QCD reads

$$i\mathcal{M}_3 = (-ig_s)^2 g_s f^{abc} T_{il}^a T_{mn}^c \left\{ g^{\alpha\beta} (k-2q)^\gamma + g^{\beta\gamma} (q-2k)^\alpha + g^{\gamma\alpha} (k+q)^\beta \right\} \\ \times \frac{(2p_A + q - k)^\beta (2p_B - q)^\alpha}{q^2 (q-k)^2} \epsilon_\gamma^{(i)*} \quad (3.66)$$

$$= (-ig_s)^2 g_s f^{abc} T_{il}^a T_{mn}^c \frac{1}{q^2} \frac{1}{(q-k)^2} \\ \times \left\{ [(2p_A + q - k) \cdot (2p_B - q)] [(2q - k) \cdot \epsilon^{(i)*}] \right. \\ + [(q - 2k) \cdot (2p_B - q)] [(2p_A + q - k) \cdot \epsilon^{(i)*}] \\ \left. + [(k + q) \cdot (2p_A + q - k)] [(2p_B - q) \cdot \epsilon^{(i)*}] \right\}. \quad (3.67)$$

Again various simplifications can be made by exploiting the approximations eqs. (3.51) and (3.52) together with the definitions of the external momenta from eqs. (3.41) to (3.46). The results are

$$[(2p_A + q - k) \cdot (2p_B - q)] [(2q - k) \cdot \epsilon^{(i)*}] \approx [2p_A^+ p_B^-] [-2q \cdot \epsilon^{(i)*}] \\ = 4s \mathbf{q}_\perp \epsilon_\perp^{(i)} \quad (3.68)$$

$$[(q - 2k) \cdot (2p_B - q)] [(2p_A + q - k) \cdot \epsilon^{(i)*}] \approx [-2xs] \left[\frac{2}{x} \mathbf{k}_\perp \epsilon_\perp^{(i)} \right] \\ = -4s \mathbf{k}_\perp \epsilon_\perp^{(i)} \quad (3.69)$$

$$[(k + q) \cdot (2p_A + q - k)] [(2p_B - q) \cdot \epsilon^{(i)*}] \approx \left[\frac{2k_\perp^2}{x} \right] [\mathbf{q}_\perp \epsilon_\perp^{(i)}] \\ = \frac{2k_\perp^2}{x} \mathbf{q}_\perp \epsilon_\perp^{(i)} \quad (3.70)$$

$$(q-k)^2 = -\frac{(\mathbf{q}_\perp - \mathbf{k}_\perp)^2}{1-x}. \quad (3.71)$$

After the smoke clears the result for the amplitude \mathcal{M}_3 turns out to be rather simple,

$$i\mathcal{M}_3 \approx -ig_s^3 T_{il}^a T_{mn}^c i f^{abc} (1-x) \frac{2s}{q_\perp^2} \frac{2(\mathbf{q}_\perp - \mathbf{k}_\perp) \epsilon_\perp^{(i)}}{(\mathbf{q}_\perp - \mathbf{k}_\perp)^2}. \quad (3.72)$$

Collisional matrix element

For further comparison it is interesting to note that the amplitude for the elastic quark-quark scattering in the same approximations is just given by

$$i\mathcal{M}_{\text{coll}} \approx -ig_s^2 T_{il}^a T_{mn}^c \delta_{ac} \frac{2s}{q_\perp^2}. \quad (3.73)$$

It is already obvious that the amplitudes for the radiative diagrams, eqs. (3.59), (3.65) and (3.72), factorize into a $2s/q_\perp^2$ term from the collisional amplitude times a term related to the emission of a gluon. This factorization will be explored in more detail below.

Combining the results

In order to get the total amplitude, the matrix elements eqs. (3.59), (3.65) and (3.72) computed above need to be summed and squared

$$|\mathcal{M}_{\text{GB}}|^2 = \left| \sum_i (\mathcal{M}_1 + \mathcal{M}_2 + \mathcal{M}_3) \right|^2 = \sum_i |\mathcal{M}_1 + \mathcal{M}_2 + \mathcal{M}_3|^2, \quad (3.74)$$

where the sum runs over the two possible polarizations $\epsilon^{(i)}$ of the emitted gluon, eq. (3.49).

To begin with, the sum of the first two diagrams, $\mathcal{M}_1 + \mathcal{M}_2$, is computed. Employing the commutation relation for the generators of $SU(3)$, $[T^a, T^b] = if^{abc}T^c$ and the approximation (3.53), this gives

$$i\mathcal{M}_1 + i\mathcal{M}_2 \approx g_s^3 f^{abc} T_{mn}^a T_{il}^c (1-x) \frac{2s}{q_\perp^2} \frac{2\mathbf{k}_\perp \boldsymbol{\epsilon}_\perp^{(i)}}{k_\perp^2}. \quad (3.75)$$

Now, adding the final contribution, \mathcal{M}_3 , is straightforward and yields

$$\begin{aligned} i\mathcal{M}_{\text{GB}} &= i\mathcal{M}_1 + i\mathcal{M}_2 + i\mathcal{M}_3 \\ &= g_s^3 f^{abc} T_{mn}^a T_{il}^c (1-x) \frac{2s}{q_\perp^2} 2 \left[\frac{\mathbf{k}_\perp \boldsymbol{\epsilon}_\perp^{(i)}}{k_\perp^2} + \frac{(\mathbf{q}_\perp - \mathbf{k}_\perp) \boldsymbol{\epsilon}_\perp^{(i)}}{(\mathbf{q}_\perp - \mathbf{k}_\perp)^2} \right]. \end{aligned} \quad (3.76)$$

Finally the squared scattering amplitude for the $qq \rightarrow qqg$ process can be computed from eq. (3.76), reproducing the result from GUNION and BERTSCH

$$|\mathcal{M}_{\text{GB}}|^2 = g_s^6 C \frac{4s^2}{q_\perp^4} \frac{4q_\perp^2}{k_\perp^2 (\mathbf{q}_\perp - \mathbf{k}_\perp)^2}, \quad (3.77)$$

that has been used in [Won96, XG05] to obtain the matrix element from eq. (3.13) for $gg \rightarrow ggg$ processes. In the above expression, $C = \frac{1}{9} \sum f^{abc} f^{a'bc'} \text{tr}(T^a T^{a'}) \text{tr}(T^c T^{c'}) = \frac{2}{3}$ is the overall color factor stemming from the average over initial colors and the sum over final colors.

As was already to be expected from the comparison of the separate amplitudes \mathcal{M}_1 , \mathcal{M}_2 and \mathcal{M}_3 for the radiative process to the amplitude of the purely collisional process $\mathcal{M}_{\text{coll}}$, the squared Gunion-Bertsch matrix element eq. (3.77) factorizes into a contribution from

the elastic scattering proportional to $\frac{4s}{q_\perp^4}$ and a contribution proportional to $\frac{4q_\perp^2}{k_\perp^2(\mathbf{q}_\perp - \mathbf{k}_\perp)^2}$ that can be interpreted as the probability to radiate a gluon. The squared matrix element for a bremsstrahlung process can then generically be written as

$$|\mathcal{M}_{\text{GB}}|^2 = |\mathcal{M}_{\text{coll}}|^2 P^g, \quad (3.78)$$

where P^g encodes the probability to radiate a gluon. The consequences of this factorization on the treatment of scattering processes with different particle species will be discussed in more detail in section 3.4.

3.2.3. Comparison of Gunion-Bertsch to the exact result

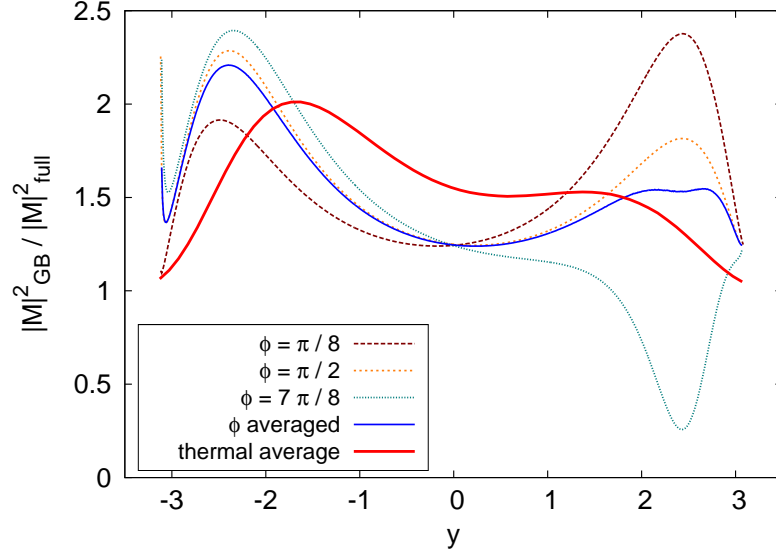
As detailed in the previous section, the Gunion-Bertsch matrix element, eq. (3.77) or eq. (3.13), is an approximation to the true matrix element, valid in the limit of small x , k_\perp and q_\perp . It is of course possible to evaluate the full matrix element from the diagrams shown in fig. 3.7 and this has been done for example by BERENDS et al. [BKDC⁺81] or by ELLIS and SEXTON [ES86] in the generalized case for an arbitrary number of dimensions. The result from [BKDC⁺81] for the process $g(p_1) + g(p_2) \rightarrow g(p_3) + g(p_4) + g(p_5)$ is considerably more complex than eq. (3.13) and reads

$$\begin{aligned} |M_{\text{full}}|^2 = & \frac{g^6}{2} [N^3/(N^2 - 1)] [(12345) + (12354) + (12435) + (12453) + (12534) \\ & + (12543) + (13245) + (13254) + (13425) + (13524) + (14235) + (14325)] \\ & \times \frac{[(p_1 p_2)^4 + (p_1 p_3)^4 + (p_1 p_4)^4 + (p_1 p_5)^4 + (p_2 p_3)^4]}{(p_1 p_2)(p_1 p_3)(p_1 p_4)(p_1 p_5)(p_2 p_3)(p_2 p_4)(p_2 p_5)(p_3 p_4)(p_3 p_5)(p_4 p_5)} \\ & + \frac{[(p_2 p_4)^4 + (p_2 p_5)^4 + (p_3 p_4)^4 + (p_3 p_5)^4 + (p_4 p_5)^4]}{(p_1 p_2)(p_1 p_3)(p_1 p_4)(p_1 p_5)(p_2 p_3)(p_2 p_4)(p_2 p_5)(p_3 p_4)(p_3 p_5)(p_4 p_5)} \quad (3.79) \end{aligned}$$

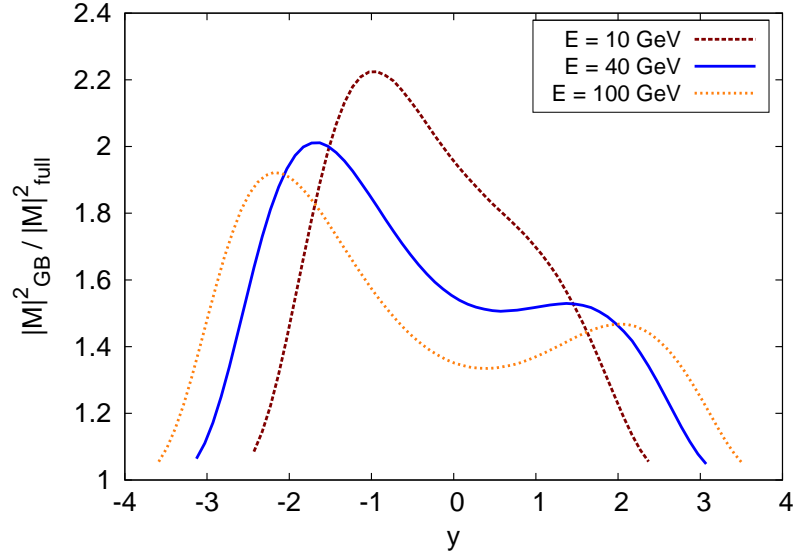
using the notation $(ijklm) = (p_i p_j)(p_j p_k)(p_k p_l)(p_l p_m)(p_m p_i)$.

In order to numerically quantify the quality of the Gunion-Bertsch approximation (3.77), or rather eq. (3.13), to the exact result (3.79), the bare matrix elements are compared for various kinematic scattering parameters in figs. 3.11 and 3.12. With *bare* meaning that no modifications due to the transformation properties of the momentum conserving delta function, see eq. (3.15) and appendix B.4, or due to the LPM cutoff (3.17) are taken into account.

Fixing the transverse momentum transfers to the thermal ($N_f = 0$) Debye mass from eq. (3.12), $q_\perp = k_\perp = m_D$, fig. 3.11a shows the ratio of the square of the approximated to the square of the exact matrix element, $|\mathcal{M}_{\text{GB}}|^2 / |\mathcal{M}_{\text{full}}|^2$, as a function of the rapidity of the radiated gluon y , where the range of y is limited by the kinematic constraint (3.23). The incoming momentum $p_A = (E, 0, 0, E)$ describes a jet-like gluon with energy $E = 40$ GeV that interacts with a thermal gluon that has momentum p_B . For the purpose of this analysis, p_B is either fixed to $p_B = (3T, 0, 0, -3T)$ or sampled from a thermal Boltzmann distribution. The outgoing momenta for use in eq. (3.79) are computed according to the procedure described in appendix B.4 with $p_{1,z}$ taken to be eq. (B.40). The angle ϕ between \mathbf{q}_\perp and \mathbf{k}_\perp is either fixed at certain values or uniformly sampled from the interval $(0, \pi)$.

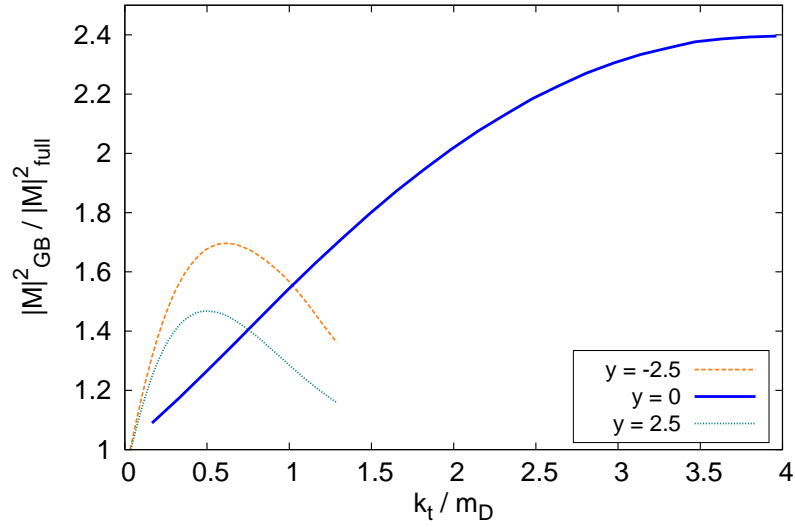


(a) $|\mathcal{M}_{GB}|^2 / |\mathcal{M}_{\text{full}}|^2$ for fixed $p_A = (E, 0, 0, E)$ with $E = 40$ GeV as a function of the rapidity y of the emitted gluon. Transverse momenta fixed at $q_\perp = k_\perp = m_D$ and $\mathbf{q}_\perp \mathbf{k}_\perp = q_\perp k_\perp \cos \phi$. The angle $\phi \in (0, \pi)$ is fixed for the dashed lines and averaged over for the solid lines. $p_B = (3T, 0, 0, -3T)$ with $T = 0.4$ GeV is fixed for all lines but the one labeled *thermal average*, where p_B is generated and averaged over from a thermal distribution with $T = 0.4$ GeV.

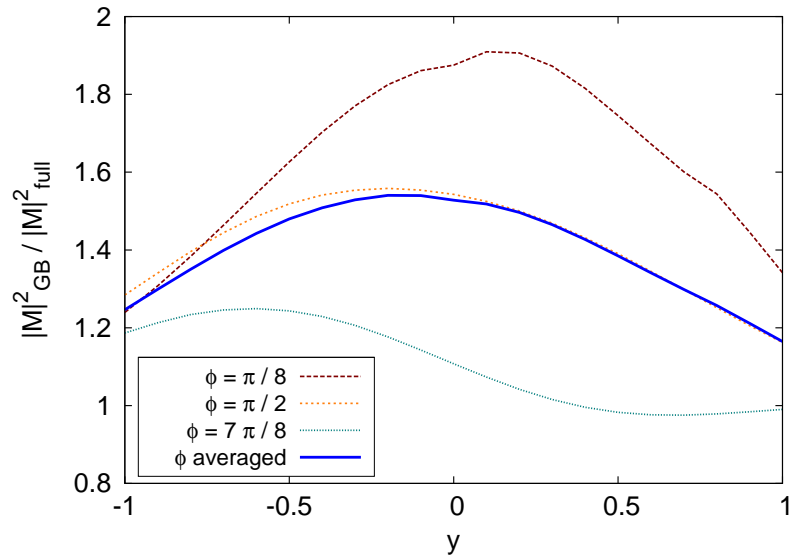


(b) $|\mathcal{M}_{GB}|^2 / |\mathcal{M}_{\text{full}}|^2$ for fixed $p_A = (E, 0, 0, E)$ and different values of E as a function of the rapidity y of the emitted gluon. Transverse momenta fixed as in fig. 3.11a, the angle ϕ is averaged over. p_B is generated and averaged over from a thermal distribution with $T = 0.4$ GeV.

Figure 3.11.: Numerical comparison of the Gunion-Bertsch matrix element (3.13) to the exact result (3.79) for $gg \rightarrow ggg$ processes. The ratio $|\mathcal{M}_{GB}|^2 / |\mathcal{M}_{\text{full}}|^2$ is shown for different parameters. See captions of subfigures, fig. 3.12 and text for more details.



(a) $|\mathcal{M}_{GB}|^2 / |\mathcal{M}_{\text{full}}|^2$ for fixed $p_A = (E, 0, 0, E)$ with $E = 40$ GeV and different values of y as a function of the transverse momentum of the radiated gluon in units of the thermal Debye mass, k_{\perp}/m_D , eq. (3.12). Transverse momenta fixed as in fig. 3.11a, the angle ϕ is averaged over. p_B is generated and averaged over from a thermal distribution with $T = 0.4$ GeV.



(b) Thermal average of $|\mathcal{M}_{GB}|^2 / |\mathcal{M}_{\text{full}}|^2$ for different values of the angle ϕ (dashed lines) and an average over ϕ (solid line), see fig. 3.11a, as a function of the rapidity of the emitted gluon. p_A and p_B from a thermal distribution with $T = 0.4$ GeV.

Figure 3.12.: Numerical comparison of the Gunion-Bertsch matrix element (3.13) to the exact result (3.79) for $gg \rightarrow ggg$ processes. The ratio $|\mathcal{M}_{GB}|^2 / |\mathcal{M}_{\text{full}}|^2$ is shown for different parameters. See captions of subfigures, fig. 3.11 and text for more details.

Figure 3.11a illustrates that the approximated result from GUNION and BERTSCH overestimates the exact result for radiative processes involving a highly energetic gluon. The approximation works best at radiation into the central rapidity region and into the extremely forward or backward directions. Averaging over all possible angles ϕ between \mathbf{q}_\perp and \mathbf{k}_\perp and thermally distributed momenta p_B of the collision partner, the exact result is overestimated by at most a factor of two. Note that the slight asymmetry in forward and backward rapidity in figs. 3.11a, 3.11b, 3.12a and 3.12b is due to the choice (B.40) for $p_{1,z}$. Selecting (B.41) instead would revert the asymmetry. Figure 3.11b confirms that the Gunion-Bertsch approximation improves with increasing available energy \sqrt{s} , in this case with increasing jet energy E . As was to be expected from the discussion in sections 3.2.1 and 3.2.2, fig. 3.12a shows that the approximation is best for small values of k_\perp . The dependence on the value of the exchanged transverse momentum q_\perp is much weaker. For thermal particles the shape of the ratio $|\mathcal{M}_{GB}|^2 / |\mathcal{M}_{\text{full}}|^2$ is slightly different, the approximation is worst for radiation into the central rapidity region and improves towards larger rapidities, see fig. 3.12b.

Combining the information from figs. 3.11a, 3.11b, 3.12a and 3.12b it is safe to conclude that the Gunion-Bertsch approximation to the lowest order gluon radiation diagrams—which is used in the Monte Carlo algorithms of the transport model BAMPS due to its comparatively simpler structure—overestimates the exact result obtained by BERENDS et al. by a factor of roughly 1.2 to 2. Though the compensation of this deviation by a phenomenological scaling factor might be conceivable, this approach is not pursued in this work, amongst other reasons due to the non-trivial dependence of the deviations on the kinematic regions.

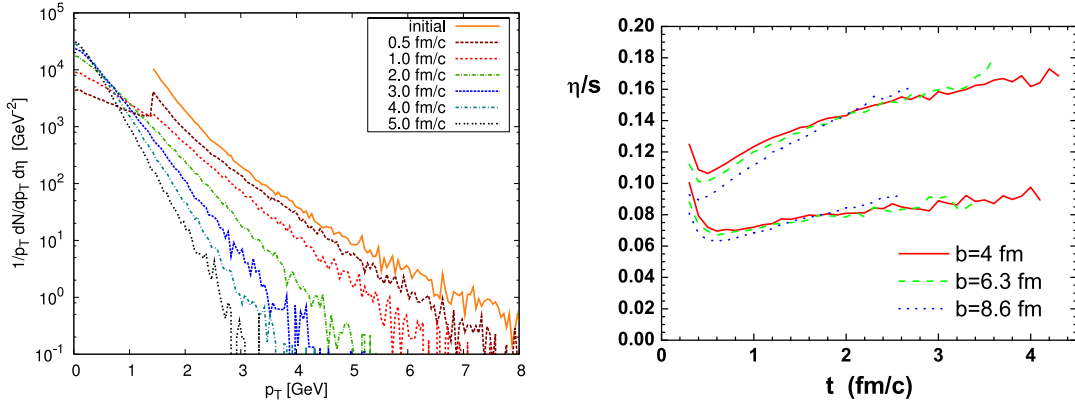
3.3. Selected results from BAMPS

The transport framework BAMPS has already been applied in various studies. For the sake of completeness this section lists some important findings that may help to put the model and its results into context.

3.3.1. Early thermalization

Early studies employing BAMPS established that the consistent inclusion of inelastic particle production and annihilation processes leads to a rapid thermalization of the gluonic medium created in central heavy ion collisions at RHIC energies [XG05]. The time evolution of the p_T -spectra (see fig. 3.13a) and of the momentum anisotropy show that the medium in the central region reaches kinetic equilibration at a timescale on the order of $1 \text{ fm } c^{-1}$. Including only binary interactions a thermalization on such short time scales cannot be achieved, unless unphysically high cross sections are used instead of the pQCD based cross sections that are employed in BAMPS.

While the thermalization of the medium is not necessary for BAMPS to operate—on the contrary, it is one of the main features and advantages of transport models that they can be used to describe the dynamics of out-of-equilibrium systems—comparison of hydrodynamic calculations to experimental data, especially to elliptic flow data, strongly suggests that the medium indeed rapidly thermalizes within roughly $1 \text{ fm } c^{-1}$ [HKH⁺01, KH03].



- (a) Time evolution of the p_T -spectrum in the innermost region ($|\eta| \leq 0.5$, $x_T < 1.5$ fm) of a central ($b = 0$) Au + Au collision at 200 A GeV. The initial (uppermost) spectrum is the distribution given from mini-jet initial conditions with $p_0 = 1.4$ GeV. Figure from [Foc06].
- (b) Time evolution of the ratio of the shear viscosity to the entropy density, η/s , extracted from the central region of simulations of Au + Au collisions with different impact parameters. The upper band shows the results with $\alpha_s = 0.3$ and the lower band the results with $\alpha_s = 0.6$. Figure from [XGS08].

Figure 3.13.: Time evolution of the p_T -spectrum and of η/s from previous studies.

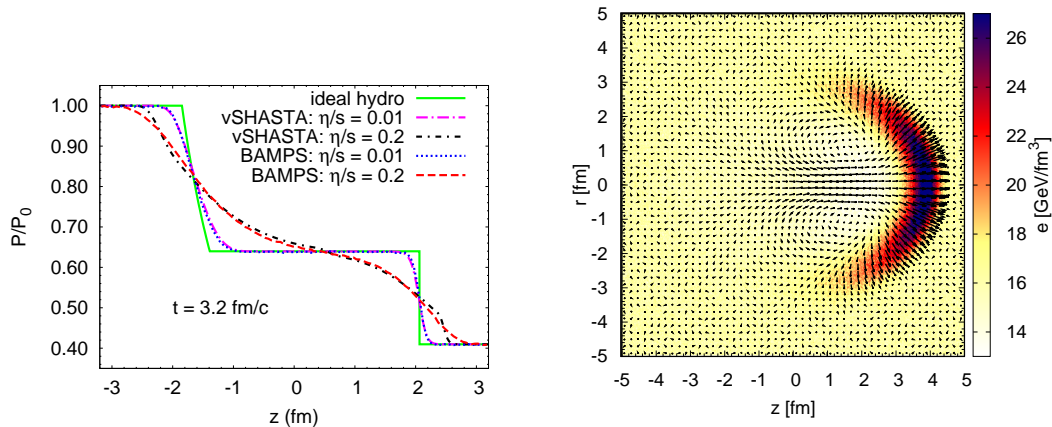
3.3.2. Small viscosity

Comparison of elliptic flow data from RHIC to ideal [HKH⁺01, KH03] and to viscous [RR07] hydrodynamical calculations suggests that the ratio of the shear viscosity to entropy density, η/s , of the medium created in heavy ion collisions is rather small, possibly close to the conjectured lower bound $\frac{\eta}{s} = \frac{1}{4\pi}$ from a correspondence between conformal field theory and string theory in an Anti-de-Sitter space [KSS05]. An investigation of the transport rates for the gluon matter in simulations of Au + Au collisions at RHIC within BAMPS shows that the inclusion of $gg \leftrightarrow ggg$ processes via (3.13) yields a ratio η/s that is compatible with the hydrodynamical findings [XG08, XGS08, XG09]. The ratio of shear viscosity to entropy density is roughly constant over the evolution of the simulated fireball at $\eta/s \approx 0.08$ for $\alpha_s = 0.6$ or $\eta/s \approx 0.15$ for $\alpha_s = 0.3$, see fig. 3.13b for the time evolution of η/s in the simulated gluon medium of Au + Au collisions at RHIC from [XGS08].

3.3.3. Hydrodynamic behavior and shock phenomena

The framework provided by BAMPS is extensively used to study collective shock phenomena in partonic matter, aiming at eventually investigating the possible existence of jet-induced Mach cone structures in heavy ion collisions.

To begin with, the evolution of hydrodynamic shocks from an initial pressure discontinuity, the so-called Riemann problem, has been successfully studied in a much simpler one-dimensional setup for various values of η/s in [BMN⁺09, BMN⁺10], see fig. 3.14a. The results from the transport calculations in fact serve as a reference for hydrodynamic implementations of the viscous Israel-Stewards formalism [Mol09]. In a next step the evolution of jet-induced shock waves is studied inside static media for various medium parameters and



(a) Pressure profile from solutions to the Riemann problem from BAMPS and the viscous hydrodynamical algorithm vSHASTA [Mol09]. Figure from [BMN⁺09].

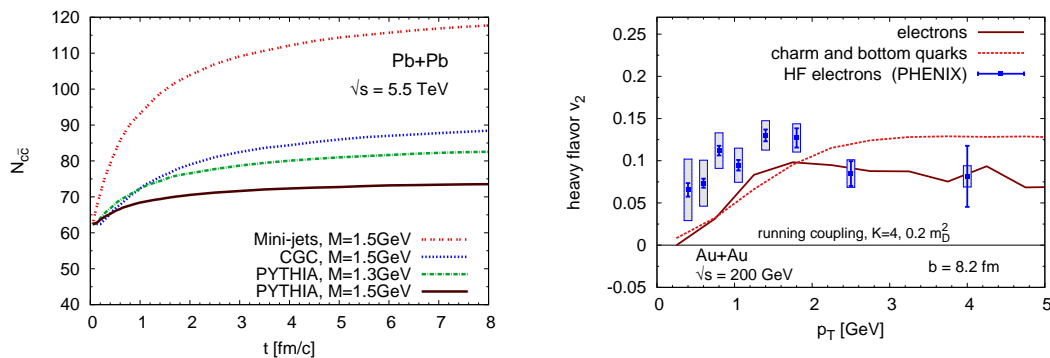
(b) Energy density and velocity profile of a hydrodynamic shock initiated by a gluon jet that traverses a gluonic medium with $\eta/s = 0.15$ and $T = 0.4$ GeV. $gg \rightarrow gg$ and $gg \leftrightarrow ggg$ processes are taken into account, the initial jet energy is $E = 20$ GeV and $\alpha_s = 0.3$ [Bou11].

Figure 3.14.: Hydrodynamic shock phenomena studied within the BAMPS framework in [BMN⁺09, BMN⁺10, BEF⁺10].

energy deposition scenarios. The emergence of shock fronts is clearly visible, see fig. 3.14b, however the ideal Mach cone like shape is distorted by finite viscosity and dependent on the energy deposition mechanism [BEF⁺10] and thus likely to not be realized in full simulations of heavy ion collisions. Investigating the emergence of shock phenomena in fully dynamic simulations of heavy ion collisions within BAMPS is numerically extremely challenging, but will be addressed in the near future.

3.3.4. Heavy quarks

The transport model BAMPS has recently also been applied to study the production and space-time evolution of heavy quarks in central and non-central heavy ion collisions at RHIC and LHC energies for various initial conditions [UFXG10a, UFXG10b]. The in-medium production of charm quarks from $gg \rightarrow Q\bar{Q}$ processes is found to be negligible for RHIC collisions, while it contributes significantly to the total charm yield at LHC energies, see fig. 3.15a. A scaling factor of $K = 4$ for the elastic $gQ \rightarrow gQ$ cross section is needed to reproduce the experimentally observed elliptic flow and nuclear modification factor of electrons from open heavy flavor decays, see fig. 3.15b. The extension of the transport model to include inelastic processes for heavy quarks, such as $gQ \rightarrow gQg$, based on the Gunion-Bertsch matrix element is currently underway and will allow for the investigation of radiative contributions to the energy loss and collective behavior of charm and bottom quarks.



(a) Charm production in a central Pb + Pb collision at LHC as simulated within the BAMPS framework for different charm quark masses and initial conditions. Figure from [UFXG10a].

(b) Heavy quark flow for a $b = 8.2$ fm Au + Au collision at RHIC as simulated within BAMPS. The $gQ \rightarrow gQ$ cross section is enlarged by a factor $K = 4$. For comparison experimental data for electrons from heavy flavor decays [PHENIX10b] is shown. Figure from [UFXG10b].

Figure 3.15.: Heavy quark flow at RHIC and charm production at LHC as studied within the BAMPS framework in [UFXG10a] and [UFXG10b].

3.4. The inclusion of light quarks

In its original version⁸ the transport model BAMPS has been limited to gluonic degrees of freedom, i.e. the number of flavors has been set to zero, $N_f = 0$. While this simplification is a rather good approximation for the investigation of bulk properties since the initially created medium in heavy ion collisions is strongly gluon dominated, a precise quantitative comparison to various experimental observables eventually requires the inclusion of light quarks into the transport model. Especially for the investigation of jet observables this extension is crucial as studies of parton distribution functions and initial jet production show that quarks dominate the hard particle production at high transverse momenta. For the mini-jet model based on GRV parton distribution functions this is the case from roughly $p_T = 20$ GeV on as has been studied in [Foc06].

This section describes an extension of the BAMPS framework to consistently incorporate light quark degrees of freedom, including elastic and inelastic processes as for the gluons in the original BAMPS version. For the purpose of this extension, the quark flavors *up*, *down*, *strange* and their antiparticles are considered to be light and their mass is set to zero. In setups containing light quarks, the number of flavors is thus set to $N_f = 3$.

3.4.1. $2 \rightarrow 2$ processes containing light quarks

The extension of the BAMPS framework for binary particle interactions to include light quarks is rather straightforward. Leading order pQCD cross sections in small angle approximation are employed analogously to the pure gluon processes described in section 3.1.2 to

⁸See section 3.3 for some examples of results obtained within this version.

include all possible binary processes involving light quarks and gluons:

$$\begin{aligned}
gg &\rightarrow gg \\
gg &\rightarrow q\bar{q} \\
q\bar{q} &\rightarrow gg \quad \text{and} \quad q\bar{q} \rightarrow q'\bar{q}' \\
qg &\rightarrow qg \quad \text{and} \quad \bar{q}g \rightarrow \bar{q}g \\
q\bar{q} &\rightarrow q\bar{q} \\
qq &\rightarrow qq \quad \text{and} \quad \bar{q}\bar{q} \rightarrow \bar{q}\bar{q} \\
qq' &\rightarrow qq' \quad \text{and} \quad q\bar{q}' \rightarrow q\bar{q}',
\end{aligned} \tag{3.80}$$

where q denotes a light quark of arbitrary flavor *up* (u), *down* (d) or *strange* (s) and \bar{q} the corresponding antiquark. q' denotes a quark with flavor different from the quark q , i.e. $ud \rightarrow ud$ would be a $qq' \rightarrow qq'$ process, while $uu \rightarrow uu$ would be a $qq \rightarrow qq$ process.

The matrix elements and cross sections for these processes can be found in appendix B.3.3.

3.4.2. $2 \leftrightarrow 3$ processes containing light quarks

In order to incorporate particle multiplication and annihilation processes containing quarks, the matrix element $|\mathcal{M}_{2 \rightarrow 3}|^2$ for these processes needs to be known. In order to be consistent with the $gg \leftrightarrow ggg$ processes from the original version of BAMPS, the matrix elements for the newly implemented processes should also be considered within the Gunion-Bertsch approximations as discussed in section 3.2.

In the derivation of the Gunion-Bertsch result it was found that the approximated and squared radiative matrix element factorizes into a contribution from the elastic scattering and a contribution representing the radiation probability, eq. (3.78),

$$|\mathcal{M}_{\text{GB}}|^2 = |\mathcal{M}_{\text{coll}}|^2 P^g. \tag{3.81}$$

From the derivation of the Gunion-Bertsch matrix element it could already be expected that this factorization is a general feature. And indeed, detailed computations of the radiation amplitudes of gluons, light quarks and heavy quarks by GUIHO in [Gui06] explicitly show that the factorization (3.78) holds regardless of the specific process. Furthermore, the radiation probability P^g is the same for the scattering of gluons and light quarks

$$P^g \sim \frac{q_{\perp}^2}{k_{\perp}^2 (\mathbf{q}_{\perp} - \mathbf{k}_{\perp})^2} \tag{3.82}$$

with all differences in the prefactors contained in the collisional component $|\mathcal{M}_{\text{coll}}|^2$. Note that due to the mass the expression P^g is different for the radiation off heavy quarks though.

Taking advantage of this factorization the already implemented matrix element for $gg \leftrightarrow ggg$ processes, $|\mathcal{M}_{gg \rightarrow ggg}|^2$, can be reused for arbitrary $X \rightarrow X + g$ processes⁹ by rescaling as

$$|\mathcal{M}_{X \rightarrow X+g}|^2 = \frac{|\mathcal{M}_{X \rightarrow X}|^2}{|\mathcal{M}_{gg \rightarrow gg}|^2} |\mathcal{M}_{gg \rightarrow ggg}|^2. \tag{3.83}$$

⁹Where X is an arbitrary two-body state of gluons and light quarks.

Going into the small angle approximation that is used for $2 \rightarrow 2$ processes in BAMPS and that is in accordance with the approximations underlying the Gunion-Bertsch matrix element as discussed in section 3.2, the scaling can be done in terms of small angle differential cross sections

$$|\mathcal{M}_{X \rightarrow X+g}|^2 = Q_X |\mathcal{M}_{gg \rightarrow ggg}|^2 = \frac{\frac{d\sigma_{X \rightarrow X}}{d\mathbf{q}_\perp}}{\frac{d\sigma_{gg \rightarrow gg}}{d\mathbf{q}_\perp}} |\mathcal{M}_{gg \rightarrow ggg}|^2. \quad (3.84)$$

With this simplification the scaling factor Q_X purely depends on the ratio of the color factors for the $2 \rightarrow 2$ processes as given in appendix B.3.3 and listed in table 3.1.

Using this technique to compute the matrix elements, the following $2 \leftrightarrow 3$ processes are included

$$\begin{aligned} gg &\leftrightarrow ggg \\ qq &\leftrightarrow qgg \quad \text{and} \quad \bar{q}g &\leftrightarrow \bar{q}gg \\ q\bar{q} &\leftrightarrow q\bar{q}g \\ qq &\leftrightarrow qqg \quad \text{and} \quad \bar{q}\bar{q} &\leftrightarrow \bar{q}\bar{q}g \\ qq' &\leftrightarrow qq'g \quad \text{and} \quad q\bar{q}' &\leftrightarrow q\bar{q}'g. \end{aligned} \quad (3.85)$$

Processes where the $2 \rightarrow 2$ contribution would be purely in the s-channel, such as $gg \rightarrow q\bar{q}g$ or $q\bar{q} \rightarrow ggg$, are omitted since these processes are different from the diagrams considered in the Gunion-Bertsch matrix element. As these processes are suppressed by $1/s$ the thereby introduced error should be modest.

$\mathbf{X} \leftrightarrow \mathbf{Xg}$	Scaling factor Q_X	Symmetry factor $\tilde{\nu}_X$
$gg \leftrightarrow ggg$	1	1
$qq \leftrightarrow qgg$	$\frac{4}{9}$	2
$\bar{q}g \leftrightarrow \bar{q}gg$	$\frac{16}{81}$	2
$q\bar{q} \leftrightarrow q\bar{q}g$	$\frac{32}{81}$	1
$qq \leftrightarrow qqg$	$\frac{16}{81}$	2
$\bar{q}\bar{q} \leftrightarrow \bar{q}\bar{q}g$	$\frac{16}{81}$	2
$qq' \leftrightarrow qq'g$	$\frac{16}{81}$	2
$q\bar{q}' \leftrightarrow q\bar{q}'g$	$\frac{16}{81}$	2

Table 3.1.: Scaling factor Q_X , eq. (3.84), and combinatorial scaling factor $\tilde{\nu}_X$ in the limit $N_g \gg 1$, eq. (3.86), relative to $gg \leftrightarrow ggg$ for all $2 \leftrightarrow 3$ processes incorporated into BAMPS. See text for details.

In addition to the scaling by $|\mathcal{M}_{X \rightarrow X}|^2 / |\mathcal{M}_{gg \rightarrow ggg}|^2$, attention needs to be paid to possible symmetry factors. It is simplest to compute these starting from the $3 \rightarrow 2$ process. In the computation of the phase space integral I_{32} , eq. (3.8), a factor $1/\nu$ enters that accounts for identical particles in the final state. It is $1/\nu = 1/2!$ for a $ggg \rightarrow gg$ process. Thus, to compute for example a $qgg \rightarrow qq$ process the phase space integral needs to be scaled by an

additional factor $\tilde{\nu}_{qg} = 2$, $I_{qgg} = \tilde{\nu}_{qg} Q_{qg} I_{ggg} = 2 Q_{qg} I_{ggg}$, or generally written

$$I_{Xg} = \tilde{\nu}_X Q_X I_{ggg}. \quad (3.86)$$

For the incorporated $2 \leftrightarrow 3$ processes (3.85) the symmetry factor for the reverse reaction is identical in the limit $N_g \gg 1$, see appendix C.2 for a more detailed discussion. Only for processes such as $gg \rightarrow q\bar{q}g$ the scaling of symmetry factors would differ for the $2 \rightarrow 3$ and the $3 \rightarrow 2$ direction, but as mentioned previously these processes are s -channel processes and currently not included.

3.4.3. Numerical test of detailed balance in a static medium

As a basic test of the extended BAMPS setup, detailed balance is investigated for a static medium of quarks and gluons that is enclosed inside a simulated box with reflecting walls. The medium is initialized in thermal and chemical equilibrium with $N_f = 3$ and $T = 0.4$ GeV, with a gluon density $n_g = 16 \frac{T^3}{\pi^2} \approx 13.5 \text{ fm}^{-3}$ and quark (antiquark) density $n_q = n_{\bar{q}} = 6N_f \frac{T^3}{\pi^2} \approx 15.2 \text{ fm}^{-3}$.

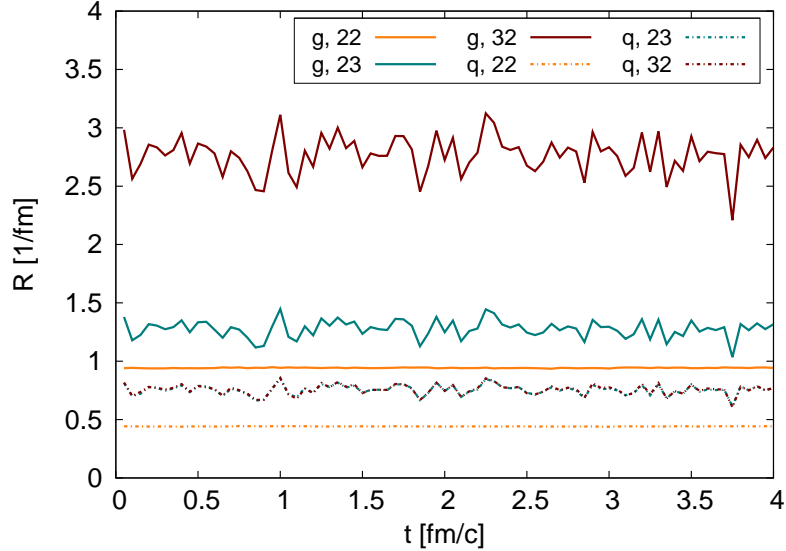


Figure 3.16.: Numerical tests of detailed balance in a static thermal medium with $T = 0.4$ GeV, $N_f = 3$, $V = 0.125 \text{ fm}^3$ and $N_{\text{test}} = 500$ including all processes as listed in eqs. (3.80) and (3.85). Shown are the rates R_{22} , R_{23} and R_{32} for gluons (solid lines) and quarks (dashed lines). Results averaged from 300 runs.

Figure 3.16 shows the rates per gluon (quark) for $2 \rightarrow 2$ processes, R_{22}^g (R_{22}^q), $2 \rightarrow 3$ processes, R_{23}^g (R_{23}^q), and $3 \rightarrow 2$ processes, R_{32}^g (R_{32}^q), as a function of time. The rates for antiquarks are identical to the rates for quarks and the rates shown are the sum over all possible processes from (3.80) and (3.85), e.g. $R_{22}^g = \sum_i R_{22,i}^g$. The rates for all particle species and process types are flat as a function of time, demonstrating that the incorporation of light quarks according to the procedures described in sections 3.4.1 and 3.4.2 successfully

passes the basic test for detailed balance. The rather strong fluctuations in the rates for $2 \leftrightarrow 3$ processes are due to oscillations introduced by the LPM cutoff, cf. section 3.1.4, since for this calculation the mean free path entering the cutoff has been dynamically computed from the rates of the previous time step and the system size is comparatively small.

4. High energy partons in a static medium

In order to obtain an adequate understanding of the mechanisms underlying the jet quenching in simulations of heavy ion collisions within BAMPS, it is important to study the evolution of jets in a simplified setup. For this the evolution of high energy partons is tracked as they propagate through a static and thermally equilibrated medium. Such a scenario is sometimes referred to as a *brick* setup¹.

The straightforward way to implement such a setup within a microscopic transport model such as BAMPS would be to populate a static system of fixed size with partons according to a thermal distribution at a given temperature T , then to inject a high energy particle with initial energy E and to track its propagation through the dynamically evolving medium, i.e. to study its energy loss, cross sections, radiation spectra, etc. To cut down on computation time, however, a more direct, Monte Carlo-type approach is chosen for all observables presented in this chapter. For a jet particle with given energy E a certain number of collision partners is generated from a thermal distribution with temperature T without actually simulating any medium constituents. This method therefore neglects possible effects of the propagating jet on the medium, i.e. the medium response such as the generation of hydrodynamic shocks, cf. section 3.3.3 and [BMN⁺09, BMN⁺10, BEF⁺10], is not taken into account. To ensure consistency, this approach has been successfully tested—with respect to the jet observables—against full calculations of static systems within BAMPS, where the dynamics of all particles are explicitly simulated.

4.1. Interaction rates and mean free paths

As discussed in section 3.1.4, the mean free path of energetic partons needs to be computed through an iterative procedure due to the LPM cutoff that dynamically depends on the current mean free path, cf. eq. (3.18),

$$\lambda = \lim_{i \rightarrow \infty} \lambda_i = \lim_{i \rightarrow \infty} \frac{1}{R_{22} + R_{23}(\lambda_{i-1}) + R_{32}(\lambda_{i-1})}. \quad (4.1)$$

The number of iterations used in the computations of the results presented in this section is $4 \leq N_{\text{it}} \leq 30$ and the iterative procedure is aborted at step $i \geq 4$ when

$$|\lambda_{i-j} - \langle \lambda \rangle_i| / \langle \lambda \rangle_i < \epsilon \quad \forall j \in \{0, 1, 2, 3\}$$

with $\langle \lambda \rangle_i = \sum_{j=0}^3 \lambda_{i-j} / 4$ and $\epsilon = 0.01$. The mean free path λ_i at each iteration step is computed from thermally averaged rates, using λ_{i-1} as input for the LPM cutoff with $\lambda_0 = \lambda_{\text{therm}}$. As detailed in appendix C.1, the rate for a given $2 \rightarrow N$ process is computed from $\langle v_{\text{rel}} \sigma_{X(2)} \rangle$, see eq. (C.2), and for a given $3 \rightarrow 2$ process from $\langle \tilde{I}_{X(3) \rightarrow Y} \rangle$, see eq. (C.4),

¹Such *brick* setups are proposed by the TECHQM collaboration, <https://wiki.bnl.gov/TECHQM>, as means of comparing results from different parton cascade models and (Monte Carlo) energy loss calculations.

where $\tilde{I}_{X(3)\rightarrow Y}$ comprises the phase space integral over the matrix element for the $3 \rightarrow 2$ process, eqs. (3.8) and (3.9). The averages are simply computed by generating a certain number N_{sample} of colliding particle pairs and triplets from a thermal Boltzmann distribution using inverse transform sampling (see appendix D.1) and evaluating $v_{\text{rel}}\sigma_{X(2)}$ and $\tilde{I}_{X(3)\rightarrow Y}$ for each pair or triplet respectively, giving $\langle v_{\text{rel}}\sigma_{X(2)} \rangle = \sum_{k=1}^{N_{\text{sample}}} v_{\text{rel}}^{(k)}\sigma_{X(2)}^{(k)}/N_{\text{sample}}$ and $\langle \tilde{I}_{X(3)\rightarrow Y} \rangle = \sum_{k=1}^{N_{\text{sample}}} \tilde{I}_{X(3)\rightarrow Y}^{(k)}/N_{\text{sample}}$. When computing the mean free path for jet particles as a function of jet energy, the projectile is held fixed at $p = (E, 0, 0, E)$ and only its collision partners are sampled from a thermal distribution. $N_{\text{sample}} = 200\,000$ is chosen for the computations presented in this section. The rates for all possible processes are then computed according to eqs. (C.5) and (C.6).

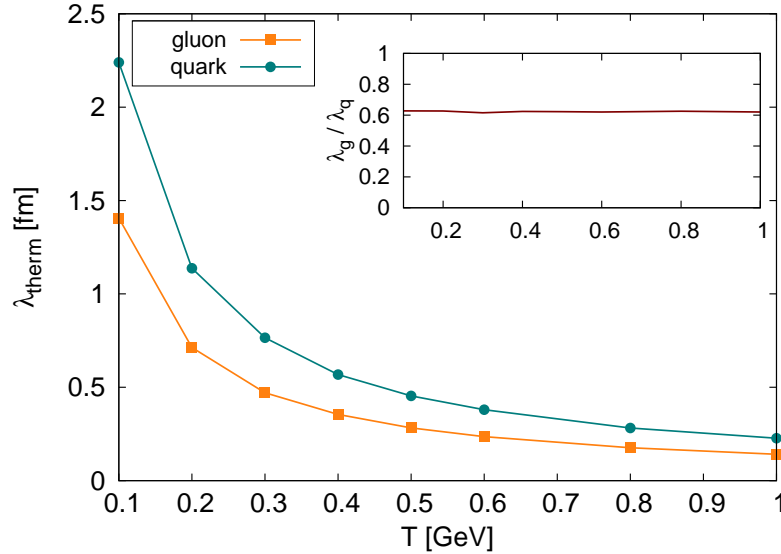


Figure 4.1.: Thermal mean free path of gluons and quarks ($N_f = 3$) as a function of the medium temperature T . The inset shows the ratio of the gluon mean free path to the quark mean free path, $\lambda_{\text{therm}}^g / \lambda_{\text{therm}}^q$.

The thermal mean free path of gluons shown in fig. 4.1 roughly varies from $\lambda_{\text{therm}}^g \approx 0.35$ fm to 0.7 fm in the temperature range $T \approx 0.4$ GeV to 0.2 GeV relevant for Au + Au collisions at RHIC energies. The thermal mean free path of quarks is distinctly larger, ranging from $\lambda_{\text{therm}}^q \approx 0.56$ fm to 1.14 fm. However, the ratio of gluon to quark mean free path is not $\lambda_{\text{therm}}^g / \lambda_{\text{therm}}^q \approx 4/9 \approx 0.44$ as would be expected from the color factors of the dominating $gq \rightarrow X$ processes, compare table 3.1, but rather $\lambda_{\text{therm}}^g / \lambda_{\text{therm}}^q \approx 0.6$ as illustrated by the inset of fig. 4.1. This is due to the self-quenching effect of the LPM cutoff on the rates for $2 \leftrightarrow 3$ processes and will be discussed below.

As shown in fig. 4.2a, the mean free path of jet partons is distinctly smaller than the thermal mean free path and levels off at roughly $\lambda_g \approx 0.16$ fm for high energy gluons and at $\lambda_q \approx 0.21$ fm for high energy quarks. The mean free path of the considered particle species at the given jet energy E is used as input for the next iteration step in these calculations with $\lambda_0^g = \lambda_{\text{therm}}^g$ or $\lambda_0^q = \lambda_{\text{therm}}^q$ respectively. The generic dependence of the mean free path for high energy particles on the medium temperature, as depicted in fig. 4.2b, is similar to

that of the thermal mean free path, fig. 4.1.

The contribution of particle annihilation processes to the total interaction rate of high energy partons is negligible, $2 \rightarrow 2$ and $2 \rightarrow 3$ processes strongly dominate as can be seen in fig. 4.3a. The rates in these plots are sums over all possible processes from eqs. (3.80) and (3.85) that contribute to the considered rate. Thus a statement in terms of cross sections is difficult, however, defining an effective cross section² from the total rate R and the particle density n as $\sigma_{\text{eff}} = R/n$, the cross section for $2 \rightarrow 3$ inside a medium with $T = 0.4$ GeV would be roughly 1 mb for a gluon jet and $\sigma_{2 \rightarrow 3, \text{eff}}^g \approx 0.9$ mb for a quark jet at $E = 400$ GeV in each case. For binary collisions the effective cross sections at $E = 400$ GeV would be $\sigma_{2 \rightarrow 2, \text{eff}}^g \approx 0.2$ mb and $\sigma_{2 \rightarrow 2, \text{eff}}^q \approx 0.4$ mb. The cross sections for single processes—where the concept of a cross section is actually meaningful—differ but are on the same order of magnitude, see for example fig. 3.5 for $\sigma_{gg \rightarrow ggg}$.

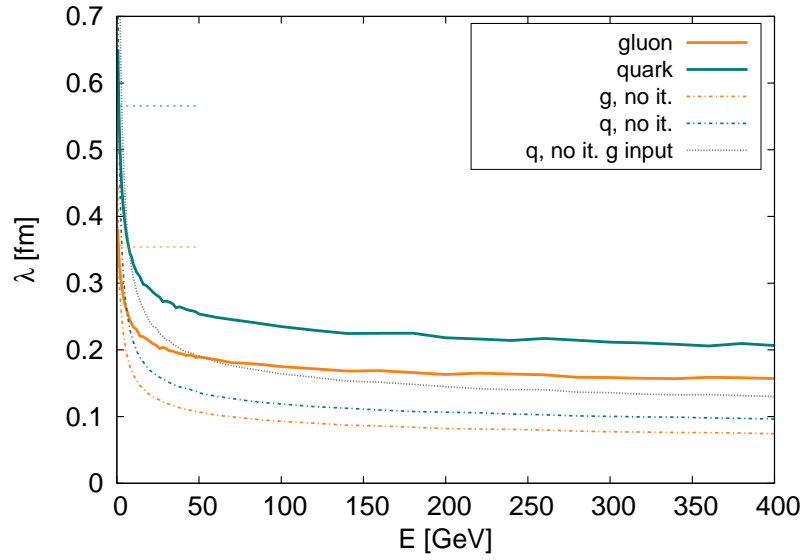
As for the thermal case the difference in the mean free path (or equivalently the total interaction rate) of gluon and quark jets is significantly smaller than the generically expected factor $9/4$. The average distance between interactions for a quark jet is only about 35% larger than for a gluon jet. Figure 4.3b shows the ratio R^g/R^q for the different types of processes. The ratio R_{22}^g/R_{22}^q is almost exactly $9/4$ as given by the color factors of the differential cross sections, while it is the $2 \leftrightarrow 3$ processes that deviate from this factor despite the fact that the same color factors are used to scale the matrix elements. This is due to a self-quenching effect introduced by the LPM cutoff discussed in section 3.1.4. The larger λ that is used as input in eq. (3.17), the larger the interaction probability and vice versa. Thus the LPM cutoff together with the iterative procedure for the computation of interaction rates, eq. (3.18), effectively attenuates changes to the bare matrix element, such as changes introduced by scaling factors relative to $|\mathcal{M}_{gg \rightarrow ggg}|^2$ that are used to compute quark processes as discussed in section 3.4.2. When omitting the iteration procedure, i.e. when using $\lambda_{i=1}$ as the final result, the weakening is less pronounced as indicated by the gray dashed lines in fig. 4.3b. Especially when the same initial value $\lambda_0 = \lambda_{\text{therm}}^g$ is used for the computation of both the gluon and the quark jet mean free path, the ratio of the non-iterated rates for $2 \rightarrow 3$ processes $R_{23, i=1}^g/R_{23, i=1}^q$ almost recovers the ratio of the color factors.

4.2. Energy loss in a static medium

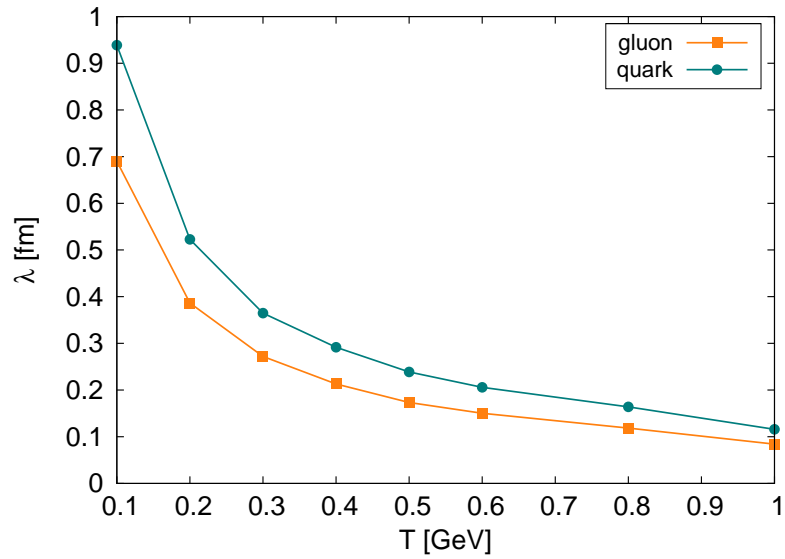
Since the quenching of jets that is observed in heavy ion collisions is commonly attributed to energy loss on the partonic level, the detailed and systematic investigation of the energy loss mechanism within the given framework is essential when studying the modification of high- p_T particles in simulations of heavy ion collisions with BAMPS. To this end the energy loss of jet partons that traverse a static and equilibrated medium is studied in this section.

As for the computation of the interaction rates and mean free paths in section 4.1, the energy loss is computed neglecting the medium response, i.e. without actually simulating the dynamics of the medium. The mean energy loss per unit path length, dE/dx , is then

²More precisely $\langle v_{\text{rel}} \sigma_{\text{eff}} \rangle = R/n$.

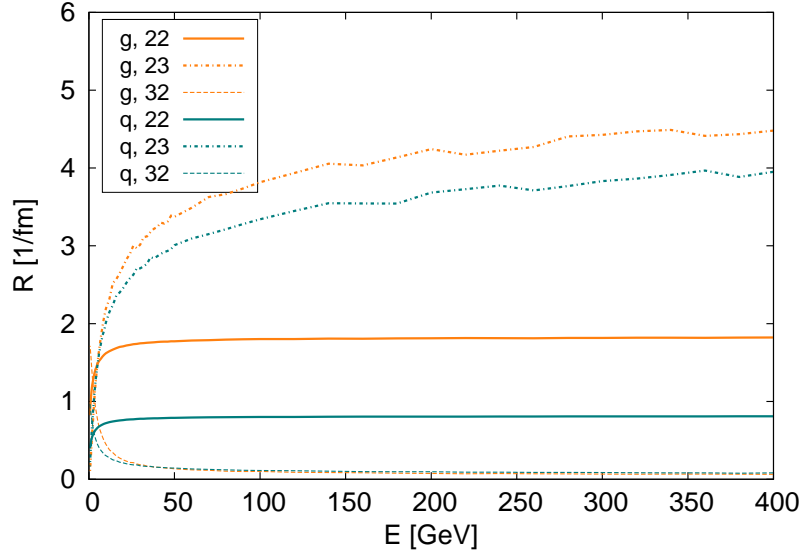


(a) Mean free path λ of gluon and quark jets traversing a static medium with $T = 0.4 \text{ GeV}$ and $N_f = 3$ as a function of jet energy E . Solid lines show the total λ after regular iteration procedure, dashed lines the result without iteration. Starting point λ_0 for the iterative procedure is the thermal mean free path as indicated by the thin horizontal dashed lines. For comparison the gray dashed line shows the non-iterated quark mean free path taking $\lambda_0 = \lambda_{\text{therm}}^g$.

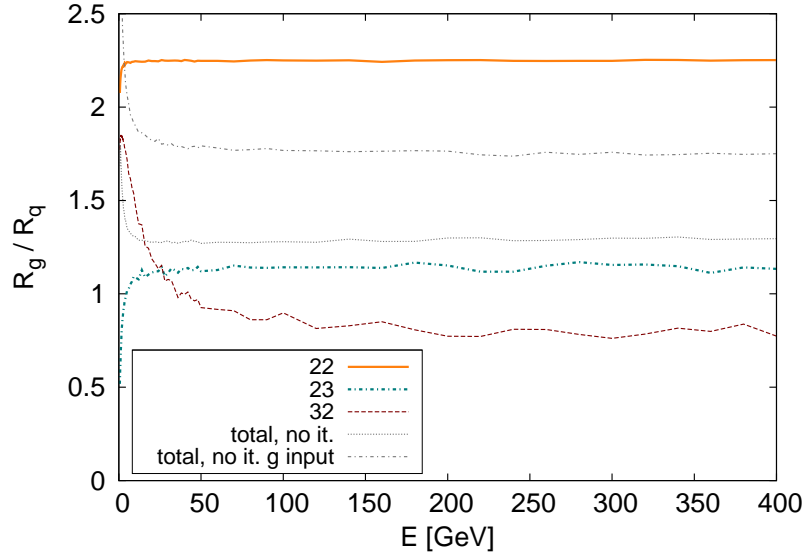


(b) Mean free path of gluon and quark jets with fixed $E = 20 \text{ GeV}$ traversing a static medium ($N_f = 3$) as a function of temperature.

Figure 4.2.: Mean free paths of high energy gluons and quarks traversing a static and equilibrated medium.



(a) Interaction rates of gluon and quark jets traversing a static medium with $T = 0.4$ GeV and $N_f = 3$ for $2 \rightarrow 2$, $2 \rightarrow 3$ and $3 \rightarrow 2$ processes as a function of jet energy E .



(b) Ratio of the interaction rates of gluon jets to the interaction rates of quark jets, R_g/R_q , as shown in fig. 4.3a for different process types as a function of jet energy. For comparison the gray dashed line shows the ratio of the non-iterated total rates, cf. fig. 4.2a, while the gray dash dotted line shows the ratio of the non-iterated total rates taking $\lambda_0 = \lambda_{\text{therm}}^g$ for the computation of the quark mean free path.

Figure 4.3.: Interaction rates of high energy gluons and quarks traversing a static and equilibrated medium.

computed as follows ($c = 1$)

$$\frac{dE^{(j)}}{dx} = \frac{dE^{(j)}}{d(ct)} = \sum_i \langle \Delta E_i^{(j)} \rangle R_i^{(j)}, \quad (4.2)$$

where j denotes the type of the jet particle, i.e. gluon or light quark, and i is the interaction type (e.g. $gq \rightarrow gq$, $gg \rightarrow ggg$, $qq \rightarrow qqg$, etc.). $R_i^{(j)}$ denotes the interaction rate for process i per particle of type j as computed in section 4.1. $\langle \Delta E_i^{(j)} \rangle$ is the mean energy loss of a jet particle of type j in a single collision of type i computed as the weighted sum

$$\langle \Delta E_i^{(j)} \rangle = \frac{\sum_{k=1}^{N_{\text{sample}}} (\Delta E_i^{(j)} \tilde{P}_i)_k}{\sum_{k=1}^{N_{\text{sample}}} (\tilde{P}_i)_k}. \quad (4.3)$$

The individual weighting factor $(\tilde{P}_i)_k$ is proportional to the probability of the given interaction process k . For $2 \rightarrow 2$ and $2 \rightarrow 3$ processes it is $(\tilde{P}_i)_k = (\sigma_i v_{\text{rel}})_k$, for particle annihilation processes it is $(\tilde{P}_i)_k = \left(\frac{I_{32,i}}{E_1 E_2 E_3} \right)_k$ with σ_i , v_{rel} and $I_{32,i}$ as given in section 3.1.2.

Unless explicitly noted otherwise, the jet particle in all computations is tagged by the energy, i.e. the particle emerging from the interaction process with the highest energy is taken to be the outgoing jet. Thus the energy loss per collision is given by

$$\Delta E = E^{\text{in}} - \max(E_1^{\text{out}}, E_2^{\text{out}}, E_3^{\text{out}}) \quad (4.4)$$

for $2 \rightarrow 3$ processes and

$$\Delta E = E^{\text{in}} - \max(E_1^{\text{out}}, E_2^{\text{out}}) \quad (4.5)$$

for $2 \rightarrow 2$ and $3 \rightarrow 2$ processes.

4.2.1. Energy loss from $2 \rightarrow 2$ interactions

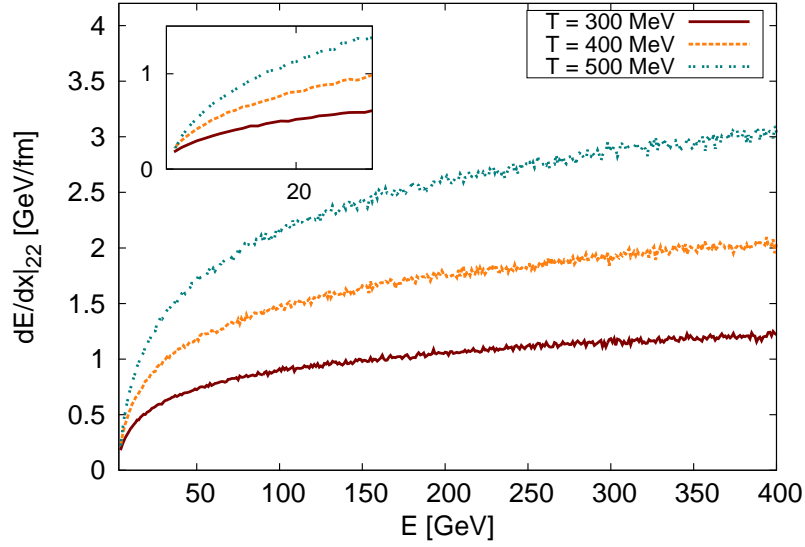
In order to provide a baseline for further investigations, the energy loss is first studied in the simplest case of pure $2 \rightarrow 2$ interactions. Figure 4.4a shows the mean differential energy loss $dE/dx|_{22}$ of a gluon jet that traverses a purely gluonic medium caused by binary $gg \rightarrow gg$ interactions as a function of the jet energy E and for different medium temperatures. The energy loss is computed as described above and the medium is represented by a thermal ensemble of gluons.

The differential energy loss exhibits the expected (see [WHDG07] for a concise overview) logarithmic dependence on the jet energy E and the dominant quadratic dependence on the medium temperature T

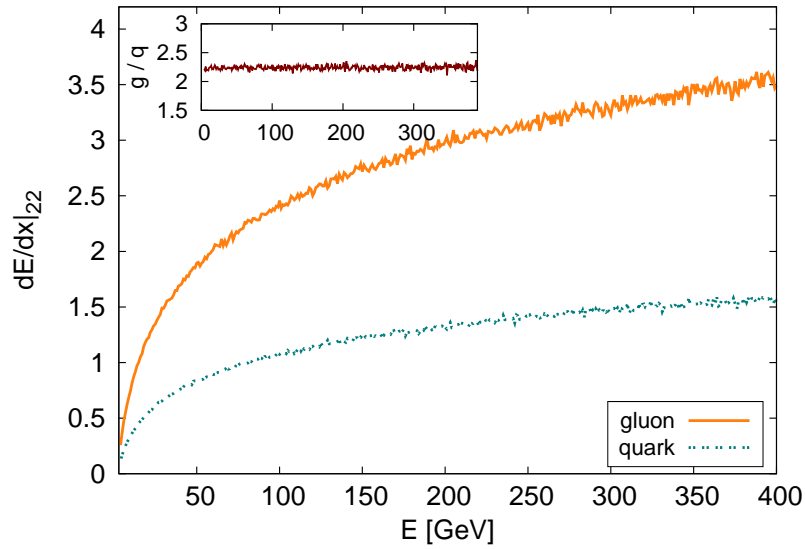
$$\left. \frac{dE}{dx} \right|_{2 \rightarrow 2} \propto C_R \pi \alpha_s^2 T^2 \ln \left(\frac{4ET}{m_D^2} \right), \quad (4.6)$$

where C_R is the quadratic Casimir of the propagating jet, $C_R = C_A = N_c$ for gluons. For $T = 0.4$ GeV, $N_f = 0$ and a jet energy of $E = 50$ GeV the elastic energy loss for a gluon jet is $\left. \frac{dE^g}{dx} \right|_{2 \rightarrow 2} \approx 1.2$ GeV fm⁻¹ and increases to $\left. \frac{dE^g}{dx} \right|_{2 \rightarrow 2} \approx 2$ GeV fm⁻¹ at $E = 400$ GeV.

Due to the increased number of scattering centers and possible interaction processes the differential energy loss per unit path length is of course larger in an equilibrated medium that additionally contains light quarks. As can be seen in fig. 4.4b, the differential energy



(a) Differential energy loss of a gluon jet in a static and thermal gluonic ($N_f = 0$) medium with temperatures $T = 0.3$ GeV, 0.4 GeV and 0.5 GeV as a function of the jet energy, taking only binary $gg \rightarrow gg$ interactions into account.



(b) Comparison of the differential energy loss from $2 \rightarrow 2$ processes for a gluon and a light quark jet as a function of jet energy. The medium parameters are $N_f = 3$ and $T = 0.4$ GeV. The inset shows the ratio of the gluon differential energy loss to the quark differential energy loss, $(dE^g/dx|_{22})/(dE^q/dx|_{22})$.

Figure 4.4.: Differential energy loss of gluon and quark jets in a static equilibrated medium from $2 \rightarrow 2$ processes.

loss of a gluon jet at $E = 400$ GeV inside a medium with $T = 0.4$ GeV increases from $\frac{dE^g}{dx}|_{2 \rightarrow 2} \approx 2 \text{ GeV fm}^{-1}$ for $N_f = 0$ to $\frac{dE^g}{dx}|_{2 \rightarrow 2} \approx 3.5 \text{ GeV fm}^{-1}$ for $N_f = 3$. The energy loss of a quark jet from $2 \rightarrow 2$ interactions is distinctly weaker, with a ratio that is entirely given by the ratio of the rates R_{22}^g/R_{22}^q , see fig. 4.3b and the inset of fig. 4.4b. The differential energy loss of a quark from $2 \rightarrow 2$ processes alone is thus smaller than that of a gluon jet in the same medium by a factor of roughly $9/4$, giving $\frac{dE^q}{dx}|_{2 \rightarrow 2} \approx 1.5 \text{ GeV fm}^{-1}$ at $E = 400$ GeV in the example discussed above.

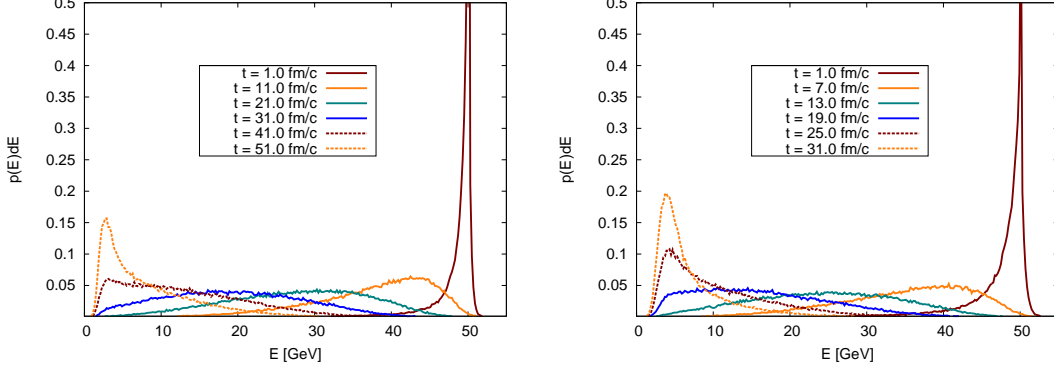


Figure 4.5.: Time evolution of the energy distribution of a gluon jet that interacts only via $gg \rightarrow gg$ processes with a static and thermal medium of gluons ($N_f = 0$) at $T = 0.4$ GeV (left panel) and $T = 0.6$ GeV (right panel). The initial ($t = 0 \text{ fm c}^{-1}$) energy of the gluon jet is $E_0 = 50$ GeV.

Though the mean energy loss of a jet parton is an important quantity to classify the effects of the medium on the jet, it may in fact hide more differentiated and potentially interesting features of the jet evolution. More sophisticated information than in the mean energy loss per unit path length is thus contained in the time evolution of the energy distribution of the jet particle propagating through the medium. As for the computation of the differential energy loss a Monte Carlo approach is chosen, where the collision partners are sampled from a thermal distribution. Given discretized and fixed time steps Δt , the medium density n and a fixed number of collision partners \tilde{N} , the implemented interactions at each time t are sampled according to their probabilities

$$P_{22}(t) = v_{rel}\sigma_{22}(t)\frac{n\Delta t}{\tilde{N}} \quad P_{23}(t) = v_{rel}\sigma_{23}(t)\frac{n\Delta t}{\tilde{N}} \quad P_{32}(t) = \tilde{I}_{32}(t)\frac{n^2\Delta t}{\tilde{N}^2}. \quad (4.7)$$

The time dependence is introduced by the dependence of the cross sections on the current jet energy $E(t)$ that is then updated to $E(t + \Delta t)$ according to the sampled interactions. Starting at $t = 0 \text{ fm/c}$ with an initial parton energy E_0 , this approach yields the evolution of the jet energy as a function of time, $E(t)$. Repeating this procedure many times, $p(E, t) dE$ is computed, the probability that a parton that started with $E(t = 0 \text{ fm/c}) = E_0$ has an energy $E \leq E(t) < E + dE$ at a given time t .

Figure 4.5 shows the time evolution of the probability distribution for the energy of a gluonic jet particle injected with an initial energy of $E_0 = 50$ GeV into a thermal medium of gluons ($N_f = 0$) with $T = 0.4$ GeV and $T = 0.6$ GeV respectively. In both cases the distribution of the jet energy induced by binary collisions with the constituents of the

medium becomes rather broad. A distinct peak at lower energies only re-emerges at very late times, roughly after $50 \text{ fm } c^{-1}$ for $T = 0.4 \text{ GeV}$ and $30 \text{ fm } c^{-1}$ for $T = 0.6 \text{ GeV}$. The mean energy loss as depicted in fig. 4.4 is therefore a valuable observable but contains only limited information. It is noteworthy that there exists a finite probability for the jet to gain energy by collisions with the constituents of the thermal medium. This effect is more pronounced for higher medium temperatures. As already found in [SGJ09], the shapes of the distributions induced by collisional energy loss significantly differ from models that employ a mean energy loss accompanied by momentum diffusion such as [WHDG07, QRG⁺08]. According to the results presented in fig. 4.4b, the evolution of the energy spectrum is swifter inside a medium that additionally contains light quarks and it is also faster for a gluon jet than for quark jet. Qualitatively however, there is no difference to the case of a gluon jet inside a purely gluonic medium.

4.2.2. Energy loss including $2 \leftrightarrow 3$ interactions

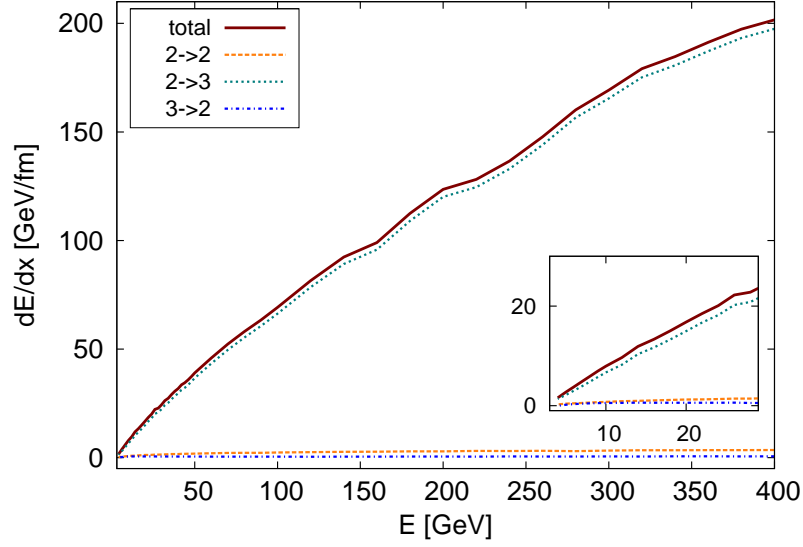
After having established the behavior of high energy partons induced by $2 \rightarrow 2$ interactions in the previous section, the evolution of jets in a static medium is now investigated including particle multiplication and annihilation processes based on the Gunion-Bertsch matrix element as discussed in chapter 3.

Figure 4.6a shows the mean differential energy loss dE/dx of a gluon jet as a function of jet energy E in a static thermal medium with $T = 0.4 \text{ GeV}$ and $N_f = 3$ caused by all possible binary $2 \rightarrow 2$ and inelastic $2 \leftrightarrow 3$ interactions that are included in the BAMPS framework according to eqs. (3.80) and (3.85). The contributions from the different processes to the total energy loss are displayed separately. From this compilation it is obvious that bremsstrahlung processes $2 \rightarrow 3$ are by far the most dominant contribution to the partonic energy loss within the BAMPS framework, whereas particle annihilation processes are negligible and binary interactions, cf. section 4.2.1, contribute only on a small level. Though not explicitly depicted in fig. 4.6a, this also holds for quark jets. The resulting differential energy loss is almost linearly rising with the energy, for example resulting in a total $dE/dx \approx 39.1 \text{ GeV fm}^{-1}$ for a gluon jet at $E = 50 \text{ GeV}$.

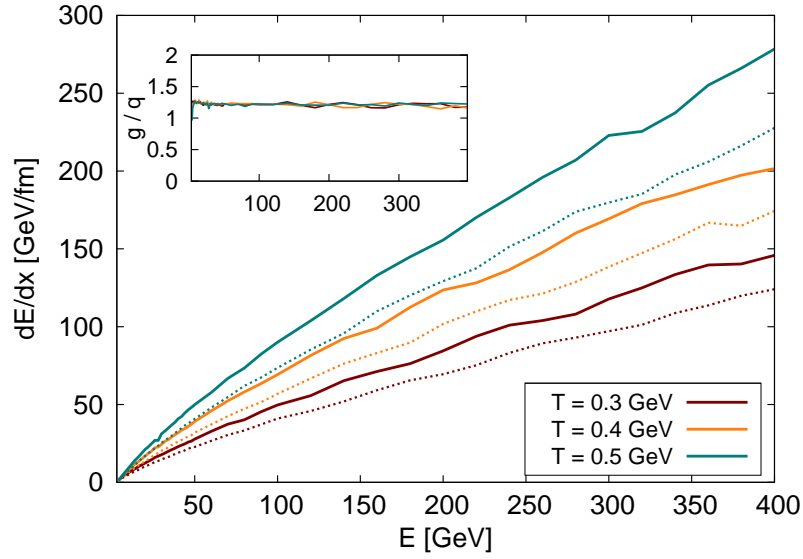
At large jet energies the temperature dependence of the resulting total differential energy loss appears to be roughly linear as can be seen from fig. 4.6b, where dE/dx is compared for medium temperatures $T = 0.3 \text{ GeV}$, $T = 0.4 \text{ GeV}$ and $T = 0.5 \text{ GeV}$. This behavior stems from the dominant $2 \rightarrow 3$ processes and is in contrast to the elastic energy loss, eq. (4.6), that exhibits a dominant quadratic dependence on the temperature. Possible logarithmic contributions to the temperature dependence cannot be resolved numerically within these calculations.

While the energy loss of gluons and quarks induced by binary $2 \rightarrow 2$ interactions does indeed differ by the color factor, roughly $9/4$, as discussed in section 4.2.1, the total energy loss of quarks is only about 20% weaker than that of gluons. This holds almost independent of medium temperature and jet energy as can be seen in fig. 4.6b. This rather weak dependence on the particle type is mainly caused by the radiative processes that dominate the total energy loss and for which the difference in the interaction rates is quenched by the effective implementation of the LPM effect as discussed in section 4.1.

As already discussed in section 4.2.1 for jets interacting only via $2 \rightarrow 2$ processes, valuable information beyond the mean energy loss is contained in the evolution of the energy distribu-



(a) Differential energy loss of a gluon jet in a static and thermal medium with $T = 0.4$ GeV and $N_f = 3$. The contributions of the different pQCD processes implemented in BAMPS to the total dE/dx are shown.



(b) Differential energy loss of gluon (solid lines) and quark (dashed lines) jet particles as a function of jet energy including all implemented $2 \rightarrow 2$ and $2 \leftrightarrow 3$ processes for temperatures of the medium $T = 0.3$ GeV, $T = 0.4$ GeV and $T = 0.5$ GeV. The inset shows the ratio of the total gluon differential energy loss to the total quark differential energy loss for the different temperatures of the medium, $(dE^g/dx)/(dE^q/dx)$.

Figure 4.6.: Differential energy loss of gluon and quark jets in a static equilibrated medium ($N_f = 3$) including $2 \rightarrow 3$ processes.

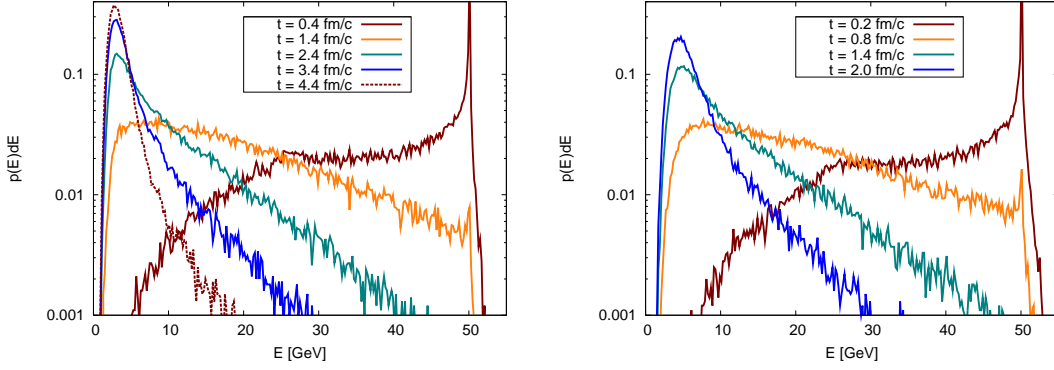


Figure 4.7.: Time evolution of the energy distribution of a gluon jet that interacts via $gg \rightarrow gg$ and $gg \leftrightarrow ggg$ processes with a static and thermal medium of gluons ($N_f = 0$) at $T = 0.4$ GeV (left panel) and $T = 0.6$ GeV (right panel). The initial ($t = 0$ fm c^{-1}) energy of the gluon jet is $E_0 = 50$ GeV.

tion $p(E, t) dE$ of the jet particle. Starting out with $p(E, t = 0 \text{ fm } c^{-1}) = \delta(E - E_0)$, fig. 4.5 has shown that elastic collisions cause a broadening of the distribution with a distinct peak at low energies only re-emerging at very large times. Because of the much stronger mean energy loss caused by radiative $2 \rightarrow 3$ processes, a more rapid evolution is to be expected when all interactions included in BAMPS are taken into account. Indeed, fig. 4.7 shows that the energy distribution of a gluon jet with $E_0 = 50$ GeV traversing a gluonic ($N_f = 0$) medium with $T = 0.4$ GeV is spread over almost the entire range after roughly 1 fm c^{-1} . A distinct peak at $E \approx 8T$ emerges at about 3.5 fm c^{-1} for $T = 0.4$ GeV and 2 fm c^{-1} for $T = 0.6$ GeV. Note that the results in fig. 4.7 have been obtained prior to implementing the constraint from the small angle approximation for $2 \rightarrow 3$ processes as outlined in section 3.1.3. However, the discussion in section 3.1.3 also shows that the effect on the energy loss would be rather mild, on the order of 15% to 20%, mostly stemming from the change in the mean free path and giving no qualitative deviation.

4.3. Detailed investigation of energy loss in $2 \rightarrow 3$ processes

Given the findings presented in section 4.2.2, it is necessary to discuss the origin of the strong energy loss from radiative processes within BAMPS. First of all, despite the large differential energy loss for gluonic jets, the individual cross sections increase only slowly, apparently logarithmically, with the jet energy as already seen in fig. 3.5 and also from the rates in fig. 4.3. For instance the average total cross sections for a gluon jet with $E = 50$ GeV in a purely gluonic medium ($N_f = 0$) with a temperature $T = 0.4$ GeV are $\langle \sigma_{gg \rightarrow gg} \rangle \approx 1.3$ mb and $\langle \sigma_{gg \rightarrow ggg} \rangle \approx 3.5$ mb. This emphasizes that BAMPS does indeed operate with reasonable partonic cross sections based on pQCD matrix elements.

The evolution of the mean cross sections for thermal $gg \rightarrow gg$ and $gg \rightarrow ggg$ processes in simulations of Au+Au collisions has been studied in [XGS08]. Apart from the α_s dependence, $\langle \sigma \rangle$ basically scales as $\sim 1/T^2$, leading to an increase in the cross sections as the systems cools. For the relevant time scales the cross sections do not exceed a few millibarn, $\langle \sigma_{gg \rightarrow gg} \rangle \lesssim 4$ mb and $\langle \sigma_{gg \rightarrow ggg} \rangle \lesssim 2$ mb. Comparing the collisional width determined by

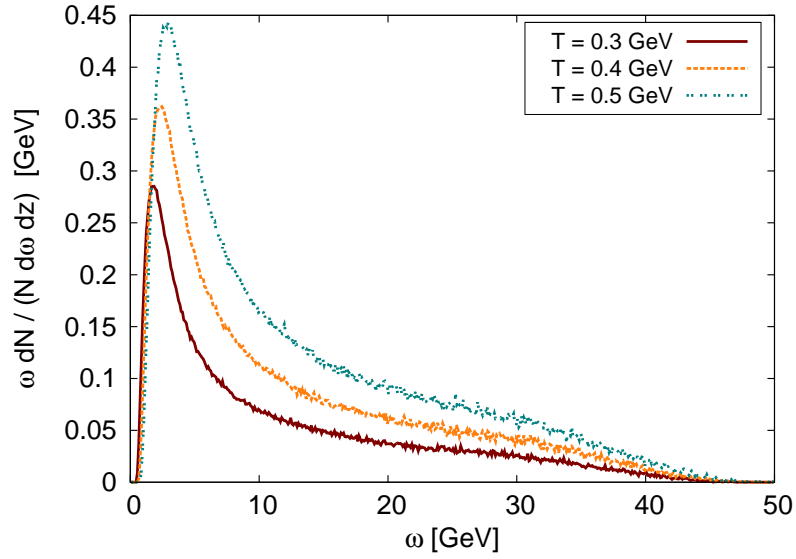
the interaction rates, $\Gamma = (R_{gg \rightarrow gg} + R_{gg \rightarrow ggg} + R_{ggg \rightarrow gg})$, to the mean energy provides an indication on the validity of semi-classical on-shell transport that holds for $\Gamma/\langle E \rangle \ll 1$. In [XG08] it is found that for thermal gluons the ratio is $\Gamma/\langle E \rangle \approx 0.5$ ($\alpha_s = 0.3$), being close to the edge of validity but still within a reasonable regime. For high energy gluons $\Gamma/\langle E \rangle \ll 1$ holds since the cross sections increase only by a factor of about 2 towards very large E , cf. fig. 3.5. Going from a purely gluonic medium to a medium that also includes light quarks, the aforementioned numbers will of course change, however the qualitative statements hold. As can be seen from the interaction rates in fig. 4.3, compare also the discussion in section 4.1, the cross sections for all processes are comparable and the resulting effective cross section is on the order of a few millibarn. Furthermore the bulk medium created in the early stage of heavy ion collisions is strongly gluon dominated, cf. chapter 5, so the findings from [XG08] are not expected to change significantly when going from $N_f = 0$ to $N_f = 3$.

4.3.1. Radiation spectra from the Gunion-Bertsch matrix element

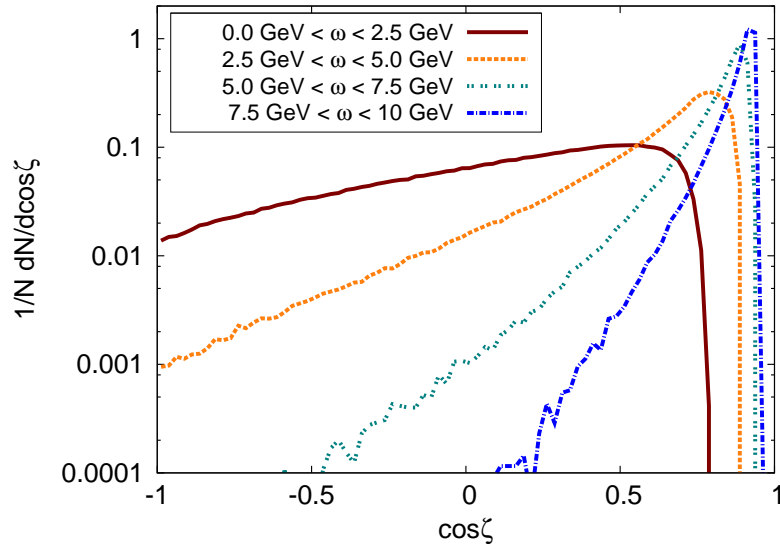
Since the cross sections for all $2 \rightarrow 3$ processes yield moderate mean free paths for jet-like particles—as discussed above and as illustrated in fig. 4.3—the cause for the large differential energy loss needs to be a large mean energy loss per single collision, $\langle \Delta E \rangle$, more specifically a large mean energy loss per radiative interaction, $\langle \Delta E_{23} \rangle$. The energy carried away by the radiated gluons, however, is in itself not sufficient to explain such large mean ΔE_{23} . From the radiation spectrum of a gluon jet with $E = 50$ GeV, shown in fig. 4.8a for different medium temperatures, a mean energy of the radiated gluon can be read off that is distinctly below the $\langle \Delta E_{23} \rangle$ that would be needed to fully explain the observed magnitude of dE/dx . This finding will be confirmed explicitly later. The spectrum is displayed for a gluon jet with fixed $E = 50$ GeV inside a purely gluonic medium as the number of radiated gluons per energy interval $d\omega$ and per distance dx scaled by the total number of emitted gluons and weighted with the gluon energy. Herein ω is the laboratory frame energy of the gluon that in the center of momentum frame is emitted with transverse momentum k_\perp according to the Gunion-Bertsch matrix element (3.13). The spectra are clearly peaked at energies that are small compared to the energy of the parent jet, with a tail reaching out to high energies. With increasing temperature the peak of the spectrum shifts towards higher energies in an apparently linear way, favoring the emission of gluons with higher energies in a natural way.

For completeness fig. 4.8b shows the angular distribution of gluons radiated off a $E = 50$ GeV gluon jet in a $T = 0.4$ GeV medium for different ranges of the energy of the radiated gluon ω . The angle ζ is taken in the laboratory frame with respect to the initial direction of the parent jet. With increasing energy ω the radiated gluons are emitted more preferably at small angles, only for soft gluons there is a sizable probability to be emitted transversely or in the backward direction. However, as is clearly visible in fig. 4.8b, due to the cutoff in transverse momentum k_\perp that is introduced by the implementation of the LPM effect eq. (3.20), the gluons cannot be emitted at very forward angles, an effect that is more pronounced for low ω .

As was to be expected from the functional form of the Gunion-Bertsch matrix element (3.13), the distributions in fig. 4.9a show that the transverse momentum transfer q_\perp and the transverse momentum of the emitted gluon are of comparable size and on the order of the Debye mass m_D . This demonstrates once more that the kinematics as sampled within the numerical routines of the transport model BAMPS are in good accordance with



(a) Energy spectrum $\omega \frac{dN}{N d\omega dz}$ of radiated gluons per energy interval $d\omega$ and distance dz . ω is the energy (laboratory frame) associated with the radiated gluon according to the Gunion-Bertsch matrix element (3.13) including the LPM cutoff (3.20). The radiating jet is a gluon with $E = 50$ GeV traversing a thermal medium with $T = 0.3$ GeV, $T = 0.4$ GeV or $T = 0.5$ GeV and $N_f = 0$.



(b) Angular distribution of the radiated gluon in the laboratory frame with respect to the original jet direction for different energies ω of the radiated gluon. Jet energy $E = 50$ GeV, medium $T = 0.4$ GeV and $N_f = 0$.

Figure 4.8.: Energy spectrum and angular distribution of radiation from the Gunion-Bertsch matrix element.

the assumptions underlying the Gunion-Bertsch matrix element as discussed in section 3.2, both q_\perp and k_\perp are typically small compared to the available energy \sqrt{s} . Furthermore, the lower bound on the transverse momentum of the emitted gluon that is introduced by the LPM cutoff, eqs. (3.17), (3.20) and (3.22), is clearly visible. With increasing jet energy the lower bound on k_\perp is slightly shifted towards larger values. While the mean energy loss per radiative interaction, ΔE_{23} , is largest for large values of q_\perp and k_\perp , the folded distribution in fig. 4.9b clearly shows that the main contribution to the energy loss in $2 \rightarrow 3$ processes stems from interactions where both q_\perp and k_\perp are of moderate size.

4.3.2. Energy loss per $2 \rightarrow 3$ process versus radiated energy

Now coming back to the issue of mean energy loss per radiative interaction, ΔE_{23} , versus the mean energy carried away by the radiated gluon, ω , fig. 4.10a explicitly shows that the two values are indeed not the same. The strong and almost linear rise in the energy loss due to $2 \rightarrow 3$ processes is only present when identifying the outgoing particle with the highest energy as the outgoing jet, thus using the definition of ΔE from eq. (4.4),

$$\Delta E = E - \max(E_1^{\text{out}}, E_2^{\text{out}}, E_3^{\text{out}}). \quad (4.8)$$

This choice corresponds to the set of dashed lines in fig. 4.10a that for example indicate a mean energy loss per radiative interaction of roughly $\Delta E_{23} \approx 11$ GeV at $E = 50$ GeV and $\Delta E_{23} \approx 44$ GeV at $E = 400$ GeV, comparatively independent on the temperature of the medium and on the type of the jet particle. The average energy ω of the radiated gluon, however, is rising much slower with the jet energy, being only $\omega \approx 6$ GeV at $E = 50$ GeV and $\omega \approx 11$ GeV at $E = 400$ GeV as illustrated by the set of solid lines in fig. 4.10a.

This discrepancy is due to the fact that—obeying exact energy and momentum conservation—the available energy in a $2 \rightarrow 3$ process is distributed among three outgoing particles, the gluon emitted with energy ω being only one of them. In fact, assuming $\omega < E^{\text{in}}/3$ in agreement with the results presented in fig. 4.10a,

$$\Delta E_{\text{min}} = \omega \quad (4.9)$$

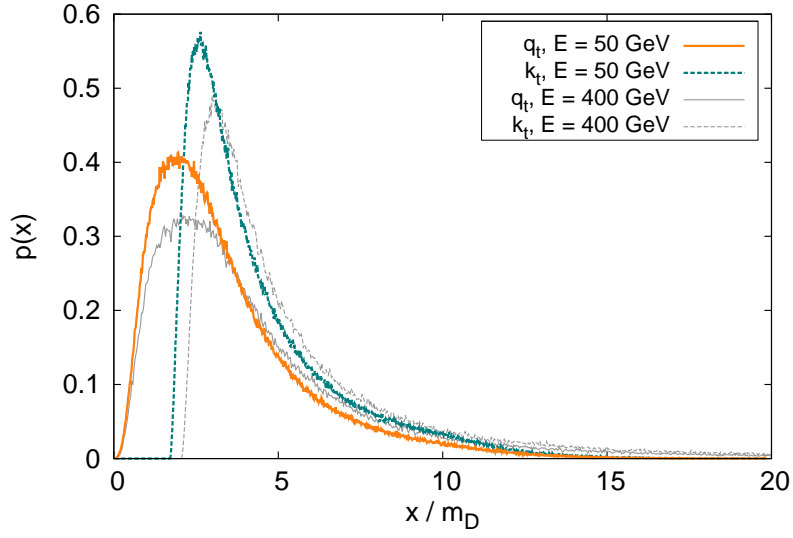
is only the smallest possible energy loss, while the largest energy loss allowed by energy and momentum conservation is

$$\Delta E_{\text{max}} = E - \left(\frac{E - \omega}{2} \right) = \frac{E + \omega}{2}. \quad (4.10)$$

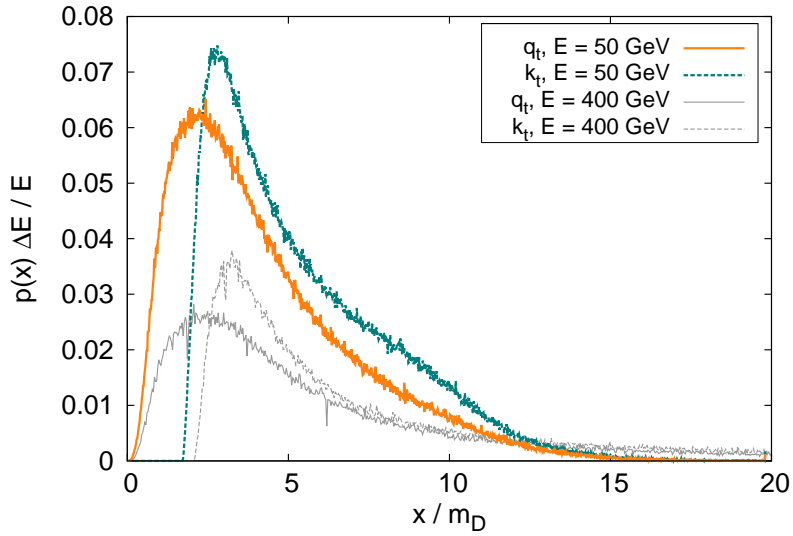
The maximum energy loss (4.10) corresponds to a configuration in which the remaining available energy after radiation of a gluon with energy ω is equally split among the two other particles in the final state. The upper bound on the energy loss per $2 \rightarrow 3$ interaction is given by $\Delta E \leq 2E/3$.

Thus, when treating radiative processes as full $2 \rightarrow 3$ interactions, the generic argumentation above illustrates that the energy carried away by the radiated gluon is in fact only a lower limit on the energy loss and that eikonal approximations in which no momentum is transferred to the propagating jet might underestimate the energy loss.

Furthermore, the energy loss per $2 \rightarrow 3$ process as depicted in fig. 4.10a is just a mean value, averaged over many interactions of a jet parton of given energy E with constituents

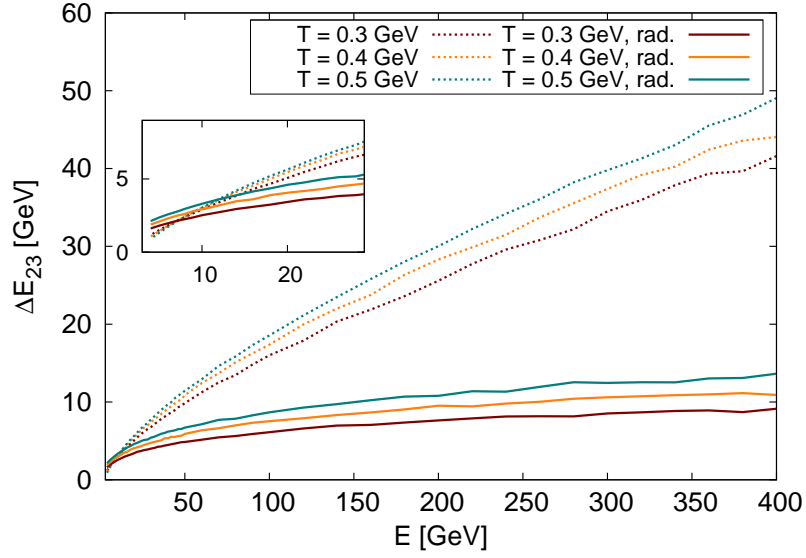


(a) Distribution $p(x) = dN/(Ndx)$ of the transverse momentum transfer, $x = q_\perp$, and of the transverse momentum of the emitted gluon, $x = k_\perp$, for $gg \rightarrow ggg$ interactions of a gluon jet with $E = 50$ GeV (colored lines) and $E = 400$ GeV (gray lines) inside a medium with $T = 0.4$ GeV and $N_f = 0$. q_\perp and k_\perp are given in units of the thermal Debye mass, eq. (3.12), $m_D = 0.6055$ GeV.

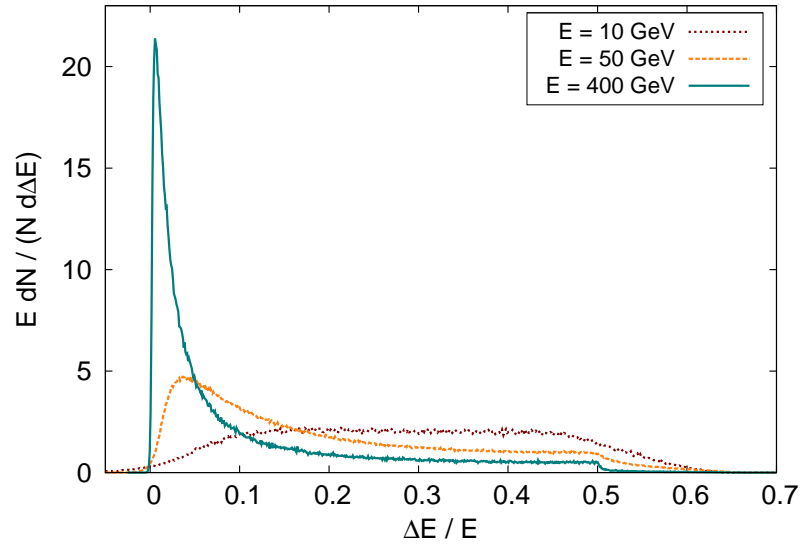


(b) Mean energy loss $\langle \Delta E_{23} \rangle$ for a single radiative process as a function of $x = q_\perp$ and $x = k_\perp$ respectively. The energy loss is scaled with the distribution of q_\perp and k_\perp . See fig. 4.9a.

Figure 4.9.: Distributions of transverse momentum transfer and transverse momenta of radiated gluons in $2 \rightarrow 3$ processes and the corresponding energy loss in $2 \rightarrow 3$ processes.



(a) Mean energy loss $\langle \Delta E_{23} \rangle$ of a gluon jet in a single $2 \rightarrow 3$ process as a function of jet energy. Two different cases are shown: One where $\Delta E = E^{\text{in}} - \max(E_1^{\text{out}}, E_2^{\text{out}}, E_3^{\text{out}})$ (dashed lines) and one (labeled “rad.”, solid lines) where $\Delta E = \omega$ is the energy of the radiated gluon.



(b) Distribution of ΔE_{23} , with $\Delta E = E^{\text{in}} - \max(E_1^{\text{out}}, E_2^{\text{out}}, E_3^{\text{out}})$, for a gluon jet with $E = 10$ GeV, 50 GeV and 400 GeV.

Figure 4.10.: Energy loss from single $2 \rightarrow 3$ interactions. Medium parameters are $T = 0.4$ GeV and $N_f = 3$.

of the thermal medium. The underlying distribution is given in fig. 4.10b for different values of the jet energy. It is immediately obvious that the mean value $\langle \Delta E_{23} \rangle$ does not correspond to a distinct peak in the distribution. On the contrary, the distributions are non-gaussian and peak at very small energy losses for large jet energies, for example at $\Delta E_{23}/E \approx 0.006$ for $E = 400$ GeV and at $\Delta E_{23}/E \approx 0.04$ for $E = 50$ GeV ($T = 0.4$ GeV, $N_f = 3$). For the jet with $E = 10$ GeV, whose energy is on the same order of magnitude as the typical energies of the radiated gluons, the distribution is very broad and exhibits no distinct typical energy loss.

4.3.3. Typical phase space configurations in $2 \rightarrow 3$ processes

While the peak at small ΔE_{23} in the energy loss distribution for asymptotically high jet energies, cf. fig. 4.10b, can be attributed to energy being carried away by the radiated gluon, it is in fact the heavy tail of the distribution that makes the averaged $\langle \Delta E_{23} \rangle$ distinctly larger than ω , as already demonstrated in fig. 4.10a. This heavy tail in the ΔE_{23} distribution is eventually caused by a highly complicated variety of configurations for the outgoing particles that are allowed by the underlying matrix element (3.13) and cannot be attributed to one specific configuration. In the following some typical examples in the parameter space of $2 \rightarrow 3$ processes are explored in order to illustrate the interplay of momentum conservation and phase space available due to the Gunion-Bertsch matrix element and the LPM cutoff that eventually leads to the a large mean energy loss.

The most specific feature of the phase space sampled in $2 \rightarrow 3$ processes is that the radiated gluon is predominantly emitted into the backward hemisphere in the center of momentum frame, compare the discussion in section 3.1.4 and especially fig. 3.6. Due to the strong bias towards negative rapidities³ that is present for large boosts (3.19), the energy of the radiated gluons in the c.m. frame is in many cases comparable to the energies of the two other outgoing particles even for small transverse momenta k_{\perp} and q_{\perp} .

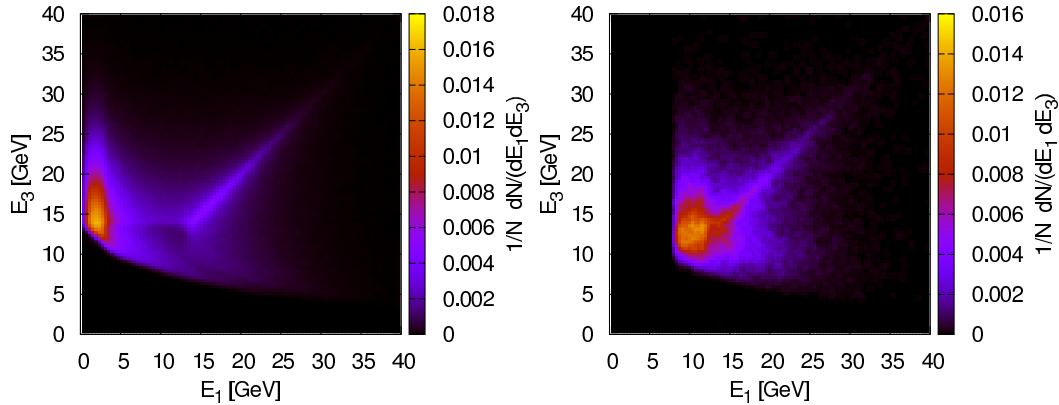


Figure 4.11.: Probability distribution of the outgoing energies E_1 and E_3 in the center of momentum frame for $gg \rightarrow ggg$ processes given a certain cut in the momentum transfer q_{\perp} , where E_3 is the energy of the emitted gluon. Jet energy $E = 400$ GeV, medium temperature $T = 0.4$ GeV, $N_f = 0$.

Left panel: $0 \text{ GeV} \leq q_{\perp} \leq 3 \text{ GeV}$. Right panel: $8 \text{ GeV} \leq q_{\perp} \leq 12 \text{ GeV}$.

³With respect to the direction of the jet momentum.

Characteristic correlations of outgoing momenta

In order to quantify the characteristics of the kinematics in $2 \rightarrow 3$ processes dictated by the Gunion-Bertsch matrix element (3.13) in combination with the LPM cutoff (3.17), the kinematics of the three outgoing particles can be described by 6 independent parameters. One such possible choice would be the set $(E_1, E_3, \cos(\theta_1), \cos(\theta_3), \phi_1, \phi_3)$, where E_1, E_3 are the energies, θ_1 and θ_3 are the angles with respect to the incoming momentum \mathbf{p}_{jet} and ϕ_1 and ϕ_3 are the azimuthal angles of the outgoing particles 1 and 3 (the emitted gluon), with all values being taken in the center of momentum frame. The corresponding values for the outgoing particle 2 can then be inferred from momentum conservation. Another choice would be to replace $\cos(\theta_1)$ and $\cos(\theta_3)$ by the momentum transfers q_\perp and k_\perp as directly given in eq. (3.13). Note however, that this choice hides the information whether $\cos(\theta_1)$ and $\cos(\theta_3)$ are larger or smaller than zero, i.e. whether particles 1 and 3 are emitted in the forward or in the backward direction. Finally, also replacing E_3 by y , the rapidity of the emitted gluon, would yield a set of parameters that is closest to the notation of the Gunion-Bertsch matrix element.

For the purpose of this discussion the set $(E_1, E_3, q_\perp, k_\perp, \phi_1, \phi_3)$ is used together with additional information from the signs of $\cos(\theta_1)$ and $\cos(\theta_3)$ as needed. Any dependence on the azimuthal angles ϕ_1, ϕ_3 is neglected. As discussed in section 4.3.1, for a fixed value of the transverse momentum transfer q_\perp , the transverse momentum of the emitted gluon, k_\perp , is typically on the same order as q_\perp , cf. fig. 4.9a. Thus $2 \rightarrow 3$ events are selected and classified according to E_1, E_3 and q_\perp .

$0 \leq q_\perp \leq 3$			
$0 \leq E_1 \leq 5$	$12 \leq E_3 \leq 20$	21.3 %	$\langle \Delta E \rangle \approx 24.3 \text{ GeV}$
$12 \leq E_1 \leq 20$	$12 \leq E_3 \leq 20$	9.9 %	$\langle \Delta E \rangle \approx 31.1 \text{ GeV}$
$8 \leq q_\perp \leq 12$			
$8 \leq E_1 \leq 15$	$8 \leq E_3 \leq 15$	1.1 %	$\langle \Delta E \rangle \approx 116.1 \text{ GeV}$

Table 4.1.: Mean energy loss for given cuts in q_\perp, E_1 and E_3 , cf. fig. 4.11. The percentage given in column 3 corresponds to the fraction of all events within these cuts relative to the total number of events. For reasons of readability the unit statement GeV is omitted for q_\perp, E_1 and E_3 .

Considering an $E = 400 \text{ GeV}$ jet-like gluon inside a thermal gluonic ($N_f = 0$) medium with $T = 0.4 \text{ GeV}$, $2 \rightarrow 3$ interactions having a low transverse momentum transfer, $0 \text{ GeV} \leq q_\perp \leq 3 \text{ GeV}$, and interactions having a rather high transverse momentum transfer, $8 \text{ GeV} \leq q_\perp \leq 12 \text{ GeV}$ are selected. Comparing with fig. 4.9a, the cut $0 \text{ GeV} \leq q_\perp \leq 3 \text{ GeV}$ roughly selects the peak region of the q_\perp distribution, while the cut $8 \text{ GeV} \leq q_\perp \leq 12 \text{ GeV}$ selects interactions from the tail of the distribution. Figure 4.11 then shows the color coded correlations between E_1 and E_3 for interactions whose transverse momentum transfer lies within these cuts.

For small values of the transverse momentum transfer that belong to the peak of the q_\perp distribution and are thus most probable, $0 \text{ GeV} \leq q_\perp \leq 3 \text{ GeV}$, two distinct regions in

the E_1 - E_3 plane are visible. The energy of the emitted gluon is quite high in all cases due to the strong preference of events with $y < 0$ caused by the LPM cutoff as discussed in section 3.1.4. One region features small energies E_1 , comparable to the value of q_\perp , while the other region is less pronounced and features large $E_1 \approx E_3$. For large values of the transverse momentum transfer, $8 \text{ GeV} \leq q_\perp \leq 12 \text{ GeV}$ only one distinct region emerges with both $E_1 \approx E_3$ being large. Table 4.1 lists the mean energy loss for events within these kinematical regions. and additionally gives the abundance of events within these regions relative to all events.

These investigations show that configurations where q_\perp and E_1 are small but E_3 , i.e. the energy of the radiated gluon in the c.m. frame, is large, yield an energy loss significantly above its most probable value. Thus these configurations contribute to the heavy tail observed in the distribution of the energy loss from $2 \rightarrow 3$ interactions, fig. 4.10. Since the radiated gluon is predominantly emitted into the backward hemisphere, cf. the discussion in section 3.1.4, there is a sizable share of configurations where due to momentum conservation the outgoing momenta of particles 1 and 2 both point into the forward hemisphere. Boosted back into the laboratory frame the available energy is thus mainly split between the particles 1 and 2 yielding a large energy loss. The same line of reasoning holds for cases where E_1 is on the order of E_3 , see the example in fig. 4.12g.

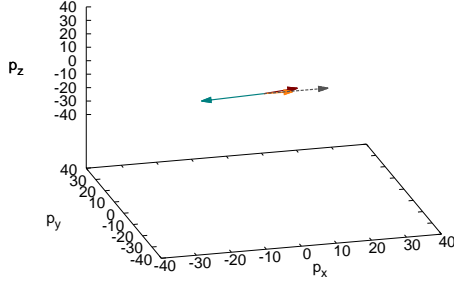
This illustrates that the tail in the ΔE_{23} distribution is mainly caused by configurations where in the center of momentum frame the radiated gluon is emitted with a large energy into the backward hemisphere and the remaining energy is split among the two other particles going into the forward hemisphere. Events with large q_\perp and k_\perp also yield a large energy loss but are significantly less probable due to the steeply falling $1/q_\perp^4$ contribution in the matrix element (3.13).

Illustration of randomly selected $2 \rightarrow 3$ events

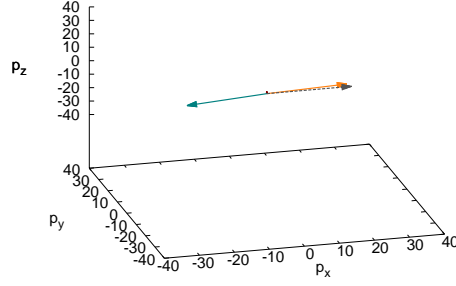
In order to further visualize the possible configurations of outgoing momenta in $2 \rightarrow 3$ interactions, figs. 4.12 and 4.12 illustrate some examples of $gg \rightarrow ggg$ events that have been randomly chosen according to the Gunion-Bertsch matrix element (3.13) including the LPM cutoff (3.17). These examples feature an incoming $E = 400 \text{ GeV}$ gluon jet that interacts with constituents from a thermal medium, $T = 0.4 \text{ GeV}$ and $N_f = 0$. All of these events are rotated such that the incoming jet momentum in the center of momentum frame points along the positive x direction and that the outgoing momentum \mathbf{p}_1 is in the x - y plane.

4.4. Conversion of jet partons

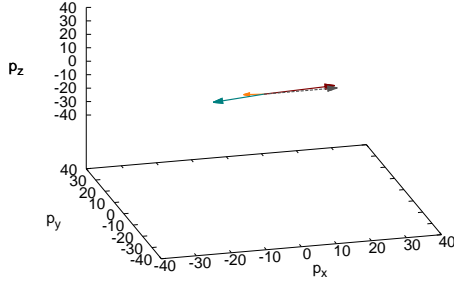
When adding light quark degrees of freedom to the model, the possibility of particle type conversions of jets needs to be taken into account in addition to the energy loss. When a high energy parton propagates through the medium it loses energy as detailed in sections 4.2 and 4.3 but the interactions with the medium might also change the type of the jet particle. Specifically, a quark jet might be converted into a gluon jet and vice versa. As in the previous sections no distinction is made between different quark flavors and their antiquarks for the purpose of this discussion since the possible interactions as given in section 3.4 are the same for all light quark flavors. As in section 4.2 jet particles are tagged according to their energy, cf. eqs. (4.4) and (4.5).



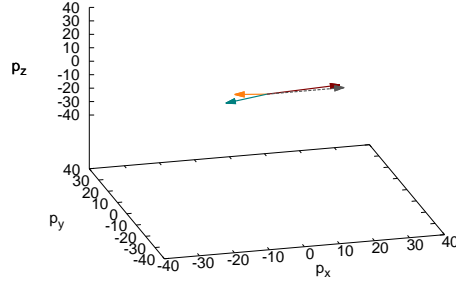
(a) $\Delta E = 175.94$ GeV,
 $\cos(\Theta_1) = 0.979$, $p_1 = (10.4, 10.2, 2.1, -0.0)$
 $\cos(\Theta_2) = 0.997$, $p_2 = (8.1, 8.0, -0.6, 0.2)$
 $\cos(\Theta_3) = -0.997$, $p_3 = (18.2, -18.2, -1.5, -0.2)$
 $(E_1^{\text{lab}}, E_2^{\text{lab}}, E_3^{\text{lab}}) = (224.1, 175.4, 1.4)$ GeV
 $q_{\perp} = 2.12$ GeV, $k_{\perp} = 1.50$ GeV



(b) $\Delta E = 20.30$ GeV,
 $\cos(\Theta_1) = 0.253$, $p_1 = (1.9, 0.5, 1.8, -0.0)$
 $\cos(\Theta_2) = 0.996$, $p_2 = (22.9, 22.8, 0.2, 1.9)$
 $\cos(\Theta_3) = -0.993$, $p_3 = (23.5, -23.3, -2.0, -1.9)$
 $(E_1^{\text{lab}}, E_2^{\text{lab}}, E_3^{\text{lab}}) = (19.3, 379.7, 2.9)$ GeV
 $q_{\perp} = 1.84$ GeV, $k_{\perp} = 2.79$ GeV

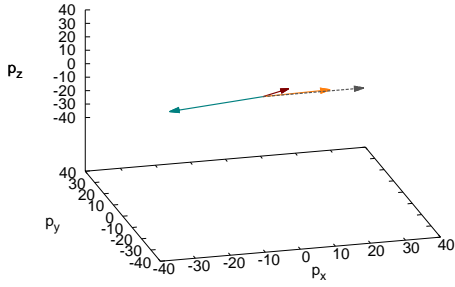


(c) $\Delta E = 2.63$ GeV,
 $\cos(\Theta_1) = 0.995$, $p_1 = (20.9, 20.8, 2.1, 0.0)$
 $\cos(\Theta_2) = -0.975$, $p_2 = (6.0, -5.8, -0.4, 1.3)$
 $\cos(\Theta_3) = -0.990$, $p_3 = (15.1, -14.9, -1.7, -1.3)$
 $(E_1^{\text{lab}}, E_2^{\text{lab}}, E_3^{\text{lab}}) = (397.4, 1.2, 2.8)$ GeV
 $q_{\perp} = 2.09$ GeV, $k_{\perp} = 2.14$ GeV

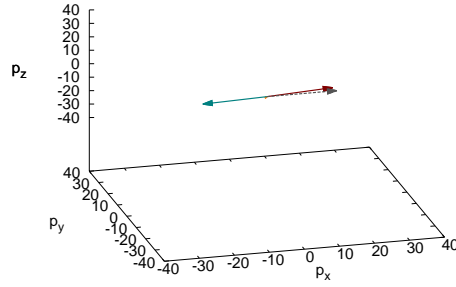


(d) $\Delta E = 8.16$ GeV,
 $\cos(\Theta_1) = 0.994$, $p_1 = (21.7, 21.5, 2.5, 0.0)$
 $\cos(\Theta_2) = -0.976$, $p_2 = (8.9, -8.6, 1.9, 0.1)$
 $\cos(\Theta_3) = -0.946$, $p_3 = (13.6, -12.9, -4.4, -0.1)$
 $(E_1^{\text{lab}}, E_2^{\text{lab}}, E_3^{\text{lab}}) = (391.8, 2.8, 6.7)$ GeV
 $q_{\perp} = 2.46$ GeV, $k_{\perp} = 4.39$ GeV

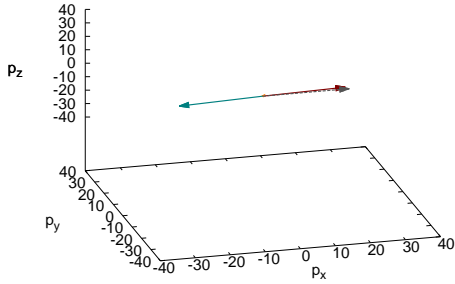
Figure 4.12.: Randomly selected $gg \rightarrow ggg$ events involving a gluon jet with $E = 400$ GeV (laboratory system) displayed in the c.m. frame ($T = 0.4$ GeV, $N_f = 0$). All events are rotated such that the incoming jet momentum (c.m.) points along the positive x-direction and that the outgoing momentum \mathbf{p}_1 is in the x - y plane. All kinematical values are given in the c.m. frame, except for the energies of the outgoing particles in the laboratory frame, $E_1^{\text{lab}}, E_2^{\text{lab}}, E_3^{\text{lab}} = \omega$. Part 1: Events 1 to 4 out of 8. Dark red: \mathbf{p}_1 , orange: \mathbf{p}_2 , blue: \mathbf{p}_3 (radiated), gray: \mathbf{p}_{jet} (incoming).



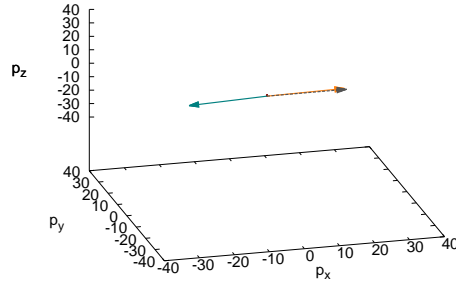
(e) $\Delta E = 132.30$ GeV,
 $\cos(\Theta_1) = 0.875$, $p_1 = (9.9, 8.7, 4.8, 0.0)$
 $\cos(\Theta_2) = 0.999$, $p_2 = (19.3, 19.3, 0.3, 0.5)$
 $\cos(\Theta_3) = -0.983$, $p_3 = (28.5, -28.0, -5.1, -0.5)$
 $(E_1^{\text{lab}}, E_2^{\text{lab}}, E_3^{\text{lab}}) = (130.8, 267.7, 3.8)$ GeV
 $q_{\perp} = 4.80$ GeV, $k_{\perp} = 5.17$ GeV



(f) $\Delta E = 6.90$ GeV,
 $\cos(\Theta_1) = 0.990$, $p_1 = (19.7, 19.6, 2.8, 0.0)$
 $\cos(\Theta_2) = -0.581$, $p_2 = (1.5, -0.9, -1.2, 0.1)$
 $\cos(\Theta_3) = -0.997$, $p_3 = (18.8, -18.7, -1.6, -0.1)$
 $(E_1^{\text{lab}}, E_2^{\text{lab}}, E_3^{\text{lab}}) = (393.1, 6.2, 1.7)$ GeV
 $q_{\perp} = 2.75$ GeV, $k_{\perp} = 1.56$ GeV



(g) $\Delta E = 12.06$ GeV,
 $\cos(\Theta_1) = 0.998$, $p_1 = (24.0, 24.0, 1.6, -0.0)$
 $\cos(\Theta_2) = 0.628$, $p_2 = (0.8, 0.5, 0.6, 0.1)$
 $\cos(\Theta_3) = -0.996$, $p_3 = (24.5, -24.5, -2.2, -0.1)$
 $(E_1^{\text{lab}}, E_2^{\text{lab}}, E_3^{\text{lab}}) = (387.9, 9.7, 5.1)$ GeV
 $q_{\perp} = 1.59$ GeV, $k_{\perp} = 2.18$ GeV



(h) $\Delta E = 16.26$ GeV,
 $\cos(\Theta_1) = 0.311$, $p_1 = (1.5, 0.5, 1.4, -0.0)$
 $\cos(\Theta_2) = 0.987$, $p_2 = (21.8, 21.5, -2.2, 2.7)$
 $\cos(\Theta_3) = -0.992$, $p_3 = (22.2, -22.0, 0.8, -2.7)$
 $(E_1^{\text{lab}}, E_2^{\text{lab}}, E_3^{\text{lab}}) = (16.1, 383.7, 2.1)$ GeV
 $q_{\perp} = 1.40$ GeV, $k_{\perp} = 2.85$ GeV

Figure 4.12.: Randomly selected $gg \rightarrow ggg$ events involving a gluon jet with $E = 400$ GeV (laboratory system) displayed in the c.m. frame ($T = 0.4$ GeV, $N_f = 0$). All events are rotated such that the incoming jet momentum (c.m.) points along the positive x-direction and that the outgoing momentum \mathbf{p}_1 is in the x - y plane. All kinematical values are given in the c.m. frame, except for the energies of the outgoing particles in the laboratory frame, $E_1^{\text{lab}}, E_2^{\text{lab}}, E_3^{\text{lab}} = \omega$. Part 2: Events 5 to 8 out of 8. Dark red: \mathbf{p}_1 , orange: \mathbf{p}_2 , blue: \mathbf{p}_3 (radiated), gray: \mathbf{p}_{jet} (incoming).

The conversion of the type of a jet particle might in principle be caused by $2 \rightarrow 2$ interactions, for example the process $gg \rightarrow q\bar{q}$ could turn a gluon jet into a quark jet. It turns out however, that the contribution of $2 \rightarrow 2$ processes to the conversion rates of high energy particles is negligible. This is due to the fact that s -channel processes such as $gg \rightarrow q\bar{q}$ are suppressed by $1/s$ and in all other $2 \rightarrow 2$ processes the particle types associated with the incoming momenta p_A and p_B cannot reverse roles due to the underlying t -channel processes that favor small angle scatterings.

It is thus $2 \rightarrow 3$ interactions that are mainly responsible for conversions of high energy partons within BAMPS. There are basically two mechanisms that can cause such conversions in $2 \rightarrow 3$ processes.

1. When due to momentum conservation the outgoing momenta p_1 and p_2 both point into the forward hemisphere with respect to the original jet direction, it is not a priori clear which of the two emerges with the highest energy in the laboratory frame and is thus considered the new jet particle according to eq. (4.4). See the discussion in section 4.3. In a $gq \rightarrow gqg$ process for example, the momentum p_A might be associated with an incoming gluon jet, while after the interaction particle 2 emerges with the highest energy, which then is a quark.
2. Though for high jet energies the radiated gluon is predominantly emitted into the backward direction as discussed in sections 3.1.4 and 4.3, there is a finite probability that the gluon is emitted into the forward direction and actually acquires the highest energy of the outgoing particles in the laboratory frame, $E_{\max} = \omega$. This would convert a quark jet into a gluon jet.

For asymptotically high jet energies the second mechanism is very unlikely, but for smaller jet energies the fraction of $2 \rightarrow 3$ interactions in which the radiated gluon acquires the highest outgoing energy in the laboratory frame is sizable as illustrated in fig. 4.13a. For $E = 50$ GeV it is roughly 4%, while for a jet energy of $E = 15$ GeV the fraction is already roughly 15%. As was to be expected this effect does not depend on the type of the incoming jet particle. The energy loss associated with such configurations is also distinctly above the mean energy loss, for $E = 50$ GeV the mean energy loss per interaction is roughly $\langle \Delta E_{23} \rangle \approx 11$ GeV, while it is $\langle \Delta E_{23} \rangle_{\text{conversion}} \approx 22$ GeV for configurations in which the radiated gluon is the outgoing jet particle. The medium parameters for the numbers given above are $T = 0.4$ GeV and $N_f = 3$.

While for conversions according to the first mechanism the ratio of jet conversions $g \rightarrow q$ to $q \rightarrow g$ does only depend on the ratio of the gluon and quark densities and is 1 for a medium with $n_g = n_q + n_{\bar{q}}$, the second mechanism only converts quarks into gluon jets and thus introduces an asymmetry in favor of $q \rightarrow g$ conversions. This is clearly visible in fig. 4.13b, which shows the probability that a gluon (quark) jet with initially $E_0 = 40$ GeV has not converted⁴ after propagating for $\Delta t = 1$ fm c^{-1} through a static medium at $T = 0.4$ GeV. The gluon fugacity is held at $n_g/n_g^{\text{eq}} = 1$, while the quark and antiquark fugacity is varied. The conversion probability $q \rightarrow g$ is larger than the conversion probability for $g \rightarrow q$ for the entire region $n_q/n_q^{\text{eq}} = n_{\bar{q}}/n_{\bar{q}}^{\text{eq}} < 1$ that is relevant for the medium created in heavy ion collisions. As was to be expected, the discrepancy is strongest for a medium in which

⁴Or has converted back.

$n_q = n_{\bar{q}} = 0$, but even for a system in full thermal and chemical equilibrium the conversion of a quark jet into a gluon jet is more likely than the conversion of a gluon jet into a quark jet due to the second mechanism described above.

4.5. Momentum broadening of jet partons

A quantity that is often used to characterize the effect of the medium on a jet-like particle is \hat{q} . It is defined as the sum of the transverse momentum transfers squared divided by the path length L the particle has traveled

$$\hat{q}(L) = \frac{1}{L} \sum_i (\Delta p_{\perp}^2)_i, \quad (4.11)$$

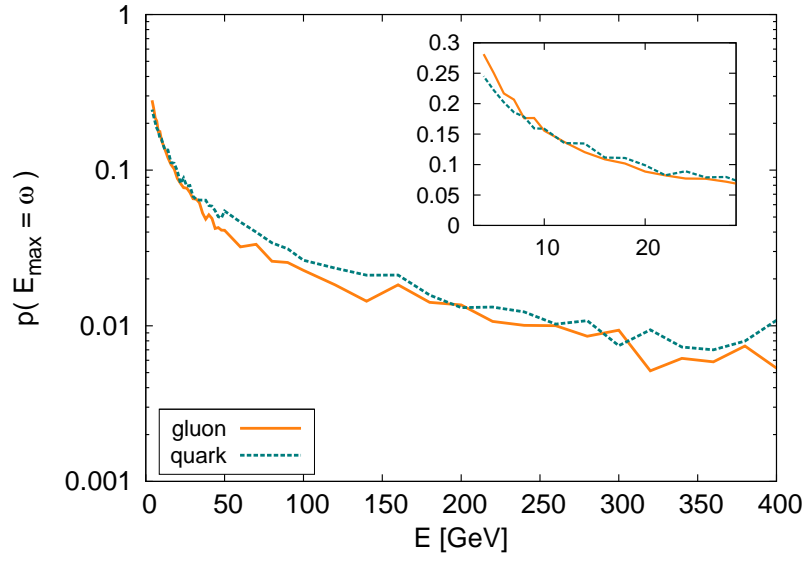
where i runs over all collisions the particle has undergone within the path length L . Since the partons considered here are taken to be massless, the problem can be simplified by using the time t instead of L from now on. Alternatively, if one knows the average momentum transfer squared per mean free path as a function of the jet energy one can compute the mean value of \hat{q} as

$$\langle \hat{q} \rangle(t) = \frac{1}{t} \int_0^t \left. \frac{\langle \Delta p_{\perp}^2 \rangle}{\lambda} \right|_{E(\tilde{t})} d\tilde{t}. \quad (4.12)$$

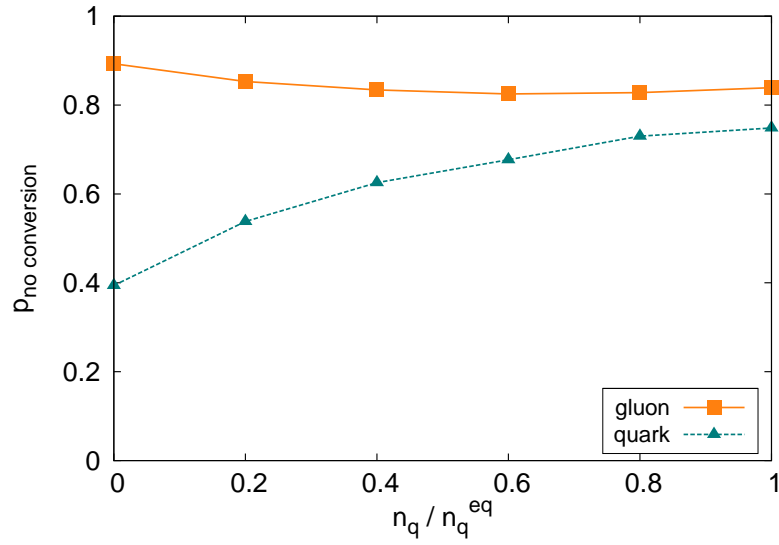
Typically \hat{q} is used to quantify the transverse momentum picked up from elastic collisions that eventually induce the radiation of bremsstrahlung gluons. In the commonly used eikonal approximation the jet particle acquires no additional transverse momentum from the radiation of gluons. In the approach presented here, however, radiative and elastic interactions are treated on equal grounds and jets can also pick up transverse momentum in inelastic $2 \rightarrow 3$ processes. In the following, the definition of \hat{q} as given above is therefore naturally extended to also describe the evolution of transverse momentum due to inelastic processes within BAMPS.

As a cross-check the result from both approaches, eqs. (4.11) and (4.12), have been compared using independent calculations and perfect agreement was found. Figure 4.14a shows the average momentum transfer squared per mean free path $\langle \Delta p_{\perp}^2 \rangle / \lambda$ as a function of the jet energy in a gluonic medium ($N_f = 0$) with $T = 0.4$ GeV. A logarithmic behavior at large energies can be seen for $\langle \Delta p_{\perp}^2 \rangle / \lambda$ from binary $gg \rightarrow gg$ interactions, with $\langle \Delta p_{\perp}^2 \rangle / \lambda \approx 2.3 \text{ GeV}^2 \text{ fm}^{-1}$ at $E = 50$ GeV rising to $\langle \Delta p_{\perp}^2 \rangle / \lambda \approx 3.7 \text{ GeV}^2 \text{ fm}^{-1}$ at $E = 400$ GeV. As reflected in the differential energy loss, the average transverse momentum transfer squared per mean free path for inelastic $gg \rightarrow ggg$ interactions is much higher, $\langle \Delta p_{\perp}^2 \rangle / \lambda \approx 22.8 \text{ GeV}^2 \text{ fm}^{-1}$ at $E = 50$ GeV and $\langle \Delta p_{\perp}^2 \rangle / \lambda \approx 64.2 \text{ GeV}^2 \text{ fm}^{-1}$ at $E = 400$ GeV, while the gluon annihilation processes $ggg \rightarrow gg$ virtually do not contribute at all. Note that these results have been obtained prior to implementing the constraint from the small angle approximation for $2 \rightarrow 3$ processes as discussed in section 3.1.3. However, the discussion in section 3.1.3 also shows that the effect on \hat{q} and $\langle \Delta p_{\perp}^2 \rangle / \lambda$ would be rather mild, on the order of 15%, mostly stemming from the change in the mean free path and giving no qualitative deviation.

Figure 4.14b shows $\langle \hat{q} \rangle$ as defined in equations eqs. (4.11) and (4.12) as a function of the path length $L = t$ for a gluon jet with initial energy $E_0 = 50$ GeV. As before, the

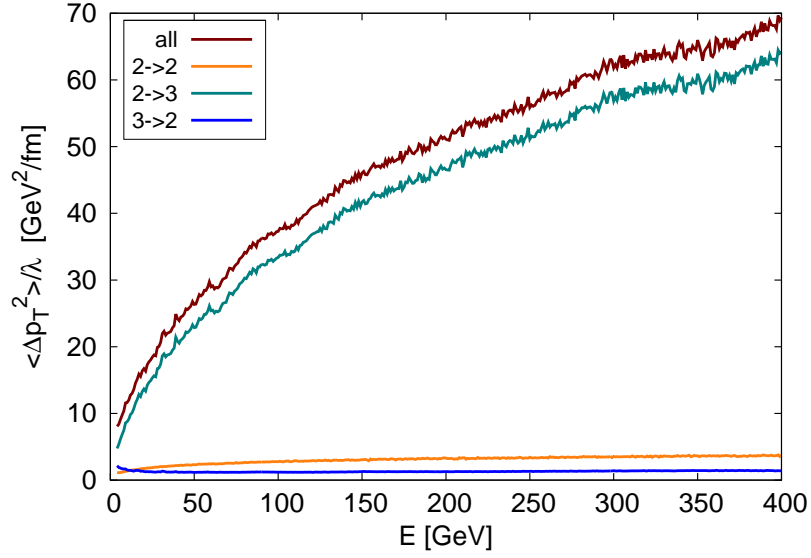


(a) Probability that the radiated gluon in a $2 \rightarrow 3$ process carries away the largest energy, $E_{\max} = \omega$, as a function of jet energy for gluon and quark jets. $T = 0.4 \text{ GeV}$, $N_f = 3$.

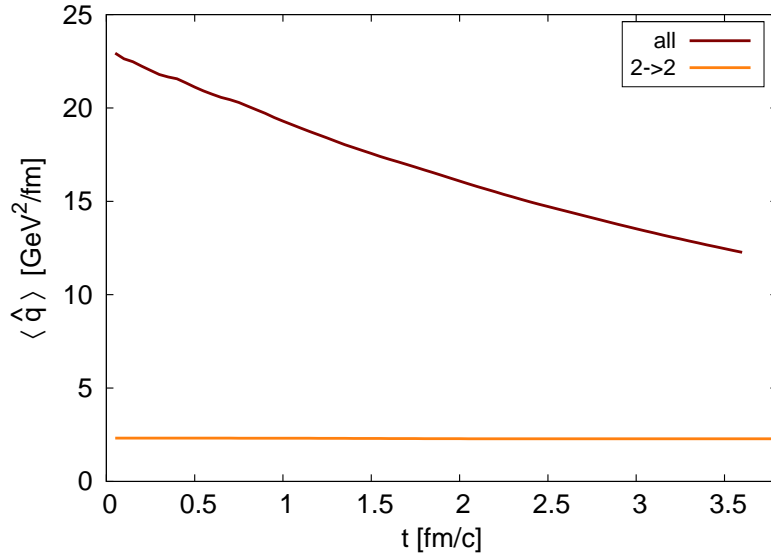


(b) Probability that a gluon (quark) starting with $E_0 = 40 \text{ GeV}$ is a gluon (quark) after propagating through a static medium for $\Delta t = 1 \text{ fm } c^{-1}$ as a function of the quark and antiquark fugacity $n_q/n_q^{\text{eq}} = n_{\bar{q}}/n_{\bar{q}}^{\text{eq}}$ with $n_q = n_{\bar{q}} = 6N_f \frac{T^3}{\pi^2}$. All $2 \rightarrow 2$ and $2 \leftrightarrow 3$ processes according to eqs. (3.80) and (3.85) are taken into account. $T = 0.4 \text{ GeV}$, $N_f = 3$.

Figure 4.13.: Particle type conversions of jet partons traversing a static medium.



(a) Average transverse momentum transfer squared per mean free path, $\langle \Delta p_T^2 \rangle / \lambda$, for $gg \rightarrow gg$, $gg \rightarrow ggg$, $ggg \rightarrow gg$ and for the sum of all processes.



(b) $\langle \hat{q} \rangle(t)$ as defined in eqs. (4.11) and (4.12) for $gg \rightarrow gg$ processes only and for all processes ($N_f = 0$) as a function of the path length $L = t$ for a gluon jet with initial energy $E_0 = 50$ GeV.

Figure 4.14.: Transverse momentum broadening of high energy gluons in a static medium with $T = 0.4$ GeV and $N_f = 0$.

medium is characterized by $T = 0.4 \text{ GeV}$ and $N_f = 0$. Over the range up to $t = 3.5 \text{ fm } c^{-1}$ shown in fig. 4.14b, the contribution from elastic interactions is almost constant at $\langle \hat{q} \rangle_{22} \approx 2.3 \text{ GeV}^2 \text{ fm}^{-1}$. For jets that interact only via binary $gg \rightarrow gg$ processes one finds that $\langle \hat{q} \rangle_{22}$ is actually slowly and linearly falling to $\langle \hat{q} \rangle_{22} \approx 1.9 \text{ GeV}^2 \text{ fm}^{-1}$ at $t = 50 \text{ fm } c^{-1}$. The combined $\langle \hat{q} \rangle$ is dominated by the radiative $gg \rightarrow ggg$ contribution and starts at $\langle \hat{q} \rangle \approx 23 \text{ GeV}^2 \text{ fm}^{-1}$, falling to $\langle \hat{q} \rangle \approx 12.5 \text{ GeV}^2 \text{ fm}^{-1}$ at $t = 3.5 \text{ fm } c^{-1}$. This indicates that the negligence of transverse momentum pick-up in radiative processes might indeed be an oversimplification.

The numbers for \hat{q} found in this work are well within the range of values found by other theoretical energy loss schemes, though the comparison is difficult since \hat{q} in these calculations often is a free parameter or related to free parameters. Fitting to experimental data the authors of [BGM⁺09] have found \hat{q}_0 for the central region of Au + Au at $\tau_0 = 0.6 \text{ fm } c^{-1}$, where conditions should be roughly comparable to the setup used in this section, to be ranging from $2.3 \text{ GeV}^2 \text{ fm}^{-1}$ based on the Higher Twist approach [MNB07], over $4.1 \text{ GeV}^2 \text{ fm}^{-1}$ based on the approach by ARNOLD, MOORE and YAFFE (AMY) [QRT⁺07], up to $18.5 \text{ GeV}^2 \text{ fm}^{-1}$ based on the approach by ARMESTO, SALGADO and WIEDEMANN (ASW) [RRNB07]. In [CGW⁺10] the application of the Higher Twist approach to jet quenching data yields $\hat{q}_0 \approx 3.2 \text{ GeV}^2 \text{ fm}^{-1}$ for a medium evolution based on BAMPS (employing $\tau_0 = 0.3 \text{ fm } c^{-1}$), while a hydro based medium evolution yields $\hat{q}_0 \approx 0.9 \text{ GeV}^2 \text{ fm}^{-1}$ ($\tau_0 = 0.6 \text{ fm } c^{-1}$).

5. Simulations of heavy ion collisions

In this chapter results for the quenching of high- p_T particles and for the elliptic flow obtained from fully dynamic simulations of heavy ion collisions within the partonic transport model BAMPS including gluon and light quark degrees of freedom are presented and compared to experimental data in sections 5.4 and 5.5. These calculations focus on Au + Au collisions at 200 A GeV as predominantly studied at RHIC. In section 5.7 first results for Pb + Pb collisions at 2.76 A TeV, the energy of the first LHC heavy ion run, are presented. The partonic results in the high- p_T regime from calculations within the BAMPS framework are converted into hadronic observables using fragmentation functions as detailed in section 5.3. Additionally, section 5.6 explores the sensitivity of the results on the implementation of the LPM effect. To begin with, however, section 5.1 offers a short introduction to the phenomenology of jet quenching and elliptic flow as observed at the Relativistic Heavy Ion Collider and to its theoretical assessment.

5.1. High- p_T physics and elliptic flow in ultra-relativistic heavy ion collisions

5.1.1. Jet quenching

As already briefly discussed in the introduction, elliptic flow and jet quenching are two key observables of the quark-gluon plasma that have been, and still are, extensively studied at RHIC and are of course equally crucial to the recently started heavy ion program at the LHC. This section briefly summarizes the experimental status and important theoretical frameworks. See for example [MN06, AAB⁺10] for in-depth reviews of the experimental findings and their theoretical assessment.

It has been established early by the experiments at the Relativistic Heavy Ion Collider that particles with high transverse momenta are suppressed in heavy ion collisions with respect to a scaled p + p reference [STAR02, PHENIX02]. This phenomenon is called jet quenching [GW94] and commonly quantified in terms of the nuclear modification factor

$$R_{AA} = \frac{d^2 N_{AA}/dy dp_T}{T_{AA} d^2 \sigma_{NN}/dy dp_T}, \quad (5.1)$$

where T_{AA} is the nuclear overlap function, commonly determined from Glauber calculations, and σ_{NN} is the nucleon-nucleon cross section that is commonly taken as $\sigma_{NN} = 42$ mb for RHIC energies [STAR03] and as $\sigma_{NN} = 64$ mb for LHC collisions at 2.76 A GeV [ALICE11]. Since the number of binary collisions is given by $N_{\text{coll}} = T_{AA} \sigma_{NN}$ the nuclear modification factor compares the yields from heavy ion collisions to an appropriately scaled p + p reference and any deviation of the nuclear modification factor from $R_{AA} = 1$ indicates initial or final state nuclear effects. At large transverse momentum the modification of particle

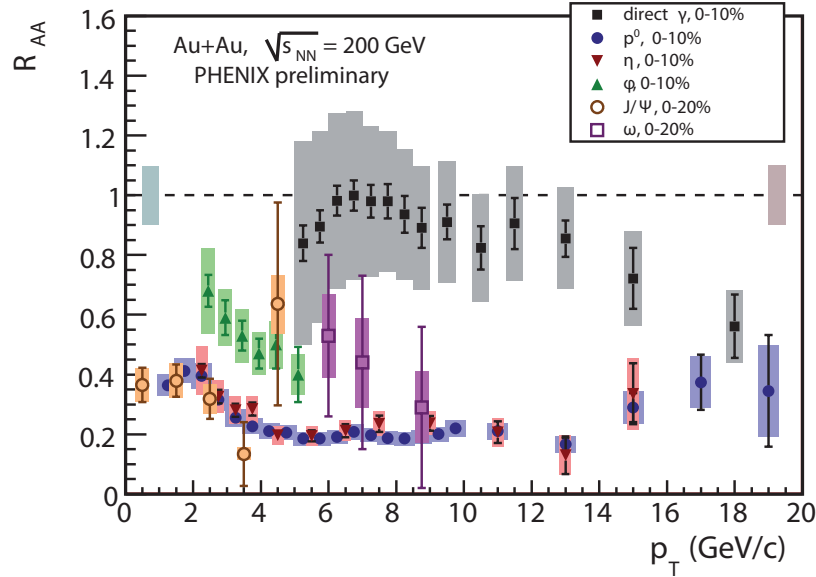


Figure 5.1.: Compilation of the nuclear modification factor R_{AA} for various identified hadrons and for direct photons from Au + Au at 200 A GeV as measured by PHENIX. Figure from [PHENIX08b].

yields is expected to be caused by the hot and dense medium created in the violent heavy ion collisions, the quark-gluon plasma. Experiments observe a strong suppression of various types of hadrons, with $R_{AA} \approx 0.2$ for pions and charged hadrons in central Au + Au collisions at 200 A GeV. See fig. 5.1 for a compilation of various measurements of the nuclear modification factor for central Au + Au collisions. Measurements of d + Au confirm that this quenching of high- p_T particles is indeed caused by medium effects [STAR05a, PHENIX05]. Additionally, the nuclear modification factor of direct photons is compatible with $R_{AA} = 1$, see fig. 5.1, which would serve as a further reference since photons do not couple strongly to a partonic (or hadronic) medium¹. The above mentioned findings also hold in measurements at distinctly larger collision energies at the LHC, see section 5.7 for more details.

The observed quenching of high- p_T particles is commonly attributed to an energy loss on the partonic level as the parton jets produced in initial hard interactions traverse the hot medium, the quark-gluon plasma, that is created in the early stages of such extremely violent heavy ion collisions. Due to the large momentum scales the energy loss of partonic jets can be treated on grounds of perturbative QCD with the main contribution to the energy loss of light partons being commonly attributed to radiative processes. The computation of partonic energy loss by medium induced gluon radiation is addressed by several theoretical formalisms. The four most important frameworks, upon which many more approaches are based, go by the names of *BDMPS*², *GLV*³, *Higher-twist* and *AMY*⁴.

BDMPS [Zak96, BDM⁺97, BDMS98] and GLV [GLV00b, GLV01, GLV00a, WHDG07]

¹However, the measurement of direct photons is extremely challenging and so far no final data on photonic R_{AA} is available.

²After the names of the original authors: BAIER, DOKSHITZER, MUELLER, PEIGNE and SCHIFF.

³After the names of the original authors: GYULASSY, LEVAI and VITEV.

⁴After the names of the original authors: ARNOLD, MOORE and YAFFE.

are both based on expansions in opacity, or the number of collisions, $n = L/\lambda$, where L is the medium length and λ the partonic mean free path. BDMPS has been the first framework to describe gluon radiation induced by multiple scatterings in hot QCD matter. It is derived in the limit of large opacity, $n \gg 1$, basically assuming an infinite medium length L . The typical momentum transferred from the (static) scattering centers that represent the medium is given by the Debye mass. The medium in this approach is naturally characterized in terms of the transport coefficient $\hat{q} = m_D/\lambda$. GLV originally worked in the limit of one hard scattering [GLV00b], i.e. the small opacity limit, $n = 1$, but the approach has later been extended to give the radiated gluon spectrum at any opacity [GLV01, GLV00a]. In the GLV formalism the medium is naturally characterized in terms of the density of scattering centers, determined by the initial gluon density dN_g/dy . Both formalism have later been used to compute so called quenching weights, basically energy loss probability distributions, that are well suited for numerical evaluation of energy loss [SW03, ASW04, EHSW05].

The higher-twist formalism [WG01, MWW07] has first been developed in the context of deep inelastic scattering and later been applied to hot QCD matter created in heavy ion collisions. It is based on an expansion in powers of $1/Q^2$, where Q determines the virtuality of the emitted gluons. The approach is valid for $E \gg Q \gg m_D$, where E is the energy of the jet parton. The AMY formalism [AMY01b, AMY01a] is based on a description of finite temperature QCD matter within thermal field theory aimed at computing thermal photon production. It has later been extended to describe gluon radiation from hard particles, that have energies on the order of T as opposed to medium that is described by modes with gT . The approach is thus valid for large temperatures where hard and soft scales are well separated, $T \gg gT \gg g^2T$. The extended version of the AMY formalism then allows for the computation of the energy loss of leading partons [JM05].

All these approaches can be tuned to fit the observed level of jet quenching, for example by tuning the transport coefficient \hat{q} in the case of the BDMPS-based computations or the gluon density dN_g/dy in the case of GLV-based computations. All approaches coincide in that the experimentally observed quenching of jets requires a dense medium and/or large transport coefficients. The quantitative comparison of the formalisms however is difficult, although more and more efforts are being made to compare different models based on a common implementation of the medium evolution. See for example [BGM⁺09, QRT⁺07, BGM⁺08]. Based on such comparisons the value of the transport coefficient extracted from different formalisms varies widely and roughly ranges from $\hat{q} = 2 \text{ GeV}^2 \text{ fm}^{-1}$ to $\hat{q} = 20 \text{ GeV}^2 \text{ fm}^{-1}$. Compare the discussion in section 4.5 for more details.

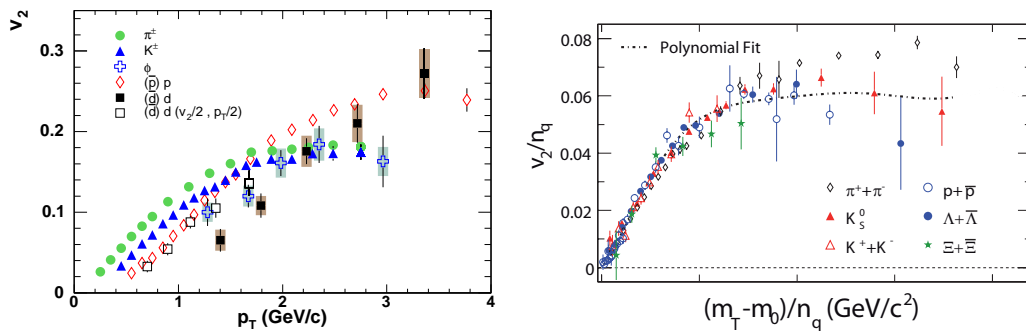
Measurements of electrons from semi-leptonic decays of D - and B -mesons indicate that the quenching of heavy quarks is comparable to that of light partons [PHENIX06, STAR07a, PHENIX07a]. This has come as a surprise since within the radiative frameworks mentioned above, mesons from heavy quarks are expected to lose less energy than hadrons from light quarks and gluons due to the so-called dead cone effect [DK01] and due to the absent contribution from gluon jets that are supposed to be more strongly suppressed. The observed suppression of heavy quarks has thus revived the interest in alternative energy loss scenarios and most importantly in collisional contributions to the energy loss [Mus05, WHDG07, Djo06].

5.1.2. Elliptic flow

In non-central heavy ion collisions the initial spatial asymmetry, often referred to as *almond shape*, causes pressure gradients that translate the spatial asymmetry into an anisotropy in the momentum distribution. The strength of this translation depends on the characteristics of the medium and can be used to deduce collective properties of the medium. The momentum anisotropy is commonly quantified in terms of a Fourier decomposition of the azimuthal dependence of the particle yield

$$E \frac{d^3 N}{d^3 p} = \frac{1}{2\pi} \frac{d^2 N}{dy dp_T} \left(1 + \sum_{n=1}^{\infty} 2v_n \cos [n(\phi - \Psi_R)] \right), \quad (5.2)$$

where Ψ_R is the angle of the reaction plane. The Fourier coefficient v_2 , the elliptic flow, is then used to quantify the collectivity of the medium as a response to the initial spatial anisotropy and the resulting pressure gradients.



(a) Elliptic flow of identified hadrons as a function of transverse momentum, $v_2(p_T)$, from 20% to 60% central Au + Au collisions (200 A GeV) at RHIC as measured by PHENIX. Figure from [PHENIX07d]. (b) Elliptic flow from minimum bias Au + Au collisions at 62.4 A GeV scaled by the number of valence quarks as measured by STAR. Figure from [STAR07b].

Figure 5.2.: Elliptic flow of identified hadrons measured at RHIC.

Experiments at RHIC have established that the collective flow of matter created in high energy heavy ion collisions is indeed rather strong [STAR05a, PHENIX05, PHOBOS05b]. The elliptic flow coefficient v_2 of identified hadrons reaches values of $v_2 \approx 0.15$ to 0.25, cf. fig. 5.2a. As already discussed in section 2.3 these values are in good agreement with calculations employing ideal hydrodynamics [HKH⁺01, KH03] or hydrodynamics with a small shear viscosity [RR07], indicating strong interactions among the medium constituents. The observed v_2 scales with the number of valence quarks as illustrated by fig. 5.2b. This strongly indicates that the elliptic flow, or at least the main part of the elliptic flow, is indeed built up during the partonic phase of the medium evolution.

Recent measurements at RHIC have extended the range of differential $v_2(p_T)$ of neutral pions up to $p_T \approx 10$ GeV [PHENIX09a]. The elliptic flow exhibits a maximum at $p_T \approx 3$ GeV and a subsequent slow decrease towards larger momenta. The data indicates that within the observed p_T -range v_2 does not yet fully saturate as would be the case for an elliptic flow that is purely given by an azimuthally dependent jet suppression.

First results on the collective flow of charged hadrons from Pb+Pb collisions at the LHC at 2.76 A GeV have very recently become available [ALICE10b]. Within experimental uncertainties no significant change in the differential $v_2(p_T)$ with respect to the RHIC results is observed up to $p_T \approx 5$ GeV. The integrated v_2 increases by about 30% with respect to the RHIC results due to the increased mean value of p_T . The similarity of elliptic flow at RHIC and LHC is consistent with predictions from ideal [NER09, KH09] and also from viscous [SJG11a] hydrodynamics, however the detailed microscopic reasons for the similarity between RHIC and LHC, both in models and experiment, still needs to be systematically investigated.

5.2. Setup for simulations of heavy ion collisions with BAMPS

5.2.1. Initial parton distribution and technical setup

Initial parton distributions from the mini-jet model and from Pythia

The choice of the initial parton distribution for simulations of heavy ion collisions within the BAMPS framework is in principle detached from the subsequent evolution of the medium. Thus, different models for the initial parton distribution can be combined with BAMPS. In this work, the mini-jet model [KLL87, EKL89] is used for simulations of heavy ion collisions at RHIC energies, presented in sections 5.4 and 5.5, while initial conditions based on the event generator PYTHIA [SMS06] are used for simulations at LHC energies, presented in section 5.7.

In the mini-jet model the initial distribution is generated by hard scatterings of partons from the incoming nucleons according to [WG91]

$$\frac{d\sigma_{jet}}{dp_T^2 dy_1 dy_2} = K \sum_{a,b} x_1 f_a(x_1, p_T^2) x_2 f_b(x_2, p_T^2) \frac{d\sigma_{ab}}{dt}, \quad (5.3)$$

where x_1 and x_2 are the fractions of the light-cone momentum carried by the initial partons, y_1 and y_2 are the rapidities of the scattered partons and f_a and f_b are the parton distribution functions (PDF) of the incoming nucleons. In this work a parametrization of the PDFs by GLÜCK, REYA and VOGT (GRV) [GRV95] is employed. Leading order pQCD is used for the differential parton-parton cross section $d\sigma_{ab}/dt$ and a phenomenological scaling factor $K = 2$ is included to effectively account for higher-order corrections to the cross sections. Produced partons are assigned a formation time $\Delta t_f = \cosh y/p_T$ during which they are considered to be off-shell and do thus not interact within the BAMPS framework. A lower momentum cutoff $p_0 = 1.4$ GeV on the initial mini-jet spectrum is introduced such that the final transverse energy density dE_T/dy is in accordance with experimental results [XG09]. The number of initial mini-jets from eq. (5.3) is scaled by the number of binary collisions $N_{coll} = T_{AA} \sigma_{NN}$, cf. section 5.1.1. See [XG05, XG09, Foc06, FXG10] for more details on this choice of the initial conditions and its implementation within the BAMPS framework.

The PYTHIA initial parton distributions used for simulations of Pb+Pb collisions at 2.76 A GeV have been kindly provided by Jan UPHOFF, details on the implementation can be found in [UFXG10a]. PYTHIA generates particles from hard and from soft events whose scaling behavior is different when going from p+p to a heavy ion collision. The yield from hard processes scales with N_{coll} as in the mini-jet model, while the scaling of the yield from

soft processes is determined from energy conservation, giving a scaling factor that is on the order of the number of participants N_{part} . Note that in contrast to the scaling employed for the initial conditions from the mini-jet model, the number of binary collisions is effectively reduced in this approach to account for shadowing effects [UFXG10a]. Nonpartonic particles from the generation via PYTHIA, mostly diquarks, excited nucleons or beam remnants, are discarded prior to the medium evolution within BAMPS.

In both approaches the geometry, i.e. the spatial sampling of production points for the partons from the initial distributions, is given by the Glauber model [MRSS07] from the overlap of Woods-Saxon distributions of the colliding nuclei

$$n_A(r) = \frac{n_0}{1 + e^{(r-R_A)/d}}, \quad (5.4)$$

with $n_0 = 0.17 \text{ fm}^{-3}$, $d = 0.54 \text{ fm}$ and $R_A = 6.37 \text{ fm}$ for Au nuclei and $R_A = 6.62 \text{ fm}$ for Pb nuclei.

Cell structure and number of test particles

The number of test particles is chosen for every impact parameter such that the total number of initial particles in the system is roughly always the same, on the order of 250 000. For simulations of Au + Au collisions at 200 A GeV with three flavors of light quarks, $N_f = 3$, the number of test particles thus ranges from $N_{\text{test}} = 70$ for $b = 0 \text{ fm}$ to $N_{\text{test}} = 464$ for $b = 9.6 \text{ fm}$. $N_{\text{test}} = 20$ is used for Pb + Pb collisions at 2.76 A TeV and $b = 0 \text{ fm}$, while for the sake of computing time the total number of initial particles in simulations of Pb + Pb at $b = 8.2 \text{ fm}$ is only on the order of 140 000, requiring $N_{\text{test}} = 45$.

In the transverse plane the cells that are used for the stochastic algorithm as described in section 3.1 have a fixed size $\Delta x = \Delta y = 0.2 \text{ fm}$ for simulations of Au + Au collisions at 200 A GeV and $\Delta x = \Delta y = 0.3 \text{ fm}$ for simulations of Pb + Pb at 2.76 A TeV. In the longitudinal direction the cell size is dynamically adjusted in space-time rapidity η such that the number of particles in each cell is roughly the same, with a target particle number of 10 test particles per cell. This procedure leads to approximately equally sized bins in the longitudinal direction, indicating an almost Bjorken-type expansion [XG09]. For the setup used in this work, the size of the cells in the longitudinal direction ranges from $\Delta\eta \approx 0.4$ for $b = 0 \text{ fm}$ to $\Delta\eta \approx 0.05$ for $b = 9.6 \text{ fm}$ for Au + Au collisions at 200 A GeV and is roughly $\Delta\eta = 0.3$ to 0.4 for the simulations of Pb + Pb at 2.76 A TeV.

Hadronization and freezeout criterion

Since only the partonic stage of the evolution of the medium can be simulated within BAMPS, a criterion for the termination of this partonic stage needs to be defined. This is done by choosing a critical local energy density ε_c . Partonic interactions are stopped in regions where the local energy density drops below ε_c . As currently no general-purpose hadronization scheme and no treatment of the hadronic stage is implemented within the BAMPS framework—cf. section 5.3 for hadronization of high- p_T partons via fragmentation though— ε_c determines the freezeout condition. Unless otherwise noted, the critical energy density is set to $\varepsilon_c = 0.6 \text{ GeV fm}^{-3}$ throughout this work. Future versions of BAMPS might feature a hadronization scheme via the Cooper-Frye prescription [PSB⁺08] and a

subsequent evolution of the hadronic medium with a hadronic transport approach, such as UrQMD [BBB⁺98, BZS⁺99], in order to model possible effects of the hadronic stage and the kinetic and chemical freezeout in more detail.

5.2.2. Simulation strategy for high- p_T observables

Due to the steeply falling parton spectra, cf. section 5.3, the production of particles at large transverse momenta is extremely rare. For example, using the mini-jet model for the initial parton distribution as described in section 5.2.1 together with the parameters from section 5.3 and appendix E, the fraction of initial produced gluons with $p_T > 10$ GeV in a Au + Au collision with $b = 3.4$ fm (0%–10% central) is only $P(p_T > 10 \text{ GeV}) \approx 2.7 \cdot 10^{-6}$. Gluons above 20 GeV are even rarer by two orders of magnitude, $P(p_T > 20 \text{ GeV}) \approx 2.9 \cdot 10^{-8}$. This presents a considerable challenge to the investigation of high- p_T observables within a transport model. In principle the following strategies to study observables at large p_T are conceivable:

Strategy 1

Compute a large number of events without any bias to obtain sufficient statistics for high- p_T observables. This is what is naturally done in experiment. For comparison, in the 2007 RHIC run the PHENIX experiment has recorded almost $5.5 \cdot 10^9$ minimum bias events [PHENIX09b, Fis10].

Strategy 2

Compute only a limited number of events that are known to contain high- p_T particles and have been selected according to a given criterion. The results need then to be recombined using appropriate weighting factors. In mathematical terms, this strategy is a type of importance sampling.

Strategy 3

Separate the simulation of high- p_T particles from the computation of the evolution of the medium. In this strategy an artificially large number of high- p_T particles is superimposed on the evolution of the bulk medium. The latter can be obtained from recorded results of few, in the most extreme case: one, randomly chosen simulated event(s).

With simulation times for a single event that—depending on the cell size, the number of test particles, etc.—range from several hours to a couple of days, strategy 1 is clearly infeasible. Importance sampling, strategy 2, is described in more detail in [Foc06] and has been used for the computation of the results presented in [FXG09, FXG10]. However, even within this strategy on the order of 1000 events need to be simulated for a given impact parameter in order to obtain sufficient statistics up to $p_T \approx 30$ GeV. Therefore the results presented in this work are based on strategy 3.

Technically this strategy is implemented as follows: in order to compute high- p_T observables at a given impact parameter, at first a couple of randomly selected events need to be fully simulated to obtain information on the bulk evolution. The full history of particle collisions, cell configurations, etc. is recorded for later use. Subsequently a number N_{jet} of high- p_T particles, for the purpose of this discussion called *jet particles*, is generated from the mini-jet model with a lower cutoff $p_{T, \text{jet}}^{\text{min}}$. These particles are then superimposed on the

previously recorded evolution of the medium. The jet particles interact with the medium particles as in the regular version of BAMPS, with the only difference that the medium particles are taken from the recorded history of the underlying event and are not affected by the interactions with the jet particles. Jet particles among themselves do not interact and jet particles whose momentum falls below a threshold p_T^{thresh} are discarded. Particles created in $2 \rightarrow 3$ interactions of jet particles with medium particles are added to the list of jet particles if their momentum is above the threshold p_T^{thresh} . Similarly to the treatment of high energy particles in a static medium in chapter 4, this approach thus neglects possible responses of the medium to the propagating jets, such as the possible creation of shock waves, cf. section 3.3.3. It is conceptually similar to approaches that use hydrodynamic models of the medium as a basis for Monte Carlo evaluation of jet quenching formalisms (section 5.1.1), see for example [Ren08, ACS09, SGJ09].

To generate sufficient statistics up to the desired value of $p_T \approx 30$ GeV, two sets of runs are used, one with $p_{T,\text{jet}}^{\text{min}} = 10$ GeV and one with $p_{T,\text{jet}}^{\text{min}} = 18$ GeV. The results from these two sets are then combined by individually fitting the initial spectra of gluonic jet particles with power laws, eq. (5.8), from which a scaling factor is derived that is then used to appropriately scale the set with $p_{T,\text{jet}}^{\text{min}} = 18$ GeV. In order to obtain particle spectra as shown and discussed in section 5.3.2, the same procedure is repeated, this time matching the spectra of the jet particles to the spectra of the medium particles. The threshold for the treatment as jet particles is set to $p_T^{\text{thresh}} = 4$ GeV. Results presented in section 5.5 are based upon 3 to 10 independent realizations of the bulk evolution and averaged over 80 to 200 sets of runs with roughly 1000 to 4000 initially added jet particles per run. As this procedure yields a comparatively large number of high- p_T particles per run and the computation time for each of these runs is cut down to a couple of hours, roughly 3 h to 30 h depending on various system parameters, it allows for the simulation of high- p_T observables with adequate statistics within reasonable computation time. Nevertheless, simulations within the BAMPS framework remain resource and time consuming.

5.2.3. Impact parameters and centrality classes

Experimentally the impact parameter of a given event cannot be determined directly and thus also the selection of events with a fixed impact parameter is of course not possible. Rather events are classified according to their centrality as given by the measured distribution of an observable that is assumed to be monotonically related to the impact parameter. The centrality is then given in terms of fractions of the total integral of this distribution, usually stating the centrality as a percentage range, e.g. “0 %-10 %” labels the 10 % most central events. Common means of centrality determination involve some sort of multiplicity distribution or the distribution of the hadronic cross section given by detector counts, see [MRSS07] for an excellent review.

In order to obtain information, for example, on the mean impact parameter $\langle b \rangle$ or the mean number of participants $\langle N_{\text{part}} \rangle$ that correspond to the experimental centrality classes, Monte-Carlo calculations of the Glauber model including simulated detector responses are used to fit the distributions that underlie the centrality class determination. From these fits information on the impact parameter, the number of participants, etc. can then be extracted.

Based on a simple Glauber calculation, as detailed in [XG05], table 5.1 lists the number of

b [fm]	0.0	2.0	2.8	3.4	4.0	4.5
N_{part}	378.3	364.7	336.6	320.7	294.9	273.2
b [fm]	5.0	5.6	6.3	7.0	8.6	9.6
N_{part}	248.3	224.5	195.2	170.5	112.3	78.22

Table 5.1.: N_{part} corresponding to impact parameters used for BAMPS simulations of Au + Au at 200 A GeV from Glauber calculation with $\sigma_{NN} = 42$ mb and parameters for the Woods-Saxon density distribution (5.4) as given in section 5.2.1.

Centrality	0 %–10 %	10 %–20 %	20 %–30 %	30 %–40 %	40 %–50 %
$\langle N_{\text{part}} \rangle$ PHENIX	325	235	167	114	74.4
b [fm] BAMPS	3.4	5.6	7.0	8.6	9.6
N_{part} BAMPS	321	224	171	112	78.2

Table 5.2.: Centrality classes and associated mean number of participants for Au + Au collisions at 200 A GeV from PHENIX [PHENIX08a] and corresponding impact parameters as used in this work to represent these centrality classes.

participants N_{part} corresponding to the values of the impact parameter b that are used for the simulations in this work. Now, in order to accurately compare results for a given observable from BAMPS to experimental results in a certain centrality class, the observable would need to be evaluated within BAMPS at a sufficiently large number of impact parameters such that reliable interpolation is possible. Then the observable would need to be averaged over the impact parameter interval that, according to Glauber Monte-Carlo modeling, corresponds to the centrality class in question. Unfortunately, due to the computation time—the simulation of a single heavy ion collisions within BAMPS with parameters as described above is very time consuming and can take up to several days—the simulation of events with sufficient statistics at an adequately large number of impact parameters is not feasible. Thus, only a limited set of impact parameters is selected for simulation, whose values are chosen as given in table 5.1 for reasons of comparability with previous BAMPS studies [XGS08, XG09]. An association with experimental centrality classes is then made in terms of the number of participants from Glauber calculations, representing each centrality class by a fixed impact parameter that roughly matches the expected number of participants, see table 5.2. While this method is certainly crude and introduces additional uncertainties into the comparison with experimental results, it should—especially in the high- p_T sector—be sufficient to allow for a critical assessment of BAMPS results on the basis of experimental data.

5.3. Spectra and fragmentation of high- p_T partons

5.3.1. Hadronization via fragmentation functions

As BAMPS is a partonic transport model the direct comparison of results to experimental observables is difficult or at least requires careful and individual consideration. So far the concept of parton-hadron duality has been employed in the interpretation of results on

bulk observables from BAMPS as detailed especially in [XG09]. Assuming that a system of thermalized partonic bulk matter retains its distribution according to thermal statistics across the phase transition and furthermore that the change in temperature during hadronization is comparatively small, observables such as the elliptic flow at low momenta, the integrated elliptic flow or the shape of transverse momentum spectra are expected to remain rather unaffected. Therefore experimentally measured pions—that dominate the hadronic bulk—can be compared to gluons—that dominate the partonic medium—from BAMPS calculations with respect to such observables. But already in the intermediate p_T range of about 1 GeV to 3 GeV this duality becomes questionable and recombination or coalescence of partons is believed to play a crucial role in the hadronization process [GKL03]. This has for example consequences on the comparison of the elliptic flow from BAMPS to experimental results in the relevant momentum range [XG09], as also briefly discussed in section 5.4. An incorporation of recombination processes into BAMPS will be the topic of upcoming studies and is not pursued further in the present work.

The probably most straightforward model of hadronization exists for high- p_T particles and goes by the descriptive name of *fragmentation*. The conceptual idea is very simple: a high energy parton fragments into hadrons that each carry a certain fraction z of the original parton momentum. This process is described in terms of so-called fragmentation functions (FF)

$$D_i^h(z, Q^2). \quad (5.5)$$

$D_i^h(z, Q^2)$ encodes the probability that a parton of type i (gluon, quark or antiquark of a certain flavor) fragments into a hadron of type h that carries a given fraction z of the parton momentum. Q^2 gives the momentum scale at which the fragmentation process occurs.

Fragmentation functions are an important ingredient of the factorization theorem and can be determined from theoretical considerations or from analysis of experimental data on jet observables in fundamental reactions such as e^+e^- . The most powerful approach is the combination of theoretical models with global fits to experimental data. The most recent and most elaborate set of thus obtained fragmentation functions comes from global fits to various experimental data by ALBINO, KNIEHL and KRAMER (AKK) [AKK08]. This set of fragmentation functions is used for the analysis in this work.

In principle the probabilities given by the fragmentation functions could be used to implement a Monte Carlo scheme for the fragmentation of partons from BAMPS on a single particle basis. However, certain subtleties would need to be addressed in doing so, for example the distribution of transverse momentum with respect to the jet axis. But since the fragmentation on a single particle basis is not compulsory for the investigation of the observables discussed in the present work, the implementation of a Monte Carlo based fragmentation scheme is left to a separate study. Instead an even simpler approach is chosen in which the hadronic observables are computed from folding the partonic observables with the fragmentation functions.

The yield of hadrons of type h at a given momentum p_{\perp}^h can then be calculated from the

partonic yields as

$$\begin{aligned} \frac{d^2 N_h}{dp_T dy}(p_T^h) &= \sum_i \int_{z_{min}}^1 dz \frac{d^2 N_i}{dp_T dy}\left(\frac{p_T^h}{z}\right) D_i^h(z, Q^2) \\ &= \sum_i \int_{p_T^h}^{p_{T,max}^i} dp_T^i \frac{p_T^h}{(p_T^i)^2} \frac{d^2 N_i}{dp_T dy}(p_T^i) D_i^h\left(\frac{p_T^h}{p_T^i}, Q^2\right), \end{aligned} \quad (5.6)$$

where p_T^h is the momentum of the hadron h transverse to the beam axis, p_T^i is the transverse momentum of a parton of type i and the momentum fraction is given by $z = p_T^h/p_T^i$. The minimum momentum fraction z_{min} would in principle be zero, corresponding to $p_T^i = \infty$, but the AKK fragmentation functions start at $z_{min} = 0.05$. Due to the steeply falling momentum spectra of particles produced in hard QCD scatterings however, very small values of z do not contribute significantly to the hadron yield at given finite momentum. The choice of the scale Q of the fragmentation process is somewhat arbitrary and conventionally taken to be on the order of the hadron momentum p_T^h , with $Q = p_T^h/2$ being used for the calculations presented in this work. The sum in eq. (5.6) runs over all relevant parton types. For simulations with three light (massless) quark flavors, i.e. $N_f = 3$, this comprises gluons, up, down and strange quarks as well as the corresponding antiquarks. In a similar way the elliptic flow of hadrons at high transverse momentum could be computed from the high- p_T elliptic flow of partons

$$v_2^h(p_T^h) = \frac{\sum_i \int_{z_{min}}^1 dz \frac{d^2 N_i}{dp_T} \left(\frac{p_T^h}{z}\right) D_i^h(z, Q^2) v_2^i\left(\frac{p_T^h}{z}\right)}{\sum_i \int_{z_{min}}^1 dz \frac{d^2 N_i}{dp_T} \left(\frac{p_T^h}{z}\right) D_i^h(z, Q^2)}, \quad (5.7)$$

where the yields are integrated over the rapidity range corresponding to the rapidity range at which v_2 is to be considered. While eq. (5.7) is theoretically correct, it is of limited benefit since in practice the most interesting p_T regions in terms of the elliptic flow are not accessible by means of fragmentation—at least not on a theoretically firm ground—and thus this approach is not pursued further in the present work. See also the discussion in section 5.4.

The above presented approach implicitly assumes that the fragmentation of high energy partons takes place in vacuum, only after possible modifications of the high energy partons by the medium. Under this assumption the use of fragmentation functions from fits to experimental results from elementary interactions, such as the AKK set of fragmentation functions, is justified. This approach is in conceptual contrast to approaches in which the fragmentation functions themselves are modified to incorporate medium effects, see for example [ACSX08, DW10].

5.3.2. Fits to parton spectra from BAMPS

The observables extracted from BAMPS simulations are necessarily binned and thus discrete variables rather than continuous functions. This also applies to particle spectra $\frac{d^2 N}{dy dp_T}$ extracted from BAMPS which are binned according to the transverse momentum p_T . The partonic spectra presented in the following are all taken at midrapidity, more specifically in a window $y \in [-0.5, 0.5]$, the bin size is $\Delta p_T = 1$ GeV and the BAMPS data reaches roughly

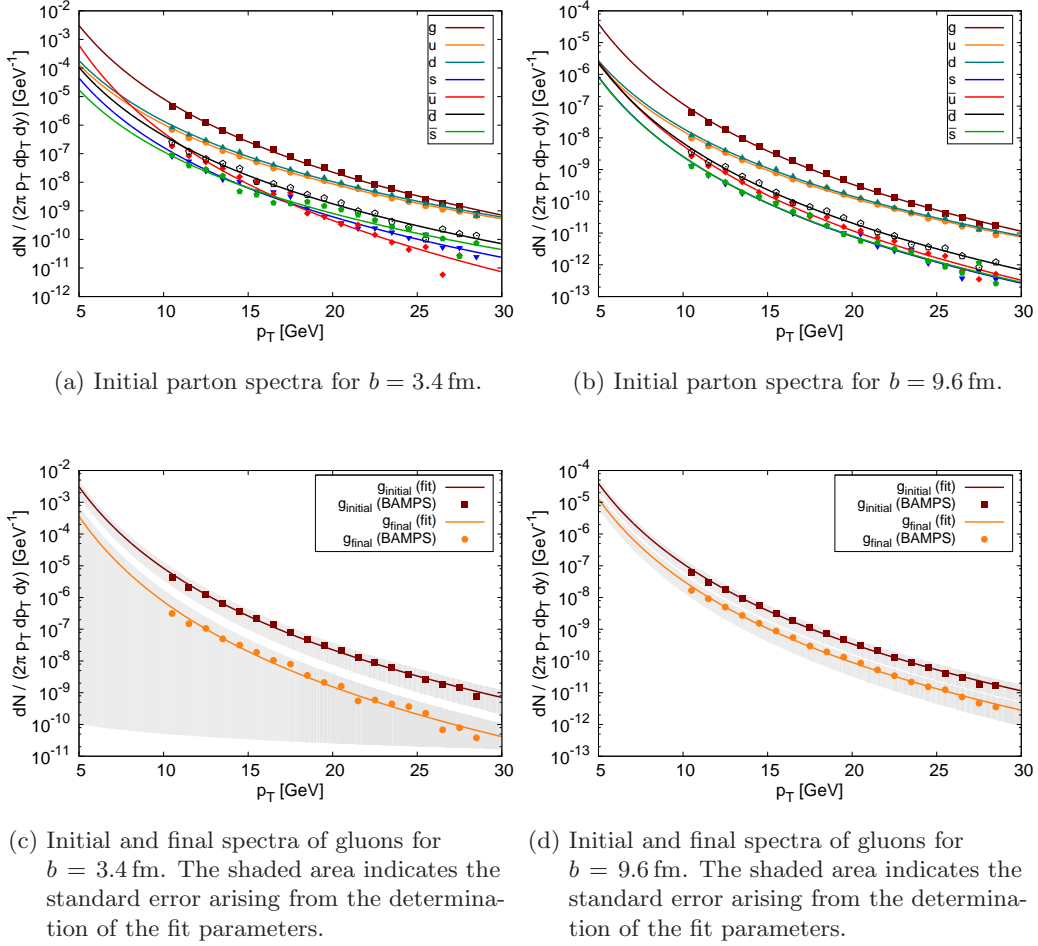


Figure 5.3.: Parton spectra from simulations of Au + Au at 200 A GeV for $b = 3.4$ fm and $b = 9.6$ fm within the BAMPS framework. Symbols represent the spectra as directly extracted from BAMPS, while lines represent the fits to the spectra according to eq. (5.8).

up to $p_T \approx 30$ GeV. While eq. (5.6) can be readily transformed into a discrete sum, it is the limited range in p_T that causes problems. The yield of hadrons at 15 GeV or 20 GeV already receives sizable contributions from partonic transverse momenta beyond the reach of the BAMPS data as illustrated in fig. 5.4 and discussed in more detail in section 5.3.3.

In order to allow for the computation of hadron yields at large transverse momenta, $p_T \gtrsim 15$ GeV, the spectra obtained from BAMPS are fitted with a power law

$$f(p_T) = a p_T^{-b} \quad (5.8)$$

for each parton species individually. The thus determined fits to the parton spectra are then used in eq. (5.6) to compute hadronic yields via fragmentation. This procedure introduces an additional uncertainty from the errors in the determination of the fit parameters that arises from fluctuations of the BAMPS data, but the advantages clearly prevail. The fit parameters for all centralities and parton species, together with the corresponding standard errors, are listed in appendix E.

5.3.3. Fragmented hadron spectra from BAMPS

The ratios with which different parton species from different momenta contribute to a hadron at given momentum not only depends on the fragmentation functions but rather, according to eq. (5.6), on the combination of fragmentation functions and parton spectra. The probability that a hadron of type h at momentum p_T^h stems from a specific parton of type i with momentum $p_T^i = p_T^h/z$ is given by

$$P^{i \rightarrow h}(z, p_T^h) = \frac{1}{\sum_i \int_{z_{\min}}^1 dz \frac{dN_i(p_T^h/z)}{dp_T} D_i^h(z, Q^2)} \frac{dN_i(p_T^h/z)}{dp_T} D_i^h(z, Q^2) \quad (5.9)$$

where the dependence of the spectra on the rapidity y is omitted. All results given in the following are from a window $y \in [-0.5, 0.5]$ around midrapidity. The probability that a hadron of type h with momentum p_T^h stems from the fragmentation of a parton i with any momentum is then simply given by the integral over the momentum fraction z

$$P^{i \rightarrow h}(p_T^h) = \int_{z_{\min}}^1 dz P^{i \rightarrow h}(z, p_T^h) \quad (5.10)$$

with z_{\min} as discussed in section 5.3.1.

Figure 5.4a shows $P^{i \rightarrow h}(z, p_T^h)$ for the fragmentation of gluons, up and down quarks into neutral pions $h = \pi^0$ at $p_T^h = 10$ GeV and $p_T^h = 20$ GeV. The parton spectra are from fits to BAMPS simulations of central, $b = 0$ fm, Au + Au collisions at 200 A GeV, as discussed in section 5.3.2. The contributions from gluons, up and down quarks are chosen for illustration since these parton species dominate the spectra as seen in figs. 5.3a and 5.3b. The contribution from quarks is largest at comparatively large z , z roughly 0.7 to 0.8, thus the momenta of quarks fragmenting into a neutral pion are mostly rather low and close to the final hadron momentum. The contribution from the fragmentation of gluons predominantly stems from smaller values of z , with a maximum roughly at 0.5 to 0.6. This confirms the point made in section 5.3.2 that hadrons already at $p_T^h = 10$ GeV or $p_T^h = 20$ GeV receive sizable contributions from partons, gluons in this case, beyond the reach $p_T \approx 30$ GeV of

the current BAMPS calculations, necessitating the use of fit functions. The contribution of fragmentation from quarks increases with increasing hadron momentum, while the peak of the $P^{i \rightarrow h}(z, p_T^h)$ shifts only slightly. Figure 5.4b confirms that the same qualitative features also hold for the fragmentation into charged hadrons and protons.

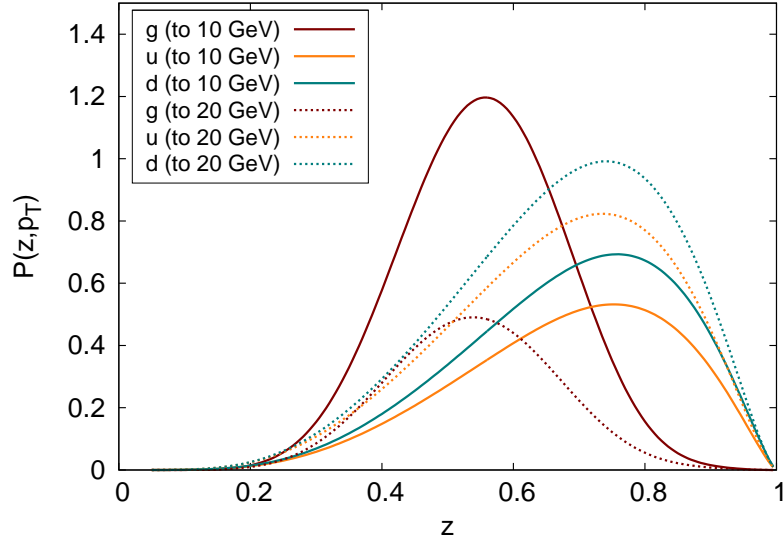
	gluons	quarks	antiquarks
π^0 ($p_T = 10$ GeV)	37.71 %	52.12 %	10.17 %
π^0 ($p_T = 20$ GeV)	15.72 %	78.30 %	5.98 %
$h^+ + h^-$ ($p_T = 10$ GeV)	45.50 %	44.85 %	9.65 %
p ($p_T = 10$ GeV)	62.27 %	31.61 %	6.12 %

Table 5.3.: Contribution of gluons, quarks and antiquarks to selected examples of hadrons at given momentum (neutral pions at 10 GeV and 20 GeV, charged hadrons and protons at 10 GeV) corresponding to fig. 5.4. The given percentage is the integrated probability $P^{i \rightarrow h}(p_T^h)$ from eq. (5.10), with $P^{q(\bar{q}) \rightarrow h} = P^{u(\bar{u}) \rightarrow h} + P^{d(\bar{d}) \rightarrow h} + P^{s(\bar{s}) \rightarrow h}$.

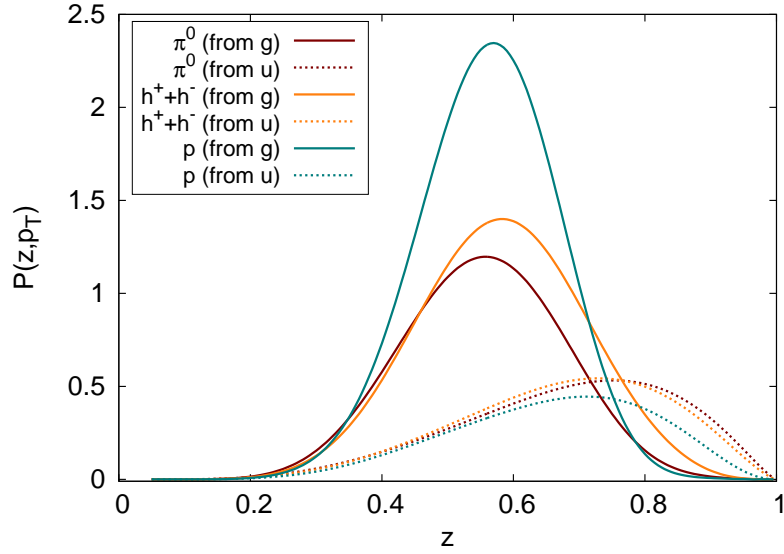
Table 5.3 lists some values of the integrated probability $P^{i \rightarrow h}(p_T^h)$ from eq. (5.10), i.e. the probability that a given hadron stems from the fragmentation of gluons, quarks or antiquarks, for the examples given in fig. 5.4. In order to complement this information, fig. 5.5 shows the contribution of fragmentation from gluons, quarks and antiquarks into neutral pions or charged hadrons as a function of hadron momentum for the initial parton spectra of Au + Au at 200 A GeV and $b = 0$ fm as simulated in BAMPS. This confirms that the contribution from quarks increases with increasing hadron momentum and is indeed the dominating contribution from roughly $p_T^h \approx 10$ GeV on, whereas hadrons with lower momentum are predominantly stemming from the fragmentation of gluons. As was to be expected from the comparison of quark to antiquark spectra in figs. 5.3a and 5.3b, the contribution of antiquarks is small, on the order of 5 % to 10 %.

Finally, fig. 5.6 shows hadronic spectra of neutral pions and charged hadrons obtained via fragmentation of initial and final parton spectra obtained from simulations of Au + Au at 200 A GeV with impact parameters $b = 3.4$ fm, corresponding to a centrality of 0 % to 10 %, and $b = 9.6$ fm, corresponding to 40 % to 50 % central collisions. Note that while for reasons of clarity the quark yields given in fig. 5.6 are the sums over all quark and antiquark flavors, the fragmentation procedure is of course done on the level of single quark flavors as indicated by the sum in eq. (5.6). At roughly 15 GeV to 20 GeV the hadron spectra obtained directly from the discrete BAMPS data points by evaluating the integral in eq. (5.6) as a sum start to deviate from the hadron spectra obtained from the power law fits to the parton spectra because of the limited BAMPS data. This explicitly confirms the argumentation from section 5.3.2. For checking purposes the fragmentation procedure has also been performed based on the fitted parton spectra but using an upper integration limit $p_{T,\max}^i = 29$ GeV, thus mimicking the limited range of the BAMPS data. The results perfectly agree with the approach based on the discrete BAMPS data points.

Already from the spectra in fig. 5.6 a suppression of the yields in the final state compared to the initial spectra is visible. This is the so called nuclear modification due to the



(a) $P^{i \rightarrow h}(z, p_T^h)$ for fragmentation into neutral pions at $p_T^h = 10$ GeV (solid lines) and $p_T^h = 20$ GeV (dashed lines) from gluons, up and down quarks.



(b) $P^{i \rightarrow h}(z, p_T^h)$ for fragmentation into neutral pions, charged hadrons and protons at $p_T^h = 10$ GeV from gluons (solid lines) and up quarks (dashed lines).

Figure 5.4.: Fragmentation probability $P^{i \rightarrow h}(z, p_T^h)$ as given by eq. (5.9) as a function of $z = p_T^h/p_T^i$ for different parton species i , hadron types h and hadron momenta p_T^h . Parton spectra from initial state of BAMPS simulations of Au + Au at 200 A GeV and $b = 0$ fm.

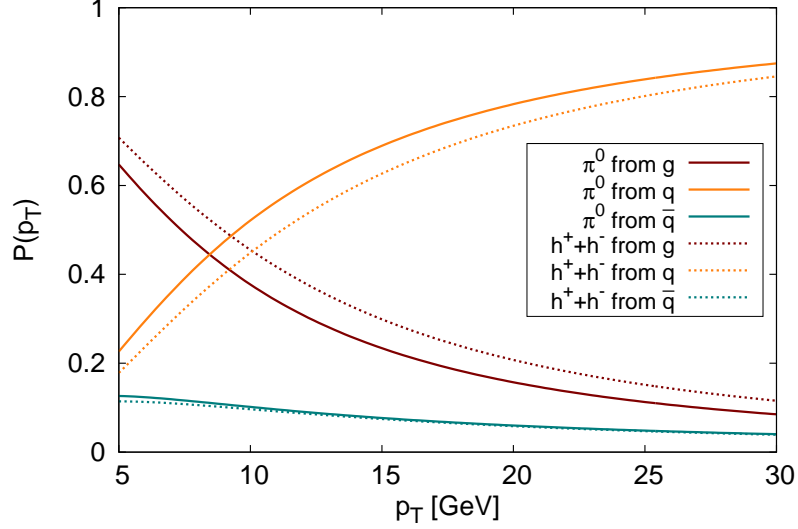


Figure 5.5.: Contribution of fragmenting gluons, quarks and antiquarks to neutral pions and charged hadrons as a function of hadron momentum p_T^h . The contribution is given in terms of the integrated probability $P^{i \rightarrow h}(p_T^h)$ from eq. (5.10), with $P^{q(\bar{q}) \rightarrow h} = P^{u(\bar{u}) \rightarrow h} + P^{d(\bar{d}) \rightarrow h} + P^{s(\bar{s}) \rightarrow h}$. Parton spectra from initial Au + Au at $b = 0$ fm are used as in fig. 5.4.

quenching of high- p_T particles in the partonic medium and will be discussed in section 5.5 in more detail. Interestingly enough, the deviation of hadron spectra computed via the direct fragmentation of discrete BAMPS data points from hadron spectra computed via the fragmentation of fitted parton spectra is very similar for initial and final spectra. The error can thus be expected to cancel to a large extent when taking the ratio of the spectra, i.e. computing the nuclear modification factor R_{AA} , as will be detailed in section 5.5.

5.4. Elliptic flow and thermalization at RHIC from simulations with BAMPS

5.4.1. Elliptic flow in a purely gluonic medium

The elliptic flow from BAMPS simulations of Au + Au collisions at 200 A GeV has already been extensively studied for the case of a purely gluonic medium ($N_f = 0$) by XU and GREINER in [XGS08, XG09]. In [FXG10] these investigations have been extended to the region of high transverse momenta, roughly up to $p_T = 8$ GeV.

The elliptic flow within BAMPS is simply calculated from the anisotropy in the transverse momentum distribution

$$v_2 = \left\langle \frac{p_x^2 - p_y^2}{p_T^2} \right\rangle \quad (5.11)$$

as the orientation of the reaction plane in the simulations is known and always fixed to the x - z plane. Assuming parton-hadron duality it has been demonstrated in [XGS08, XG09]

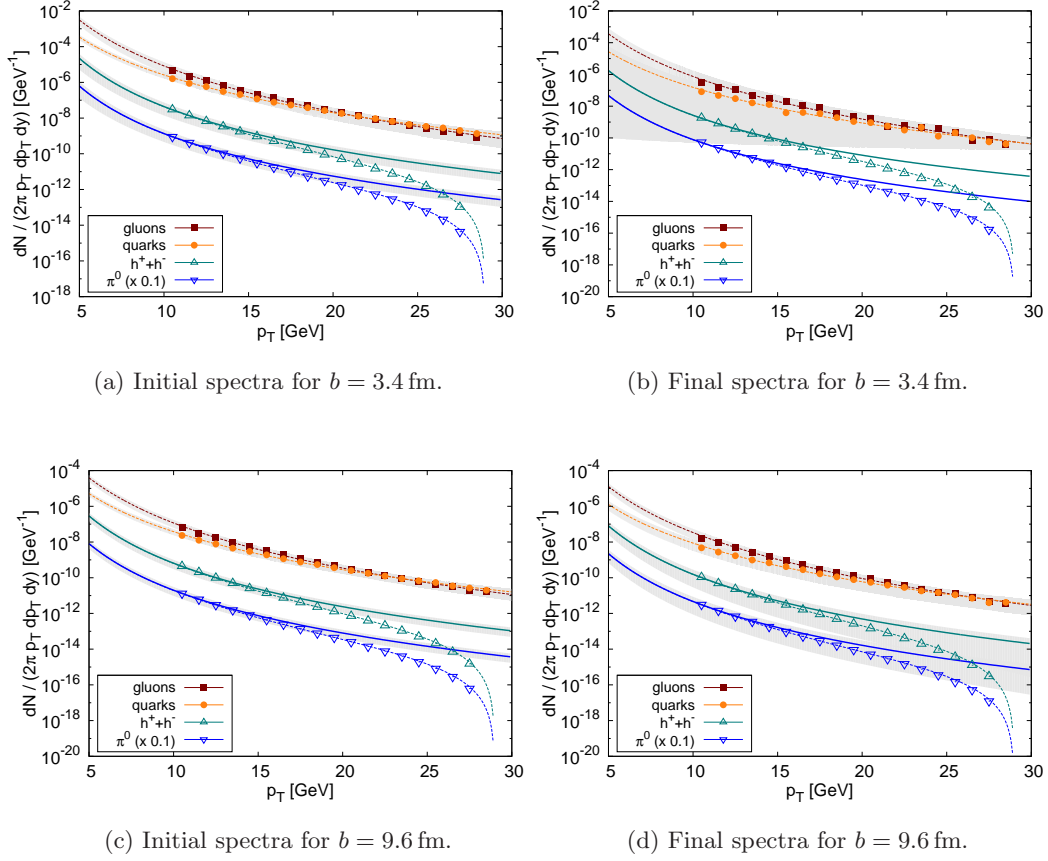


Figure 5.6.: Spectra of neutral pions (scaled by a factor of 0.1) and charged hadrons from fragmentation of partonic spectra from BAMPS simulations of Au+Au at 200 A GeV with impact parameters $b = 3.4$ fm (upper panels) and $b = 9.6$ fm (lower panels). Initial spectra in the left panels are compared with final spectra in the right panels. All spectra taken at midrapidity, $y \in [-0.5, 0.5]$. Gluon and quark spectra from BAMPS (symbols) are shown together with power law fits to the spectra (solid lines). The given quark yield is the sum over all quark and antiquark flavors. Solid lines for the hadrons represent the fragmented spectra based on the power law fits to the parton spectra, symbols represent the fragmented spectra directly based on the parton spectra by evaluating eq. (5.6) as a discrete sum and dashed lines represent fragmented spectra based on the power law fits but limiting the integration range by $p_{T,\max}^i = 29$ GeV in eq. (5.6). Shaded areas indicate the standard error from the uncertainty in the fit parameters. For the final hadron spectra at $b = 3.4$ fm the shaded area would touch the lower bounds of the plot and is not shown.

that matter as simulated within BAMPS exhibits a considerable collectivity and that the integrated v_2 is in very good agreement with experimental data for almost all centralities as illustrated in fig. 5.7a. Different combinations for the values of α_s and ε_c have been explored in these studies, giving best results for either $\alpha_s = 0.6$ and $\varepsilon_c = 1.0 \text{ GeV fm}^{-3}$ or for $\alpha_s = 0.3$ and $\varepsilon_c = 0.6 \text{ GeV fm}^{-3}$, with the latter set of values being the parameters used in this work. Although the integrated v_2 agrees very well with experimental data, the differential $v_2(p_T)$, i.e. the elliptic flow as a function of transverse momentum, shows significant deviations from the experimental results. Especially at intermediate momenta, $1.5 \text{ GeV} \lesssim p_T \lesssim 4.0 \text{ GeV}$ the BAMPS results underestimate the data by roughly 20 % to 50 %. See fig. 5.7b for examples.

As discussed in great detail in [XG09], the complex—and still not thoroughly understood—process of hadronization is crucial to the interpretation of elliptic flow observables at low and intermediate transverse momenta. Based on the picture of parton-hadron duality, the comparison of particle yields, transverse energy and mean transverse momentum suggests that at low transverse momenta, $p_T \lesssim 1 \text{ GeV}$, a gluon on the average hadronizes into 1.5 to 2 pions [XG09]. In the intermediate p_T range however, quark recombination is expected to play a substantial role in the hadronization process. In a simple estimate, the elliptic flow of a pion would be roughly twice as large as that of the recombining quarks $v_2^\pi(p_T) \approx 2v_2^q(p_T/2) \approx 2v_2^g(p_T)$. In this picture gluons are converted into quark-antiquark pairs first.

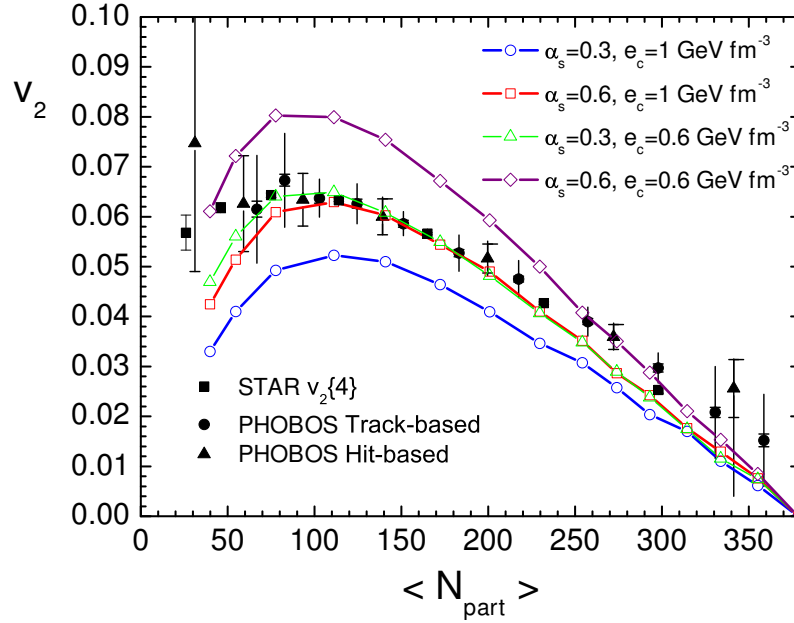
The issues of hadronization at low and intermediate p_T and the incorporation of possible hadronization models into the BAMPS framework will not be resolved in this work. Rather the question how the inclusion of light quarks affects the elliptic flow on the partonic level will be addressed in the following. The full centrality scan from fig. 5.7a is not repeated for $N_f = 3$ however, the comparison is limited to a fixed impact parameter, $b = 7.0 \text{ fm}$, roughly corresponding to 20 %–30 % centrality.

5.4.2. Thermalization of the medium including light quarks

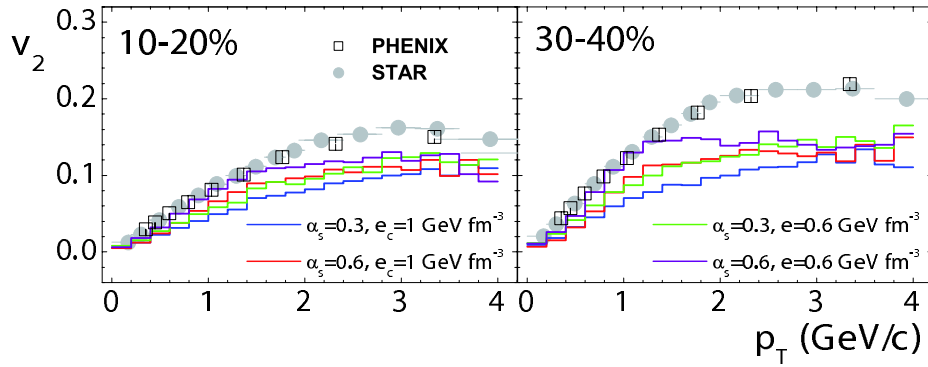
The early thermalization of the gluonic medium created in heavy ion collisions at RHIC energies in simulations including pQCD based $2 \leftrightarrow 3$ interactions has been one of the major results obtained within the BAMPS framework, cf. section 3.3.1 and [XG05]. To demonstrate that the early thermalization of the medium still holds when including light quark degrees of freedom, fig. 5.9a shows the time evolution of gluon and quark spectra in the central, $|\eta| < 0.5$ and $x_T < 1.5 \text{ fm}$, region of a Au + Au collisions with an impact parameter $b = 7.0 \text{ fm}$. As was to be expected, the time scale for the kinetic equilibration does not change when including light quarks into the simulation. Furthermore the slopes of gluon and quark spectra are equal already after 1 fm c^{-1} and evolve identically, indicating that quarks and gluons reach a common kinetic equilibrium. Compared with the purely gluonic case of previous versions of BAMPS, indicated by the gray dot-dashed line in fig. 5.9a, the slope of the spectra in simulations with $N_f = 3$ is slightly steeper, yielding a temperature that is reduced by about 10 %.

Already from the spectra however, it is clearly visible that the total number of quarks⁵, $N_q + N_{\bar{q}}$, stays below the number of gluons throughout the whole evolution of the medium. As quarks are produced by $gg \rightarrow q\bar{q}$ processes during the evolution, the difference in the

⁵Unless otherwise noted, *quarks* signifies a sum or an average over all quark and antiquark flavors.

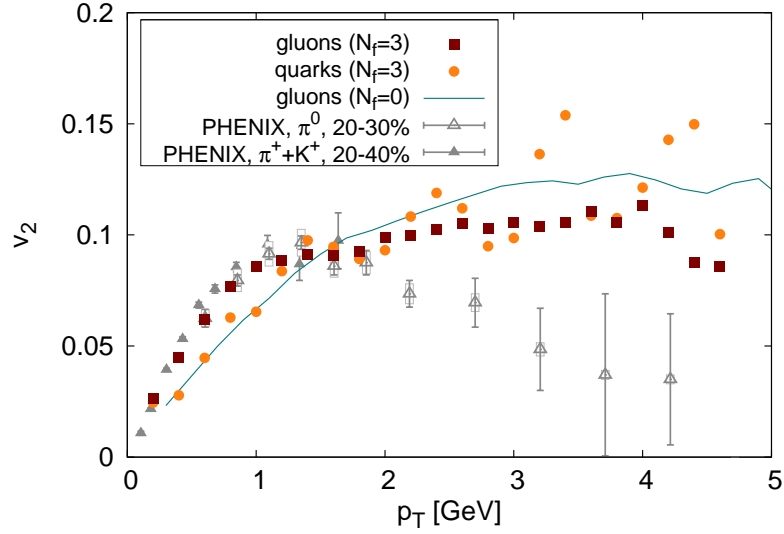


(a) Integrated v_2 as a function of N_{part} for Au + Au collisions at 200 A GeV. Lines represent results from BAMPS for different combinations of the parameters α_s and ε_c obtained for $|\eta| < 1.0$. Experimental data points for charged hadrons from STAR [STAR05b] and PHOBOS [PHOBOS05a]. Figure from [XG09].

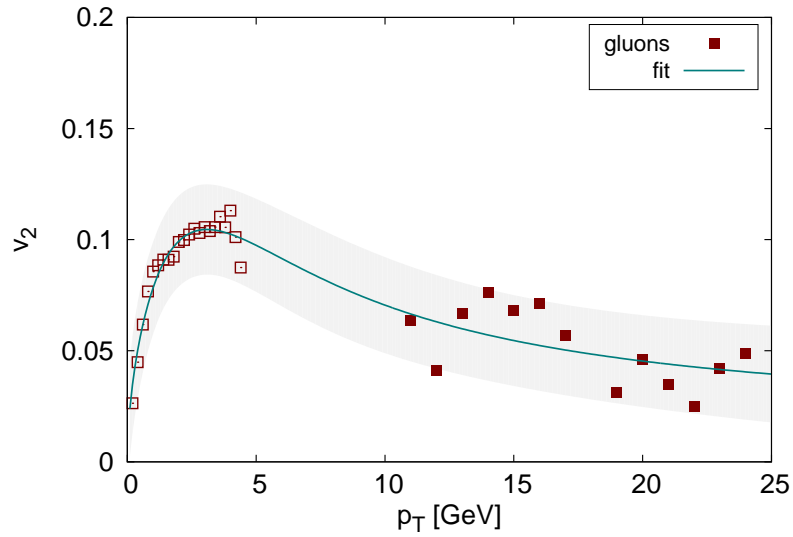


(b) Differential $v_2(p_T)$ for 10%–20% and 30%–40% central Au + Au collisions at 200 A GeV. Lines represent results from BAMPS for different combinations of the parameters α_s and ε_c obtained for $|\eta| < 0.5$. Experimental data points from PHENIX [PHENIX03, PHENIX07b] and STAR [STAR05b]. Figure from [XG09].

Figure 5.7.: Results for the elliptic flow from previous studies with BAMPS for a purely gluonic medium ($N_f = 0$) compared to experimental data.

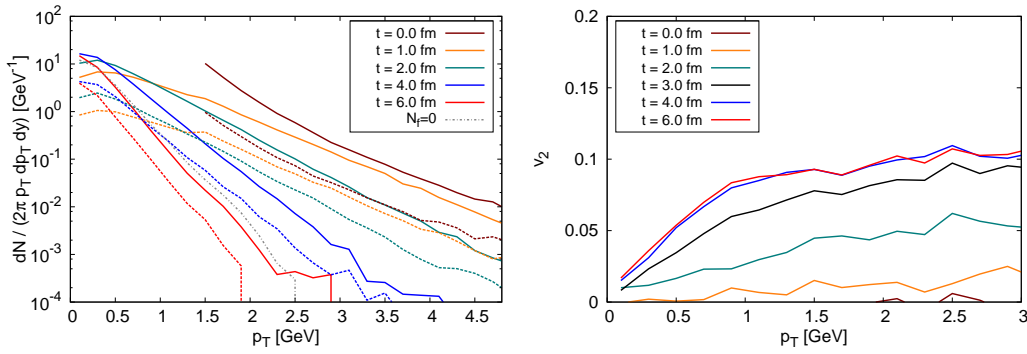


(a) Differential v_2 of gluons and quarks from simulations ($N_f = 3$) of Au + Au at 200 A GeV and $b = 7.0$ fm extracted at $|\eta| < 0.5$. Simulation parameters: $\alpha_s = 0.3$ and $\varepsilon_c = 0.6$ GeV/fm³. For comparison the solid line shows the gluon $v_2(p_T)$ from simulations with $N_f = 0$ [FXG10]. Experimental data from PHENIX is shown for $\pi^+ + K^+$ from 20%-40% central [PHENIX03] and for π^0 from 20%-30% central [PHENIX09a] Au + Au at 200 A GeV. Experimental data is scaled by the number of constituent quarks, $n_q = 2$ for pions and kaons, as $v_2(p_T/n_q)/n_q$.



(b) Differential v_2 of gluons from simulations ($N_f = 3$) of Au + Au at 200 A GeV and $b = 7.0$ fm extracted at $|\eta| < 0.5$. Open symbols from simulation of the bulk evolution, filled symbols from superimposed high- p_T particles. Simulation parameters: $\alpha_s = 0.3$ and $\varepsilon_c = 0.6$ GeV/fm³. The solid line represents a fit to the data according to eq. (5.12), the shaded area indicates the single prediction band for the fit. See text for details.

Figure 5.8.: Elliptic flow for Au + Au at $b = 7.0$ fm from BAMPS studies including light quarks.



(a) Time evolution of gluon (solid lines) and quark (dashed lines) spectra in the central region, $|\eta| < 0.5$ and $x_T < 1.5$ fm. For comparison the gray dash-dotted line shows the gluon spectra at $t = 6.0$ fm c^{-1} in a simulation with $N_f = 0$.

(b) Build-up of elliptic flow $v_2(p_T)$ of gluons. $v_2(p_T)$ extracted at $|\eta| < 0.5$.

Figure 5.9.: Time evolution of the elliptic flow and of parton spectra in simulations of Au + Au at $b = 7.0$ fm including light quarks ($N_f = 3$). Simulation parameters: $\alpha_s = 0.3$ and $\varepsilon_c = 0.6$ GeV/fm³.

yields decreases but is still sizable towards the freezeout of the partonic medium as given by the critical energy density ε_c . Of all particles with $p_T < 5.0$ GeV that are initially created at midrapidity, $|\eta| < 0.5$, for Au + Au at $b = 7.0$ fm from the mini-jet model using GRV parton distribution functions and a lower cutoff in transverse momentum $p_0 = 1.4$ GeV, cf. section 5.2.1, only 9.6% are quarks or antiquarks. During the evolution of the medium this ratio increases to roughly 14.1%. In the most central region, $x_T < 1.5$ fm, for which the spectra in fig. 5.9a are shown and that clearly reaches kinetic equilibrium, the ratio of quarks increases to 21.1%. In full equilibrium however, Boltzmann statistics of massless partons gives a ratio of quarks to gluons of 9/4 and the fraction of quarks in the system should hence be roughly 69.2%. It is thus clear that although the system reaches kinetic equilibrium it remains far from chemical equilibrium and quarks are strongly undersaturated throughout the entire evolution of the partonic medium.

5.4.3. Elliptic flow including light quarks

Elliptic flow at low and intermediate transverse momenta

Figure 5.8a shows the differential $v_2(p_T)$ of gluons and quarks as extracted from simulations of Au + Au at 200 A GeV and a fixed impact parameter of $b = 7.0$ fm including light quarks, $N_f = 3$. For comparison the gluon $v_2(p_T)$ from a previous study that was limited to $N_f = 0$ [FXG10] is also included. Compare fig. 5.9b for the time evolution of the elliptic flow of gluons. While the build-up of the v_2 of quarks is not explicitly shown in fig. 5.9b, it does not significantly differ from the build-up of gluon v_2 .

The most notable feature of the results is the great similarity of $v_2(p_T)$ of gluons and quarks. v_2 as a function of transverse momentum steeply rises from 0 GeV to 1 GeV up to

$v_2 \approx 0.09$, then the increase slows down but v_2 keeps gradually rising up to $p_T \approx 4$ GeV. As was to be expected from the similarity of the cross sections of $2 \leftrightarrow 3$ processes for gluons and quarks, cf. section 4.1, that are crucial to the strong build-up of elliptic flow in BAMPS [XGS08, XG09], the elliptic flow of gluons and quarks does not differ much. Only at low transverse momenta, $p_T < 1$ GeV, an excess of gluon v_2 over quark v_2 is visible that might be the result of the larger interaction rates of gluons. However, statistics in the BAMPS data are limited and the slight difference might not be significant.

Compared with the elliptic flow of gluons from calculations using $N_f = 0$ the changes from the inclusion of light quarks are small. v_2 is slightly enhanced at low transverse momenta, $p_T \lesssim 1.5$ GeV, and slightly decreased at intermediate transverse momenta, 1.5 GeV $\lesssim p_T \lesssim 4$ GeV. But magnitude and general behavior of the differential elliptic flow remain the same. The elliptic flow from BAMPS is also compared to experimental data from PHENIX in fig. 5.8a, specifically to v_2 of positively charged pions and kaons from 20%–40% central Au + Au collisions at 200 A GeV [PHENIX03] and to v_2 of neutral pions from 20%–30% central Au + Au collisions at 200 A GeV [PHENIX09a]. The experimental $v_2(p_T)$ is scaled by the number of constituent quarks as $v_2(p_T/n_q)/n_q$, with $n_q = 2$ in the case of pions and kaons, in order to compare to the quark elliptic flow. While the consistency of the comparison of BAMPS data at fixed $b = 7.0$ fm to experimental data at different centralities, 20%–30% or 20%–40%, might be improved by scaling the results with the initial eccentricity of the system, the comparison of the “raw” data is sufficient for the purpose of this work.

The magnitude to which the elliptic flow rises in the BAMPS results for quarks and gluons agrees rather well with the maximum value of $v_2 \approx 0.1$ in the experimental data, the latter scaled by the number of constituent quarks. This nicely confirms that the difference in the bare v_2 at intermediate transverse momenta can indeed be reconciled by virtue of a quark recombination picture for the hadronization as discussed briefly in section 5.4.1 and in more detail in [XG09]. However, recent experimental data consistently indicates that $v_2(p_T)$ of mesons reaches a maximum in the range 2 GeV $< p_T < 3$ GeV [PHENIX09a, STAR08]. The position of the peak appears to be rather insensitive to the centrality selection and the particle species. Translated into quark transverse momentum by means of the recombination picture, the peak is located at $p_T \approx 1.0$ GeV to 1.5 GeV as is clearly visible in fig. 5.8a. The BAMPS data however continues to rise beyond this value of p_T , or at least does not start to decrease. Indeed, from a fit to the gluon v_2 including high- p_T results, see fig. 5.8b and the discussion below, partonic v_2 from BAMPS is found to peak at $p_T \approx 3$ GeV to 4 GeV. Thus, while the magnitude of elliptic flow is in good agreement, the position of the peak in $v_2(p_T)$ found in BAMPS cannot be reconciled with the position of the peak found in experimental data within a simple quark recombination picture.

Elliptic flow at high transverse momenta

In [FXG10] the range of differential elliptic flow $v_2(p_T)$ for simulations of a purely gluonic medium created in Au + Au at 200 A GeV and a fixed impact parameter of $b = 7.0$ fm has already been extended up to $p_T \approx 8$ GeV. As shown in fig. 5.8b, the present study further extends the range in transverse momentum, up to 25 GeV. Due to the simulation strategy for high- p_T observables, as described in section 5.2.2, results for the elliptic flow of bulk particles, $p_T \lesssim 5$ GeV, and results for the elliptic flow of high- p_T particles, $p_T > 10$ GeV, are obtained

using different simulation techniques. While the elliptic flow of the bulk particles is obtained from conventional BAMPS simulations, the elliptic flow at high transverse momenta is computed from superimposed high- p_T particles as detailed in section 5.2.2. The different treatments cause a gap in the accessible p_T range from 5 GeV to 10 GeV.

In spite of these technical difficulties and poor statistics in the v_2 signal at large p_T , a clear picture emerges. As discussed above and already in [FXG10], the differential $v_2(p_T)$ rises up to $p_T \approx 3$ GeV to 4 GeV with a peak value of $v_2 \approx 0.1$ and from $p_T \approx 5$ GeV on $v_2(p_T)$ starts to decrease again. The high- p_T data in fig. 5.8b clearly confirm the decrease in v_2 towards large transverse momenta. And though statistics in this region is limited, the elliptic flow of gluons in the BAMPS simulation of Au + Au at $b = 7.0$ fm is clearly non-zero up to partonic momenta of 20 GeV to 25 GeV. The results are nicely described by a phenomenological fit function devised in [PHENIX09a]

$$v_2(p_T) = \left(a + \frac{1}{p_T^n} \right) \frac{(p_T/\lambda)^m}{1 + (p_T/\lambda)^m}. \quad (5.12)$$

In this fit function the second term describes a rapidly rising and saturating elliptic flow at low and intermediate momenta, while the first term accounts for the transition from bulk to high- p_T physics. In the latter the elliptic flow is ultimately determined by the angular dependence of the jet suppression, cf. section 5.5. The constant a in the first term thus models the asymptotic value of v_2 that would appear if the elliptic flow was purely due to jet quenching and the nuclear modification factor was constant in p_T as the experimental data suggest, cf. section 5.1.1. The fit parameters as used in fig. 5.8b are $\lambda = 4.33 \pm 7.4$, $m = 1.639 \pm 0.21$, $n = 1.149 \pm 0.18$ and $a = 0.0168 \pm 0.0171$, with p_T in eq. (5.12) being taken as a dimensionless quantity, p_T/GeV .

The BAMPS results of gluonic $v_2(p_T)$ at $b = 7.0$ fm are thus in good qualitative agreement with recent high- p_T data from PHENIX for neutral pions in 20%–30% central Au + Au collisions at 200 A GeV presented in [PHENIX09a] that can also be fitted by the generic form from eq. (5.12): a steep rise in $v_2(p_T)$ that peaks at intermediate transverse momenta followed by a slow decrease in $v_2(p_T)$ that over the observed p_T range does not fully saturate. On the quantitative level however, differences are visible, most notably in the position of the maximum value of $v_2(p_T)$ as already discussed above.

5.5. Jet quenching at RHIC from simulations with BAMPS

5.5.1. Nuclear modification factor of high- p_T particles

The nuclear modification factor R_{AA} from eq. (5.1) is evaluated in simulations within the BAMPS framework by simply taking the ratio of final to initial spectra. This is possible since by construction the initial parton distribution in BAMPS is a superposition of independent p + p collision according to a Glauber model, compare section 5.2.1. In this approach possible cold nuclear matter effects—such as shadowing, anti-shadowing, Cronin effect and EMC effect, see [AAB⁺04, AAB⁺10] for reviews—are currently neglected in simulations of Au + Au. But in the high- p_T region that is of interest here, such effects are not expected to play an important role and any deviations from $R_{AA} = 1$ should be related to the modification of high- p_T particles by the hot medium. Another virtue of the observable R_{AA} is the circumstance that deviations present in both the initial and the final spectra should

cancel and thus R_{AA} can be expected to be only mildly sensitive on subtleties of the initial distribution, for example the underlying parton distribution functions.

All results in this section are computed for Au + Au collisions at 200 A GeV and extracted at midrapidity, $|y| < 0.5$. A fixed $\alpha_s = 0.3$ is used in the BAMPS simulations together with a freezeout energy density $\varepsilon_c = 0.6 \text{ GeV fm}^{-3}$. The nuclear modification factor of hadrons is calculated by separately fragmenting the initial and the final parton spectra using AKK fragmentation functions as described in section 5.3 and subsequently taking the ratio of final to initial hadron spectra. The fragmentation is done according to eq. (5.6) on the level of individual quark and antiquark flavors, while the R_{AA} of quarks that is shown for comparison in some plots of this section represents a combined value of all quark flavors. In all plots of the nuclear modification factor shown in this section, lines represent values of R_{AA} that are obtained based on fits of the initial and final parton spectra as detailed in section 5.3.2, while symbols represent R_{AA} computed directly from the binned values of the parton yields as extracted from BAMPS. As already discussed in section 5.3.3, the deviations of the two methods, that are caused by a limited range of the parton spectra as directly extracted from BAMPS, to a large extent cancel in the observable R_{AA} . PHENIX results on the suppression of neutral pions [PHENIX08a] are chosen as the experimental reference since these datasets cover a large range in transverse momentum and are readily available at different centralities. Since STAR and PHENIX perfectly agree on the suppression of high- p_T particles [STAR05a, PHENIX05, STAR02, PHENIX02, STAR03, PHENIX08a], since the measured suppression of for example charged hadrons does not differ from the suppression of neutral pions and since charged hadrons and neutral pions from the fragmentation of BAMPS results are also equally quenched, compare fig. 5.6, this specific choice of experimental reference does not affect the interpretation of the results.

Figure 5.10 shows an overview of the nuclear modification factor of neutral pions from BAMPS simulations at different impact parameters. A clear ordering of R_{AA} with the impact parameter b is observed, with high- p_T particles from peripheral collisions (large b) being less suppressed than high- p_T particles from central collisions (small b). The values for the suppression of π^0 roughly range from $R_{AA} \approx 0.05$ for most central, $b = 0 \text{ fm}$, to $R_{AA} \approx 0.25$ for peripheral collisions at $b = 9.6 \text{ fm}$. The behavior of R_{AA} as a function of transverse momentum is similar for all impact parameters, slight deviations from the common behavior are most likely to be attributed to statistical fluctuations. If a trend was to be extracted from the results, the data from BAMPS seems to indicate a slight decrease of R_{AA} towards higher transverse momenta. However, the trend is rather weak and within the statistical errors, that are not explicitly shown here, the results could also be consistent with a constant value of R_{AA} . Also note that the values of R_{AA} for $p_T < 10 \text{ GeV}$ are based on extrapolations of fits to the underlying parton spectra, cf. section 5.3. A conclusive statement on the behavior of R_{AA} extracted from simulations of Au + Au collisions with BAMPS as a function of transverse momentum is thus difficult to make, but the results suggest a slight decrease towards large p_T .

Figure 5.11 then compares the results on the nuclear modification factor of neutral pions to experimental data from PHENIX for different centrality classes. The fixed impact parameter from BAMPS is mapped to experimental centrality classes according to table 5.2 based on a comparison of N_{part} from Glauber calculations, see the discussion in section 5.2.3 for details. For comparison R_{AA} as extracted from BAMPS is also shown for gluons and quarks, where the quark R_{AA} is an inclusive value based on spectra that combine all quark and antiquark

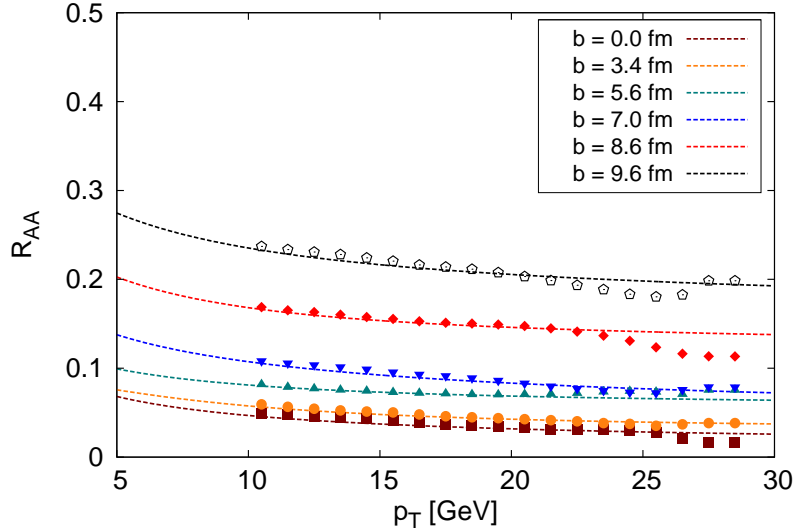


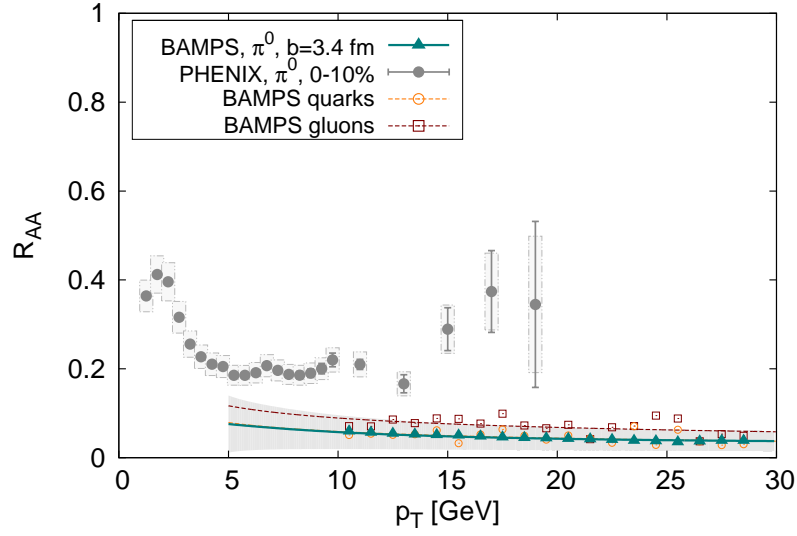
Figure 5.10.: Nuclear modification factor R_{AA} for neutral pions from BAMPS simulations of Au + Au at 200 A GeV for different impact parameters as a function of transverse momentum. Lines indicate R_{AA} computed from π^0 spectra obtained via fragmentation of fits to the parton spectra from BAMPS, while symbols indicate R_{AA} computed from π^0 spectra directly obtained from fragmentation of the parton spectra, cf. section 5.3.

flavors as already discussed above.

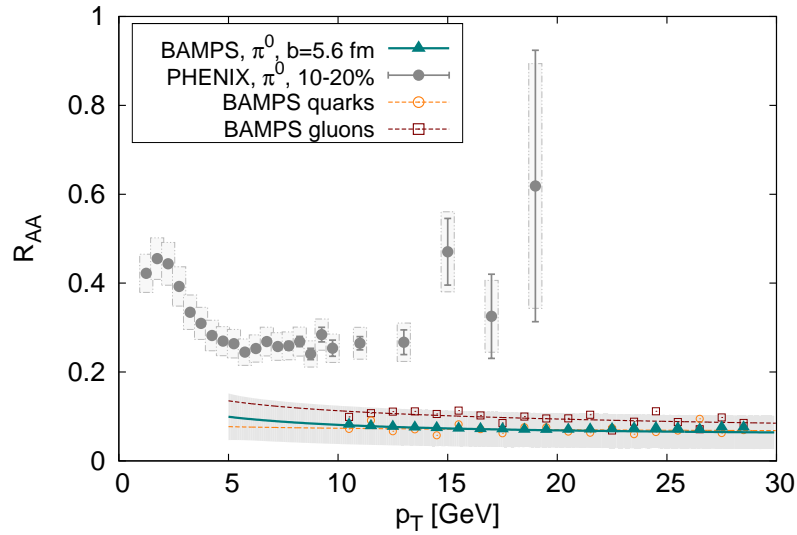
The shape of the suppression pattern does not significantly differ from gluons to quarks, but strikingly quarks are slightly more suppressed than gluons, i.e. their R_{AA} is closer to zero. At first glance this is surprising since the energy loss of quarks is weaker than that of gluons, even though due to the LPM cutoff the difference is distinctly smaller than given by the color factors, see section 4.2 for details. As discussed in section 4.4 however, the conversion of quark jets into gluon jets is a crucial issue in a medium in which quarks are strongly undersaturated. In the medium simulated within BAMPS quarks are distinctly undersaturated throughout the entire evolution of the fireball, cf. the discussion in section 5.4.2, thus high energy quarks will convert into gluons which results in an increased suppression of quarks, i.e. a decreased quark R_{AA} . Indeed, at $b = 3.4$ fm for example, roughly 33% of all (no cut in rapidity) quarks produced with $p_T > 10$ GeV are converted to gluons as they propagate through the medium, while only about 2.5% of all gluons with initial $p_T > 10$ GeV are converted to quarks⁶. Of all gluons that leave the medium with $p_T > 10$ GeV, 12% have been converted from initial high- p_T quarks while only about 2% of the quarks that emerge with $p_T > 10$ GeV originate from initial high- p_T gluons. These conversions finally cause the suppression of high- p_T quarks to be even stronger than the suppression of gluons.

In [FXG09] and [FXG10]—prior to the inclusion of light quarks into the model—it had

⁶For the computation of these numbers the final particle type is evaluated either after the transverse momentum has dropped below 10 GeV or after the particle has left the medium.

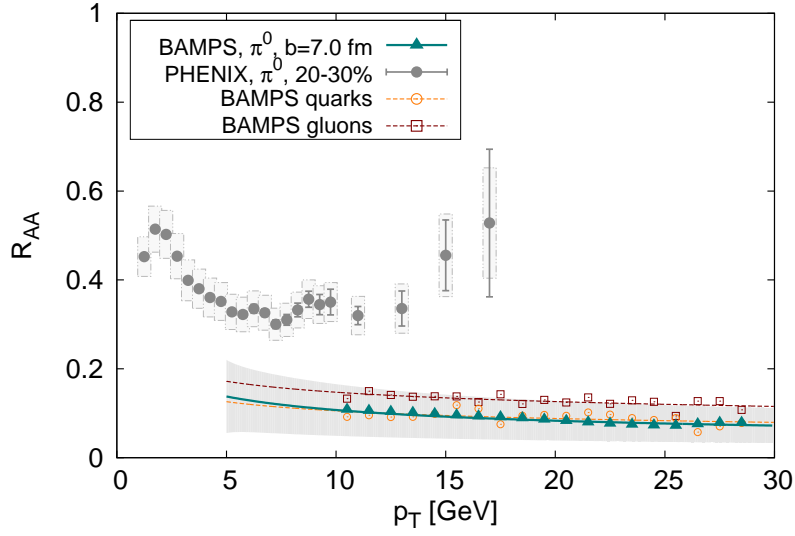


(a) Nuclear modification factor from BAMPS at $b = 3.4$ fm compared to 0%–10% central π^0 data from PHENIX.

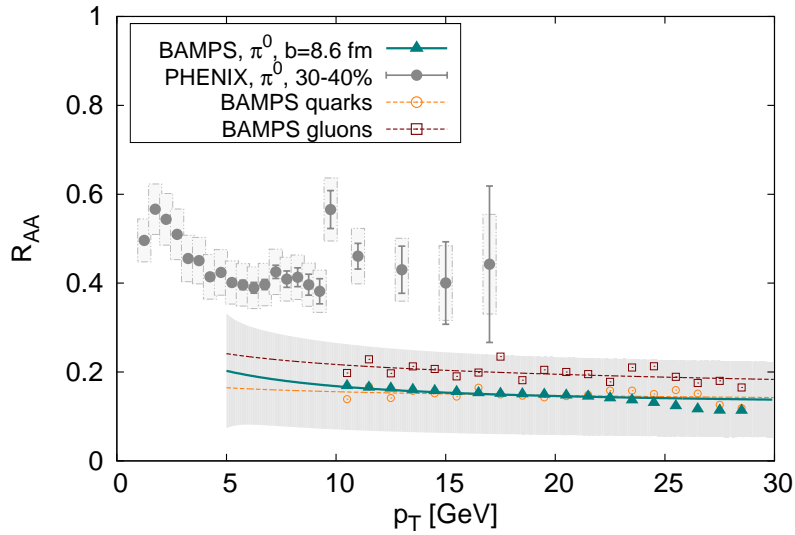


(b) Nuclear modification factor from BAMPS at $b = 5.6$ fm compared to 10%–20% central π^0 data from PHENIX.

Figure 5.11.: Nuclear modification factor R_{AA} for neutral pions from BAMPS simulations of Au + Au at 200 A GeV compared to PHENIX results [PHENIX08a] at different centralities. R_{AA} of gluons and quarks is shown for comparison. Lines indicate R_{AA} computed from fits to the parton spectra, while symbols indicate R_{AA} computed directly from the parton spectra as obtained from BAMPS.

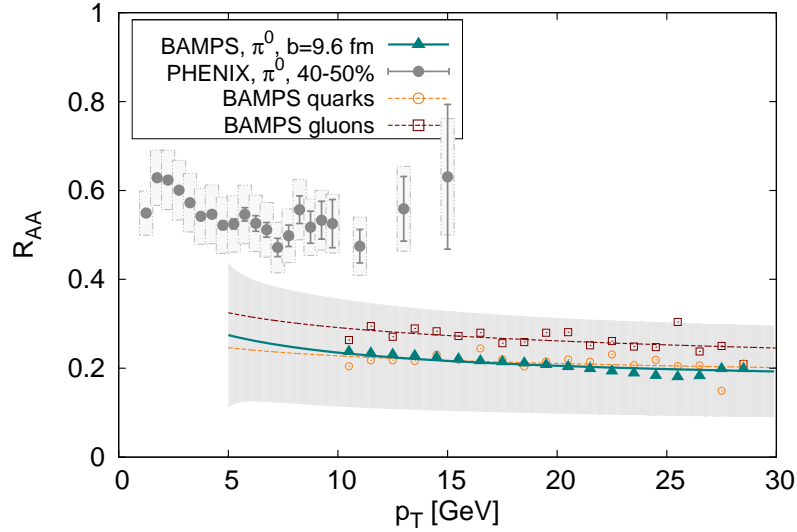


(c) Nuclear modification factor from BAMPS at $b = 7.0$ fm compared to 20%–30% central π^0 data from PHENIX.



(d) Nuclear modification factor from BAMPS at $b = 8.6$ fm compared to 30%–40% central π^0 data from PHENIX.

Figure 5.11.: Nuclear modification factor R_{AA} for neutral pions from BAMPS simulations of Au + Au at 200 A GeV compared to PHENIX results [PHENIX08a] at different centralities. R_{AA} of gluons and quarks is shown for comparison. Lines indicate R_{AA} computed from fits to the parton spectra, while symbols indicate R_{AA} computed directly from the parton spectra as obtained from BAMPS.



(e) Nuclear modification factor from BAMPs at $b = 9.6$ fm compared to 40%-50% central π^0 data from PHENIX.

Figure 5.11.: Nuclear modification factor R_{AA} for neutral pions from BAMPs simulations of Au + Au at 200 A GeV compared to PHENIX results [PHENIX08a] at different centralities. R_{AA} of gluons and quarks is shown for comparison. Lines indicate R_{AA} computed from fits to the parton spectra, while symbols indicate R_{AA} computed directly from the parton spectra as obtained from BAMPs.

been argued that the level of jet quenching is in reasonable agreement with experimental data since the gluon R_{AA} from BAMPs agrees with analytic results on the suppression of gluons by WICKS et al. [WHDG07], that in their GLV-based approach together with the quark contribution reproduces the experimental data of central Au + Au collisions at RHIC. For gluons they obtain a value of $R_{AA}^g \approx 0.07$ to 0.09 , while the suppression of gluons from simulations with BAMPs at $b = 0$ fm has been determined to be $R_{AA}^g \approx 0.053$ for a medium with $N_f = 0$ [FXG09]. This agreement still holds, in fact it has improved since for $b = 3.4$ fm—which is a more reasonable representation of central Au + Au collisions than $b = 0$ fm, cf. section 5.2.3—and including light quarks the value of gluon suppression obtained from BAMPs is $R_{AA}^g \approx 0.08$ assuming a flat suppression pattern in the range $p_T = 10$ GeV to 20 GeV. However, in the approach by WICKS et al. the experimental level of jet quenching is only reproduced because light quarks⁷ are distinctly less suppressed. They find the nuclear modification factor of light quarks to be roughly 2 to 3 times larger than the nuclear modification factor of gluons, corresponding to the usual color factor $9/4$. This is clearly not the case for the suppression on the partonic level as extracted from BAMPs simulations, where quarks are suppressed even stronger than gluons. The inclusive suppression of quarks at $b = 3.4$ fm for example is $R_{AA} \approx 0.05$, again assuming a flat suppression pattern in the range $p_T = 10$ GeV to 20 GeV. The conversion of quark and gluon jets is not included in the formalism underlying the results of WICKS et al. [WHDG07],

⁷Actually they consider only up and down quarks as light quarks. This would correspond to $N_f = 2$ in the approach presented in this work. However, as strange quarks are very rare, this makes no difference.

neither for elastic nor for inelastic processes. But note that also without the conversion of high- p_T quarks into gluons, the quark suppression in BAMPS would be distinctly stronger than the suppression found in [WHDG07] as due to the LPM cutoff in $2 \rightarrow 3$ processes that dominate the energy loss of high energy partons, the difference in the energy loss of quarks and gluons is not given by a color factor $9/4$ but rather only on the level of 20 %, see the discussion in section 4.2 for details.

Correspondingly, the suppression of neutral pions as obtained from the fragmentation of parton spectra in BAMPS is distinctly stronger than in the experimental data. The R_{AA} from BAMPS is below the experimental reference for all centralities, see fig. 5.11, by roughly a factor of 2 to 4. The same is true when considering for example the suppression of charged hadrons instead of neutral pions.

Centrality dependence of the suppression of high- p_T particles

The above discussed results clearly show that the suppression of high- p_T particles as obtained from simulations with BAMPS is stronger than measured in experiment. Figure 5.12a illustrates that the BAMPS results not only differ from the experimental data by a constant factor. Comparing the integrated R_{AA} for $p_T > 10$ GeV, the ratio of the experimental nuclear modification factor to the nuclear modification factor as extracted from BAMPS varies from $R_{AA}^{\text{PHENIX}}/R_{AA}^{\text{BAMPS}} \approx 2$ for peripheral to $R_{AA}^{\text{PHENIX}}/R_{AA}^{\text{BAMPS}} \approx 4$ for central collisions.

Both in the experimental data and in the BAMPS results, the magnitude of jet quenching as quantified by R_{AA} changes with centrality while the shape of the suppression pattern remains rather unaffected. This suggests that R_{AA} mainly depends on N_{part} as a measure of centrality rather than on the specific geometry of the collision region. Figure 5.12b thus shows the integrated R_{AA} of π^0 for $p_T > 10$ GeV as a function of N_{part} both for experimental data from PHENIX [PHENIX08a] and for results obtained from simulations with BAMPS. As already suggested by fig. 5.12a, the centrality dependence of R_{AA} differs from the measured data.

In order to quantify this difference the data is matched to a simple picture in which the suppression of high- p_T particles is expressed in terms of a horizontal shift of the power law p_T -spectrum [PHENIX07c] rather than a vertical reduction of the yields. This model is valid if R_{AA} is flat as a function of p_T , i.e. if both the particle spectrum from the heavy ion collision and the scaled p+p reference can be described by a power law spectrum $dN/(p_T dp_T) \propto p_T^{-n}$ with the same exponent n . In the experimental data this assumption is fulfilled rather nicely with $n = 8.10 \pm 0.05$ for π^0 spectra from p+p [PHENIX07c] and $n = 8.00 \pm 0.12$ for π^0 spectra from most central Au+Au at 200 A GeV. The slope of the π^0 spectrum obtained in BAMPS by fragmentation of the initial parton spectra generated by the mini-jet model is in very good agreement with these measurements, for $b = 3.4$ fm a value of $n = 8.023 \pm 0.015$ is obtained. Reflecting the slight decrease of R_{AA} with p_T that is observed in the BAMPS results when computing R_{AA} from the fragmentation of fitted parton spectra, the final π^0 spectra as extracted from BAMPS are slightly steeper, for example $n = 8.436 \pm 0.016$ at $b = 3.4$ GeV. For the following analysis however, the quantitative impact of these differences in the exponents is rather weak and for simplicity a value of $n = 8.1$ is used.

The shift in the spectra is expressed in terms of $S(p_T)$, in the sense that a final particle with transverse momentum p_T has initially been produced with transverse momentum $p'_T =$

$p_T + S(p_T)$. As discussed above, the assumption of a constant shift is well justified and thus⁸ $S(p_T)/p_T = \tilde{S}_0$. As $p'_T = (1 + \tilde{S}_0)p_T$ this implies a fractional energy loss $S_{\text{loss}} = (p'_T - p_T)/p'_T = 1 - 1/(1 + \tilde{S}_0)$. Expressing the final spectrum in terms of this shift, taking the Jacobian into account and assuming a centrality dependence as $S_{\text{loss}} = S_0 N_{\text{part}}^a$ finally leads to [PHENIX07c]

$$R_{AA} = (1 - S_0 N_{\text{part}}^a)^{n-2}. \quad (5.13)$$

Using (5.13) as a fit function, the centrality dependence of the integrated R_{AA} from BAMPS and from PHENIX can be nicely described for $N_{\text{part}} > 20$ as illustrated in fig. 5.12b. The fit to the experimental data yields $a = 0.57 \pm 0.13$ and $S_0 = (9.0 \pm 6.1) \cdot 10^{-3}$ [PHENIX08a], while the fit to the BAMPS data gives⁹ $a = 0.39 \pm 0.02$ and $S_0 = (4.23 \pm 0.38) \cdot 10^{-2}$. The centrality dependence of the suppression of high- p_T particles, given by the parameter a , is thus distinctly and significantly stronger in BAMPS than in the experimental data. The centrality dependence of the experimental data is in agreement [PHENIX07c] with results from the GLV formalism [GLV00a] and the Parton Quenching Model [Loi07] that give $a \approx 2/3$.

Explicitly evaluating the fractional energy loss S_{loss} —which, due to a bias introduced by the steeply falling spectra, is smaller than the average energy loss at a given transverse momentum [PHENIX07c]—yields $S_{\text{loss}} \approx 0.4$ for the most central collisions within BAMPS, while experimental data gives $S_{\text{loss}} \approx 0.2$ [PHENIX07c].

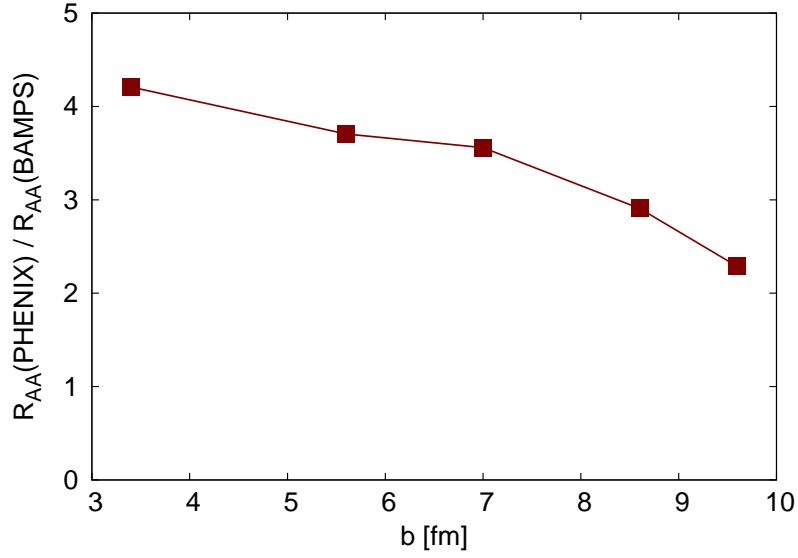
5.5.2. Origin and interaction history of high- p_T particles

In any energy loss scenario particles that emerge from the medium with large p_T are naturally expected to have a certain surface bias, i.e. they are more likely to originate from regions close to the surface of the medium than from the inner region of the medium. The strong level of jet quenching and the flat quenching pattern, similar at all centralities, suggest that the surface bias is rather pronounced for the medium created in Au + Au collisions at RHIC. Indeed, basically all energy loss formalisms predict a shift of the production points of surviving high energy particles towards the surface of the medium, see [WHDG07, Loi07, ZOWW07] and [BGM⁺09] for a direct comparison. Figure 5.13 nicely illustrates that also in BAMPS the production points of high- p_T particles that survive the propagation through the evolving medium are clearly biased towards the surface of the overlap region.

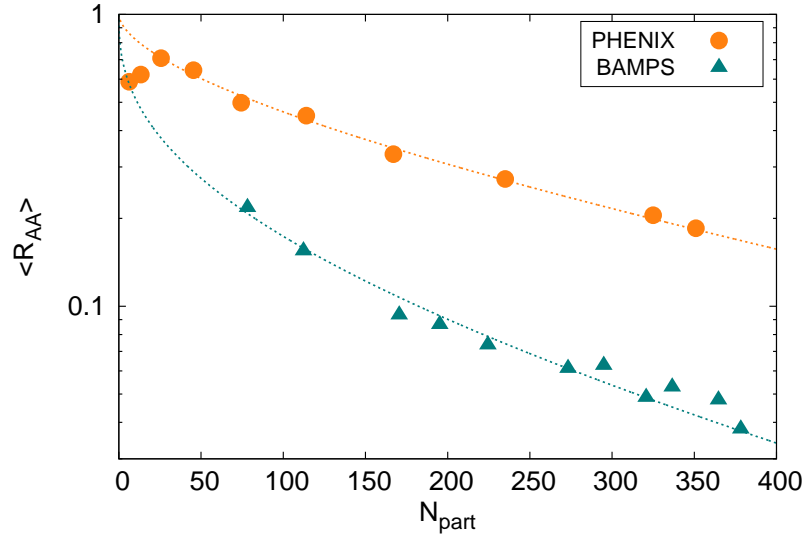
In order to quantify this finding, fig. 5.14 shows the distribution of the path length L of partons that escape the simulated medium with $p_T > 10$ GeV. In this analysis, L measures the distance in the transverse plane from the production point of a parton to the surface of the initial overlap region given by the Woods-Saxon parameter $R_A = 6.37$ fm in the direction of the initial transverse momentum. Thus defined, it does not take the expansion of the medium into account and is therefore different from the effective path length that is used in some jet quenching formalisms to model the geometry and evolution of the system, for example in [WHDG07, EHSW05]. Nevertheless it provides a good measure of the distance that a parton propagates through the medium and is applicable to collisions with $b \neq 0$ fm. For comparison the gray dashed line in fig. 5.14 shows the distribution of L for all particles

⁸As the shift is in dN/dp_T rather than in $dN/(p_T dp_T)$ an additional factor p_T enters

⁹The quoted errors for the fit to the BAMPS data solely comprise the standard error of the fit parameters.



(a) Ratio of the integrated R_{AA} from BAMPS to PHENIX for π^0 as a function of impact parameter b . Association of impact parameter and experimental centrality classes as in table 5.2 and fig. 5.11.



(b) Integrated R_{AA} of π^0 as a function of centrality expressed in terms of N_{part} for BAMPS results and PHENIX data. Dashed lines indicate fits according to eq. (5.13).

Figure 5.12.: Comparison of the integrated R_{AA} of neutral pions from simulations of Au + Au at 200 A GeV with BAMPS to experimental data from PHENIX [PHENIX08a]. Integrated R_{AA} obtained from 10 GeV $< p_T < 20$ GeV for the BAMPS results and from $p_T > 10$ GeV for PHENIX data.

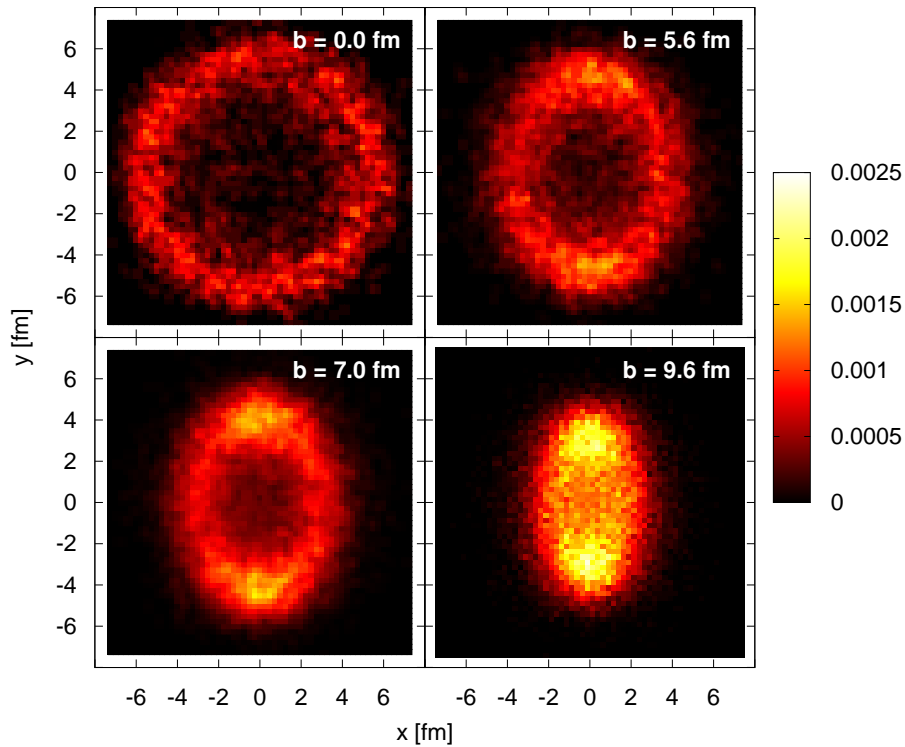


Figure 5.13.: Illustration of the geometric origin of particles (gluons and quarks) that leave the the medium (Au + Au at 200 A GeV) with $p_T > 10$ GeV for different impact parameters. The probability that an emerging particle with $p_T > 10$ GeV originates from a certain region in the transverse plane is color coded.

produced with $p_T > 10$ GeV, regardless of their fate during the further evolution of the medium.

A strong shift towards the surface of the overlap region is observed for particles that survive the evolution of the medium and escape with $p_T > 10$ GeV. For most central collisions, $b = 0$ fm, the survival probability reaches a maximum in the range $L = 1$ fm to 2 fm, corresponding to the ring that is visible in fig. 5.13. Caused by the conversion of quarks into gluons, the distribution of production points of surviving quarks is shifted even more towards the surface than that of gluons. Note that there is a sizable probability that surviving partons have been produced outside the region that is given by the parameter R_A of the Woods-Saxon distributions, i.e. in the “corona”, and have not traveled through the dense regions of the medium at all. Qualitatively, the same holds for the most peripheral collisions explored within this work, at $b = 9.6$ fm. Due to the geometry however, no distinct peak is visible any more, rather the distribution of L continuously increases towards the surface and emission from the corona in fact accounts for roughly 50 % of all surviving particles. The difference between quark and gluon jets is slightly visible at intermediate L , but distinctly less pronounced than for central collisions.

As was to be expected from the strong differential energy loss that parton jets suffer within

the BAMPS framework, the surface bias is rather strong. Of course this is not a black and white picture. Despite the strong shift of production points of surviving high- p_T particles there is still a sizable fraction that stems from more central regions of the medium. For $b = 0$ fm roughly 36 % of the surviving high- p_T gluons and 23 % of the surviving high- p_T quarks have been produced at a distance $L > 2$ fm from the surface of the initial overlap region. For $b = 9.6$ fm these values drop to 20 % for gluons and 13 % for quarks. The average production distance¹⁰ of particles emerging with $p_T > 10$ GeV is $\langle L^g \rangle = 2.1$ fm for gluons and $\langle L^q \rangle = 1.7$ fm for quarks in collisions with $b = 0$ fm. For $b = 9.6$ fm the mean production distances are $\langle L^g \rangle = 0.9$ fm and $\langle L^q \rangle = 0.8$ fm. Compared with results from other jet quenching formalisms the surface bias is more pronounced [BGM⁺09, WHDG07, ZOWW07, Loi07], i.e. surviving jets in BAMPS tend to originate from production points that are closer to the surface compared with the cited jet quenching formalisms.

Correspondingly, the number of interactions that surviving high- p_T particles have undergone, is rather small. In the most central collisions with $b = 0$ fm partons that leave the medium with $p_T > 10$ GeV have undergone on the average $\langle N_{22} \rangle = 1.85$ binary interactions, $\langle N_{23} \rangle = 0.74$ radiative interactions and $\langle N_{32} \rangle = 0.13$ particle annihilation processes. For $b = 9.6$ fm the average collision numbers of surviving jets are $\langle N_{22} \rangle = 2.11$, $\langle N_{23} \rangle = 0.50$ and $\langle N_{32} \rangle = 0.04$. No discrimination between quarks and gluons is made in this analysis. The underlying distribution of the collision numbers for surviving jet partons is depicted in fig. 5.15. The most remarkable feature is certainly the fact that in most cases a single $2 \rightarrow 3$ interaction is sufficient to “kill” the jet particle, the fraction of surviving high- p_T partons that have undergone at least one $2 \rightarrow 3$ interaction is on the order of 35 % to 40 %, the fraction of surviving high- p_T partons that have undergone at least two $2 \rightarrow 3$ interactions is on the order of 10 % to 15 %. There is virtually no change in the distribution of collision numbers going from central to peripheral collisions, again confirming a rather strong surface bias.

5.6. Sensitivity of the results on the LPM cutoff

5.6.1. Scaling the LPM cutoff

Every effective model comes with a set of free parameters whose choice can be motivated by physical arguments or by fits to experimental data. The most notable free parameter in the transport model BAMPS is the coupling strength α_s that has been fixed to the canonical value of $\alpha_s = 0.3$ throughout this work. The consequences of different choices of α_s , especially on elliptic flow observables, have been studied in previous works [XGS08, XG09]. See also the discussion in section 6.2.1 for possible consequences of a modified or running coupling on energy loss and jet quenching. In simulations of heavy ion collisions the freeze out energy density ε_c , cf. section 5.2, is also a parameter that can be adjusted within certain limits.

When investigating radiative $2 \leftrightarrow 3$ processes within BAMPS there basically enters another parameter due to the effective modeling of the LPM effect via a cutoff. In BAMPS the LPM cutoff is incorporated into the Gunion-Bertsch matrix element via a Theta function eq. (3.17) that essentially compares the formation time τ of the radiated gluon to the mean

¹⁰Surviving jets that do not traverse the inner region are counted as $L = 0$ fm.

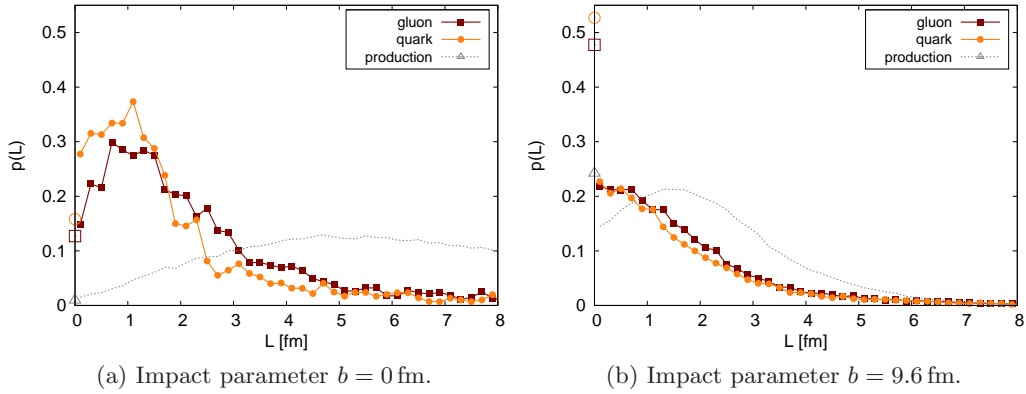


Figure 5.14.: Distribution of the path length L from the production point of particles (gluons and quarks) leaving the medium with $p_T > 10$ GeV to the surface of the initial interaction region given by the parameter $R_A = 6.37$ fm in the Woods-Saxon distribution (5.4). Open symbols at $L = 0$ fm indicate the fraction of emerging high- p_T particles that were produced outside the interaction region as given by R_A . For comparison the gray dashed line and the gray open symbol indicate the corresponding path length for all particles produced with $p_T > 10$ GeV.

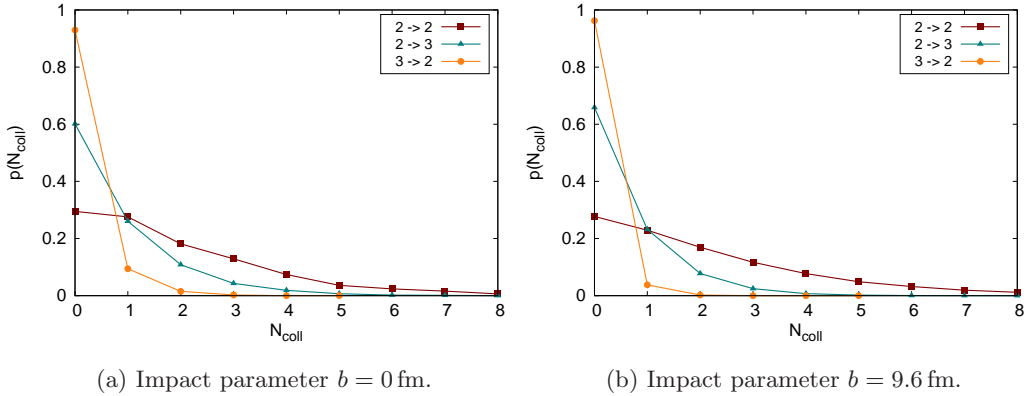


Figure 5.15.: Distribution of the number of $2 \rightarrow 2$, $2 \rightarrow 3$ and $3 \rightarrow 2$ interactions that a particle (gluon or quark) emerging with $p_T > 10$ GeV has undergone in simulations of Au + Au at 200 A GeV within BAMPS.

free path of the the parent particle λ as discussed in section 3.1.4 in full detail. However, the argument underlying the distinction between coherent and incoherent processes via a threshold $\tau = \lambda$ is of course a qualitative one. When effectively modeling the LPM effect via a cutoff the Theta function (3.20) could therefore be replaced by a more general form

$$\Theta\left(k_{\perp} - \frac{\gamma}{\lambda}\right) \rightarrow \Theta\left(k_{\perp} - X \frac{\gamma}{\lambda}\right), \quad (5.14)$$

where X is a real number not too far from 1.

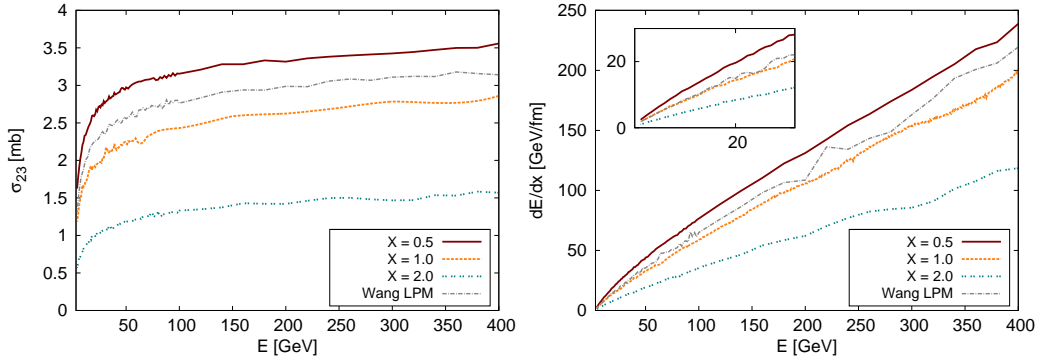
In this section the consequences of modifying the LPM cutoff by a factor X , as given in eq. (5.14), are discussed. Specifically $X = 0.5$, $X = 1$ (the usual choice) and $X = 2$ are chosen. This should provide a grasp on how sensitive the results for partonic energy loss and collective flow within BAMPS simulations are on the specific prescription for including the LPM effect.

The computation of the total cross section for radiative $2 \rightarrow 3$ processes involves an integral of the matrix element, eqs. (3.13) and (3.17), over the transverse momentum k_{\perp} , cf. eq. (3.37). It is therefore straightforward to conclude that a larger X in the cutoff (5.14) corresponds to a smaller total cross section. Though the actual dependence is not linear and indeed non-trivial, fig. 5.16a confirms this simple qualitative consideration. It shows the total cross section for $gg \rightarrow ggg$ processes in a gluonic medium with $T = 0.4$ GeV for different choices of X . The change in the cross section naturally corresponds to a change in the rate for this process via $R_{23} = \langle n\sigma_{23} \rangle$ and thus in the mean free path between radiative processes, $\lambda_{23} = 1/R_{23}$.

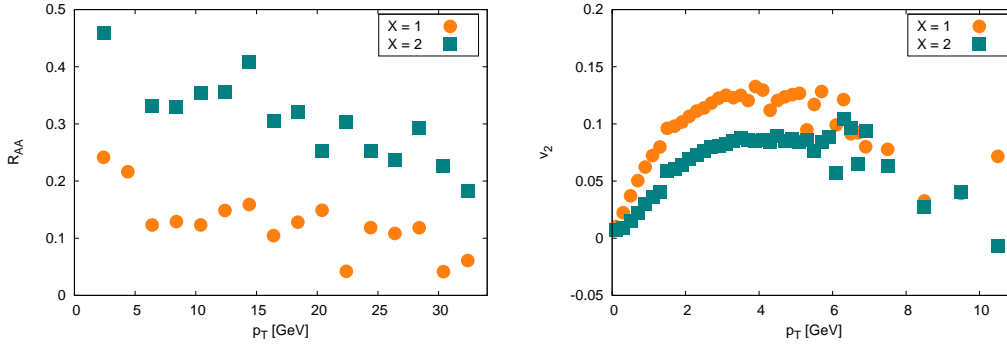
Correspondingly the differential energy loss dE/dx is affected by a change in the parameter X as illustrated in fig. 5.16b. Larger X leads to a larger mean free path and thus a smaller energy loss per path length. The change in dE/dx is mainly due to the change in the total cross section, while the effect of changes in X on the energy lost per single $2 \rightarrow 3$ interaction, ΔE_{23} , is rather small. A plot of ΔE_{23} and ω for different values of X is not explicitly given here but can be found in [FXG10].

Due to limited computing resources the investigation of the effect of a modified LPM cutoff (5.14) on observables in full simulations of heavy ion collisions is restricted to a comparison of the cases $X = 1$ and $X = 2$. As was to be expected from the change in the energy loss in a static medium, the level of jet quenching is considerably reduced when going from $X = 1$ to $X = 2$, as shown in fig. 5.16c. The nuclear modification factor of gluon jets is reduced by a factor of roughly 2 to 3 and the shape appears to be slightly more tilted, though the statistics of the data for this specific investigation hardly allow for a conclusive statement on the slope. The elliptic flow as depicted in fig. 5.16d is reduced by roughly 30% to 35% when going from $X = 1$ to $X = 2$, but the qualitative features as a function of p_T remain unaffected.

Note that the calculations underlying figs. 5.16c and 5.16d have been performed for a purely gluonic medium, $N_f = 0$. Also the slight violation of the small angle approximation for $2 \rightarrow 3$ processes, as discussed in section 3.1.3, had not yet been corrected for these calculations. However, the results in section 3.1.3 also showed that the quantitative consequences are small and thus the findings from figs. 5.16c and 5.16d hold: A parametric change in the LPM cutoff may strongly affect the level of jet quenching, while the effect on the magnitude of the elliptic flow is distinctly less pronounced.



- (a) Cross section $\sigma_{gg \rightarrow ggg}$ for a gluon jet that traverses a static medium with $T = 0.4$ GeV and $N_f = 0$ as a function of jet energy E . Shown are three different values for the factor X that modifies the effective LPM cutoff according to eq. (5.14). The gray dashed curve indicates the cross section when employing a radiation formation factor as discussed in section 5.6.2.
- (b) Total differential energy loss dE/dx of a gluon jet that traverses a static medium with $T = 0.4$ GeV and $N_f = 0$ as a function of jet energy E . Coding of lines as in fig. 5.16a.



- (c) Comparison of gluonic R_{AA} for different values of the parameter X in the effective LPM cutoff eq. (5.14). R_{AA} extracted at midrapidity ($y \in (-0.5, 0.5)$) for Au + Au at 200 A GeV with fixed impact parameter $b = 7$ fm and $N_f = 0$. Critical freeze out energy density is $\varepsilon_c = 0.6$ GeV/fm³.
- (d) Comparison of elliptic flow v_2 of gluons for different values of the parameter X in the effective LPM cutoff eq. (5.14). Simulation parameters as in fig. 5.16c.

Figure 5.16.: Comparison of crucial results for different schemes of the effective inclusion of the LPM effect.

5.6.2. LPM effect via a radiation formation factor

Modeling the LPM effect by a cutoff as detailed in section 3.1.4 is certainly a severe simplification of a rather complex and intrinsically quantum mechanical phenomenon. This procedure also introduces some freedom in the numerical implementation as illustrated in the previous section by means of a scaling factor X in the cutoff (5.14). Future studies should investigate the feasibility of a more fundamental incorporation of the LPM effect into a full scale transport model such as BAMPS. An interesting approach is provided by ZAPP et al. [ZSW09], who present a Monte Carlo model for in medium jet evolution that reproduces analytic results from the Bethe-Heitler to the deep incoherent regime. Whether this promising approach would be applicable to a full transport prescription that takes the dynamics of all particles into account as opposed to the usage of Monte Carlo generated scattering centers, needs careful consideration and is beyond the scope of this work. See also the discussion in section 6.2.2.

A more readily testable approach is provided by an early work of WANG, GYULASSY and PLÜMMER [WGP95]. They formulate the suppression of induced radiation from multiple scatterings in terms of a radiation formation factor that interpolates between the fully coherent factorization limit and the incoherent Bethe-Heitler limit. They find the spectrum of radiation associated with m scatterings to be proportional to the spectrum associated with a single scattering

$$\frac{dn^{(m)}}{dyd^2k_{\perp}} = C_m(k) \frac{dn^{(1)}}{dyd^2k_{\perp}}. \quad (5.15)$$

The radiation formation factor $C_m(k)$ is given as a coherent sum over all phase factors associated with the multiple scatterings and in the eikonal approximation for soft radiation with $k_{\perp} \ll q_{\perp} \sim m_D$ simplifies to

$$C_m(k) \approx m \frac{\chi^2}{1 + \chi^2} \frac{1 - (1 - 2r_2)\chi^2}{r_2(1 + \chi^2)^2}, \quad (5.16)$$

where $r_2 = C_A/(2C_2)$ is a simple color factor, $r_2 = 1/2$ for gluons and $r_2 = 8/9$ for quarks, and

$$\chi(k) = \lambda/\tau \quad (5.17)$$

is the ratio of the mean free path to the formation time of the emitted gluon. The parameter χ is readily identified with the argument of the Theta function in the cutoff (3.17). For large m the first term in eq. (5.16) dominates and the radiation from multiple scattering can therefore be regarded as being additive in the number of scatterings with each radiation suppressed by

$$\tilde{C}(k) = \frac{\chi^2}{1 + \chi^2}. \quad (5.18)$$

The formation factor $\tilde{C}(k)$ interpolates between the Bethe-Heitler ($\tau \ll \lambda$, $\tilde{C}(k) \approx 1$) and the factorization regime ($\tau \gg \lambda$, $\tilde{C}(k) \approx 0$ and $\tilde{C}_m \approx 1/r_2$).

Note that the work of WANG et al. does not take the rescattering of the radiated gluons into account in the derivation of the abovementioned results, an effect that plays a crucial role in the QCD case. Also the number of scatterings m might actually not be large in setups simulated within BAMPS, cf. fig. 5.15. Nevertheless, this discussion serves as a motivation to explore the consequences of substituting the strict cutoff (3.17) by a smooth interpolation

given by eq. (5.18). The gray dashed lines in figs. 5.16a and 5.16b illustrate the results of this study in terms of the cross section σ_{23} and the differential energy loss dE/dx for a purely gluonic setup, $N_f = 0$. To make the k_\perp integration in eq. (3.37) infrared safe in the absence of the cutoff function, the Debye mass is introduced as a lower bound for k_\perp for these calculations. The results in figs. 5.16a and 5.16b from using a smooth interpolation show no drastic deviation from the standard BAMPS cutoff (3.17) that is employed for the rest of the calculations presented in this work.

5.7. Jet quenching and elliptic flow at LHC from simulations with BAMPS

Very recently first results on Pb+Pb collisions at 2.76 A TeV have been published by the LHC experiments, most notably by the ALICE experiment [ALICE11, ALICE10b, ALICE10a] that is dedicated to heavy ion physics, but also by ATLAS [ATLAS10] and CMS [CMS11]. In this section a first attempt to explore the nuclear modification factor and the elliptic flow of Pb+Pb at 2.76 A TeV within the BAMPS framework is presented. A systematic study of simulations at various impact parameters is not repeated, rather exemplary calculations for $b = 0$ fm and for $b = 8.2$ fm are investigated. The choice of these impact parameters is determined by the reutilization of initial parton distributions computed via PYTHIA from [UFXG10a] as discussed in section 5.2.1.

5.7.1. Thermalization of the medium in Pb + Pb at 2.76 A TeV

Figure 5.17a shows the evolution of gluon spectra in the most central region, $|\eta| < 0.5$ and $x_T < 1.5$ fm, of Pb+Pb collisions simulated within the BAMPS framework with an impact parameter of $b = 0$ fm. The initial parton distribution is based on the PYTHIA event generator as detailed in section 5.2.1. The spectra show a thermalization of the medium at a time scale that is comparable to the thermalization in simulations of Au+Au at 200 A GeV, cf. section 5.4.2. The slope of quark spectra, not explicitly shown in fig. 5.17a, is identical to that of the gluon spectra after roughly $1 \text{ fm } c^{-1}$ to $2 \text{ fm } c^{-1}$. While in the initial parton distribution from PYTHIA the ratio of gluons to quarks is strongly dependent on the transverse momentum, varying from about 40 at $p_T = 0.5$ GeV to about 5 at $p_T = 5.0$ GeV, it becomes constant over the considered momentum range after $t = 1.5 \text{ fm } c^{-1}$. As for Au+Au at RHIC energies, cf. section 5.4.2, the quark yield however remains below the gluon yield throughout the whole evolution of the medium. At $t = 8 \text{ fm } c^{-1}$, roughly the time scale at which the central region reaches the critical energy density and freezes out, the yield of gluons at a given $p_T < 3$ GeV is roughly twice that of quarks at the same p_T .

5.7.2. Particle spectra and nuclear modification factor

While the initial parton distribution of the bulk for simulations at 2.76 A GeV is based on the PYTHIA event generator, the method of superimposed high- p_T particles based on GRV parton distribution functions is again employed for the investigation of jet suppression. As the GRV set of parton distribution functions is somewhat outdated, this might not be the most accurate choice for simulations at LHC energies. However it allows for direct compar-

ison to the results on the suppression of high- p_T particles from simulations of Au + Au at 200 A GeV and for a general assessment of the generic behavior of the suppression pattern.

Figure 5.17b shows the initial distribution of high- p_T partons for Pb + Pb at $b = 0$ fm that are thus obtained. The ratio of gluons to quarks is distinctly larger than in the initial parton distributions at 200 A GeV and gluons dominate over the entire transverse momentum range ($p_T < 35$ GeV) shown in fig. 5.17b. The spectra obtained from the mini-jet model using GRV parton distribution functions are harder than the experimentally measured spectra at 2.76 A TeV. The initial power law spectrum $d^2N/(p_T dp_T dy) \propto p_T^{-n}$ of charged hadrons obtained from the initial mini-jet distribution via fitting and fragmentation, as described in section 5.3, has a power law exponent of $n \approx 6.3$, while the scaled p + p reference at 2.76 A TeV, interpolated from measurements at $\sqrt{s_{NN}} = 0.9$ TeV and $\sqrt{s_{NN}} = 7.0$ TeV, on the other hand has $n \approx 7.4$ [ALICE11]. This confirms that the GRV set of parton distribution functions is not well suited to describe particle production at LHC energies. However, the results and discussions in section 5.5 showed that the nuclear modification factor is not very sensitive on the slope of the spectra and thus the approach should provide a solid first impression on how the suppression of high- p_T particles evolves when going from $\sqrt{s_{NN}} = 200$ GeV to $\sqrt{s_{NN}} = 2.76$ TeV.

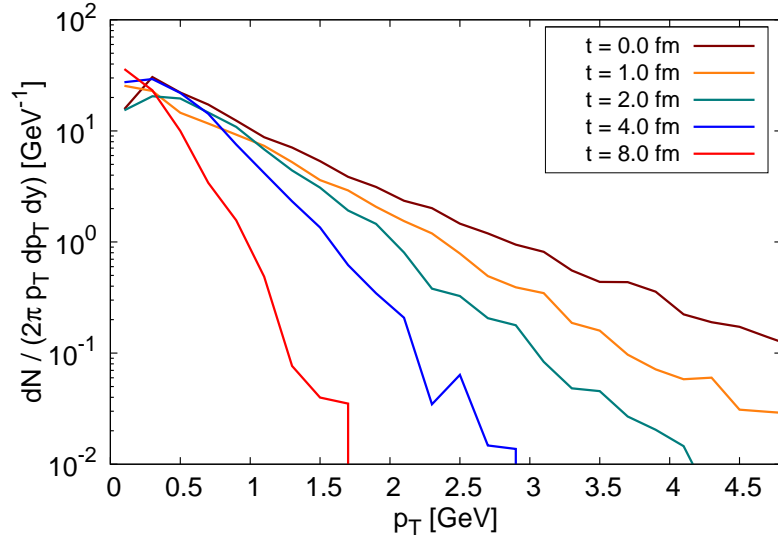
In fig. 5.18a the nuclear modification factor for charged hadrons in Pb + Pb at 2.76 A TeV obtained from simulations with BAMPS at $b = 0$ fm is shown. As in section 5.5 the R_{AA} of gluons and quarks is also shown for comparison and lines represent values of R_{AA} obtained from fits to the parton spectra, while symbols represent R_{AA} computed directly from the binned values of the parton yields. Furthermore, the nuclear modification factor of charged hadrons from simulations of Au + Au at 200 A GeV and $b = 0$ fm is included for comparison as a red dashed line. Finally R_{AA} of charged hadrons as recently published by the ALICE experiment [ALICE11] for 0%–5% central Pb + Pb collisions at 2.76 A TeV is also included.

Within the statistic fluctuations there is no significant difference in the suppression of charged hadrons simulated with BAMPS between Pb + Pb collisions at 2.76 A TeV and Au + Au collisions at 200 A GeV. As already for Au + Au the level of suppression computed from BAMPS is much stronger than the experimentally observed suppression. Furthermore, R_{AA} of charged hadrons as measured by ALICE exhibits a significant rise towards large p_T , a feature that is not reproduced by the results from BAMPS.

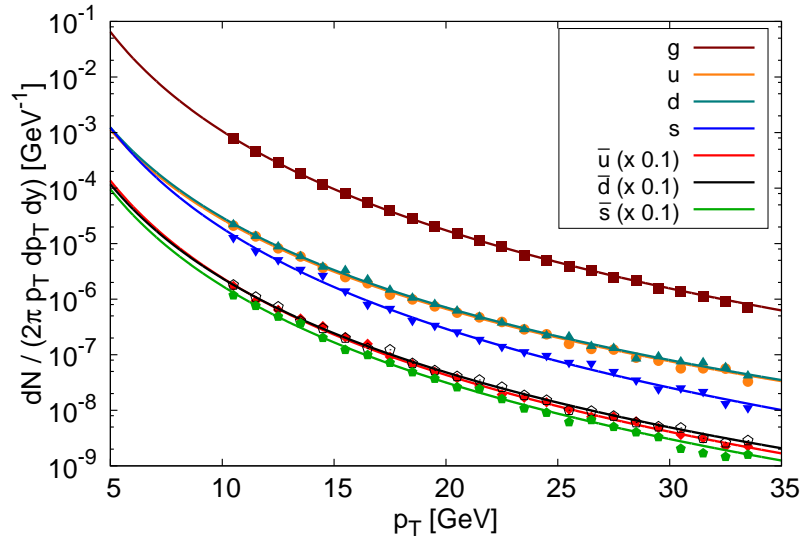
Within the transport model approach the insensitivity to the changes in the medium properties can be interpreted in terms of the strong surface bias that has been discussed in section 5.5. This interpretation however cannot account for the rather pronounced rise in R_{AA} , given that the energy loss within the BAMPS framework indeed strongly increases with the jet energy. Keeping possible caveats from the initial parton distribution and the crude comparison of $b = 0$ fm to 0%–5% centrality in mind, the simulated suppression of high- p_T charged hadrons in Pb + Pb is not only stronger than experimentally measured but also does not reproduce the behavior of R_{AA} as a function of p_T .

5.7.3. Elliptic flow

The elliptic flow in simulations of Pb + Pb collisions at the LHC energy of 2.76 A TeV is studied at the fixed impact parameter $b = 8.2$ fm using PYTHIA initial parton distributions. As discussed above, the choice $b = 8.2$ fm is motivated by the reutilization of initial parton distributions computed via PYTHIA from [UFXG10a]. A Glauber calculation using $\sigma_{NN} =$

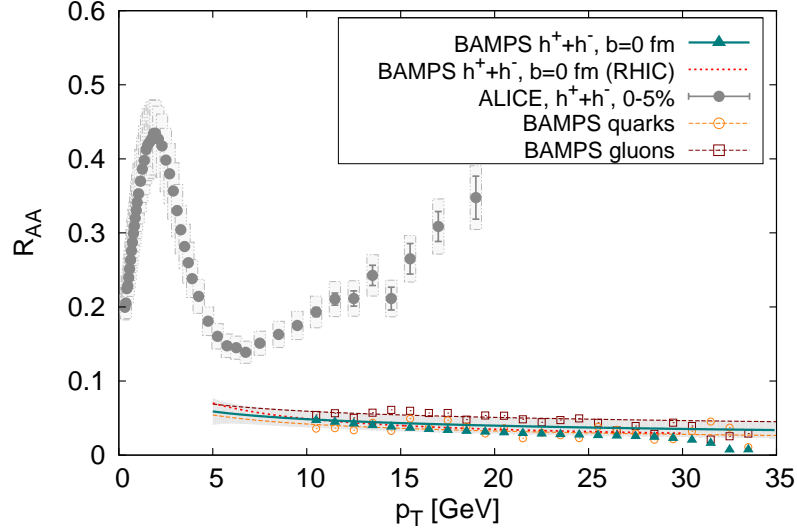


(a) Time evolution of the gluon spectra in the central region, $|\eta| < 0.5$ and $x_T < 1.5$ fm, for a Pb+Pb collision at 2.76 A TeV and $b = 0$ fm using initial distributions from PYTHIA.

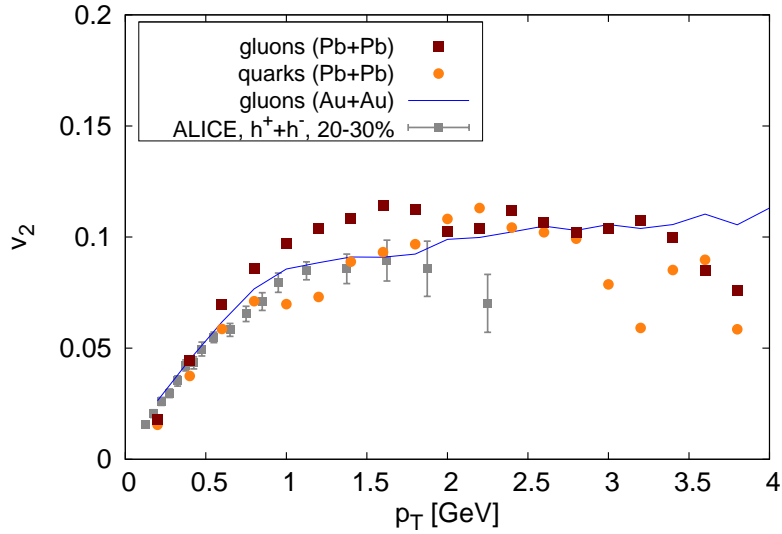


(b) Initial parton spectra from GRV parton distribution functions for simulations of high- p_T particles in Pb+Pb at 2.76 A TeV with an impact parameter $b = 0$ fm within the BAMPS framework. Symbols represent the spectra as directly extracted from BAMPS, while lines represent the fits to the spectra according to eq. (5.8).

Figure 5.17.: Parton spectra for simulations of Pb+Pb at 2.76 A TeV from simulations within the BAMPS framework.



(a) Nuclear modification factor R_{AA} of charged hadrons, gluons and quarks from BAMPS simulations of Pb + Pb at $b = 0$ fm compared to results from ALICE for 0%–5% central Pb + Pb collisions [ALICE11]. Lines indicate R_{AA} computed from fits to the parton spectra, while symbols indicate R_{AA} computed directly from the parton spectra as obtained from BAMPS. For comparison the R_{AA} of charged hadrons from simulations of Au + Au at 200 A GeV and $b = 0$ fm is also shown.



(b) Differential $v_2(p_T)$ of gluons and quarks from simulations of Pb + Pb at $b = 8.2$ fm extracted at $|\eta| < 0.75$. Simulation parameters: $\alpha_s = 0.3$ and $\varepsilon_c = 0.6$ GeV/fm³. For comparison the solid line shows the gluon v_2 from simulations of Au + Au at 200 A GeV and $b = 7.0$ fm. The Pb + Pb data from BAMPS is rescaled with eccentricity, cf. eq. (5.20). Experimental data from ALICE is shown for charged hadrons from 10%–20% and 20%–30% central Pb + Pb ($|\eta| < 0.8$) [ALICE10b], scaled by $n_q = 2$ as $v_2(p_T/n_q)/n_q$.

Figure 5.18.: Nuclear modification factor R_{AA} and differential elliptic flow $v_2(p_T)$ from simulations of Pb + Pb collisions at the LHC energy of 2.76 A TeV.

64 mb [ALICE10a] and based on a Woods-Saxon distribution with radius $R_A = 6.62$ fm and skin depth $d = 0.546$ fm yields $N_{\text{part}} \approx 232$ for Pb + Pb at $b = 8.2$ fm. The centrality class 10%–20% as measured by the ALICE experiment corresponds to a mean number of participants of $\langle N_{\text{part}} \rangle = 260.5 \pm 4.4$, while 20%–30% corresponds to $\langle N_{\text{part}} \rangle = 186.4 \pm 3.9$ [ALICE10a]. The fixed impact parameter $b = 8.2$ fm thus corresponds to a number of participants that is somewhere in between the centrality classes 10%–20% and 20%–30%. Future studies will require a more careful matching of experimental centrality classes. For the first assessment of LHC simulations within BAMPS that is presented in this work, however, the usage of $b = 8.2$ fm results that are rescaled by the initial eccentricity to roughly match the experimental centrality class 20%–30% is reasonably justified.

Figure 5.18b shows the differential elliptic flow $v_2(p_T)$ of gluons and quarks extracted from simulations of Pb + Pb at 2.76 A TeV and fixed impact parameter $b = 8.2$ fm within the BAMPS framework. For comparison the elliptic flow of gluons from simulations of Au + Au at 200 A GeV is shown by the thin lines for the impact parameter $b = 7.0$ fm, $N_{\text{part}} = 171$ corresponding to 20%–30% central Au + Au, cf. section 5.2.3. In order to accurately compare $v_2(p_T)$ from Pb + Pb at $b = 8.2$ fm to $v_2(p_T)$ from Au + Au at $b = 7.0$ fm and to the experimental data from ALICE at 20%–30% centrality [ALICE10b], the elliptic flow from Pb + Pb is rescaled by the initial eccentricity

$$\varepsilon = \frac{\langle y^2 - x^2 \rangle}{\langle y^2 + x^2 \rangle} \quad (5.19)$$

obtained from the Woods-Saxon distributions. The rescaling of the elliptic flow from Pb + Pb is done as

$$v_2^*(p_T) = v_2^{\text{PbPb}}(p_T, b = 8.2 \text{ fm}) \frac{\varepsilon^{\text{AuAu}}(b = 7.0 \text{ fm})}{\varepsilon^{\text{PbPb}}(b = 8.2 \text{ fm})}, \quad (5.20)$$

with $\varepsilon^{\text{AuAu}}(b = 7.0 \text{ fm}) = 0.323$ and $\varepsilon^{\text{PbPb}}(b = 8.2 \text{ fm}) = 0.377$. The experimental data for $v_2(p_T)$ of charged hadrons is scaled with the number of constituent quarks as $v_2(p_T/n_q)/n_q$ in order to compare to the partonic v_2 in a picture inspired by quark recombination models, cf. section 5.4.3. $n_q = 2$ is chosen for the rescaling of the data even though the measurement of charged hadrons also comprises charged baryons. Since the yields can be expected to be clearly dominated by pions however, the scaling with $n_q = 2$ should be sufficient for a first comparison.

The qualitative and most quantitative features of the differential elliptic flow from simulations of Pb + Pb at 2.76 A TeV are very similar to those from simulations of Au + Au at 200 A GeV. This similarity is in good agreement with the experimental finding that the differential $v_2(p_T)$ does not change when going from RHIC energies to LHC energies [ALICE10b]. Only the integrated v_2 is increased by roughly 30% due to an increased mean p_T . However, taking a closer look at the results from BAMPS simulations, some differences are in fact visible. The slight excess of gluon v_2 over quark v_2 at $p_T < 1$ GeV that has been seen in simulations of Au + Au seems not to be present in Pb + Pb at 2.76. Whereas around $p_T \approx 1.5$ GeV the elliptic flow of gluons is larger than that of quarks and also larger than found in Au + Au. The decrease towards large p_T appears to set in slightly earlier than observed in the Au + Au results. However, caution should be exercised in the quantitative assessment and comparison of the results from BAMPS, as statistics—especially for quarks—is still severely limited.

This should also be kept in mind when comparing to the experimental data points. As is the case in the Au + Au results, the experimental $v_2(p_T)$ scaled with the number of constituent quarks is in rather good agreement with the quark v_2 from BAMPS at $p_T \lesssim 2$ GeV. The gluon v_2 overshoots the rescaled v_2 of experimentally measured charged hadrons in the region 1 GeV to 2 GeV. But then—as already discussed in section 5.4—the details of hadronization in the low and intermediate p_T region are far from clear. The drop of v_2 towards larger p_T seems to set in slightly earlier in the Pb + Pb results than in the Au + Au results, but the last two data points vaguely suggest that the peak might still be away from the experimental data.

Which part of these features and quantitative deviations is in fact due to systematic differences in the description of the medium between simulations of Au + Au at RHIC energies and Pb + Pb energies and which part is still due to statistical fluctuations or the choice of the initial parton distributions—Au + Au at RHIC energy has been simulated using mini-jet distributions, while PYTHIA is used for Pb + Pb at LHC energy—cannot be answered decisively here and needs to be settled in future studies.

6. Summary and conclusions

In this chapter the main findings that have been presented in this work are summarized and discussed. Based on these results possible future studies and extensions of the transport model BAMPS are proposed.

6.1. Summary of the findings presented in this work

In this work the microscopic transport model BAMPS has been applied to describe the time evolution of the hot partonic medium that is created in heavy ion collisions at high energies, the quark-gluon plasma. More specifically, the ability of the BAMPS framework to simultaneously describe the suppression of high- p_T particles, quantified in terms of the nuclear modification factor R_{AA} , and the collective behavior of the medium, quantified in terms of the elliptic flow v_2 , has been studied. To this end the nuclear modification factor in simulations of Au + Au collisions at an energy per nucleon pair of $\sqrt{s_{NN}} = 200$ GeV, as measured at the experiments at the Relativistic Heavy Ion Collider, has been systematically studied at different impact parameters. The investigation of v_2 is based on previous works by XU and GREINER and has been extended to large transverse momenta.

The transport model BAMPS has been extended to include light quark degrees of freedom, i.e. to operate with a number of flavors $N_f = 3$, as compared to previous versions that had been limited to the description of a purely gluonic medium, $N_f = 0$. While many features of the medium created in heavy ion collisions can be investigated by studying a purely gluonic scenario, the incorporation of light quarks is crucial to facilitate a more detailed comparison to experimental results. In the context of the present work this is especially true for the comparison of the elliptic flow at intermediate transverse momenta, where a scaling with the number of valence quarks is experimentally observed. But primarily for high- p_T observables, such as the nuclear modification factor, it is essential to include light quarks as they dominate the initially produced parton spectra from $p_T \approx 20$ GeV on.

In the region of high transverse momenta in-vacuum fragmentation has been applied to the partonic spectra obtained from simulations within the BAMPS framework in order to compute hadronic spectra and the hadronic nuclear modification factor, cf. section 5.3. This had not been possible prior to the incorporation of light quarks into the model. The fragmentation of high energy partons is based on the recent AKK set of fragmentation functions that is obtained from global fits to experimental data.

The transport model BAMPS is based on leading order pQCD matrix elements and in addition to binary $2 \leftrightarrow 2$ processes consistently features particle multiplication and annihilation processes, $2 \leftrightarrow 3$. The strong coupling has been fixed to $\alpha_s = 0.3$ throughout this work. The radiative $2 \rightarrow 3$ processes are based on the Gunion-Bertsch matrix element, eq. (3.13), that has been studied together with its underlying approximations and assumptions in some detail within this work. The Landau-Pomeranchuk-Migdal effect is modeled in BAMPS via the introduction of a cutoff that effectively discards the coherent contribution

from multiple induced gluon radiation. This is done by comparing the mean free path of the radiating particle to the formation time of the emitted gluon. In order to consistently describe this comparison within the BAMPS framework, the correct treatment of Lorentz frames involved in this comparison has been presented in section 3.1.4. The incorporation of the Lorentz boost between different reference frames in the LPM cutoff has consequences on the shape of the phase space in $2 \leftrightarrow 3$ processes, especially for the interaction of a high energy particle with thermal constituents where due to the large boost an emission of the radiated gluon into the backward hemisphere is preferred.

6.1.1. High energy particles in a static medium

In order to systematically assess the quenching of high- p_T particles in simulations of heavy ion collisions, the evolution of high energy partons has first been studied within a simplified setup in chapter 4, namely for a scenario in which high energy partons traverse a thermal and static medium of light quarks and gluons. Both the collisional energy loss and the contribution of radiative processes implemented in BAMPS via the Gunion-Bertsch matrix element have been discussed in great detail. Inelastic $2 \rightarrow 3$ processes have been found to be the dominant source of energy loss for high energy partons in computations within the BAMPS framework, resulting in a strong differential energy loss that rises almost linearly with the jet energy. A gluon with $E = 50$ GeV traversing a medium with $T = 0.4$ GeV and $N_f = 3$ for example exhibits a total differential energy loss of $dE/dx \approx 39.1$ GeV fm⁻¹. While for the collisional energy loss the difference between gluon and quark jets is essentially determined by the relative color factor $9/4$, i.e. the collisional energy loss of gluon jets is roughly twice as strong as that of quark jets, the difference for radiative processes is much weaker within BAMPS. The resulting total energy loss of gluon jets is only roughly 20% larger than that of quark jets. This is due to the LPM cutoff for $2 \rightarrow 3$ processes, eq. (3.20), that depends on the current mean free path of the jet particle and thus in an iterative computation of the true mean free path effectively attenuates changes to the bare Gunion-Bertsch matrix element.

The strong mean energy loss in radiative processes is caused by a complex interplay of phase space configurations of outgoing particles in $2 \rightarrow 3$ interactions as dictated by the Gunion-Bertsch matrix element in combination with the effective LPM cutoff. This prefers the emission of radiated gluons into the backward hemisphere with energies that in the center of momentum frame are comparable to that of the remaining outgoing particles, while they are small in the laboratory frame. The jet energy in these cases can be almost evenly distributed among the two remaining particles, yielding a large energy loss. At high jet energies this causes a heavy tail in the ΔE distribution, shifting the mean energy loss per collision away from the most probable energy loss per collision.

There is a small but finite probability that the radiated gluon in $2 \rightarrow 3$ processes acquires the highest energy of all emerging particles and is thus regarded as the new jet particle. This probability decreases with increasing jet energy. Additionally, configurations in which the radiated gluon is emitted into the backward direction and the two remaining particles, due to momentum conservation, into the forward direction can cause conversions of the jet particle type in $qg \rightarrow qgg$ ($\bar{q}g \rightarrow \bar{q}gg$) processes. In environments in which quarks are undersaturated, as is the case for the medium created in heavy ion collisions, this effect strongly decreases the survival probability of quarks jets as they are converted into gluon

jets, cf. section 4.4.

For a purely gluonic medium with $T = 0.4$ GeV the transport parameter \hat{q} as defined in eqs. (4.11) and (4.12) stemming from binary $gg \rightarrow gg$ interactions has been found to be roughly constant at $\hat{q} = 2.3 \text{ GeV}^2 \text{ fm}^{-1}$. When including inelastic $gg \leftrightarrow ggg$ processes, \hat{q} as a measure of the accumulated transverse momentum exhibits a stronger dependence on the path length and is much larger than for elastic interactions, $\hat{q} = 12 \text{ GeV}^2 \text{ fm}^{-1}$ to $23 \text{ GeV}^2 \text{ fm}^{-1}$.

6.1.2. Simulations of heavy ion collisions

The simulations of the evolution of the partonic medium created in heavy ion collisions have been based on initial parton distributions from the mini-jet model for Au + Au collisions at the RHIC energy of 200 A GeV and on initial distributions obtained from the event generator PYTHIA for Pb + Pb collisions at the LHC energy of 2.76 A TeV. The interactions of medium constituents are stopped when the local energy density drops below $\varepsilon_c = 0.6 \text{ GeV fm}^{-3}$. This marks the freezeout criterion of the partonic matter within the BAMPS framework. The computation of observables at high transverse momenta, $p_T > 10 \text{ GeV}$, has been performed by superimposing particles generated from mini-jet spectra, both for RHIC and LHC, on a previously recorded medium evolution as described in section 5.2.1.

At low and intermediate transverse momenta the medium is dominated by gluons throughout the entire evolution of the fireball both in simulations of Au + Au at RHIC and in simulations of Pb + Pb at LHC. While the medium thus never reaches chemical equilibrium, the central region of the medium kinetically equilibrates on time scales on the order of $1 \text{ fm } c^{-1}$ to $2 \text{ fm } c^{-1}$ for both RHIC and LHC simulations. This is in perfect agreement with previous studies on thermalization for RHIC setups with a purely gluonic medium, cf. section 3.3.1. The temperature as obtained from the slope of the exponential particle spectra is identical for gluons and quarks after kinetic equilibration. Compared to calculations with $N_f = 0$, the temperature at a given time step is about 15% smaller in simulations including light quarks. This is due to the production of light quarks that are initially strongly undersaturated.

In the following the main findings are listed that have been obtained in this work from the simulations of heavy ion collisions within the BAMPS framework. The compilation focuses on the observables R_{AA} and v_2 and their comparison to experimental results. The discussion of $v_2(p_T)$ results for RHIC is based on a comparison at fixed impact parameter $b = 7.0 \text{ fm}$, roughly corresponding to 20%–30% central Au + Au collisions.

Au + Au at RHIC energy

Suppression of high- p_T particles

- The suppression of neutral pions and charged hadrons in BAMPS is distinctly stronger than experimentally measured by the PHENIX and STAR experiments.
- The nuclear modification factor $R_{AA}(p_T)$ extracted from BAMPS is slightly decreasing towards large transverse momenta but could within the statistic uncertainties also be compatible with a flat suppression pattern, which is within the experimental errors in agreement with data. The shape of the nuclear modification factor is similar at all simulated centralities.

- The nuclear modification factor of light quarks is smaller than that of gluons due to the strong conversion of quark jets into gluon jets.
- The surviving jets within the BAMPS framework exhibit a strong bias towards emission from regions close to the surface of the overlap region.
- The difference between the integrated R_{AA} from BAMPS and the integrated R_{AA} measured by the PHENIX experiment at RHIC depends on centrality. It varies from $R_{AA}^{\text{PHENIX}}/R_{AA}^{\text{BAMPS}} \approx 2$ for 40 %–50 % central Au + Au to $R_{AA}^{\text{PHENIX}}/R_{AA}^{\text{BAMPS}} \approx 4$ for 0 %–10 % Au + Au.
- Fitting the centrality dependence of R_{AA} by means of a fractional energy loss, $R_{AA} = (1 - S_0 N_{\text{part}}^a)^{n-2}$, yields a characteristic exponent $a = 0.39 \pm 0.02$, while fits to the experimental data give $a = 0.57 \pm 0.13$. The fractional energy loss $S_{\text{loss}} = S_0 N_{\text{part}}^a$ in this picture is $S_{\text{loss}} \approx 0.4$ for BAMPS simulations of 0 %–10 % central Au + Au, experimental data gives $S_{\text{loss}} \approx 0.2$.

Elliptic flow

- The differential v_2 of gluons and quarks is identical within the statistical uncertainties at low and intermediate transverse momenta. Only at $p_T \lesssim 1$ GeV a slight excess of gluon v_2 over quark v_2 is visible.
- The magnitude of elliptic flow has not changed much compared to calculations with $N_f = 0$. It is slightly enhanced at low transverse momenta, $p_T \lesssim 1.5$ GeV, and slightly decreased at intermediate transverse momenta, $1.5 \text{ GeV} \lesssim p_T \lesssim 4$ GeV.
- The partonic $v_2(p_T)$ from BAMPS simulations peaks at $p_T \approx 3$ GeV with $v_2(p_T = 3 \text{ GeV}) \approx 0.1$. Towards larger transverse momenta the elliptic flow slowly decreases which is in qualitative agreement with results from PHENIX.
- Scaling the measured $v_2(p_T)$ of neutral pions from PHENIX with the number of constituent quarks as $v_2^*(p_T) = v_2(p_T/n_q)/n_q$, the maximum magnitude of elliptic flow from BAMPS is in good agreement with the data. The peak in $v_2^*(p_T)$ within this picture of quark number scaling, however, is located at $p_T \approx 1.0$ GeV to 1.5 GeV and thus not in agreement with the results from BAMPS.

Pb + Pb at LHC energy

- The nuclear modification factor in simulations of central Pb + Pb at 2.76 A TeV is identical in shape and magnitude to the nuclear modification factor in simulations of central Au + Au at 200 A GeV.
- The value of R_{AA} in central Pb + Pb collisions computed with BAMPS is distinctly below the experimental value of R_{AA} measured by ALICE. Furthermore, the result from BAMPS does not reproduce the increase of R_{AA} towards large p_T that is observed at the LHC.
- The differential elliptic flow in simulations of Pb + Pb at 2.76 A GeV is very similar to that extracted from simulations of Au + Au at 200 A GeV. The peak of $v_2(p_T)$ appears to have shifted and is roughly located in the range $p_T \approx 1.5$ GeV to 2.5 GeV. The maximum value is slightly increased.
- The magnitude of the quark v_2 is in good agreement with experimental v_2 of charged

hadrons that is scaled with $n_q = 2$ as $v_2^*(p_T) = v_2(p_T/n_q)/n_q$ for $p_T \lesssim 1.75$ GeV. The elliptic flow of gluons is slightly above the experimental data for $p_T \gtrsim 1$ GeV.

Conclusions

While simulations of heavy ion collisions within the transport model BAMPS can reproduce many qualitative and some quantitative features of the experimentally observed R_{AA} and v_2 , the above summarized results of the present work lead to the conclusion that, in its current version using a fixed α_s , BAMPS cannot simultaneously describe the elliptic flow of the partonic bulk matter and the suppression of high- p_T particles on a quantitative level.

The collective flow of the partonic medium in the transport simulations is largely compatible with experimental results, especially in terms of the centrality dependence of the integrated v_2 , but the suppression of high- p_T particles is systematically stronger than indicated by the experimentally measured R_{AA} . Also, and maybe more severely, the centrality dependence of R_{AA} in BAMPS systematically differs from the experimental observations. The observed increase of R_{AA} towards large p_T in first measurements of R_{AA} at LHC is clearly not reproduced within the current setup of the BAMPS framework. On closer examination also the interpretation of the differential elliptic flow results at intermediate p_T is rather involved. While an interpretation in terms of a quark recombination picture is needed to successfully explain the magnitude of v_2 at intermediate p_T , the very same picture shifts the position of the maximum in the differential elliptic flow in a way that cannot be readily reconciled with experimental data.

The strong quenching of high- p_T particles within the BAMPS framework is due to radiative interactions based on the Gunion-Bertsch matrix element in a complex interplay with the effective implementation of the LPM effect via a cutoff that depends on the formation time τ of the radiated gluon and the current mean free path λ . This has three major consequences that together cause the strong suppression of high- p_T particles:

1. The large mean energy loss per radiative interaction

The large mean energy loss per radiative interaction, $\langle \Delta E_{23} \rangle$, is caused by the preferred emission of the radiated gluon into the backward direction due to the distortion of the phase space by the Lorentz boost that is involved in the comparison of τ and λ . This in turn leads to configurations in which the two remaining outgoing particles are emitted into the forward direction and might roughly split the available energy in equal shares, yielding a large energy loss ΔE_{23} .

2. The strong conversion of high energy quarks into gluons

This is also caused by the preferred emission of the radiated gluon into the backward direction. As there exist configurations in which the two remaining particles are both emitted into the forward direction, in $qg \rightarrow qgg$ processes the second gluon instead of the quark might obtain the largest outgoing energy. Additionally, at moderate jet energies there is a small but finite probability that the radiated gluon acquires the largest outgoing energy in the laboratory frame, further enhancing the conversion of quarks jets into gluons.

3. The small difference in the energy loss of quarks and gluons

The differential energy loss of quark jets is only about 20% smaller than that of

gluons even though the underlying Gunion-Bertsch matrix element is scaled by the conventional color factors that would roughly give a factor of 2 difference. This is caused by the dependence of the LPM cutoff on the current mean free path that requires an iterative computation of the interaction rates and effectively weakens the change introduced by the color factors.

While the results presented in this work thus demonstrate that the simultaneous description of R_{AA} and v_2 within the standard setup of BAMPS fails on the quantitative level, the discussion in section 5.6 has already illustrated that there are of course parameters to the model. The tuning of these parameters—within reasonable limits—might bring the results in better agreement with experimental data and should be explored in future studies. The two most crucial parameters in BAMPS enter when fixing the strong coupling and the LPM cutoff. Possible consequences of employing a dynamically determined coupling—a running coupling—instead of the canonically fixed value of $\alpha_s = 0.3$ are discussed below, in section 6.2.1. The discussion in section 5.6 has shown that parametric changes to the LPM cutoff, $\Theta(k_\perp - \frac{\lambda}{\lambda}) \rightarrow \Theta(k_\perp - X\frac{\lambda}{\lambda})$, might considerably reduce the suppression of high- p_T particles, while the changes to the differential elliptic flow would be rather modest. An appropriate tuning of the scaling factor X —to roughly $X = 1.5$ or $X = 2$, judging from the results in fig. 5.16—in combination with a running coupling scheme might thus provide phenomenological leverage to bring the BAMPS results in quantitative agreement with experimental data. See also section 6.2.2 for a discussion of a more fundamental treatment of the LPM effect that would dispense with the modeling via a kinematical cutoff altogether.

6.2. Future projects and possible extensions of the model

Based on the results and observations presented in this work, some possible extensions and enhancements of the transport model BAMPS are proposed in this section that might provide means of addressing the above discussed issues in future projects. Additionally, systematic studies are proposed that might help to assess the sensitivity of different observables on details of the modeling and to further improve the comparison to experimental data.

6.2.1. Implementation of running coupling

Throughout this work the strong coupling has been fixed to $\alpha_s = 0.3$. While this is a rather canonical—and certainly the most simple—approach, it is of course not entirely accurate. As already discussed in the introduction, the strong coupling depends on the momentum scale of the considered process, $\alpha_s(Q^2)$, cf. eq. (2.4), and decreases with increasing Q^2 . An incorporation of running coupling into the BAMPS framework might therefore lead to less energy loss and thus less suppression at high- p_T , while the coupling of bulk particles at low and intermediate p_T might be even enhanced. The dependence of α_s on the momentum scale might also help to bring the nuclear modification factor from BAMPS into accordance with the increase of R_{AA} towards large p_T that is observed at LHC. Even if that was the case, however, a qualitatively different behavior of R_{AA} as a function of p_T at RHIC and LHC would be difficult to describe. But, within the experimental errors, the measurement of R_{AA} at large transverse momenta at RHIC can currently not discriminate between a flat

suppression pattern and a moderate increase towards large p_T . Some data points suggest [PHENIX08a] that R_{AA} is actually also increasing with p_T at RHIC, in agreement with the qualitative behavior observed at LHC. This issue still needs to be settled experimentally.

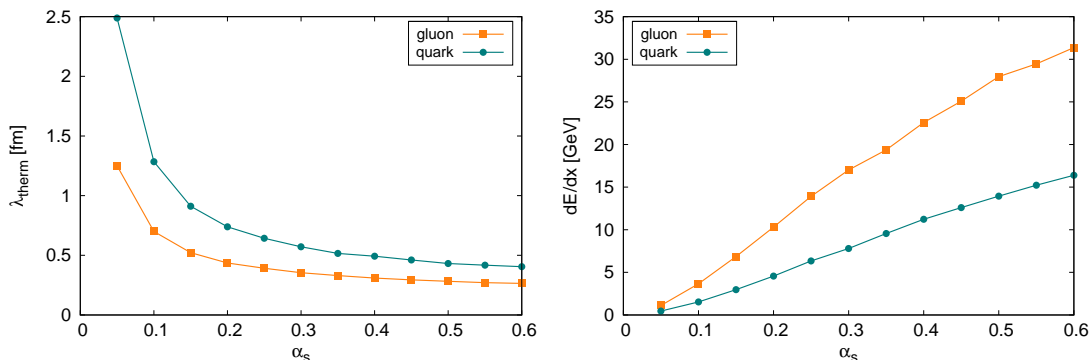


Figure 6.1.: Thermal mean free path λ_{therm} (left panel) and differential energy loss dE/dx (right panel) of gluons and quarks as a function of α_s . The given values are obtained from calculations of a static medium at $T = 0.4$ GeV as detailed in sections 4.1 and 4.2. The energy of the jet particle for which dE/dx is given in the right panel is $E = 20$ GeV.

Figure 6.1 illustrates the dependence of the thermal mean free path and of the differential energy loss on α_s . While the change in the thermal mean free path is rather moderate when going from the current choice of $\alpha_s = 0.3$ to larger values of α_s , the differential energy loss depends rather strongly on α_s . This reinforces the qualitative arguments made above. Note however, that the results in fig. 6.1 have been obtained within the current framework, i.e. by using fixed values of α_s . In a correct treatment of the running coupling, $\alpha_s(Q^2)$ needs to be explicitly included on the level of the matrix elements, with α_s being evaluated at the virtuality of the respective channel. The momentum dependent coupling would thus be included in the integration of the matrix elements yielding the total cross sections as well as in the sampling of phase space configurations according to the matrix elements. This approach is already pursued in studies of collisional energy loss and elliptic flow of heavy quarks within BAMPS [UFXXG10b, UFXXG11]. The numerical evaluation is thus considerably more involved than what can be concluded from the simple qualitative arguments given above.

The approach is indeed promising, but a conclusive assessment of its impact on elliptic flow and jet quenching results from BAMPS and their comparison with experimental results requires a careful and quantitative investigation.

6.2.2. Reassessment of Gunion-Bertsch and the modeling of the LPM effect

As pointed out in the summary of the results that have been presented in this work, it is the peculiar and complex features of radiative processes based on the Gunion-Bertsch matrix element in cooperation with the effective treatment of the Landau-Pomeranchuk-Migdal effect via a mean free path dependent cutoff that ultimately lead to the strong suppression of high- p_T particles within the BAMPS framework. An independent validation

of this approach would therefore be extremely beneficial.

As discussed in great detail in section 3.2, the Gunion-Bertsch matrix element is based on various assumptions. The implementation of a more general treatment of $2 \rightarrow 3$ processes would therefore be desirable. However, the numerical and conceptual challenges would be very high, as can be readily guessed from the exact matrix element (3.79). Moreover, a comparison of the Gunion-Bertsch matrix element to the exact solution that has been presented in section 3.2.3, shows only rather moderate deviations. Although the magnitude of the deviations also depends on the specific configuration, which might affect the available phase space for $2 \rightarrow 3$ interactions.

More crucial would be an independent reassessment of the modeling of the LPM effect. A fundamental and exact incorporation of this inherently quantum mechanical effect into a microscopic transport model that operates with semi-classical Boltzmann particles is certainly not possible. However, ZAPP et al. have presented a promising approach in their Monte Carlo model for in medium jet evolution that reproduces analytic results from the Bethe-Heitler to the deep incoherent regime [ZSW09]. It is based on the idea of dynamically changing the formation time of the radiated gluon by subsequent momentum transfers from elastic scatterings. Whether this approach could be applicable to a full scale transport model calls for a thorough investigation. An implementation, if conceptually possible, would require changes to the very core of the BAMPS algorithms. At the very least, particles involved in radiative processes would need to “remember” their association with each other, such that the current formation time of the previously radiated gluon can be evaluated when deciding whether a new radiative process could occur and whether the radiated gluon is formed and thus allowed to scatter itself.

Judging from the experience gained in the course of the studies presented in this work, the implementation of this procedure should in principle be possible. See also [CSBS11] for a first attempt to incorporate this approach into a partonic transport model. In case of excessive numerical expense, the limitation to high- p_T processes might be conceivable. The comparison to the current approach would be very exciting and although this is clearly not a short-term project, it should thus be pursued.

6.2.3. Investigation of possible hadronization scenarios

As already extensively discussed, the hadronization of the partonic degrees of freedom present in BAMPS is crucial to the comparison of the results to experimental data. Important examples are the differential elliptic flow at low and intermediate p_T , cf. section 5.4, and the different contributions of high- p_T quarks and gluons to the suppression of hadrons at large transverse momenta, cf. sections 5.3 and 5.5.

The application of fragmentation functions to the partonic spectra for large transverse momenta has been presented in this work in section 5.3. However, the direct implementation of a Monte Carlo fragmentation scheme on a single particle level within the BAMPS framework—as already discussed in section 5.3.1—would certainly be desirable and would allow for the analysis of more differential observables on a single hadron level and also for the analysis of jet reconstruction schemes via cone [SS07] or k_\perp [DLMW97] and anti- k_\perp algorithms [CSS08]. The latter would for example facilitate the investigation of dijet asymmetry as measured at the LHC by ATLAS [ATLAS10] and CMS [CMS11], while the former would include the study of azimuthal single hadron correlations.

For the hadronization of the bulk particles different schemes are conceivable. Inspired by hydrodynamic models, the hadronization could be done by a Cooper-Frye freezeout prescription [CF74]. In an approach very similar to the combination of hydrodynamics with the UrQMD model by PETERSEN et al. [PSB⁺08], the partonic stage might then be followed by a hadronic transport model. The clear disadvantage of this hadronization scheme is that all microscopic information is lost within the freezeout procedure. More microscopic approaches might be provided by quark recombination models [FMNB03, MV03, GKL03] or by the dynamic generation of hadrons via an effective approach that is based on gluons scattering into pions.

The investigation of these possibilities is underway but also not a short-term project. In any case the question how the hadronization of high- p_T particles via fragmentation can be consistently matched to the hadronization of bulk particles will need to be carefully investigated.

6.2.4. Systematic studies of the sensitivity on initial conditions and fluctuations

Independent of the above discussed extensions of the model, systematic studies of different initial parton distributions and the sensitivity of the result on fluctuations of these initial distributions might be useful to further evaluate the robustness and predictive power of results extracted from simulations within the BAMPS framework.

The GRV parton distribution functions used in the mini-jet model, cf. section 5.2.1, are clearly outdated and should be superseded by more recent parametrizations of the parton distribution functions provided by the Les Houches Accord PDF Interface [WBG05]. The results based on these initial distributions should be systematically compared to initial distributions from other approaches such as the Monte Carlo event generator PYTHIA, cf. section 5.2.1, or parametrizations of the color glass condensate [MV94, DM02]. Also the consequences of cold nuclear matter effects, see the discussion in section 5.5.1, could be included in such systematic studies.

Additionally, the investigation of event-by-event fluctuations within the BAMPS framework might be worthwhile, especially with respect to flow observables. As the use of test particles intrinsically washes out initial fluctuations, an approach similar to hydrodynamic studies of fluctuating initial distributions would have to be pursued. The initial distribution of real particles from nucleon-nucleon collisions according to the Glauber model would have to be translated to a continuous distribution that reflects the fluctuations of these initial production points, for example by representing each real particle by a Gaussian and subsequently adding these to obtain a global distribution. The sampling of test particles would then be done according to the so generated distribution instead of the smooth Woods-Saxon distribution. See for example [SJG11b, PSB⁺08]. To facilitate a more realistic comparison of flow observables from such studies to experimental data, it might be advisable to adopt and explore different experimental schemes for determining flow observables, such as the cumulant method. See [VPS08] for an extensive review.

The main obstacle for such studies, however, is the very severe requirement of computing resources for simulations of heavy ion collisions within the BAMPS framework. With the computation time for a single event ranging from a couple of hours to a couple of days, a systematic comparison of different initial distributions becomes very difficult. Unless substantial improvements to the performance of the underlying algorithms are made, the

assessment of the sensitivity of the results on, for example, various initial conditions will therefore be limited to isolated studies.

Appendices

A. Notation and conventions

A.1. Units

As in most publications on particle or high-energy nuclear physics, natural units [HM84] are used throughout this document. In these units the speed of light, the Planck constant and the Boltzmann constant are set to unity, i.e.

$$c = \hbar = k_B := 1. \quad (\text{A.1})$$

This implies that momenta, masses, temperatures and energies can all be expressed in units of energy. Conventionally the electron-volt

$$1 \text{ eV} = 1.602\,176\,487(40) \cdot 10^{-19} \text{ J} \quad (\text{A.2})$$

is chosen with appropriate SI-prefixes. Energies and temperatures in the physical settings covered in this work are usually in the megaelectronvolt (MeV) or gigaelectronvolt (GeV) range. Since the charge radius of a proton is on the order of a femtometer ($1 \text{ fm} = 1 \cdot 10^{-15} \text{ m}$), lengths and times are usually expressed in multiples of a femtometer. Note that, though the choice $c = 1$ is made and thus length and time have the same unit, it is nevertheless often useful to explicitly denote times in units of $\text{fm } c^{-1}$.

Due to the choice (A.1) the units GeV and fm are linked via

$$0.1972 \text{ GeV fm} := 1. \quad (\text{A.3})$$

Thus length can be expressed in units of inverse energy and vice versa, with the conversions

$$1 \text{ GeV} = \frac{1}{0.1972} \text{ fm}^{-1} \quad (\text{A.4})$$

$$1 \text{ fm} = \frac{1}{0.1972} \text{ GeV}^{-1}. \quad (\text{A.5})$$

For illustrative purposes, in the following some conversions from natural to SI-units (rounded to three significant digits) are listed:

Energy	$1 \text{ GeV} = 1.60 \cdot 10^{-10} \text{ J}$
Momentum	$1 \text{ GeV} = 5.34 \cdot 10^{-19} \text{ kg m s}^{-1}$
Mass	$1 \text{ GeV} = 1.78 \cdot 10^{-27} \text{ kg}$
Temperature	$1 \text{ GeV} = 1.16 \cdot 10^{13} \text{ K}$
Length	$1 \text{ GeV}^{-1} = 1.97 \cdot 10^{-16} \text{ m}$
Time	$1 \text{ fm } c^{-1} = 3.34 \cdot 10^{-24} \text{ s}$
Cross section	$1 \text{ GeV}^{-2} = 0.389 \text{ mb}.$

When quoting the center of mass energy \sqrt{s} of a heavy ion collision, usually the number is given per nucleon-nucleon pair, since this is the relevant quantity when comparing to proton-proton collisions. For this, two notations are commonly used

$$\sqrt{s_{NN}} = 200 \text{ GeV}$$

or, for symmetric collisions with identical nuclei,

$$\sqrt{s} = 200 A \text{ GeV} .$$

A is the mass number, i.e. the number of protons plus number of neutrons, $A = Z + N$, of the colliding nuclei. The total energy of the collision is then A times the given number. In this work mostly the notation of the center of mass energy in units of A GeV is used.

A.2. Notation

Vectors

\mathbf{p} three-vector

p, p^μ four-vector

Rates and probabilities

$R_{X \rightarrow Y}^g$ Contribution to the rate per single gluon from the process $X \rightarrow Y$.
 $R_{X \rightarrow Y}^q$ and $R_{X \rightarrow Y}^{\bar{q}}$ accordingly.

R_i^g Contribution to the rate per single gluon from the process of type i
(index for summation etc.). R_i^q and $R_i^{\bar{q}}$ accordingly.

$R_i^{(j)}$ Contribution to the rate per particle of type j from the process i .

R_{22}^g Rate per single gluon from all $2 \rightarrow 2$ processes. R_{22}^q, R_{23}^g etc. accordingly.

R_{22} Generic notation for the rate from all $2 \rightarrow 2$ processes when the type of the considered particle is not relevant or clear from the context.

R^g Total rate per single gluon, $R^g = \sum_i R_i^g$. R^q and $R^{\bar{q}}$ accordingly.

$P_{X \rightarrow Y}$ Probability for the process $X \rightarrow Y$ to occur within a spatial volume ΔV
and a time interval Δt .

Particle numbers and densities

N_g	Number of gluons in a given volume.
$N_q^{(f)}$	Number of quarks of flavor f (up, down, strange) in a given volume.
$N_{\bar{q}}^{(f)}$	Number of antiquarks of flavor f (anti-up, anti-down, anti-strange) in a given volume.
N_q	Number of quarks in a given volume. $N_q = \sum_f N_q^{(f)}$.
$N_{\bar{q}}$	Number of antiquarks in a given volume. $N_{\bar{q}} = \sum_f N_{\bar{q}}^{(f)}$.
N	Total number of particles in a given volume. $N = N_g + N_q + N_{\bar{q}}$.
n_g	Density of gluons.
$n_q^{(f)}$	Density of quarks of flavor f (up, down, strange).
$n_{\bar{q}}^{(f)}$	Density of antiquarks of flavor f (anti-up, anti-down, anti-strange).
n_q	Density of quarks. $n_q = \sum_f n_q^{(f)}$.
$n_{\bar{q}}$	Density of antiquarks. $n_{\bar{q}} = \sum_f n_{\bar{q}}^{(f)}$.
n	Total density of particles. $n = n_g + n_q + n_{\bar{q}}$.

Miscellaneous

N_c	Number of colors. $N_c = 3$.
N_f	Number of flavors. In this work only the cases $N_f = 0$ (only gluons) and $N_f = 3$ (gluons plus three flavors of light quarks with mass $m = 0$ GeV) are considered.
N_{test}	Number of test particles per real particle.
$N_{X \rightarrow Y}$	Number of $X \rightarrow Y$ processes in a given cell ΔV and time step Δt .
$2 \rightarrow 2$	Symbolic shorthand for: Interaction with two-particle initial state and two-particle final state, e.g. $gq \rightarrow gq$.
$2 \rightarrow 3$	Symbolic shorthand for: Interaction with two-particle initial state and three-particle final state, e.g. $gg \rightarrow ggg$.
$3 \rightarrow 2$	Symbolic shorthand for: Interaction with three-particle initial state and two-particle final state, e.g. $ggg \rightarrow gg$.

A.3. On the term “jet”

When physicists from different areas of heavy ion physics are brought into a room to discuss jet physics, there is likely to be some dissent on what the term “jet” actually refers to.

On the partonic level immediately after the initial hard collision the situation is probably the clearest. The emerging parton with high transverse momentum is a jet. Subsequently this parton evolves in virtuality by radiating off (soft) gluons—either in vacuum or in medium. Now the jet can either be the leading parton or the leading parton plus the associated shower of gluons.

These partons are of course not accessible experimentally due to confinement—what is measured are the emerging hadrons that for high energy partons are produced in fragmentation processes. In experimental discussions the term “jet” can therefore either be used for a single measured hadron with high transverse momentum or for the collection of hadrons emerging from the parton shower related to the initially produced hard parton. In the latter case the hadrons belonging to the shower need to be carefully identified by special algorithms in order to recover energy and momentum of the initial hard parton as accurately as possible. So called *cone* [SS07], k_T [DLMW97] and *anti- k_T* [CSS08] algorithms are the most widely used types of algorithms to perform this clustering. With the recent progress in this sort of analysis at RHIC [STAR09, PHENIX09c] and the jet reconstruction analysis of the first LHC data [ATLAS10, CMS11], this notion of the term “jet” is more and more becoming the new paradigm.

In this work however, the term “jet” refers to a single hard parton traversing a partonic medium. Since BAMPS is an on shell transport model (i.e. there is no gluon radiation due to an evolution in virtuality) that exclusively deals with partonic degrees of freedom, this notation is the most obvious choice.

B. Matrix elements and cross sections

The purpose of this appendix is to provide an overview of the fundamental terms and the basic definitions and relations for the reader. It does not comprehend mathematically rigorous or self-contained derivations of the presented quantities. Detailed discussions can be found in various textbooks on the subject, such as [PS95, HM84, Gro80], and in the reviews of the Particle Data Group [PDG10].

B.1. The invariant matrix element

To establish a basis, the definition of the invariant matrix element is briefly reviewed¹. The transition probability between two initial wavepacket states $|\phi_A\phi_B\rangle_{in}$ and several final wavepacket states $|\phi_1\phi_2\cdots\rangle_{out}$ in an interacting field theory is given by the overlap of the two states

$$\mathcal{P} = |{}_{out}\langle\phi_1\phi_2\cdots|\phi_A\phi_B\rangle_{in}|^2. \quad (\text{B.1})$$

Using this notation, the ingoing wavepackets are prepared at the infinite past, while the outgoing wavepackets are taken at a time infinitely in the future. Expanding the wavepackets as superpositions of definite momentum states $\langle\phi| = \int \frac{d^3p}{(2\pi)^3} \frac{\phi(\mathbf{p})}{\sqrt{2E}} \langle\mathbf{p}|$ and leaving the integrations in phase space for later, the transition probability is governed by the overlap of the momentum states

$${}_{out}\langle\mathbf{p}_1\mathbf{p}_2\cdots|\mathbf{p}_A\mathbf{p}_B\rangle_{in}. \quad (\text{B.2})$$

In order to compute this overlap, the states need to be taken at a common time. The necessary time evolution is mediated by an operator \mathcal{S} , the \mathcal{S} -matrix

$${}_{out}\langle\mathbf{p}_1\mathbf{p}_2\cdots|\mathbf{p}_A\mathbf{p}_B\rangle_{in} = \langle\mathbf{p}_1\mathbf{p}_2\cdots|\mathcal{S}|\mathbf{p}_A\mathbf{p}_B\rangle. \quad (\text{B.3})$$

All information on the interacting features of the field theory are contained in the \mathcal{S} -matrix. Since there is in general a finite probability of no interaction at all, the non-interacting part is split off and the \mathcal{S} -matrix can be written as

$$\mathcal{S} = \mathbf{1} + i\mathcal{T} \quad (\text{B.4})$$

where \mathcal{T} now solely contains the information on the interaction between the incoming states (particles). To ensure four-momentum conservation, \mathcal{T} always contains $\delta^{(4)}(\mathbf{p}_A + \mathbf{p}_B - \sum_i \mathbf{p}_i)$. Extracting this factor finally yields the invariant matrix element \mathcal{M} , defined via

$$\langle\mathbf{p}_1\mathbf{p}_2\cdots|i\mathcal{T}|\mathbf{p}_A\mathbf{p}_B\rangle = (2\pi)^4 \delta^{(4)}(\mathbf{p}_A + \mathbf{p}_B - \sum_i \mathbf{p}_i) \cdot i\mathcal{M}. \quad (\text{B.5})$$

The merit of this notation is that the invariant matrix element \mathcal{M} can be computed from a perturbative expansion of the field theory using the technique of Feynman diagrams.

¹The rough outline presented here follows the argumentation of PESKIN and SCHROEDER [PS95], see their book for a more detailed and rigorous derivation.

B.2. The definition of the cross section

The question is how the invariant matrix element \mathcal{M} , computed from Feynman diagrams, can be connected with a measurable quantity. For this, typically the *cross section*, σ , is chosen to characterize a specific interaction. It has units of area (usually given in *barn*, $1 \text{ b} = 10 \cdot 10^{-24} \text{ cm}^2$) and represents a hypothetical area around the target particle. It can be interpreted analogously to the geometrical cross section of a particle, i.e. an interaction takes place when a beam particle hits the target particle within this area. The cross section can be related to a measurable quantity in a scattering experiment in various ways. For example the counting rate of a given type of interactions for a beam with flux $F_b = n_b v_b$, where n_b is the particle density of the beam and v_b its velocity, hitting N_T target particles at rest is given by

$$R = F_b N_T \sigma . \quad (\text{B.6})$$

The definition of the cross section itself contains a flux factor $1/F$, where $F = 2E_A 2E_B |\mathbf{v}_A - \mathbf{v}_B|$ in the laboratory frame for particle A hitting particle B with the relative velocity $|\mathbf{v}_A - \mathbf{v}_B|$. In the center of momentum frame this can be rewritten as $F = 4|\mathbf{p}_A| \sqrt{s}$, which in the case of massless particles further simplifies to

$$F = 2s . \quad (\text{B.7})$$

Combining the flux factor with the definition of the matrix element (B.5) and recollecting all the phase space integration omitted previously, the *total cross section* for a given process $AB \rightarrow 12 \dots f$ (with massless particles) finally reads

$$\sigma = \frac{1}{2s} \frac{1}{\nu} \left(\prod_{i=1}^f \int \frac{d^3 p_i}{(2\pi)^3 2E_i} \right) (2\pi)^4 \delta^{(4)}(p_A + p_B - \sum_{i=1}^f p_i) |\mathcal{M}_{AB \rightarrow 12 \dots f}|^2 , \quad (\text{B.8})$$

where $\left(\prod_{i=1}^f \int \frac{d^3 p_i}{(2\pi)^3 2E_i} \right)$ symbolically represents the f -dimensional phase space integral with the integration applying to the terms outside the parentheses as well. The factor $1/\nu$ is inserted to account for identical particles in the final state.

In addition to the total cross section one is often interested in *differential cross sections* that characterize the scattering into a specific part of phase space. The differential cross section can be obtained by omitting the integration over the phase space variable in question in eq. (B.8), possibly after an adequate transformation of variables. Formally, the differential cross section $d\sigma/dx$ with $x = x(\mathbf{p}_1, \mathbf{p}_2, \dots, \mathbf{p}_f) \equiv x(\underline{\mathbf{p}})$ can be represented as

$$\frac{d\sigma}{dx} = \frac{1}{2s} \frac{1}{\nu} \left(\prod_{i=1}^f \int \frac{d^3 p_i}{(2\pi)^3 2E_i} \right) (2\pi)^4 \delta^{(4)}(p_A + p_B - \sum_{i=1}^f p_i) \delta(x - x(\underline{\mathbf{p}})) |\mathcal{M}_{AB \rightarrow 12 \dots f}|^2 . \quad (\text{B.9})$$

Popular examples of differential cross sections are $d\sigma/dt$, the differential cross section for a given Mandelstam t , and $d\sigma/dq_{\perp}^2$, the differential cross section for a given transverse momentum transfer q_{\perp}^2 . They can be related to $d\sigma/d\Omega$, the differential cross section for a scattering into a given solid angle $d\Omega = \sin \theta d\theta d\phi$.

B.3. Parton-parton cross sections in small angle approximation

B.3.1. Kinematics

Let us first consider some basic kinematics of a binary scattering of massless partons. In the center of momentum frame the two incoming particles have momenta $k_A = (E, k\mathbf{e}_z)$ and $k_B = (E, -k\mathbf{e}_z)$. The outgoing particles have momenta $p_1 = (E, \mathbf{p})$ and $p_2 = (E, -\mathbf{p})$. The scattering angle is θ with $\cos\theta = \frac{\mathbf{p}\cdot\mathbf{e}_z}{|\mathbf{p}|}$, see fig. B.1.

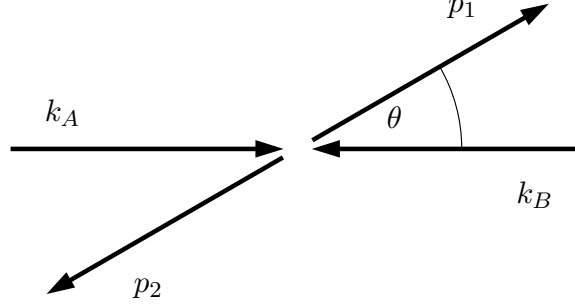


Figure B.1.: Illustration of the kinematics for a binary collision in the center of momentum frame.

The Mandelstam variables for this process are

$$s = (k_A + k_B)^2 = (p_1 + p_2)^2 \quad (\text{B.10a})$$

$$t = (p_1 - k_A)^2 = (p_2 - k_B)^2 \quad (\text{B.10b})$$

$$u = (p_1 - k_B)^2 = (p_2 - k_A)^2. \quad (\text{B.10c})$$

The three-momentum transfer is given by

$$\mathbf{q}^2 = (\mathbf{p}_1 - \mathbf{k}_A)^2 = \frac{s}{2}(1 - \cos\theta) \quad (\text{B.11})$$

since $k = |\mathbf{p}| = E = \sqrt{s}/2$. Furthermore, from the definitions of the Mandelstam variables one obtains

$$t = -\frac{s}{2}(1 - \cos\theta) = -\mathbf{q}^2 \quad (\text{B.12a})$$

and

$$u = -\frac{s}{2}(1 + \cos\theta). \quad (\text{B.12b})$$

The latter could also be derived from $s + t + u = 0$ (in general $s + t + u = \sum_i m_i^2$). Projecting onto the direction of $\mathbf{k}_A = k\mathbf{e}_z$ the momentum transfer can be decomposed into $\mathbf{q}^2 = \mathbf{q}_{\parallel}^2 + \mathbf{q}_{\perp}^2$, with

$$\mathbf{q}_{\parallel}^2 = \frac{s}{4}(1 - \cos\theta)^2 \quad (\text{B.13a})$$

$$\mathbf{q}_{\perp}^2 = \frac{s}{4}\sin^2\theta. \quad (\text{B.13b})$$

Expanding the parallel component, \mathbf{q}_{\parallel}^2 , and the transversal component, \mathbf{q}_{\perp}^2 , to the momentum transfer in Taylor series around $\theta = 0$ one obtains $\mathbf{q}_{\parallel}^2 = \frac{s}{16}\theta^4 + \mathcal{O}(\theta^6)$ and $\mathbf{q}_{\perp}^2 = \frac{s}{4}\theta^2 + \mathcal{O}(\theta^4)$. For $\theta \rightarrow 0$ thus \mathbf{q}_{\perp}^2 dominates the total momentum transfer and for *small angle scattering*

$$t \underset{\theta \rightarrow 0}{\approx} -\mathbf{q}_{\perp}^2. \quad (\text{B.14})$$

For angles larger than $\pi/2$ the Mandelstam variables t and u basically switch roles, as

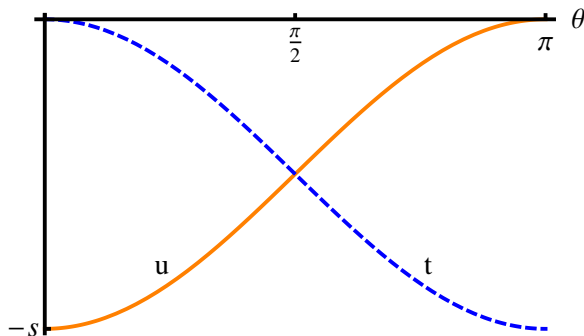


Figure B.2.: Mandelstam t and u as a function of the scattering angle θ .

illustrated in fig. B.2. For $\theta \rightarrow \pi$ one therefore obtains $u \approx -\mathbf{q}_{\perp}^2$.

B.3.2. The small angle approximation

Computing differential cross sections from Feynman diagrams, the results are often in terms of Mandelstam variables, most prominently $d\sigma/dt$. For the numerical sampling of the outgoing momenta a representation in terms of the momentum transfer \mathbf{q} is more convenient. The connection can be made via eq. (B.12a) and $\sigma = \int_{-s}^0 \frac{d\sigma}{dt} dt = \int_0^s \frac{d\sigma}{d\mathbf{q}^2} d\mathbf{q}^2$, so one obtains the differential cross section in \mathbf{q} simply via²

$$\frac{d\sigma}{d\mathbf{q}^2} = \left. \frac{d\sigma}{dt} \right|_{t=-\mathbf{q}^2}. \quad (\text{B.15})$$

Even more convenient in terms of numerical sampling is the *small angle approximation* eq. (B.14), $t \approx -\mathbf{q}_{\perp}^2$. The differential cross section then reads $\frac{d\sigma}{d\mathbf{q}^2} \approx \left. \frac{d\sigma}{dt} \right|_{t=-\mathbf{q}_{\perp}^2}$. Since the cross sections we will discuss below are dominated by small angle scatterings, the approximation is not so bad and it is used for all binary cross sections in this work.

For identical particles in the final state the Mandelstam variables t and u are interchangeable. In this case the small angle limit of a differential cross section can be computed by taking the limit $t \rightarrow 0$ and multiplying the result by 2 instead of taking the limits $t \rightarrow 0$ ($\theta \rightarrow 0$) and $u \rightarrow 0$ ($\theta \rightarrow \pi$) separately. In the limit of small t , the variable $u = -s - t$ can be approximated as $u \approx -s$. Likewise $u \rightarrow 0$ leads to $t \approx -s$.

While the timelike propagators $\sim 1/s$ of s -channel diagrams are infrared-safe due to phase space constraints, the spacelike propagators of t - and u -channel are infrared divergent

²The sign is fixed such that $\sigma = \int_{-s}^0 \frac{d\sigma}{dt} dt = \int_0^s \frac{d\sigma}{d\mathbf{q}^2} d\mathbf{q}^2$ holds.

as $\sim 1/t$ and $\sim 1/u$ respectively. Inspired from hard thermal loop (HTL) calculations where infrared divergences are screened by a thermally generated self energy $\Pi \sim g_s^2 T^2$ the propagators are screened by introducing a thermal mass (Debye mass) $\mu^2 \sim g_s^2 T^2$. As detailed in chapter 3 the Debye mass for Boltzmann particles reads, i.e.

$$\mu^2 = m_D^2 = d_G \pi \alpha_s \int \frac{d^3 p}{(2\pi)^3} \frac{1}{p} (N_c f_g + N_f f_q) \quad (\text{B.16})$$

for gluon propagators and

$$\mu^2 = m_q^2 = 4\pi \alpha_s \frac{N_c^2 - 1}{2N_c} \int \frac{d^3 p}{(2\pi)^3} \frac{1}{p} (f_g + f_q) \quad (\text{B.17})$$

for quark propagators.

Summing up, the following recipe describes how to obtain $\frac{d\sigma}{dq_\perp^2}$ in small angle approximation from $\frac{d\sigma}{dt}$ expressed in terms of Mandelstam variables. Only the case where the expression is symmetric in t and u is explicitly discussed.

1. Take the limit $t \rightarrow 0$ and replace u with $u \approx -s$.
2. Multiply by 2 to account for $u \rightarrow 0$.
3. Screen propagator terms $\sim 1/t$ with the appropriate screening mass

$$\frac{1}{t} \rightarrow \frac{1}{t - \mu^2}.$$

The minus sign is chosen since $t, u < 0$.

4. Replace $t = -\mathbf{q}_\perp^2$

B.3.3. Binary parton-parton cross sections

In this appendix we summarize the cross sections for all possible types of binary partonic processes for gluons and light quarks ($N_f = 3$, all masses taken to be zero) from leading order perturbative QCD. The differential cross section in t , $d\sigma/dt$, is taken from [PS95]. The small angle differential cross section $d\sigma/d\mathbf{q}_\perp^2$ is computed according to the procedure described above. Additionally the total (integrated) cross section in small angle approximation is shown, computed from

$$\sigma = \int_0^{s/4} \frac{d\sigma}{d\mathbf{q}_\perp^2} d\mathbf{q}_\perp^2. \quad (\text{B.18})$$

gg \rightarrow **gg**

$$\text{Differential cross section} \quad \frac{d\sigma_{gg \rightarrow gg}}{dt} = \frac{9\pi\alpha_s^2}{2s^2} \left[3 - \frac{tu}{s^2} - \frac{su}{t^2} - \frac{st}{u^2} \right] \quad (\text{B.19a})$$

$$\text{Small angle approximation} \quad \frac{d\sigma_{gg \rightarrow gg}}{d\mathbf{q}_\perp^2} = 9\pi\alpha_s^2 \frac{1}{(\mathbf{q}_\perp^2 + m_D^2)^2} \quad (\text{B.19b})$$

$$\text{Total cross section} \quad \sigma_{gg \rightarrow gg} = 9\pi\alpha_s^2 \frac{s}{m_D^2(4m_D^2 + s)} \quad (\text{B.19c})$$

$q\bar{q} \rightarrow gg$

$$\text{Differential cross section} \quad \frac{d\sigma_{q\bar{q} \rightarrow gg}}{dt} = \frac{32\pi\alpha_s^2}{27s^2} \left[\frac{u}{t} - \frac{t}{u} - \frac{9}{4} \left(\frac{t^2 + u^2}{s^2} \right) \right] \quad (\text{B.20a})$$

$$\text{Small angle approximation} \quad \frac{d\sigma_{q\bar{q} \rightarrow gg}}{d\mathbf{q}_\perp^2} = \frac{64\pi\alpha_s^2}{27s} \frac{1}{\mathbf{q}_\perp^2 + m_q^2} \quad (\text{B.20b})$$

$$\text{Total cross section} \quad \sigma_{q\bar{q} \rightarrow gg} = \frac{64\pi\alpha_s^2}{27s} \ln \left(1 + \frac{s}{4m_q^2} \right) \quad (\text{B.20c})$$

$qg \rightarrow qg$ and $\bar{q}g \rightarrow \bar{q}g$

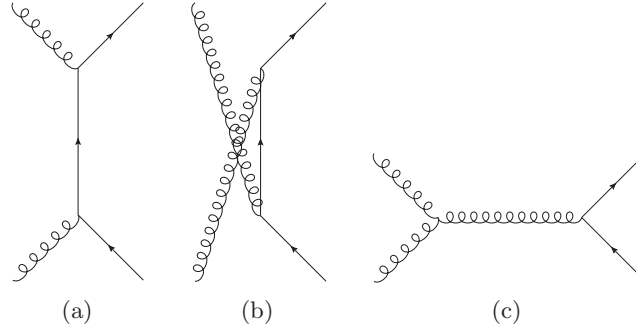


Figure B.3.: Feynman diagrams for a $qg \rightarrow qg$ process.

$$\text{Differential cross section} \quad \frac{d\sigma_{qg \rightarrow qg}}{dt} = \frac{4\pi\alpha_s^2}{9s^2} \left[-\frac{u}{s} - \frac{s}{u} - \frac{9}{4} \left(\frac{s^2 + u^2}{t^2} \right) \right] \quad (\text{B.21a})$$

$$\text{Small angle approximation} \quad \frac{d\sigma_{qg \rightarrow qg}}{d\mathbf{q}_\perp^2} = 2\pi\alpha_s^2 \frac{1}{(\mathbf{q}_\perp^2 + m_D^2)^2} \quad (\text{B.21b})$$

$$\text{Total cross section} \quad \sigma_{qg \rightarrow qg} = 2\pi\alpha_s^2 \frac{s}{m_D^2(4m_D^2 + s)} \quad (\text{B.21c})$$

The screening of the propagators in $qg \rightarrow qg$ or $\bar{q}g \rightarrow \bar{q}g$ needs some consideration. As can be seen from fig. B.3 there are two quark propagators and one gluon propagator involved. The s -channel diagram (fig. B.3a) clearly needs to be screened by m_q . The question which of the other channels gets m_D and which m_q can be answered by recalling the crossing symmetries of Feynman diagrams. The process $qg \rightarrow qg$ can be obtained from $q\bar{q} \rightarrow gg$ by crossing. For this specific crossing the roles of s and t switch, therefore it is the t -channel that needs to be screened by m_D in $qg \rightarrow qg$ processes.

gg → q \bar{q}

$$\text{Differential cross section} \quad \frac{d\sigma_{gg \rightarrow q\bar{q}}}{dt} = \frac{\pi\alpha_s^2}{6s^2} \left[\frac{u}{t} - \frac{t}{u} - \frac{9}{4} \left(\frac{t^2 + u^2}{s^2} \right) \right] \quad (\text{B.22a})$$

$$\text{Small angle approximation} \quad \frac{d\sigma_{gg \rightarrow q\bar{q}}}{d\mathbf{q}_\perp^2} = \frac{\pi\alpha_s^2}{3s} \frac{1}{\mathbf{q}_\perp^2 + m_q^2} \quad (\text{B.22b})$$

$$\text{Total cross section} \quad \sigma_{gg \rightarrow q\bar{q}} = \frac{\pi\alpha_s^2}{3s} \ln \left(1 + \frac{s}{4m_q^2} \right) \quad (\text{B.22c})$$

qq → qq and $\bar{q}\bar{q} \rightarrow \bar{q}\bar{q}$

$$\text{Differential cross section} \quad \frac{d\sigma_{qq \rightarrow qq}}{dt} = \frac{4\pi\alpha_s^2}{9s^2} \left[\frac{u^2 + s^2}{t^2} - \frac{t^2 + s^2}{u^2} - \frac{2}{3} \frac{s^2}{ut} \right] \quad (\text{B.23a})$$

$$\text{Small angle approximation} \quad \frac{d\sigma_{qq \rightarrow qq}}{d\mathbf{q}_\perp^2} = \frac{16\pi\alpha_s^2}{9} \frac{1}{(\mathbf{q}_\perp^2 + m_D^2)^2} \quad (\text{B.23b})$$

$$\text{Total cross section} \quad \sigma_{qq \rightarrow qq} = \frac{16\pi\alpha_s^2}{9} \frac{s}{m_D^2(4m_D^2 + s)} \quad (\text{B.23c})$$

q \bar{q} → q \bar{q}

$$\text{Differential cross section} \quad \frac{d\sigma_{q\bar{q} \rightarrow q\bar{q}}}{dt} = \frac{4\pi\alpha_s^2}{9s^2} \left[\frac{u^2 + s^2}{t^2} + \frac{t^2 + u^2}{s^2} - \frac{2}{3} \frac{u^2}{st} \right] \quad (\text{B.24a})$$

$$\text{Small angle approximation} \quad \frac{d\sigma_{q\bar{q} \rightarrow q\bar{q}}}{d\mathbf{q}_\perp^2} = \frac{8\pi\alpha_s^2}{9} \frac{1}{(\mathbf{q}_\perp^2 + m_D^2)^2} \quad (\text{B.24b})$$

$$\text{Total cross section} \quad \sigma_{q\bar{q} \rightarrow q\bar{q}} = \frac{8\pi\alpha_s^2}{9} \frac{s}{m_D^2(4m_D^2 + s)} \quad (\text{B.24c})$$

qq' → qq'

$$\text{Differential cross section} \quad \frac{d\sigma_{qq' \rightarrow qq'}}{dt} = \frac{4\pi\alpha_s^2}{9s^2} \left[\frac{u^2 + s^2}{t^2} \right] \quad (\text{B.25a})$$

$$\text{Small angle approximation} \quad \frac{d\sigma_{qq' \rightarrow qq'}}{d\mathbf{q}_\perp^2} = \frac{8\pi\alpha_s^2}{9} \frac{1}{(\mathbf{q}_\perp^2 + m_D^2)^2} \quad (\text{B.25b})$$

$$\text{Total cross section} \quad \sigma_{qq' \rightarrow qq'} = \frac{8\pi\alpha_s^2}{9} \frac{s}{m_D^2(4m_D^2 + s)} \quad (\text{B.25c})$$

q \bar{q} ' → q \bar{q} '

$$\text{Differential cross section} \quad \frac{d\sigma_{q\bar{q}' \rightarrow q\bar{q}'}}{dt} = \frac{4\pi\alpha_s^2}{9s^2} \left[\frac{t^2 + u^2}{s^2} \right] \quad (\text{B.26a})$$

$$\text{Total cross section} \quad \sigma_{q\bar{q}' \rightarrow q\bar{q}'} = \int_{-s}^0 \frac{d\sigma_{q\bar{q}' \rightarrow q\bar{q}'}}{dt} dt = \frac{8\pi\alpha_s^2}{27s} \quad (\text{B.26b})$$

For $q\bar{q}' \rightarrow q\bar{q}'$ processes the cross section is not divergent in t or u , thus no screening mass needs to be introduced. Furthermore the small angle approximation is not applicable in this case for which reason the full cross section (B.26a) is used in BAMPS.

B.4. Computation of the differential $2 \rightarrow 3$ cross section

This appendix details the computation of the differential cross section for a radiative $2 \rightarrow 3$ process, eq. (3.15),

$$\frac{d\sigma_{2 \rightarrow 3}}{dq_{\perp}^2 dk_{\perp}^2 dy d\phi} = \frac{d_g}{256\pi^4 s \nu} |\mathcal{M}_{2 \rightarrow 3}|^2 \sum \left(\left| \frac{\partial F}{\partial y_1} \right|_{F=0} \right)^{-1}, \quad (\text{B.27})$$

from the Gunion-Bertsch matrix element (3.13)³.

According to eq. (3.7) the total cross section is given by

$$\begin{aligned} \sigma_{23} = \frac{d_g}{2s} \frac{1}{\nu} \iiint \frac{d^3 p_1}{(2\pi)^3 2E_1} \frac{d^3 p_2}{(2\pi)^3 2E_2} \frac{d^3 p_3}{(2\pi)^3 2E_3} \\ \times (2\pi)^4 \delta^{(4)}(p_A + p_B - (p_1 + p_2 + p_3)) |\mathcal{M}_{2 \rightarrow 3}|^2, \end{aligned} \quad (\text{B.28})$$

where ν accounts for identical particles in the final state and d_g is the degeneracy factor $d_g = 16$ for gluons. Employing the transformation properties of the delta function

$$\delta(f(x)) = \sum_i \frac{1}{|f'(x_i)|} \delta(x - x_i) \quad (\text{B.29})$$

where $f(x_i) = 0$, the integration variables in eq. (B.28) can be rewritten as

$$\int \frac{d^3 p}{2E} \equiv \int d^4 p \delta(p^2 - m^2) \Theta(p^0). \quad (\text{B.30})$$

The constraint $\Theta(p^0)$ ensures that only the positive solution of $p^2 - m^2 = 0$ for E is taken into account. Integrating eq. (B.28) over $d^3 p_2$ then yields

$$\sigma_{23} = \frac{d_g}{256} \frac{1}{\pi^5} \frac{1}{\nu} \frac{1}{s} \iint \frac{d^3 p_1}{E_1} \frac{d^3 p_3}{E_3} \delta((p_A + p_B - p_1 - p_3)^2) |\mathcal{M}_{2 \rightarrow 3}|^2. \quad (\text{B.31})$$

Let

$$\begin{aligned} F &= (p_A + p_B - p_1 - p_3)^2 \\ &= s - 2\sqrt{s}q_{\perp} \cosh y_1 - 2\sqrt{s}k_{\perp} \cosh y + 2\mathbf{q}_{\perp} \mathbf{k}_{\perp} \\ &\quad + 2q_{\perp} k_{\perp} \cosh y_1 \cosh y - 2q_{\perp} k_{\perp} \sinh y_1 \sinh y \end{aligned} \quad (\text{B.32})$$

be the argument of the delta function in eq. (B.31), where y is the rapidity of the emitted gluon (p_3) and y_1 denotes the rapidity of the outgoing particle 1. The connection between rapidity and energy is given by

$$E_3 = k_{\perp} \cosh y \quad (\text{B.33})$$

$$E_1 = q_{\perp} \cosh y_1. \quad (\text{B.34})$$

³See section 3.4 for the generalization to processes involving light quarks.

Using $y = \frac{1}{2} \ln \frac{E+p_z}{E-p_z} = \ln \frac{E+p_z}{p_\perp}$ and thus $\frac{dy}{dp_z} = \frac{1}{E}$, the remaining integration variables can be further transformed

$$\frac{d^3 p_1}{E_1} \equiv d^2 \mathbf{q}_\perp dy_1 \quad (\text{B.35})$$

$$\frac{d^3 p_3}{E_3} \equiv d^2 \mathbf{k}_\perp dy. \quad (\text{B.36})$$

Finally, noting that $\int d^2 \mathbf{q}_\perp \equiv \int dq_\perp^2 \int_0^\pi d\phi$, the total cross section is given by

$$\sigma_{23} = \frac{d_g}{256} \frac{1}{\pi^5} \frac{1}{\nu} \frac{1}{s} \pi \int dq_\perp^2 dy_1 dk_\perp^2 dy \int_0^\pi d\phi \delta(F) |\mathcal{M}_{2 \rightarrow 3}|^2, \quad (\text{B.37})$$

where one angular integration has already been performed and the remaining angle ϕ is taken to be between \mathbf{q}_\perp and \mathbf{k}_\perp . In order to further evaluate this expression by integrating over y_1 , the derivative of F with respect to y_1 is needed

$$\frac{\partial F}{\partial y_1} = -2\sqrt{s} p_{1,z} + 2E_3 p_{1,z} - 2E_1 p_{3,z}. \quad (\text{B.38})$$

The strategy is then to solve $F = 0$ for $p_{1,z}$, plug this into eq. (B.38) together with eqs. (B.33) and (B.34) and to evaluate the remaining integral

$$\sigma_{23} = \frac{d_g}{256} \frac{1}{\pi^4} \frac{1}{\nu} \frac{1}{s} \int_0^{s/4} dq_\perp^2 \int_{1/\lambda^2}^{s/4} dk_\perp^2 \int_{y_{\min}}^{y_{\max}} dy \int_0^\pi d\phi |\mathcal{M}_{2 \rightarrow 3}|^2 \sum \left(\frac{\partial F}{\partial y_1} \Big|_{F=0} \right)^{-1}, \quad (\text{B.39})$$

where the limits on the k_\perp and y integration are given from a combination of the LPM cutoff and kinematic constraints, see section 3.1.4. After some algebra the solutions to $F = 0$ are given by

$$p_{1,z}^{(1)} = \frac{-B + \sqrt{B^2 - 4AC}}{2A} \quad (\text{B.40})$$

$$p_{1,z}^{(2)} = \frac{-B - \sqrt{B^2 - 4AC}}{2A}, \quad (\text{B.41})$$

with

$$A = (\sqrt{s} - E_3)^2 - p_{3,z}^2 \quad (\text{B.42})$$

$$B = p_{3,z} (s - 2\sqrt{s}E_3 + 2q_\perp k_\perp \cos \phi) \quad (\text{B.43})$$

$$C = (\sqrt{s} - E_3)^2 q_\perp^2 - \frac{1}{4} (s - 2\sqrt{s}E_3 + 2q_\perp k_\perp \cos \phi)^2. \quad (\text{B.44})$$

However, eqs. (B.40) and (B.41) are only valid solutions for $p_{1,z}$ if the constraint

$$s - 2\sqrt{s}E_3 + 2\sqrt{s}E_3 + 2q_\perp k_\perp \cos \phi \geq 2p_{1,z} p_{3,z} \quad (\text{B.45})$$

is fulfilled. See also the discussion in section 3.1.3 on further constraints on the solutions (B.40) and (B.41) from the small angle approximation.

C. Interaction rates and probabilities

C.1. Computation of thermal rates

The interaction rates for given particle types and processes are for example needed for computing the differential energy loss or the mean free path of partons, see section 4.1. In a thermal and equilibrated system the rates can be computed from simple averages of the cross sections—without the need to actually simulate the full scattering processes or the dynamics of the medium and thus greatly reducing the computational expenses.

When computing the rate per particle for given processes¹ from averages of the cross sections, some attention needs to be paid to the prefactors. This section lists the rates for all processes implemented in BAMPS.

Let N_g , N_q and $N_{\bar{q}}$ be the number of gluons, quarks and antiquarks respectively, in a given volume ΔV and $n_g = N_g/\Delta V$, $n_q = N_q/\Delta V$, $n_{\bar{q}} = N_{\bar{q}}/\Delta V$ the corresponding particle densities. Furthermore $N_q^{(f)}$ denotes the number of quarks of a given flavor f with $N_q = \sum_f N_q^{(f)}$ and $N_q = 3N_q^{(1)} = 3N_q^{(\text{up})}$ in thermal equilibrium. $n_q^{(f)}$ is the corresponding density of quarks with flavor f .

The interaction probability for an arbitrary $2 \rightarrow Y$ process $X_{(2)} \rightarrow Y$ within ΔV and a time interval Δt is given by

$$P_{X_{(2)} \rightarrow Y} = v_{\text{rel}} \sigma_{X_{(2)} \rightarrow Y} \frac{\Delta t}{\Delta V}. \quad (\text{C.1})$$

Let $m_{X_{(2)}}^i$ denote the number of particles of type i involved in the initial state of the $X_{(2)} \rightarrow Y$ process, and $M_{X_{(2)}}$ the number of all possible particle pairs in the volume ΔV that contribute to the initial state $X_{(2)}$. Then the contribution to the rate per particle of type i from the process $X_{(2)} \rightarrow Y$ is given by

$$\begin{aligned} R_{X_{(2)} \rightarrow Y}^i &= \frac{m_{X_{(2)}}^i}{N_i} M_{X_{(2)}} \left\langle P_{X_{(2)} \rightarrow Y} \right\rangle \frac{1}{\Delta t} \\ &= \frac{m_{X_{(2)}}^i}{N_i} M_{X_{(2)}} \left\langle v_{\text{rel}} \sigma_{X_{(2)} \rightarrow Y} \right\rangle \frac{1}{\Delta V}. \end{aligned} \quad (\text{C.2})$$

The formula for $3 \rightarrow 2$ processes is very similar. $X_{(3)}$ then denotes a three-particle initial state and $M_{X_{(3)}}$ the number of all contributing particle triplets. The probability $P_{X_{(3)} \rightarrow Y}$ can be expressed as

$$P_{X_{(3)} \rightarrow Y} = \tilde{I}_{X_{(3)} \rightarrow Y} \frac{\Delta t}{(\Delta V)^2}, \quad (\text{C.3})$$

where $\tilde{I}_{X_{(3)} \rightarrow Y}$ comprises the phase space integral over the matrix element for the process $X_{(3)} \rightarrow Y$ and some prefactors, cf. eqs. (3.8) and (3.9). Then the rate per particle of type i

¹See appendix A.2 for the conventions used in the notation.

from the process $X_{(3)} \rightarrow Y$ is computed, analogous to eq. (C.2), from

$$\begin{aligned} R_{X_{(3)} \rightarrow Y}^i &= \frac{m_{X_{(3)}}^i}{N_i} M_{X_{(3)}} \langle P_{X_{(3)} \rightarrow Y} \rangle \frac{1}{\Delta t} \\ &= \frac{m_{X_{(3)}}^i}{N_i} M_{X_{(3)}} \langle \tilde{I}_{X_{(3)} \rightarrow Y} \rangle \frac{1}{(\Delta V)^2}. \end{aligned} \quad (\text{C.4})$$

Thermal gluon rates

$$R_{gg \rightarrow Y}^g = \frac{2}{N_g} \binom{N_g}{2} \langle P_{gg \rightarrow Y} \rangle \frac{1}{\Delta t} = \langle v_{\text{rel}} \sigma_{gg \rightarrow Y} \rangle n_g \quad (\text{C.5a})$$

$$R_{gq \rightarrow Y}^g = \frac{1}{N_g} N_g N_q \langle P_{gq \rightarrow Y} \rangle \frac{1}{\Delta t} = \langle v_{\text{rel}} \sigma_{gq \rightarrow Y} \rangle n_q \quad (\text{C.5b})$$

$$R_{g\bar{q} \rightarrow Y}^g = R_{gq \rightarrow Y}^g = \langle v_{\text{rel}} \sigma_{gq \rightarrow Y} \rangle n_q \quad (\text{C.5c})$$

$$R_{ggg \rightarrow Y}^g = \frac{3}{N_g} \binom{N_g}{3} \langle P_{ggg \rightarrow Y} \rangle \frac{1}{\Delta t} = \frac{\langle \tilde{I}_{ggg \rightarrow Y} \rangle}{2} n_g^2 \quad (\text{C.5d})$$

$$R_{gqg \rightarrow Y}^g = \frac{2}{N_g} N_q \binom{N_g}{2} \langle P_{gqg \rightarrow Y} \rangle \frac{1}{\Delta t} = \langle \tilde{I}_{gqg \rightarrow Y} \rangle n_g n_q \quad (\text{C.5e})$$

$$R_{g\bar{q}g \rightarrow Y}^g = R_{gqg \rightarrow Y}^g = \langle \tilde{I}_{gqg \rightarrow Y} \rangle n_g n_q \quad (\text{C.5f})$$

$$R_{q\bar{q}g \rightarrow Y}^g = \frac{1}{N_g} \sum_f N_g N_q^{(f)} N_{\bar{q}}^{(f)} \langle P_{q\bar{q}g \rightarrow Y} \rangle \frac{1}{\Delta t} = \langle \tilde{I}_{q\bar{q}g \rightarrow Y} \rangle \frac{n_q^2}{3} \quad (\text{C.5g})$$

$$R_{qqg \rightarrow Y}^g = \frac{2}{N_g} \sum_f N_g \binom{N_q^{(f)}}{2} \langle P_{qqg \rightarrow Y} \rangle \frac{1}{\Delta t} = \langle \tilde{I}_{qqg \rightarrow Y} \rangle \frac{n_q^2}{6} \quad (\text{C.5h})$$

$$R_{\bar{q}\bar{q}g \rightarrow Y}^g = R_{qqg \rightarrow Y}^g = \langle \tilde{I}_{qqg \rightarrow Y} \rangle \frac{n_q^2}{6} \quad (\text{C.5i})$$

$$\begin{aligned} R_{qq'g \rightarrow Y}^g &= \frac{1}{2!} \frac{1}{N_g} \sum_{f_1, f_2 \neq f_1} N_g N_q^{(f_1)} N_q^{(f_2)} \langle P_{qq'g \rightarrow Y} \rangle \frac{1}{\Delta t} \\ &= \frac{(N_f - 1) N_f}{2!} \langle \tilde{I}_{qq'g \rightarrow Y} \rangle \left(n_q^{(1)} \right)^2 = \langle \tilde{I}_{qq'g \rightarrow Y} \rangle \frac{n_q^2}{3} \end{aligned} \quad (\text{C.5j})$$

$$R_{q\bar{q}'g \rightarrow Y}^g = R_{qq'g \rightarrow Y}^g = \langle \tilde{I}_{qq'g \rightarrow Y} \rangle \frac{n_q^2}{3} \quad (\text{C.5k})$$

$$R_{\bar{q}\bar{q}'g \rightarrow Y}^g = R_{qq'g \rightarrow Y}^g = \langle \tilde{I}_{qq'g \rightarrow Y} \rangle \frac{n_q^2}{3} \quad (\text{C.5l})$$

Thermal quark rates

$$R_{gg \rightarrow Y}^q = \frac{1}{3} \sum_f \frac{1}{N_q^{(f)}} N_g N_q^{(f)} \langle P_{gg \rightarrow Y} \rangle \frac{1}{\Delta t} = \langle v_{\text{rel}} \sigma_{gg \rightarrow Y} \rangle n_g \quad (\text{C.6a})$$

$$R_{q\bar{q} \rightarrow Y}^q = \frac{1}{3} \sum_f \frac{1}{N_q^{(f)}} N_q^{(f)} N_{\bar{q}}^{(f)} \langle P_{q\bar{q} \rightarrow Y} \rangle \frac{1}{\Delta t} = \langle v_{\text{rel}} \sigma_{q\bar{q} \rightarrow Y} \rangle \frac{n_q}{3} \quad (\text{C.6b})$$

$$R_{qq \rightarrow Y}^q = \frac{1}{3} \sum_f \frac{2}{N_q^{(f)}} \binom{N_q^{(f)}}{2} \langle P_{qq \rightarrow Y} \rangle \frac{1}{\Delta t} = \langle v_{\text{rel}} \sigma_{qq \rightarrow Y} \rangle \frac{n_q}{3} \quad (\text{C.6c})$$

$$R_{qq' \rightarrow Y}^q = \frac{1}{3} \sum_{f_1, f_2 \neq f_1} \frac{1}{N_q^{(f_1)}} N_q^{(f_1)} N_q^{(f_2)} \langle P_{qq' \rightarrow Y} \rangle \frac{1}{\Delta t} = \langle v_{\text{rel}} \sigma_{qq' \rightarrow Y} \rangle \frac{2n_q}{3} \quad (\text{C.6d})$$

$$R_{q\bar{q}' \rightarrow Y}^q = R_{qq' \rightarrow Y}^q = \langle v_{\text{rel}} \sigma_{qq' \rightarrow Y} \rangle \frac{2n_q}{3} \quad (\text{C.6e})$$

$$R_{gqg \rightarrow Y}^q = \frac{1}{3} \sum_f \frac{1}{N_q^{(f)}} \binom{N_g}{2} N_q^{(f)} \langle P_{gqg \rightarrow Y} \rangle \frac{1}{\Delta t} = \langle \tilde{I}_{gqg \rightarrow Y} \rangle \frac{n_g^2}{2} \quad (\text{C.6f})$$

$$R_{q\bar{q}g \rightarrow Y}^q = \frac{1}{3} \sum_f \frac{1}{N_q^{(f)}} N_g N_q^{(f)} N_{\bar{q}}^{(f)} \langle P_{q\bar{q}g \rightarrow Y} \rangle \frac{1}{\Delta t} = \langle \tilde{I}_{q\bar{q}g \rightarrow Y} \rangle \frac{n_q n_g}{3} \quad (\text{C.6g})$$

$$R_{qqg \rightarrow Y}^q = \frac{1}{3} \sum_f \frac{2}{N_q^{(f)}} \binom{N_q^{(f)}}{2} N_g \langle P_{qqg \rightarrow Y} \rangle \frac{1}{\Delta t} = \langle \tilde{I}_{qqg \rightarrow Y} \rangle \frac{n_q n_g}{3} \quad (\text{C.6h})$$

$$R_{qq'g \rightarrow Y}^q = \frac{1}{3} \sum_{f_1, f_2 \neq f_1} \frac{1}{N_q^{(f_1)}} N_q^{(f_1)} N_q^{(f_2)} N_g \langle P_{qq'g \rightarrow Y} \rangle \frac{1}{\Delta t} = \langle \tilde{I}_{qq'g \rightarrow Y} \rangle \frac{2n_q n_g}{3} \quad (\text{C.6i})$$

$$R_{q\bar{q}'g \rightarrow Y}^q = R_{qq'g \rightarrow Y}^q = \langle \tilde{I}_{qq'g \rightarrow Y} \rangle \frac{2n_q n_g}{3} \quad (\text{C.6j})$$

C.2. Scaling factors for $2 \leftrightarrow 3$ processes including light quarks

As discussed in section 3.4.2 the incorporation of $2 \leftrightarrow 3$ processes for light quarks is based on scaling the $gg \rightarrow ggg$ matrix element in the Gunion-Bertsch approximation by $Q_X = \frac{d\sigma_{X \rightarrow X}}{d\mathbf{q}_\perp} / \frac{d\sigma_{gg \rightarrow gg}}{d\mathbf{q}_\perp}$. Additionally the the difference in the symmetry factors for the final states of $X \leftrightarrow Xg$ compared to $gg \leftrightarrow ggg$ needs to be accounted for. This is done by a further scaling factor $\tilde{\nu}_X$ as in eq. (3.86), whose value is given in table 3.1 in the limit $N_g \gg 1$. In this appendix the derivation of the scaling for combinatorial symmetry factors is discussed in some more detail. For simplicity only one quark flavor is explicitly considered (except for the discussion of $qq' \leftrightarrow qq'g$ processes), the generalization to $N_f = 3$ is trivial.

gg \leftrightarrow ggg

The purely gluonic processes $gg \leftrightarrow ggg$ as implemented in the original version of BAMPS serve as a reference for the purpose of this discussion. The number of collisions in a given

volume per time step are given by

$$N_{gg \rightarrow ggg} = \binom{N_g}{2} P_{gg \rightarrow ggg} \quad N_{ggg \rightarrow gg} = \binom{N_g}{3} 6 I_{ggg \rightarrow gg} \quad (\text{C.7})$$

where $P_{gg \rightarrow ggg}$ is the probability for the radiative process as defined in eq. (3.4) and $I_{ggg \rightarrow gg}$ represents the phase space integral (3.9) that corresponds to the cross section of $2 \rightarrow N$ processes. The difference between the actual probability $P_{ggg \rightarrow gg}$ and $I_{ggg \rightarrow gg}$, see eq. (3.8), can be ignored for the sake of simplicity here since it is not relevant for the arguments to come. The factor 6 in the above expression for $N_{ggg \rightarrow gg}$ stems from a technical detail in the implementation of BAMPS. The contributions of all possible combinations—gluon 1 absorbed by gluon 2, gluon 1 absorbed by gluon 3, etc.—are computed separately and summed to give the total collision integral $I_{ggg \rightarrow gg}^{\text{total}} = \sum I_{ggg \rightarrow gg}^i$ giving $I_{ggg \rightarrow gg}^{\text{total}} = 6 I_{ggg \rightarrow gg}$ in the thermal average.

Now detailed balance in thermal and chemical equilibrium requires that the number of particle production and annihilation processes is equal, i.e. $N_{gg \rightarrow ggg}/N_{ggg \rightarrow gg} = 1$, giving

$$\frac{P_{gg \rightarrow ggg}}{I_{ggg \rightarrow gg}} = 2(N_g - 2). \quad (\text{C.8})$$

$qg \leftrightarrow qgg$

The number of production processes is

$$N_{qg \rightarrow qgg} = N_g N_q P_{qg \rightarrow qgg} = N_g N_q \tilde{\nu}_{qg \rightarrow qgg} Q_{qg} P_{gg \rightarrow ggg}, \quad (\text{C.9})$$

while the number of annihilation processes is given by

$$N_{qgg \rightarrow qg} = \binom{N_g}{2} N_q 4 I_{qgg \rightarrow qg} = \binom{N_g}{2} N_q 4 \tilde{\nu}_{qgg \rightarrow qg} Q_{qg} I_{ggg \rightarrow gg}. \quad (\text{C.10})$$

Requesting thermal and chemical equilibrium, i.e. $N_{qg \rightarrow qgg} = N_{qgg \rightarrow qg}$, and using eq. (C.8) yields a relation between the combinatorical scaling factors

$$\tilde{\nu}_{qgg \rightarrow qg} = \tilde{\nu}_{qg \rightarrow qgg} \frac{N_g - 2}{N_g - 1}. \quad (\text{C.11})$$

From the number of identical particles in the final state of $qgg \rightarrow qg$ compared to $ggg \rightarrow gg$ it is known that $\tilde{\nu}_{qgg \rightarrow qg} = 2$ for large N_g and thus

$$\tilde{\nu}_{qg} \equiv \tilde{\nu}_{qgg \rightarrow qg} \approx \tilde{\nu}_{qg \rightarrow qgg} \approx 2 \quad (\text{C.12})$$

for $N_g \gg 1$.

$q\bar{q} \leftrightarrow q\bar{q}g$

The number of production processes is

$$N_{q\bar{q} \rightarrow q\bar{q}g} = N_q N_{\bar{q}} P_{q\bar{q} \rightarrow q\bar{q}g} = N_q N_{\bar{q}} \tilde{\nu}_{q\bar{q} \rightarrow q\bar{q}g} Q_{q\bar{q}} P_{gg \rightarrow ggg}, \quad (\text{C.13})$$

while the number of annihilation processes is given by

$$N_{q\bar{q}g \rightarrow q\bar{q}g} = N_g N_q N_{\bar{q}} 2 I_{q\bar{q}g \rightarrow q\bar{q}} = N_g N_q N_{\bar{q}} 2 \tilde{\nu}_{q\bar{q}g \rightarrow q\bar{q}} Q_{q\bar{q}} I_{ggg \rightarrow gg}. \quad (\text{C.14})$$

Arguing as above this gives

$$\tilde{\nu}_{q\bar{q}g \rightarrow q\bar{q}} = \tilde{\nu}_{q\bar{q} \rightarrow q\bar{q}g} \frac{N_g - 2}{N_g} \quad (\text{C.15})$$

and in the limit $N_g \gg 1$

$$\tilde{\nu}_{q\bar{q}} \equiv \tilde{\nu}_{q\bar{q}g \rightarrow q\bar{q}} \approx \tilde{\nu}_{q\bar{q} \rightarrow q\bar{q}g} \approx 2. \quad (\text{C.16})$$

$qq \leftrightarrow qqg$

For the process $qq \leftrightarrow qqg$ one obtains

$$N_{qq \rightarrow qqg} = \binom{N_q}{2} P_{qq \rightarrow qqg} = \binom{N_q}{2} \tilde{\nu}_{qq \rightarrow qqg} Q_{qq} P_{gg \rightarrow ggg} \quad (\text{C.17})$$

and

$$N_{qqg \rightarrow qqg} = N_g \binom{N_q}{2} 2 I_{qqg \rightarrow qq} = N_g \binom{N_q}{2} 2 \tilde{\nu}_{qqg \rightarrow qq} Q_{qq} I_{ggg \rightarrow gg}. \quad (\text{C.18})$$

Leading to

$$\tilde{\nu}_{qqg \rightarrow qq} = \tilde{\nu}_{qq \rightarrow qqg} \frac{N_g - 2}{N_g}. \quad (\text{C.19})$$

and in the limit $N_g \gg 1$

$$\tilde{\nu}_{qq} \equiv \tilde{\nu}_{qqg \rightarrow qq} \approx \tilde{\nu}_{qq \rightarrow qqg} \approx 1. \quad (\text{C.20})$$

$qq' \leftrightarrow qq'g$

From a combinatorial point of view this process is similar to $q\bar{q} \leftrightarrow q\bar{q}g$ and thus

$$\tilde{\nu}_{qq'g \rightarrow qq'} = \tilde{\nu}_{qq' \rightarrow qq'g} \frac{N_g - 2}{N_g}, \quad (\text{C.21})$$

in the limit $N_g \gg 1$ giving

$$\tilde{\nu}_{qq'} \equiv \tilde{\nu}_{qq'g \rightarrow qq'} \approx \tilde{\nu}_{qq' \rightarrow qq'g} \approx 2. \quad (\text{C.22})$$

D. Numerical sampling methods

In Monte Carlo or transport calculations it is generally necessary to sample values from given, possibly multivariate¹, distributions. This appendix briefly sketches three different methods that are being used in transport simulations with BAMPS—deliberately without mathematical rigorousness and proofs, see [PTVF07, NB99, RC04, Kle09] or other textbooks on the subject for more details and in-depth discussions.

All sampling methods in principal rely upon the generation of uniformly distributed random numbers in a given interval. For convenience the interval $[0, 1)$ is chosen. The random number generator² used in this work is based on the Mersenne Twister algorithm [MN98] as implemented in the Boost library³.

D.1. Inverse transform sampling

Let $f(u)$ be a continuous univariate probability density such that $P[a \leq X \leq b] = \int_a^b f(u)du$ gives the probability of the random variable X to fall into the interval $[a, b]$. $f(u)$ shall be normalized such that $\int_{-\infty}^{\infty} f(u)du = 1$. Then the cumulative distribution function⁴

$$F(x) = \int_{-\infty}^x f(u)du \quad (\text{D.1})$$

gives the probability for X being smaller than x , i.e. $P[X \leq x]$, or intuitively speaking the area under the density function up to x .

The goal is now to randomly pick values x that are distributed according to the density f or equivalently the distribution F . This is easily achieved by generating a uniformly distributed random number y from the interval $[0, 1)$ (with a random number generator as discussed above) and computing

$$x = F^{-1}(y) \quad (\text{D.2})$$

from the inverse of the cumulative distribution function.

This is the most direct and easiest approach. But it fails if the inverse F^{-1} is not known or if multiple random variables need to be sampled according to a multivariate distribution.

¹A *multivariate* distribution is a distribution of more than one random number, whereas a *univariate* distribution is a distribution of one random number.

²In fact it is of course a *pseudo* random number generator.

³<http://www.boost.org>. The *mt19937* variant of the Mersenne Twister algorithm provided by the Boost libraries is used in this work.

⁴Or just *distribution function*. The notation varies widely. Sometimes also the probability density is called distribution function.

D.2. Rejection sampling

Rejection sampling can be used when the inverse of the cumulative distribution is not known or too complicated and is even applicable for multivariate distributions. The univariate case will be discussed first and then generalized to multivariate distributions.

As above, $f(u)$ is a continuous univariate probability density with cumulative distribution $F(x) = \int_{-\infty}^x f(u)du$. For the rejection method one needs to find an Lebesgue integrable envelope function $g(u)$ such that $f(u) \leq g(u) \forall u$. This envelope function $g(u)$ needs to be sufficiently simple such that one can sample according to $g(u)$, for example by means of the inverse transform method as described above.

The rejection method can then be summarized as follows:

1. Sample x according to g (for example using the inverse transform method).
2. Sample y uniformly from $[0, 1)$.
3. Accept x if $y < \frac{f(x)}{g(x)}$ otherwise reject x and start again.

Put in words, this procedure samples points $(x, v = yg(x))$ uniformly distributed under the curve of g . For each of these points a decision has to be made whether $v = yg(x)$ is below $f(x)$ or not. If $yg(x) < f(x)$ the value x is accepted, otherwise it is rejected. By doing so the area under $f(x)$ is sampled uniformly and thus x is sampled according to f .

This procedure can also be used for distributions of multiple random variables. But due to the fact that the inverse transform method is only applicable to univariate distributions, the envelope function g needs to be very simple. Choosing $g(x_1, \dots, x_n) = A = \text{const.}$ with $A \leq \sup\{f(x) : x \in \mathbb{R}\}$ ⁵, step No. 1 of the algorithm above becomes trivial since all points (x_1, \dots, x_n) are equally probable.

The advantages of the rejection method are clearly the flexibility and the possibility to sample multivariate distributions. The disadvantage is the dependence on a good choice of the envelope function g . If g is “too far away” from f then the rejection probability in step No. 3 becomes very high and the procedure has to be repeated many times until a value is accepted, thus severely increasing the computational expenses. This is especially a problem for multivariate distributions when the probability density f exhibits some sharp peaks.

D.3. Metropolis sampling

The Metropolis algorithm [MRR⁺53, HAS70], sometimes also called Metropolis-Hastings algorithm, is based on the rejection method and is a widely used Monte Carlo technique. It is a Markov chain process that basically employs a random walk in probability space combined with an acceptance-rejection criterion to obtain samples from a probability distribution. The Metropolis algorithm offers some considerable advantages over the methods presented above. It works for multivariate distributions, no envelope function needs to be known and even the normalization factor of the probability density is not necessary⁶.

⁵As a probability density $f(x)$ is bounded and positive.

⁶Especially for multidimensional distributions when only the raw dependence on the random variables is known, the normalization might be very hard (numerically expensive) to compute.

In order to generate random values $\underline{x} = (x_1, \dots, x_f)$ from a f -dimensional density $f(\underline{x}) = f(x_1, \dots, x_f)$ a proposal density $Q(\underline{x}, \underline{x}')$ needs to be chosen. $Q(\underline{x}, \underline{x}')$ encodes the probability to go from \underline{x} to \underline{x}' . After randomly choosing an initial value \underline{x}_0 , the algorithm then reads as follows:

1. Being at position \underline{x}_i , propose a new value \underline{x}_{i+1} according to $Q(\underline{x}_i, \underline{x}_{i+1})$.
2. Compute

$$\alpha = \min \left\{ \frac{f(\underline{x}_{i+1}) Q(\underline{x}_i, \underline{x}_{i+1})}{f(\underline{x}_i) Q(\underline{x}_{i+1}, \underline{x}_i)}, 1 \right\} .$$

3. Accept \underline{x}_{i+1} if a random number $u \in [0, 1)$ is smaller than α , otherwise reject it and go back to step No. 1.

The so obtained sequence \underline{x}_i represents a sample of the distribution given by $f(\underline{x})$. But in order to eliminate any dependence on the randomly chosen initial value \underline{x}_0 , the first couple of steps need to be discarded. This is sometimes called *burn-in*. If the proposal function is symmetric, i.e. $Q(\underline{x}, \underline{x}') = Q(\underline{x}', \underline{x})$ then the acceptance probability α only depends on the ratio of f at \underline{x}_{i+1} and \underline{x}_i . A common choice for Q is a multivariate Gaussian distribution but the proposal function and the length of the burn-in phase need to be tuned to the specific problem at hand.

Within the algorithms employed in this work only one randomly generated value \underline{x} is needed at a time since the parameters of the density f can change. For example the matrix element governing the sampling of momenta for $3 \rightarrow 2$ processes depends on parameters unique to each processes, such as the Mandelstam s . Therefore a slightly modified strategy is adopted in this work: a fixed number N of the values \underline{x}_i is computed according to the algorithm described above. N needs to be chosen sufficiently larger than the burn-in phase such that \underline{x}_N is not influenced by the random initial value \underline{x}_0 any more. Then \underline{x}_N is the value that is taken to be a sample of the density f . For simplicity, a uniform distribution over the whole range $[x_{i,\min}, x_{i,\max}] \forall i$ is mostly employed for the proposal function Q .

In case the rejection method is not applicable because no envelope function is known or the normalization is difficult to compute, one can thus resort to the Metropolis algorithm. But even if the rejection method is in principle applicable, the Metropolis algorithm might be faster because in the above described version it always needs a fixed number of N steps to generate a random value \underline{x} . If $1/N$ is larger than the average acceptance rate of the rejection method, the Metropolis algorithm is faster. This is clearly the case when the envelope function for the rejection method only poorly approximates the probability distribution that needs to be sampled and thus the rejection probability is very high.

E. Power law fits to parton spectra

This appendix lists values of the fit parameters and the corresponding standard errors from fits of a power law $f(p_T) = a p_T^{-b}$ to initial and final parton spectra $\frac{d^2 N}{dy dp_T}$ at midrapidity from BAMPS simulations of heavy ion collisions.

			a	b	σ_a	σ_b
$b = 0.0$ fm	initial	g	$4.87 \cdot 10^7$	7.482	$1.43 \cdot 10^7$	0.099
		u	$2.13 \cdot 10^5$	6.009	$4.57 \cdot 10^4$	0.072
		d	$3.68 \cdot 10^5$	6.117	$1.08 \cdot 10^5$	0.099
		s	$1.67 \cdot 10^5$	6.754	$1.51 \cdot 10^5$	0.306
		\bar{u}	$8.10 \cdot 10^6$	8.031	$5.80 \cdot 10^6$	0.243
		\bar{d}	$1.01 \cdot 10^6$	7.081	$4.41 \cdot 10^5$	0.148
		\bar{s}	$1.46 \cdot 10^6$	7.595	$1.14 \cdot 10^6$	0.267
	final	g	$9.46 \cdot 10^6$	7.907	$6.59 \cdot 10^6$	0.237
		u	$2.28 \cdot 10^4$	6.335	$1.38 \cdot 10^4$	0.206
		d	$8.79 \cdot 10^4$	6.810	$1.23 \cdot 10^5$	0.475
		s	$2.42 \cdot 10^2$	5.485	$3.87 \cdot 10^2$	0.552
		\bar{u}	$2.11 \cdot 10^5$	7.824	$3.10 \cdot 10^5$	0.515
		\bar{d}	$3.97 \cdot 10^5$	7.032	$7.46 \cdot 10^4$	0.658
		\bar{s}	$2.27 \cdot 10^4$	7.095	$5.82 \cdot 10^4$	0.876
$b = 2.0$ fm	initial	g	$9.65 \cdot 10^7$	7.741	$3.59 \cdot 10^7$	0.126
		u	$4.44 \cdot 10^5$	6.273	$1.28 \cdot 10^5$	0.097
		d	$3.15 \cdot 10^5$	6.065	$1.01 \cdot 10^5$	0.109
		s	$1.05 \cdot 10^6$	7.469	$8.73 \cdot 10^5$	0.283
		\bar{u}	$8.30 \cdot 10^5$	7.149	$6.97 \cdot 10^5$	0.288
		\bar{d}	$4.06 \cdot 10^5$	6.729	$1.80 \cdot 10^5$	0.151
		\bar{s}	$1.78 \cdot 10^8$	9.487	$2.19 \cdot 10^8$	0.418
	final	g	$1.45 \cdot 10^7$	8.051	$1.11 \cdot 10^7$	0.260
		u	$5.07 \cdot 10^4$	6.613	$5.46 \cdot 10^4$	0.365
		d	$6.43 \cdot 10^3$	5.817	$4.64 \cdot 10^3$	0.245
		s	$7.03 \cdot 10^3$	6.804	$1.50 \cdot 10^4$	0.775
		\bar{u}	$2.79 \cdot 10^3$	6.117	$4.45 \cdot 10^3$	0.556
		\bar{d}	$4.98 \cdot 10^3$	6.232	$3.77 \cdot 10^3$	0.266
		\bar{s}	$2.66 \cdot 10^5$	8.164	$7.70 \cdot 10^5$	1.03

Table E.1.: Fit parameters for parton spectra from BAMPS simulations of Au + Au at 200 A GeV using $f(p_T) = a p_T^{-b}$.

			a	b	σ_a	σ_b
$b = 2.8$ fm	initial	g	$2.66 \cdot 10^7$	7.238	$7.59 \cdot 10^6$	0.097
		u	$2.10 \cdot 10^5$	5.998	$5.74 \cdot 10^4$	0.093
		d	$2.22 \cdot 10^5$	5.939	$6.57 \cdot 10^4$	0.101
		s	$2.34 \cdot 10^5$	6.877	$1.49 \cdot 10^4$	0.218
		\bar{u}	$9.66 \cdot 10^5$	7.170	$6.85 \cdot 10^5$	0.241
		\bar{d}	$7.00 \cdot 10^5$	6.908	$4.82 \cdot 10^5$	0.234
		\bar{s}	$1.63 \cdot 10^5$	6.742	$7.91 \cdot 10^5$	0.165
	final	g	$2.53 \cdot 10^6$	7.358	$9.56 \cdot 10^5$	0.128
		u	$1.28 \cdot 10^4$	6.087	$1.03 \cdot 10^4$	0.275
		d	$6.71 \cdot 10^3$	5.806	$4.46 \cdot 10^3$	0.226
		s	$3.58 \cdot 10^3$	5.457	$9.84 \cdot 10^3$	0.980
		\bar{u}	$2.23 \cdot 10^4$	6.890	$3.91 \cdot 10^4$	0.632
		\bar{d}	$3.30 \cdot 10^3$	6.069	$3.63 \cdot 10^3$	0.376
		\bar{s}	$5.57 \cdot 10^1$	4.903	$1.09 \cdot 10^2$	0.702
$b = 3.4$ fm	initial	g	$5.50 \cdot 10^7$	7.531	$1.80 \cdot 10^7$	0.111
		u	$1.79 \cdot 10^5$	5.935	$3.50 \cdot 10^4$	0.066
		d	$2.96 \cdot 10^5$	6.043	$7.90 \cdot 10^4$	0.090
		s	$3.74 \cdot 10^5$	7.064	$2.48 \cdot 10^5$	0.225
		\bar{u}	$1.65 \cdot 10^8$	9.196	$2.09 \cdot 10^8$	0.435
		\bar{d}	$7.08 \cdot 10^5$	6.928	$4.83 \cdot 10^5$	0.232
		\bar{s}	$3.49 \cdot 10^4$	6.183	$3.34 \cdot 10^4$	0.324
	final	g	$1.20 \cdot 10^7$	7.919	$8.90 \cdot 10^6$	0.252
		u	$3.92 \cdot 10^4$	6.487	$3.46 \cdot 10^4$	0.300
		d	$4.15 \cdot 10^4$	6.435	$3.47 \cdot 10^4$	0.284
		s	$1.31 \cdot 10^3$	5.961	$2.21 \cdot 10^3$	0.593
		\bar{u}	$1.03 \cdot 10^6$	8.478	$1.47 \cdot 10^6$	0.513
		\bar{d}	$7.93 \cdot 10^3$	6.288	$5.86 \cdot 10^3$	0.256
		\bar{s}	$3.54 \cdot 10^1$	4.580	$5.45 \cdot 10^1$	0.542
$b = 4.0$ fm	initial	g	$5.89 \cdot 10^7$	7.554	$1.98 \cdot 10^7$	0.114
		u	$3.01 \cdot 10^5$	6.123	$8.80 \cdot 10^4$	0.099
		d	$3.06 \cdot 10^5$	6.061	$8.91 \cdot 10^4$	0.098
		s	$3.46 \cdot 10^5$	7.064	$3.01 \cdot 10^5$	0.297
		\bar{u}	$1.53 \cdot 10^7$	8.211	$1.64 \cdot 10^7$	0.363
		\bar{d}	$3.20 \cdot 10^6$	7.539	$1.26 \cdot 10^6$	0.134
		\bar{s}	$4.43 \cdot 10^5$	7.112	$4.71 \cdot 10^5$	0.364
	final	g	$1.20 \cdot 10^7$	7.898	$6.83 \cdot 10^6$	0.193
		u	$2.75 \cdot 10^4$	6.295	$1.90 \cdot 10^4$	0.238
		d	$1.12 \cdot 10^4$	5.887	$7.10 \cdot 10^3$	0.217
		s	$1.98 \cdot 10^3$	6.136	$2.75 \cdot 10^3$	0.487
		\bar{u}	$2.86 \cdot 10^3$	6.107	$3.70 \cdot 10^3$	0.449
		\bar{d}	$1.93 \cdot 10^4$	6.759	$2.46 \cdot 10^4$	0.440
		\bar{s}	$2.14 \cdot 10^3$	6.125	$2.28 \cdot 10^3$	0.374

Table E.2.: Fit parameters for parton spectra from BAMPS simulations of Au + Au at 200 A GeV using $f(p_T) = a p_T^{-b}$.

			a	b	σ_a	σ_b
$b = 4.5$ fm	initial	g	$4.85 \cdot 10^7$	7.481	$1.38 \cdot 10^7$	0.096
		u	$3.32 \cdot 10^5$	6.169	$9.62 \cdot 10^4$	0.098
		d	$2.17 \cdot 10^5$	5.924	$6.08 \cdot 10^4$	0.095
		s	$1.74 \cdot 10^5$	6.836	$1.18 \cdot 10^5$	0.231
		\bar{u}	$2.23 \cdot 10^7$	8.393	$2.11 \cdot 10^7$	0.321
		\bar{d}	$2.38 \cdot 10^6$	7.396	$1.28 \cdot 10^6$	0.183
		\bar{s}	$9.84 \cdot 10^5$	7.454	$9.98 \cdot 10^5$	0.345
	final	g	$5.70 \cdot 10^6$	7.609	$3.43 \cdot 10^6$	0.205
		u	$4.30 \cdot 10^4$	6.488	$4.43 \cdot 10^4$	0.350
		d	$1.26 \cdot 10^4$	5.931	$6.48 \cdot 10^3$	0.175
		s	$3.79 \cdot 10^2$	5.680	$8.24 \cdot 10^2$	0.760
		\bar{u}	$3.71 \cdot 10^4$	7.000	$6.92 \cdot 10^4$	0.652
		\bar{d}	$1.32 \cdot 10^5$	7.317	$2.10 \cdot 10^5$	0.555
		\bar{s}	$6.63 \cdot 10^3$	6.588	$1.24 \cdot 10^4$	0.655
$b = 5.0$ fm	initial	g	$5.34 \cdot 10^7$	7.516	$1.62 \cdot 10^7$	0.103
		u	$5.00 \cdot 10^5$	6.325	$1.33 \cdot 10^5$	0.090
		d	$3.38 \cdot 10^5$	6.094	$9.84 \cdot 10^4$	0.098
		s	$1.71 \cdot 10^5$	6.778	$1.28 \cdot 10^5$	0.255
		\bar{u}	$1.30 \cdot 10^6$	7.328	$7.65 \cdot 10^5$	0.201
		\bar{d}	$6.31 \cdot 10^5$	6.878	$4.24 \cdot 10^5$	0.228
		\bar{s}	$2.45 \cdot 10^5$	6.955	$2.73 \cdot 10^5$	0.379
	final	g	$1.09 \cdot 10^7$	7.814	$4.65 \cdot 10^6$	0.145
		u	$1.80 \cdot 10^4$	6.158	$1.43 \cdot 10^4$	0.271
		d	$3.20 \cdot 10^4$	6.183	$2.15 \cdot 10^4$	0.228
		s	$1.40 \cdot 10^4$	6.812	$3.13 \cdot 10^4$	0.802
		\bar{u}	$3.40 \cdot 10^4$	6.948	$3.94 \cdot 10^4$	0.412
		\bar{d}	$5.80 \cdot 10^4$	6.955	$5.53 \cdot 10^4$	0.335
		\bar{s}	$2.17 \cdot 10^3$	6.052	$3.11 \cdot 10^3$	0.502
$b = 5.6$ fm	initial	g	$2.90 \cdot 10^7$	7.277	$7.37 \cdot 10^6$	0.086
		u	$2.34 \cdot 10^5$	6.029	$7.17 \cdot 10^4$	0.104
		d	$1.67 \cdot 10^5$	5.835	$3.48 \cdot 10^4$	0.070
		s	$4.02 \cdot 10^5$	7.120	$3.01 \cdot 10^5$	0.254
		\bar{u}	$1.36 \cdot 10^7$	8.239	$6.31 \cdot 10^6$	0.157
		\bar{d}	$1.79 \cdot 10^6$	7.315	$7.36 \cdot 10^5$	0.140
		\bar{s}	$2.45 \cdot 10^5$	6.889	$2.70 \cdot 10^5$	0.374
	final	g	$5.96 \cdot 10^6$	7.537	$2.39 \cdot 10^6$	0.136
		u	$2.75 \cdot 10^4$	6.220	$2.09 \cdot 10^4$	0.258
		d	$1.50 \cdot 10^4$	5.915	$7.94 \cdot 10^3$	0.179
		s	$1.12 \cdot 10^3$	5.907	$1.53 \cdot 10^3$	0.481
		\bar{u}	$8.32 \cdot 10^4$	7.304	$5.99 \cdot 10^4$	0.248
		\bar{d}	$2.57 \cdot 10^5$	7.579	$2.52 \cdot 10^4$	0.337
		\bar{s}	$1.28 \cdot 10^3$	5.910	$1.17 \cdot 10^3$	0.316

Table E.3.: Fit parameters for parton spectra from BAMPS simulations of Au + Au at 200 A GeV using $f(p_T) = a p_T^{-b}$.

			a	b	σ_a	σ_b
$b = 6.3$ fm	initial	g	$4.66 \cdot 10^7$	7.457	$1.44 \cdot 10^7$	0.105
		u	$2.30 \cdot 10^5$	6.013	$6.07 \cdot 10^4$	0.089
		d	$4.08 \cdot 10^5$	6.173	$1.13 \cdot 10^5$	0.093
		s	$1.18 \cdot 10^6$	7.538	$7.66 \cdot 10^5$	0.221
		\bar{u}	$4.07 \cdot 10^6$	7.722	$2.51 \cdot 10^6$	0.209
		\bar{d}	$4.55 \cdot 10^6$	7.636	$2.89 \cdot 10^6$	0.216
		\bar{s}	$2.73 \cdot 10^5$	6.979	$1.44 \cdot 10^5$	0.180
	final	g	$8.71 \cdot 10^6$	7.626	$3.83 \cdot 10^6$	0.149
		u	$1.64 \cdot 10^4$	6.003	$9.66 \cdot 10^3$	0.200
		d	$2.46 \cdot 10^4$	6.071	$1.04 \cdot 10^4$	0.144
		s	$1.26 \cdot 10^4$	6.804	$9.96 \cdot 10^3$	0.275
		\bar{u}	$6.78 \cdot 10^4$	7.130	$6.03 \cdot 10^4$	0.307
		\bar{d}	$5.07 \cdot 10^5$	7.772	$6.51 \cdot 10^5$	0.444
		\bar{s}	$4.63 \cdot 10^3$	6.293	$4.79 \cdot 10^3$	0.360
$b = 7.0$ fm	initial	g	$4.84 \cdot 10^7$	7.477	$1.50 \cdot 10^7$	0.105
		u	$2.78 \cdot 10^5$	6.107	$4.88 \cdot 10^4$	0.059
		d	$2.70 \cdot 10^5$	6.016	$6.74 \cdot 10^4$	0.084
		s	$6.99 \cdot 10^5$	7.327	$4.53 \cdot 10^5$	0.220
		\bar{u}	$7.05 \cdot 10^6$	7.953	$3.97 \cdot 10^6$	0.191
		\bar{d}	$1.46 \cdot 10^6$	7.198	$5.49 \cdot 10^5$	0.128
		\bar{s}	$1.40 \cdot 10^6$	7.588	$7.38 \cdot 10^5$	0.179
	final	g	$1.19 \cdot 10^7$	7.700	$4.69 \cdot 10^6$	0.134
		u	$4.59 \cdot 10^4$	6.323	$2.66 \cdot 10^4$	0.197
		d	$6.64 \cdot 10^4$	6.358	$3.66 \cdot 10^4$	0.187
		s	$3.82 \cdot 10^3$	6.332	$5.59 \cdot 10^3$	0.501
		\bar{u}	$1.96 \cdot 10^6$	8.368	$1.90 \cdot 10^6$	0.332
		\bar{d}	$1.06 \cdot 10^5$	7.123	$1.00 \cdot 10^5$	0.321
		\bar{s}	$1.86 \cdot 10^5$	7.673	$1.97 \cdot 10^5$	0.365
$b = 8.6$ fm	initial	g	$5.42 \cdot 10^7$	7.519	$1.76 \cdot 10^7$	0.110
		u	$4.36 \cdot 10^5$	6.265	$1.19 \cdot 10^5$	0.092
		d	$3.23 \cdot 10^5$	6.081	$7.88 \cdot 10^4$	0.082
		s	$5.97 \cdot 10^5$	7.258	$2.21 \cdot 10^5$	0.126
		\bar{u}	$2.37 \cdot 10^6$	7.539	$7.79 \cdot 10^5$	0.112
		\bar{d}	$2.43 \cdot 10^6$	7.388	$1.04 \cdot 10^6$	0.146
		\bar{s}	$6.48 \cdot 10^5$	7.312	$3.29 \cdot 10^5$	0.173
	final	g	$1.68 \cdot 10^7$	7.672	$6.85 \cdot 10^6$	0.139
		u	$7.13 \cdot 10^4$	6.304	$2.68 \cdot 10^4$	0.128
		d	$6.92 \cdot 10^4$	6.203	$2.35 \cdot 10^4$	0.116
		s	$7.21 \cdot 10^4$	7.195	$6.69 \cdot 10^4$	0.315
		\bar{u}	$5.15 \cdot 10^5$	7.690	$4.30 \cdot 10^5$	0.284
		\bar{d}	$1.10 \cdot 10^6$	7.801	$1.28 \cdot 10^6$	0.396
		\bar{s}	$4.31 \cdot 10^5$	7.837	$3.71 \cdot 10^5$	0.293

Table E.4.: Fit parameters for parton spectra from BAMPS simulations of Au + Au at 200 A GeV using $f(p_T) = a p_T^{-b}$.

			a	b	σ_a	σ_a
$b = 9.6 \text{ fm}$	initial	g	$3.89 \cdot 10^7$	7.398	$9.79 \cdot 10^6$	0.085
		u	$2.11 \cdot 10^5$	5.988	$4.28 \cdot 10^4$	0.069
		d	$3.21 \cdot 10^5$	6.085	$7.45 \cdot 10^4$	0.078
		s	$7.88 \cdot 10^5$	7.359	$4.89 \cdot 10^5$	0.211
		\bar{u}	$5.74 \cdot 10^6$	7.879	$3.67 \cdot 10^6$	0.217
		\bar{d}	$2.21 \cdot 10^6$	7.380	$1.05 \cdot 10^6$	0.161
		\bar{s}	$6.87 \cdot 10^5$	7.300	$4.54 \cdot 10^5$	0.225
	final	g	$1.63 \cdot 10^7$	7.554	$5.16 \cdot 10^6$	0.108
		u	$8.71 \cdot 10^4$	6.227	$4.10 \cdot 10^4$	0.160
		d	$7.48 \cdot 10^4$	6.106	$2.74 \cdot 10^4$	0.125
		s	$2.90 \cdot 10^5$	7.604	$2.36 \cdot 10^5$	0.279
		\bar{u}	$8.20 \cdot 10^5$	7.727	$8.14 \cdot 10^5$	0.343
		\bar{d}	$1.21 \cdot 10^6$	7.738	$1.02 \cdot 10^6$	0.290
		\bar{s}	$8.57 \cdot 10^4$	7.093	$8.87 \cdot 10^4$	0.354

Table E.5.: Fit parameters for parton spectra from BAMPS simulations of Au + Au at 200 A GeV using $f(p_T) = a p_T^{-b}$.

			a	b	σ_a	σ_a
$b = 0.0 \text{ fm}$	initial	g	$2.01 \cdot 10^5$	4.845	$1.91 \cdot 10^4$	0.033
		u	$3.02 \cdot 10^3$	4.567	$8.66 \cdot 10^2$	0.102
		d	$2.68 \cdot 10^3$	4.522	$1.02 \cdot 10^3$	0.135
		s	$1.99 \cdot 10^3$	4.627	$1.41 \cdot 10^3$	0.251
		\bar{u}	$1.51 \cdot 10^3$	4.394	$6.31 \cdot 10^2$	0.149
		\bar{d}	$4.51 \cdot 10^3$	4.799	$1.38 \cdot 10^3$	0.109
		\bar{s}	$7.49 \cdot 10^2$	4.227	$3.55 \cdot 10^2$	0.168
	final	g	$1.40 \cdot 10^4$	4.949	$5.28 \cdot 10^3$	0.134
		u	$1.21 \cdot 10^3$	5.421	$1.30 \cdot 10^3$	0.380
		d	$2.79 \cdot 10^2$	4.946	$5.82 \cdot 10^2$	0.749
		s	$4.46 \cdot 10^1$	4.477	$7.45 \cdot 10^1$	0.642
		\bar{u}	$1.48 \cdot 10^3$	5.531	$3.89 \cdot 10^3$	0.934
		\bar{d}	$8.72 \cdot 10^2$	5.369	$2.00 \cdot 10^3$	0.813
		\bar{s}	$5.27 \cdot 10^1$	4.308	$8.95 \cdot 10^1$	0.608

Table E.6.: Fit parameters for parton spectra from BAMPS simulations of Pb + Pb at 2.76 A TeV using $f(p_T) = a p_T^{-b}$.

Bibliography

- [AAB⁺04] A. Accardi, N. Armesto, M. Botje, S. Brodsky, B. Cole et al., *Hard probes in heavy ion collisions at the LHC: PDFs, shadowing and p+A collisions*, (2004), [hep-ph/0308248](#).
- [AAB⁺10] A. Accardi, F. Arleo, W. K. Brooks, D. D’Enterria and V. Muccifora, *Parton propagation and fragmentation in QCD matter*, Riv.Nuovo Cim. **32**, 439–553 (2010), [0907.3534](#).
- [ACS09] N. Armesto, L. Cunqueiro and C. A. Salgado, *Q-PYTHIA: A medium-modified implementation of final state radiation*, Eur.Phys.J. **C63**, 679–690 (2009), [0907.1014](#).
- [ACSX08] N. Armesto, L. Cunqueiro, C. A. Salgado and W.-C. Xiang, *Medium-evolved fragmentation functions*, JHEP **0802**, 048 (2008), [0710.3073](#).
- [AEF⁺06] Y. Aoki, G. Endrodi, Z. Fodor, S. Katz and K. Szabo, *The order of the quantum chromodynamics transition predicted by the standard model of particle physics*, Nature **443**, 675–678 (2006), [hep-lat/0611014](#).
- [AFKS06] Y. Aoki, Z. Fodor, S. Katz and K. Szabo, *The QCD transition temperature: Results with physical masses in the continuum limit*, Phys.Lett. **B643**, 46–54 (2006), [hep-lat/0609068](#).
- [AKK08] S. Albino, B. Kniehl and G. Kramer, *AKK update: Improvements from new theoretical input and experimental data*, Nucl.Phys. **B803**, 42–104 (2008), [0803.2768](#).
- [ALICE10a] K. Aamodt et al. (ALICE Collaboration), *Charged-particle multiplicity density at mid-rapidity in central Pb+Pb collisions at $\sqrt{s_{NN}} = 2.76$ TeV*, (2010), [1011.3916](#).
- [ALICE10b] K. Aamodt et al. (ALICE Collaboration), *Elliptic Flow of Charged Particles in Pb+Pb Collisions at $\sqrt{s_{NN}} = 2.76$ TeV*, Phys. Rev. Lett. **105**, 252302 (2010), [1011.3914](#).
- [ALICE11] K. Aamodt et al. (ALICE Collaboration), *Suppression of charged particle production at large transverse momentum in central Pb+Pb collisions at $\sqrt{s_{NN}} = 2.76$ TeV*, Phys.Lett. **B696**, 30–39 (2011), [1012.1004](#).
- [AMY01a] P. B. Arnold, G. D. Moore and L. G. Yaffe, *Photon emission from quark-gluon plasma: Complete leading order results*, JHEP **0112**, 009 (2001), [hep-ph/0111107](#).

- [AMY01b] P. B. Arnold, G. D. Moore and L. G. Yaffe, *Photon emission from ultra-relativistic plasmas*, JHEP **0111**, 057 (2001), [hep-ph/0109064](#).
- [AMY02] P. B. Arnold, G. D. Moore and L. G. Yaffe, *Photon and gluon emission in relativistic plasmas*, JHEP **0206**, 030 (2002), [hep-ph/0204343](#).
- [ASW04] N. Armesto, C. A. Salgado and U. A. Wiedemann, *Medium induced gluon radiation off massive quarks fills the dead cone*, Phys.Rev. **D69**, 114003 (2004), [hep-ph/0312106](#).
- [ATLAS10] G. Aad et al. (ATLAS Collaboration), *Observation of a centrality-dependent dijet asymmetry in Pb+Pb collisions at $\sqrt{s_{NN}} = 2.76$ TeV with the ATLAS Detector at the LHC*, Phys. Rev. Lett. **105**, 252303 (2010), [1011.6182](#).
- [B⁺10] S. Borsanyi et al., *Is there still any Tc mystery in lattice QCD? Results with physical masses in the continuum limit III*, JHEP **1009**, 073 (2010), [1005.3508](#), Wuppertal-Budapest Collaboration.
- [Bay02] G. Baym, *RHIC: From dreams to beams in two decades*, Nucl.Phys. **A698**, XXIII–XXXII (2002), [hep-ph/0104138](#).
- [BBB⁺98] S. Bass, M. Belkacem, M. Bleicher, M. Brandstetter, L. Bravina et al., *Microscopic models for ultra-relativistic heavy ion collisions*, Prog.Part.Nucl.Phys. **41**, 255–369 (1998), [nucl-th/9803035](#).
- [BC76] G. Baym and S. Chin, *Can a neutron star be a giant MIT bag?*, Phys.Lett. **B62**, 241–244 (1976).
- [BDM⁺97] R. Baier, Y. L. Dokshitzer, A. H. Mueller, S. Peigne and D. Schiff, *Radiative energy loss and p(T)-broadening of high energy partons in nuclei*, Nucl. Phys. **B484**, 265–282 (1997), [hep-ph/9608322](#).
- [BDMS98] R. Baier, Y. L. Dokshitzer, A. H. Mueller and D. Schiff, *Radiative energy loss of high energy partons traversing an expanding QCD plasma*, Phys. Rev. **C58**, 1706–1713 (1998), [hep-ph/9803473](#).
- [BdVS06] D. Boyanovsky, H. de Vega and D. Schwarz, *Phase transitions in the early and present universe*, Annual Review of Nuclear and Particle Science **56**(1), 441–500 (2006).
- [BEF⁺10] I. Bouras, A. El, O. Fochler, F. Lauciello, F. Reining et al., *Mach cones in viscous matter*, (2010), [1008.4072](#).
- [Beth09] S. Bethke, *The 2009 world average of alpha(s)*, Eur.Phys.J. **C64**, 689–703 (2009), [arXiv:0908.1135](#).
- [BGM⁺08] S. Bass, C. Gale, A. Majumder, C. Nonaka, G.-Y. Qin et al., *Systematic comparison of jet energy loss schemes in a 3D hydrodynamic medium*, J.Phys.G **G35**, 104064 (2008), [0805.3271](#).

- [BGM⁺09] S. A. Bass, C. Gale, A. Majumder, C. Nonaka, G.-Y. Qin, T. Renk and J. Ruppert, *Systematic comparison of jet energy loss schemes in a realistic hydrodynamic medium*, Phys. Rev. **C79**, 024901 (2009), [0808.0908](#).
- [Bjo83] J. D. Bjorken, *Highly relativistic nucleus-nucleus collisions: The central rapidity region*, Phys. Rev. **D27**, 140–151 (1983).
- [BKDC⁺81] F. A. Berends, R. Kleiss, P. De Causmaecker, R. Gastmans and T. T. Wu, *Single bremsstrahlung processes in gauge theories*, Phys. Lett. **B103**, 124 (1981).
- [BMN⁺09] I. Bouras, E. Molnar, H. Niemi, Z. Xu, A. El, O. Fochler, C. Greiner and D. Rischke, *Relativistic shock waves in viscous gluon matter*, Phys. Rev. Lett. **103**, 032301 (2009), [0902.1927](#).
- [BMN⁺10] I. Bouras, E. Molnar, H. Niemi, Z. Xu, A. El, O. Fochler, C. Greiner and D. Rischke, *Investigation of shock waves in the relativistic Riemann problem: A comparison of viscous fluid dynamics to kinetic theory*, Phys.Rev. **C82**, 024910 (2010), [1006.0387](#).
- [BMS03] S. Bass, B. Muller and D. Srivastava, *Parton rescattering and screening in Au+Au collisions at RHIC*, Phys.Lett. **B551**, 277–283 (2003), [nucl-th/0207042](#).
- [BMW08] P. Braun-Munzinger and J. Wambach, *The phase diagram of strongly interacting matter*, Rev.Mod.Phys. (2008), [arXiv:0801.4256](#).
- [BNL05] RHIC Scientists Serve Up “Perfect” Liquid, http://www.bnl.gov/bnlweb/pubaf/pr/pr_display.asp?prid=05-38, 2005.
- [Bou11] I. Bouras, 2011, private communication.
- [BP10] A. Bazavov and P. Petreczky, *Deconfinement and chiral transition with the highly improved staggered quark (HISQ) action*, J.Phys.Conf.Ser. **230**, 012014 (2010), [1005.1131](#), HotQCD.
- [BRAHMS05] I. Arsene et al. (BRAHMS Collaboration), *Quark-gluon plasma and color glass condensate at RHIC? The perspective from the BRAHMS experiment*, Nucl. Phys. **A757**, 1–27 (2005), [nucl-ex/0410020](#).
- [Bub05] M. Buballa, *NJL model analysis of quark matter at large density*, Phys.Rept. **407**, 205–376 (2005), [hep-ph/0402234](#).
- [BZS⁺99] M. Bleicher, E. Zabrodin, C. Spieles, S. Bass, C. Ernst et al., *Relativistic hadron hadron collisions in the ultra-relativistic quantum molecular dynamics model*, J.Phys.G **G25**, 1859–1896 (1999), [hep-ph/9909407](#).
- [CCD⁺06] M. Cheng, N. Christ, S. Datta, J. van der Heide, C. Jung et al., *The transition temperature in QCD*, Phys.Rev. **D74**, 054507 (2006), [hep-lat/0608013](#).

- [CF74] F. Cooper and G. Frye, *Comment on the single particle distribution in the hydrodynamic and statistical thermodynamic models of multiparticle production*, Phys.Rev. **D10**, 186 (1974).
- [CGW⁺10] X.-F. Chen, C. Greiner, E. Wang, X.-N. Wang and Z. Xu, *Bulk matter evolution and extraction of jet transport parameter in heavy ion collisions at RHIC*, (2010), [1002.1165](#).
- [CJJ⁺74] A. Chodos, R. L. Jaffe, K. Johnson, C. B. Thorn and V. F. Weisskopf, *A new extended model of hadrons*, Phys. Rev. **D9**, 3471–3495 (1974).
- [CMS11] S. Chatrchyan et al. (CMS Collaboration), *Observation and studies of jet quenching in Pb+Pb collisions at nucleon-nucleon center of mass energy = 2.76 TeV*, (2011), [1102.1957](#).
- [CN77] G. Chapline and M. Nauenberg, *Asymptotic freedom and the baryon-quark phase transition*, Phys.Rev. **D16**, 450 (1977).
- [CP75] J. C. Collins and M. Perry, *Superdense matter: Neutrons Or asymptotically free quarks?*, Phys.Rev.Lett. **34**, 1353 (1975).
- [CSBS11] C. E. Coleman-Smith, S. A. Bass and D. K. Srivastava, *Implementing the LPM effect in a parton cascade model*, (2011), [1101.4895](#).
- [CSS08] M. Cacciari, G. P. Salam and G. Soyez, *The anti-kt jet clustering algorithm*, JHEP **04**, 063 (2008), [0802.1189](#).
- [dFP07] P. de Forcrand and O. Philipsen, *The Chiral critical line of $N(f) = 2+1$ QCD at zero and non-zero baryon density*, JHEP **0701**, 077 (2007), [hep-lat/0607017](#).
- [dFP08] P. de Forcrand and O. Philipsen, *The curvature of the critical surface $(m_{u,d}, m_s)^{crit}(\mu)$: A progress report*, PoS **LATTICE2008**, 208 (2008), [0811.3858](#).
- [Djo06] M. Djordjevic, *Collisional energy loss in a finite size QCD matter*, Phys.Rev. **C74**, 064907 (2006), [nucl-th/0603066](#).
- [DK01] Y. L. Dokshitzer and D. Kharzeev, *Heavy quark colorimetry of QCD matter*, Phys.Lett. **B519**, 199–206 (2001), [hep-ph/0106202](#).
- [DLMW97] Y. L. Dokshitzer, G. D. Leder, S. Moretti and B. R. Webber, *Better jet clustering algorithms*, JHEP **08**, 001 (1997), [hep-ph/9707323](#).
- [DM02] A. Dumitru and L. D. McLerran, *How protons shatter colored glass*, Nucl.Phys. **A700**, 492–508 (2002), [hep-ph/0105268](#).
- [dPeM06] B. I. des Poids et Mesures, *The International System of Units (SI)*, Bureau International des Poids et Mesures, 8th edition, 2006.

- [DW10] W.-t. Deng and X.-N. Wang, *Multiple parton scattering in nuclei: Modified DGLAP evolution for fragmentation functions*, Phys.Rev. **C81**, 024902 (2010), [0910.3403](#).
- [EHSW05] K. Eskola, H. Honkanen, C. Salgado and U. Wiedemann, *The Fragility of high- p_T hadron spectra as a hard probe*, Nucl.Phys. **A747**, 511–529 (2005), [hep-ph/0406319](#).
- [EKL89] K. Eskola, K. Kajantie and J. Lindfors, *Quark and gluon production in high energy nucleus-nucleus collisions*, Nucl.Phys. **B323**, 37 (1989).
- [ES86] R. K. Ellis and J. C. Sexton, *QCD radiative corrections to parton-parton scattering*, Nucl. Phys. **B269**, 445 (1986).
- [Fis10] W. Fischer, *Run overview of the Relativistic Heavy Ion Collider*, <http://www.agsrhichome.bnl.gov/RHIC/Runs/>, November 2010.
- [FM77] B. A. Freedman and L. D. McLerran, *Fermions and gauge vector mesons at finite temperature and density. 3) The ground state energy of a relativistic quark gas*, Phys.Rev. **D16**, 1169 (1977).
- [FMNB03] R. Fries, B. Muller, C. Nonaka and S. A. Bass, *Hadronization in heavy ion collisions: Recombination and fragmentation of partons*, Phys.Rev.Lett. **90**, 202303 (2003), [nucl-th/0301087](#).
- [Foc06] O. Fochler, *Energy loss of high- p_T partons in transport simulations of heavy ion collisions*, Diplomarbeit, Goethe-Universität Frankfurt, 2006.
- [FXG09] O. Fochler, Z. Xu and C. Greiner, *Towards a unified understanding of jet quenching and elliptic flow within perturbative QCD parton transport*, Phys. Rev. Lett. **102**, 202301 (2009), [0806.1169](#).
- [FXG10] O. Fochler, Z. Xu and C. Greiner, *Energy loss in a partonic transport model including bremsstrahlung processes*, Phys.Rev. **C82**, 024907 (2010), [1003.4380](#).
- [GB82] J. F. Gunion and G. Bertsch, *Hadronization by color bremsstrahlung*, Phys. Rev. **D25**, 746 (1982).
- [Gel95] M. Gell-Mann, *The quark and the jaguar: Adventures in the simple and the complex*, St. Martin's Griffin, September 1995.
- [GKL03] V. Greco, C. Ko and P. Levai, *Parton coalescence and anti-proton / pion anomaly at RHIC*, Phys.Rev.Lett. **90**, 202302 (2003), [nucl-th/0301093](#).
- [GKP98] S. Gubser, I. R. Klebanov and A. M. Polyakov, *Gauge theory correlators from noncritical string theory*, Phys.Lett. **B428**, 105–114 (1998), [hep-th/9802109](#).
- [GKT98] S. S. Gubser, I. R. Klebanov and A. A. Tseytlin, *Coupling constant dependence in the thermodynamics of $N=4$ supersymmetric Yang-Mills theory*, Nucl.Phys. **B534**, 202–222 (1998), [hep-th/9805156](#).

- [GLV00a] M. Gyulassy, P. Levai and I. Vitev, *Non-abelian energy loss at finite opacity*, Phys.Rev.Lett. **85**, 5535–5538 (2000), [nucl-th/0005032](#).
- [GLV00b] M. Gyulassy, P. Levai and I. Vitev, *Jet quenching in thin quark gluon plasmas. I. Formalism*, Nucl.Phys. **B571**, 197–233 (2000), [hep-ph/9907461](#).
- [GLV01] M. Gyulassy, P. Levai and I. Vitev, *Reaction operator approach to non-abelian energy loss*, Nucl. Phys. **B594**, 371–419 (2001), [nucl-th/0006010](#).
- [GM05] M. Gyulassy and L. McLerran, *New forms of QCD matter discovered at RHIC*, Nucl.Phys. **A750**, 30–63 (2005), [nucl-th/0405013](#), RIKEN BNL Research Center Scientific Articles, Vol.9.
- [Gro80] S. R. D. Groot, *Relativistic kinetic theory - principles and applications*, North-Holland, January 1980.
- [GRV95] M. Gluck, E. Reya and A. Vogt, *Dynamical parton distributions of the proton and small-x physics*, Z. Phys. **C67**, 433–448 (1995).
- [GSS03] M. Gazdzicki, R. Stock and P. Seyboth, *Has the deconfinement phase transition been seen?*, <http://cerncourier.com/cws/article/cern/28914>, 2003.
- [Gui06] V. Guiho, *Production de charmonia dans les collisions d'ions lourds ultra-relativistes: vers une approche unifiée*, Thèse de doctorat, Université de Nantes, 2006.
- [GW94] M. Gyulassy and X.-N. Wang, *Multiple collisions and induced gluon Bremsstrahlung in QCD*, Nucl. Phys. **B420**, 583–614 (1994), [nucl-th/9306003](#).
- [HAS70] W. K. HASTINGS, *Monte Carlo sampling methods using Markov chains and their applications*, Biometrika **57**(1), 97–109 (April 1970).
- [HKH⁺01] P. Huovinen, P. Kolb, U. W. Heinz, P. Ruuskanen and S. Voloshin, *Radial and elliptic flow at RHIC: Further predictions*, Phys.Lett. **B503**, 58–64 (2001), [hep-ph/0101136](#).
- [HM84] F. Halzen and A. D. Martin, *Quarks and leptons: An introductory course in modern particle physics*, John Wiley & Sons, 1st edition, February 1984.
- [JM05] S. Jeon and G. D. Moore, *Energy loss of leading partons in a thermal QCD medium*, Phys. Rev. **C71**, 034901 (2005), [hep-ph/0309332](#).
- [Joy99] J. Joyce, *Finnegans Wake*, Penguin Classics, December 1999.
- [Kan10] K. Kanaya, *Finite temperature QCD on the lattice – Status 2010*, PoS **LATTICE2010**, 012 (2010), [1012.4247](#).

- [KH03] P. F. Kolb and U. W. Heinz, *Hydrodynamic description of ultra-relativistic heavy ion collisions*, (2003), [nucl-th/0305084](#), Invited review for 'Quark Gluon Plasma 3'. Editors: R.C. Hwa and X.N. Wang, World Scientific, Singapore.
- [KH09] G. Kestin and U. W. Heinz, *Hydrodynamic radial and elliptic flow in heavy ion collisions from AGS to LHC energies*, Eur.Phys.J. **C61**, 545–552 (2009), [0806.4539](#).
- [Kle09] A. Klenke, *Wahrscheinlichkeitstheorie*, Springer, Berlin, 2., korrigierte auflage edition, August 2009.
- [KLL87] K. Kajantie, P. Landshoff and J. Lindfors, *Minijet production in high energy nucleus-nucleus collisions*, Phys.Rev.Lett. **59**, 2527 (1987).
- [Koc97] V. Koch, *Aspects of chiral symmetry*, Int.J.Mod.Phys. **E6**, 203–250 (1997), [nucl-th/9706075](#).
- [KSS05] P. Kovtun, D. T. Son and A. O. Starinets, *Viscosity in strongly interacting quantum field theories from black hole physics*, Phys. Rev. Lett. **94**, 111601 (2005), [hep-th/0405231](#).
- [Lee05] T. D. Lee, *The strongly interacting quark-gluon plasma and future physics*, Nucl. Phys. **A750**, 1–8 (2005).
- [Lep78] G. P. Lepage, *A new algorithm for adaptive multidimensional integration*, Journal of Computational Physics **27**(2) (May 1978).
- [LKL⁺05] Z.-W. Lin, C. M. Ko, B.-A. Li, B. Zhang and S. Pal, *A Multi-phase transport model for relativistic heavy ion collisions*, Phys.Rev. **C72**, 064901 (2005), [nucl-th/0411110](#).
- [Loi07] C. Loizides, *High transverse momentum suppression and surface effects in Cu+Cu and Au+Au collisions within the PQM model*, Eur.Phys.J. **C49**, 339–345 (2007), [hep-ph/0608133](#).
- [LP53] L. D. Landau and I. Pomeranchuk, *Limits of applicability of the theory of bremsstrahlung electrons and pair production at high energies*, Dokl. Akad. Nauk Ser. Fiz. **92**, 535–536 (1953).
- [LP04] J. M. Lattimer and M. Prakash, *The physics of neutron stars*, Science **304**(5670), 536–542 (April 2004).
- [Mal98] J. M. Maldacena, *The large N limit of superconformal field theories and supergravity*, Adv.Theor.Math.Phys. **2**, 231–252 (1998), [hep-th/9711200](#).
- [MG00] D. Molnar and M. Gyulassy, *New solutions to covariant nonequilibrium dynamics*, Phys.Rev. **C62**, 054907 (2000), [nucl-th/0005051](#).
- [Mig56] A. B. Migdal, *Bremsstrahlung and pair production in condensed media at high energies*, Phys. Rev. **103**, 1811–1820 (1956).

- [MN98] M. Matsumoto and T. Nishimura, *Mersenne twister: A 623-dimensionally equidistributed uniform pseudo-random number generator*, ACM Trans. Model. Comput. Simul. **8**, 3–30 (January 1998).
- [MN06] B. Mueller and J. L. Nagle, *Results from the Relativistic Heavy Ion Collider*, Ann. Rev. Nucl. Part. Sci. **56**, 93–135 (2006), [nucl-th/0602029](#).
- [MNB07] A. Majumder, C. Nonaka and S. A. Bass, *Jet modification in three dimensional fluid dynamics at next-to-leading twist*, Phys. Rev. **C76**, 041902 (2007), [nucl-th/0703019](#).
- [Mol09] E. Molnar, *Comparing the first and second order theories of relativistic dissipative fluid dynamics using the 1+1 dimensional relativistic flux corrected transport algorithm*, Eur.Phys.J. **C60**, 413–429 (2009), [0807.0544](#).
- [MRR⁺53] N. Metropolis, A. W. Rosenbluth, M. N. Rosenbluth, A. H. Teller and E. Teller, *Equation of state calculations by fast computing machines*, The Journal of Chemical Physics **21**(6), 1087 (1953).
- [MRSS07] M. L. Miller, K. Reygers, S. J. Sanders and P. Steinberg, *Glauber modeling in high energy nuclear collisions*, Ann.Rev.Nucl.Part.Sci. **57**, 205–243 (2007), [nucl-ex/0701025](#).
- [Mus05] M. G. Mustafa, *Energy loss of charm quarks in the quark-gluon plasma: Collisional versus radiative*, Phys.Rev. **C72**, 014905 (2005), [hep-ph/0412402](#).
- [MV94] L. D. McLerran and R. Venugopalan, *Computing quark and gluon distribution functions for very large nuclei*, Phys.Rev. **D49**, 2233–2241 (1994), [hep-ph/9309289](#).
- [MV03] D. Molnar and S. A. Voloshin, *Elliptic flow at large transverse momenta from quark coalescence*, Phys.Rev.Lett. **91**, 092301 (2003), [nucl-th/0302014](#).
- [MW00] G. Munster and M. Walzl, *Lattice gauge theory: A short primer*, pages 127–160 (2000), [hep-lat/0012005](#).
- [MWW07] A. Majumder, E. Wang and X.-N. Wang, *Modified dihadron fragmentation functions in hot and nuclear matter*, Phys.Rev.Lett. **99**, 152301 (2007), [nucl-th/0412061](#).
- [NA4904] C. Alt et al. (NA49 Collaboration), *Strangeness from 20-AGeV to 158-AGeV*, J.Phys.G **G30**, S119–S128 (2004), [nucl-ex/0305017](#).
- [NB99] M. Newman and G. T. Barkema, *Monte Carlo methods in statistical physics*, Oxford Univ Pr, April 1999.
- [NER09] H. Niemi, K. Eskola and P. Ruuskanen, *Elliptic flow in nuclear collisions at the Large Hadron Collider*, Phys.Rev. **C79**, 024903 (2009), [0806.1116](#).

- [NGT09] J. Noronha, M. Gyulassy and G. Torrieri, *Constraints on AdS/CFT gravity dual models of heavy ion collisions*, (2009), [0906.4099](#).
- [Njl61a] Y. Nambu and G. Jona-Lasinio, *Dynamical model of elementary particles based on an analogy with superconductivity. I*, Phys. Rev. **122**, 345–358 (1961).
- [Njl61b] Y. Nambu and G. Jona-Lasinio, *Dynamical model of elementary particles based on an analogy with superconductivity. II*, Phys. Rev. **124**, 246–254 (1961).
- [Nob10] Nobelprize.org, The Nobel Prize in Physics 2004, http://nobelprize.org/nobel_prizes/physics/laureates/2004/, 2010.
- [PDG10] K. Nakamura and P. D. Group (PDG Collaboration), *Review of particle physics*, Journal of Physics G: Nuclear and Particle Physics **37**(7A), 075021 (2010).
- [PHENIX02] K. Adcox et al. (PHENIX Collaboration), *Suppression of hadrons with large transverse momentum in central Au+Au collisions at $\sqrt{s_{NN}} = 130$ GeV*, Phys. Rev. Lett. **88**, 022301 (2002), [nucl-ex/0109003](#).
- [PHENIX03] S. S. Adler et al. (PHENIX Collaboration), *Elliptic flow of identified hadrons in Au+Au collisions at $\sqrt{s_{NN}} = 200$ GeV*, Phys. Rev. Lett. **91**, 182301 (2003), [nucl-ex/0305013](#).
- [PHENIX05] K. Adcox et al. (PHENIX Collaboration), *Formation of dense partonic matter in relativistic nucleus-nucleus collisions at RHIC: Experimental evaluation by the PHENIX collaboration*, Nucl. Phys. **A757**, 184–283 (2005), [nucl-ex/0410003](#).
- [PHENIX06] S. Adler et al. (PHENIX Collaboration), *Nuclear modification of electron spectra and implications for heavy quark energy loss in Au+Au collisions at $\sqrt{s_{NN}} = 200$ GeV*, Phys.Rev.Lett. **96**, 032301 (2006), [nucl-ex/0510047](#).
- [PHENIX07a] A. Adare et al. (PHENIX Collaboration), *Energy loss and flow of heavy quarks in Au+Au collisions at $\sqrt{s_{NN}} = 200$ GeV*, Phys.Rev.Lett. **98**, 172301 (2007), [nucl-ex/0611018](#).
- [PHENIX07b] A. Adare et al. (PHENIX Collaboration), *Scaling properties of azimuthal anisotropy in Au+Au and Cu+Cu collisions at $\sqrt{s_{NN}} = 200$ GeV*, Phys.Rev.Lett. **98**, 162301 (2007), [nucl-ex/0608033](#).
- [PHENIX07c] S. S. Adler et al. (PHENIX Collaboration), *A detailed study of high- p_T neutral pion suppression and azimuthal anisotropy in Au+Au collisions at $\sqrt{s_{NN}} = 200$ GeV*, Phys.Rev. **C76**, 034904 (2007), [nucl-ex/0611007](#).
- [PHENIX07d] S. Afanasiev et al. (PHENIX Collaboration), *Elliptic flow for phi mesons and (anti)deuterons in Au+Au collisions at $\sqrt{s_{NN}} = 200$ GeV*, Phys.Rev.Lett. **99**, 052301 (2007), [nucl-ex/0703024](#).

- [PHENIX08a] A. Adare et al. (PHENIX Collaboration), *Suppression pattern of neutral pions at high transverse momentum in Au+Au collisions at $\sqrt{s_{NN}} = 200$ GeV and constraints on medium transport coefficients*, Phys. Rev. Lett. **101**, 232301 (2008), [0801.4020](#).
- [PHENIX08b] K. Reygers (PHENIX Collaboration), *Characteristics of parton energy loss studied with high- p_T particle spectra from PHENIX*, J.Phys.G **G35**, 104045 (2008), [0804.4562](#).
- [PHENIX09a] S. Afanasiev et al. (PHENIX Collaboration), *High- p_T π^0 Production with Respect to the Reaction Plane in Au+Au Collisions at $\sqrt{s_{NN}} = 200$ GeV*, Phys. Rev. **C80**, 054907 (2009), [0903.4886](#).
- [PHENIX09b] R. Belmont (PHENIX Collaboration), *Deuteron and antideuteron measurements in Au+Au collisions at $\sqrt{s_{NN}} = 200$ GeV at RHIC PHENIX*, Eur.Phys.J. **C62**, 243–248 (2009).
- [PHENIX09c] Y.-S. Lai (PHENIX Collaboration), *Probing medium-induced energy loss with direct jet reconstruction in p+p and Cu+Cu collisions at PHENIX*, Nucl.Phys. **A830**, 251C–254C (2009), [0907.4725](#).
- [PHENIX10a] A. Adare et al. (PHENIX Collaboration), *Enhanced production of direct photons in Au+Au collisions at $\sqrt{s_{NN}} = 200$ GeV and implications for the initial temperature*, Phys. Rev. Lett. **104**, 132301 (2010), [0804.4168](#).
- [PHENIX10b] A. Adare et al. (PHENIX Collaboration), *Heavy quark production in p+p and energy loss and flow of heavy quarks in Au+Au collisions at $\sqrt{s_{NN}}=200$ GeV*, (2010), [1005.1627](#).
- [Phi10] O. Philipsen, *Lattice QCD at non-zero temperature and baryon density*, (2010), [arXiv:1009.4089](#).
- [PHOBOS05a] B. B. Back et al. (PHOBOS Collaboration), *Centrality and pseudorapidity dependence of elliptic flow for charged hadrons in Au+Au collisions at $\sqrt{s_{NN}} = 200$ GeV*, Phys. Rev. **C72**, 051901 (2005), [nucl-ex/0407012](#).
- [PHOBOS05b] B. B. Back et al. (PHOBOS Collaboration), *The PHOBOS perspective on discoveries at RHIC*, Nucl. Phys. **A757**, 28–101 (2005), [nucl-ex/0410022](#).
- [PS95] M. E. Peskin and D. V. Schroeder, *An introduction to quantum field theory*, Westview Press, 1995.
- [PSB⁺08] H. Petersen, J. Steinheimer, G. Burau, M. Bleicher and H. Stocker, *A fully integrated transport approach to heavy ion reactions with an intermediate hydrodynamic stage*, Phys.Rev. **C78**, 044901 (2008), [0806.1695](#).
- [PTVF07] W. H. Press, S. A. Teukolsky, W. T. Vetterling and B. P. Flannery, *Numerical Recipes 3rd Edition: The art of scientific computing*, Cambridge University Press, 3 edition, September 2007.

- [QRG⁺08] G.-Y. Qin, J. Ruppert, C. Gale, J. Sangyong, G. D. Moore and M. G. Mustafa, *Radiative and collisional jet energy loss in the quark-gluon plasma at RHIC*, Phys. Rev. Lett. **100**, 072301 (2008), [0710.0605](#).
- [QRT⁺07] G.-Y. Qin, J. Ruppert, S. Turbide, G. Charles, C. Nonaka and S. A. Bass, *Radiative jet energy loss in a three-dimensional hydrodynamical medium and high- p_T azimuthal asymmetry of π^0 suppression at mid and forward rapidity in Au+Au collisions at $\sqrt{s_{NN}} = 200$ GeV*, Phys. Rev. **C76**, 064907 (2007), [0705.2575](#).
- [RC04] C. P. Robert and G. Casella, *Monte Carlo statistical methods*, Springer, Berlin, 2. a. edition, September 2004.
- [Ren08] T. Renk, *Parton shower evolution in a 3-d hydrodynamical medium*, Phys.Rev. **C78**, 034908 (2008), [0806.0305](#).
- [RR07] P. Romatschke and U. Romatschke, *Viscosity information from relativistic nuclear collisions: How perfect is the fluid observed at RHIC?*, Phys. Rev. Lett. **99**, 172301 (2007), [0706.1522](#).
- [RRNB07] T. Renk, J. Ruppert, C. Nonaka and S. A. Bass, *Jet quenching in a 3D hydrodynamic medium*, Phys. Rev. **C75**, 031902 (2007), [nucl-th/0611027](#).
- [Sch06] C. Schmidt, *Lattice QCD at finite density*, PoS **LAT2006**, 021 (2006), [hep-lat/0610116](#).
- [SGJ09] B. Schenke, C. Gale and S. Jeon, *MARTINI: An event generator for relativistic heavy ion collisions*, Phys. Rev. **C80**, 054913 (2009), [0909.2037](#).
- [Shu78a] E. V. Shuryak, *Quark-gluon plasma and hadronic production of leptons, photons and psions*, Phys.Lett. **B78**, 150 (1978).
- [Shu78b] E. V. Shuryak, *Theory of hadronic plasma*, Sov.Phys.JETP **47**, 212–219 (1978).
- [Shu80] E. V. Shuryak, *Quantum chromodynamics and the theory of superdense matter*, Phys.Rept. **61**, 71–158 (1980).
- [Shu05] E. V. Shuryak, *What RHIC experiments and theory tell us about properties of quark-gluon plasma?*, Nucl.Phys. **A750**, 64–83 (2005), [hep-ph/0405066](#).
- [SJG11a] B. Schenke, S. Jeon and C. Gale, *Anisotropic flow in $\sqrt{s_{NN}} = 2.76$ TeV Pb+Pb collisions at the LHC*, (2011), [1102.0575](#).
- [SJG11b] B. Schenke, S. Jeon and C. Gale, *Elliptic and triangular flow in event-by-event (3+1)D viscous hydrodynamics*, Phys.Rev.Lett. **106**, 042301 (2011), [1009.3244](#).
- [SMS06] T. Sjostrand, S. Mrenna and P. Z. Skands, *PYTHIA 6.4: Physics and manual*, JHEP **0605**, 026 (2006), [hep-ph/0603175](#).

- [Sol10] W. Soldner, *Chiral aspects of improved staggered fermions with 2+1 flavors from the HotQCD collaboration*, PoS **LATTICE2010**, 215 (2010), [1012.4484](#).
- [SRMF09] C. G. Salzmann, P. G. Radaelli, E. Mayer and J. L. Finney, *Ice XV: A new thermodynamically stable phase of ice*, Physical Review Letters **103**(10), 105701 (2009).
- [SS07] G. P. Salam and G. Soyez, *A practical seedless infrared-safe cone jet algorithm*, JHEP **05**, 086 (2007), [0704.0292](#).
- [STAR02] C. Adler et al. (STAR Collaboration), *Centrality dependence of high- p_T hadron suppression in Au+Au collisions at $\sqrt{s_{NN}} = 130$ GeV*, Phys. Rev. Lett. **89**, 202301 (2002), [nucl-ex/0206011](#).
- [STAR03] J. Adams et al. (STAR Collaboration), *Transverse momentum and collision energy dependence of high- p_T hadron suppression in Au+Au collisions at ultra relativistic energies*, Phys. Rev. Lett. **91**, 172302 (2003), [nucl-ex/0305015](#).
- [STAR05a] J. Adams et al. (STAR Collaboration), *Experimental and theoretical challenges in the search for the quark gluon plasma: The STAR collaboration's critical assessment of the evidence from RHIC collisions*, Nucl. Phys. **A757**, 102–183 (2005), [nucl-ex/0501009](#).
- [STAR05b] J. Adams et al. (STAR Collaboration), *Azimuthal anisotropy in Au+Au collisions at $\sqrt{s_{NN}} = 200$ GeV*, Phys. Rev. **C72**, 014904 (2005), [nucl-ex/0409033](#).
- [STAR07a] B. Abelev et al. (STAR Collaboration), *Erratum: Transverse momentum and centrality dependence of high- p_T non-photonic electron suppression in Au+Au collisions at $\sqrt{s_{NN}} = 200$ GeV*, Phys.Rev.Lett. **98**, 192301 (2007), [nucl-ex/0607012](#).
- [STAR07b] B. Abelev et al. (STAR Collaboration), *Mass, quark-number, and $\sqrt{s_{NN}}$ dependence of the second and fourth flow harmonics in ultra-relativistic nucleus-nucleus collisions*, Phys.Rev. **C75**, 054906 (2007), [nucl-ex/0701010](#).
- [STAR08] B. I. Abelev et al. (STAR Collaboration), *Centrality dependence of charged hadron and strange hadron elliptic flow from $\sqrt{s_{NN}} = 200$ GeV Au+Au collisions*, Phys. Rev. **C77**, 054901 (2008), [0801.3466](#).
- [STAR09] M. Ploskon (STAR Collaboration), *Inclusive cross section and correlations of fully reconstructed jets in $\sqrt{s_{NN}} = 200$ GeV Au+Au and p+p collisions*, Nucl.Phys. **A830**, 255C–258C (2009), [0908.1799](#).
- [Ste06] M. Stephanov, *QCD phase diagram: An Overview*, PoS **LAT2006**, 024 (2006), [hep-lat/0701002](#).

- [SW03] C. A. Salgado and U. A. Wiedemann, *Calculating quenching weights*, Phys. Rev. **D68**, 014008 (2003), [hep-ph/0302184](#).
- [UFXG10a] J. Uphoff, O. Fochler, Z. Xu and C. Greiner, *Heavy quark production at RHIC and LHC within a partonic transport model*, Phys.Rev. **C82**, 044906 (2010), [1003.4200](#).
- [UFXG10b] J. Uphoff, O. Fochler, Z. Xu and C. Greiner, *Heavy quarks at RHIC and LHC within a partonic transport model*, (2010), [1011.6183](#).
- [UFXG11] J. Uphoff, O. Fochler, Z. Xu and C. Greiner, *Elliptic flow and energy loss of heavy quarks in ultra-relativistic heavy ion collisions*, (2011), to be published.
- [VPS08] S. A. Voloshin, A. M. Poskanzer and R. Snellings, *Collective phenomena in non-central nuclear collisions*, (2008), [0809.2949](#).
- [Wag99] W. Wagner, *The IAPWS formulation 1995 for the thermodynamic properties of ordinary water substance for general and scientific use*, Journal of Physical and Chemical Reference Data **31**(2), 387 (1999).
- [WBG05] M. R. Whalley, D. Bourilkov and R. C. Group, *The Les Houches Accord PDFs (LHAPDF) and Lhaglu*, (2005), [hep-ph/0508110](#).
- [WG91] X.-N. Wang and M. Gyulassy, *HIJING: A Monte Carlo model for multiple jet production in p+p, pA and A+A collisions*, Phys.Rev. **D44**, 3501–3516 (1991).
- [WG01] X.-N. Wang and X.-f. Guo, *Multiple parton scattering in nuclei: Parton energy loss*, Nucl.Phys. **A696**, 788–832 (2001), [hep-ph/0102230](#).
- [WGP95] X.-N. Wang, M. Gyulassy and M. Plumer, *Landau-Pomeranchuk-Migdal effect in QCD and radiative energy loss in a quark-gluon plasma*, Phys.Rev. **D51**, 3436–3446 (1995), [hep-ph/9408344](#).
- [WHDG07] S. Wicks, W. Horowitz, M. Djordjevic and M. Gyulassy, *Elastic, inelastic, and path length fluctuations in jet tomography*, Nucl. Phys. **A784**, 426–442 (2007), [nucl-th/0512076](#).
- [Wit98] E. Witten, *Anti-de Sitter space and holography*, Adv.Theor.Math.Phys. **2**, 253–291 (1998), [hep-th/9802150](#).
- [Won96] S. Wong, *Thermal and chemical equilibration in a gluon plasma*, Nucl.Phys. **A607**, 442–456 (1996), [hep-ph/9606305](#).
- [XG05] Z. Xu and C. Greiner, *Thermalization of gluons in ultra relativistic heavy ion collisions by including three-body interactions in a parton cascade*, Phys. Rev. **C71**, 064901 (2005), [hep-ph/0406278](#).
- [XG07] Z. Xu and C. Greiner, *Transport rates and momentum isotropization of gluon matter in ultrarelativistic heavy-ion collisions*, Phys. Rev. **C76**, 024911 (2007), [hep-ph/0703233](#).

- [XG08] Z. Xu and C. Greiner, *Shear viscosity in a gluon gas*, Phys. Rev. Lett. **100**, 172301 (2008), [0710.5719](#).
- [XG09] Z. Xu and C. Greiner, *Elliptic flow of gluon matter in ultra relativistic heavy ion collisions*, Phys. Rev. **C79**, 014904 (2009), [0811.2940](#).
- [XGS08] Z. Xu, C. Greiner and H. Stocker, *PQCD calculations of elliptic flow and shear viscosity at RHIC*, Phys. Rev. Lett. **101**, 082302 (2008), [0711.0961](#).
- [Zak96] B. G. Zakharov, *Fully quantum treatment of the Landau-Pomeranchuk-Migdal effect in QED and QCD*, JETP Lett. **63**, 952–957 (1996), [hep-ph/9607440](#).
- [Zha98] B. Zhang, *ZPC 1.0.1: A Parton cascade for ultra-relativistic heavy ion collisions*, Comput.Phys.Commun. **109**, 193–206 (1998), [nucl-th/9709009](#).
- [ZOWW07] H. Zhang, J. Owens, E. Wang and X.-N. Wang, *Dihadron tomography of high energy nuclear collisions in NLO pQCD*, Phys.Rev.Lett. **98**, 212301 (2007), [nucl-th/0701045](#).
- [ZSW09] K. Zapp, J. Stachel and U. A. Wiedemann, *A local Monte Carlo implementation of the non-abelian Landau-Pomeranchuk-Migdal effect*, Phys. Rev. Lett. **103**, 152302 (2009), [0812.3888](#).

Danksagung

Ich möchte mich an dieser Stelle ganz herzlich bei Prof. Dr. Carsten Greiner und Dr. Zhe Xu für die Betreuung der vorliegenden Arbeit bedanken. Sie haben die Entwicklung dieser Arbeit stets mit großem Interesse verfolgt, waren Ansprechpartner bei sich stellenden Problemen und haben mir vielfältige Möglichkeiten zum wissenschaftlichen Austausch geboten.

Ein ganz besonderer Dank gilt selbstverständlich meinen Eltern, die mir jegliche Unterstützung während des Studiums geboten und so letztlich die Erstellung dieser Arbeit überhaupt erst ermöglicht haben.

Des weiteren möchte ich mich vielmals bedanken bei: Björn Schenke und Jan Uphoff für das Korrekturlesen von Teilen dieser Arbeit, für eine ausgezeichnete Arbeitsatmosphäre im Büroalltag und für unzählige Diskussionen – auch und gerade über das Fachliche hinaus. Andrea Wesche für das Korrekturlesen von Teilen dieser Arbeit und die Unterstützung in all den Jahren ihrer Entstehung. Außerdem bei: Mauricio Martinez Guerrero für etliche Diskussionen, insbesondere zur Berechnung des Gunion-Bertsch Matrixelements. Den Mitgliedern und Organisatoren der Helmholtz Research School for Quark Matter Studies, H-QM, ganz besonders bei Henner Büsching. Sowie allen, deren namentliche Erwähnung mir an dieser Stelle entgangen ist.

Die Entstehung dieser Arbeit wurde unterstützt durch das Helmholtz International Center for FAIR im Rahmen des LOEWE-Programms des Landes Hessen, durch die Helmholtz Research School for Quark Matter Studies (H-QM), sowie die Helmholtz Graduate School for Hadron and Ion Research (HGS-HIRE). Die numerischen Berechnungen wurden auf den Rechenclustern des Center for Scientific Computing (CSC) der Goethe-Universität Frankfurt durchgeführt.

Erklärung

Ich versichere hiermit, die vorliegende Arbeit selbstständig verfasst und keine anderen als die angegebenen Hilfsmittel verwendet zu haben. Des weiteren sind sämtliche Stellen, die benutzten Werken im Wortlaut oder dem Sinn nach entnommen sind, mit Quellen- beziehungsweise Herkunftsangaben kenntlich gemacht.

Ort, Datum

Oliver Fochler

Lebenslauf

Angaben zur Person

Name: FOCHLER, Oliver
Anschrift: Rödelheimer Landstraße 174
60489 Frankfurt am Main
Geburtsdatum: 19.06.1981 in Frankfurt am Main
Nationalität: Deutsch
Familienstand: Ledig

Universitäre und schulische Bildung

Seit 10/2006 Promotion im Fach Physik an der Goethe-Universität Frankfurt
Thema: „Investigation of high- p_T phenomena in transport simulation of heavy ion collisions“
Mitglied der Helmholtz Research School for Quark Matter Studies (H-QM)
Mitglied der Helmholtz Graduate School for Hadron and Ion Research (HGS-Hire)

2001 – 2006 Studium der Physik an der Goethe-Universität Frankfurt

08/2006 Abschluss: Diplom-Physiker (*mit Auszeichnung*)
Thema: „Energy loss of high- p_T partons in transport simulations of heavy ion collisions“

10/2003 Vordiplom (1,0)

1991 – 2000 Liebiggymnasium Frankfurt am Main
Leistungskurse: Mathematik, Chemie

06/2000 Abitur (1,0)

Erfahrungen

Seit 10/2006 Wissenschaftlicher Angestellter der Goethe-Universität Frankfurt

Seit 06/2007 Mitarbeit in der Betreuung der IT-Systeme des Instituts für Theoretische Physik

2004 – 2007 Betreuung von Übungsgruppen in der Theoretischen Physik
Von 10/2004 bis 10/2006 als Studentische Hilfskraft, danach im Rahmen der Tätigkeit als Wissenschaftlicher Angestellter

- 2001 – 2004 Tätigkeit als lizenziertes Übungsleiter bei der TG Römerstadt, Betreuung von Volleyballmannschaften im Jugend- und Erwachsenenbereich
- 2000 – 2001 Zivildienstleistender bei der TSG Nordwest 1898

Publikationen

- O. Fochler, Z. Xu and C. Greiner, *Energy loss in a partonic transport model including bremsstrahlung processes*, *Phys.Rev.* **C82** (2010) 024907.
- O. Fochler, Z. Xu and C. Greiner, *Towards a unified understanding of jet quenching and elliptic flow within perturbative QCD parton transport*, *Phys. Rev. Lett.* **102** (2009) 202301.
- O. Fochler, S. Vogel, M. Bleicher, C. Greiner *et. al.*, *Canonical suppression in microscopic transport models*, *Phys.Rev.* **C74** (2006) 034902.
- J. Uphoff, O. Fochler, Z. Xu and C. Greiner, *Heavy quark production at RHIC and LHC within a partonic transport model*, *Phys.Rev.* **C82** (2010) 044906.
- J. Uphoff, O. Fochler, Z. Xu and C. Greiner, *Elliptic flow and energy loss of heavy quarks in ultra-relativistic heavy ion collisions*, (2011), to be published.
- I. Bouras, E. Molnar, H. Niemi, Z. Xu, A. El, O. Fochler, C. Greiner and D. Rischke, *Relativistic shock waves in viscous gluon matter*, *Phys. Rev. Lett.* **103** (2009) 032301.
- I. Bouras, E. Molnar, H. Niemi, Z. Xu, A. El, O. Fochler, C. Greiner and D. Rischke, *Investigation of shock waves in the relativistic Riemann problem: A comparison of viscous fluid dynamics to kinetic theory*, *Phys.Rev.* **C82** (2010) 024910.

Frankfurt am Main, 6. Juni 2011